ISSN 2461-4254

EUREKA: PHYSICS AND ENGINEERING

- Chemical Engineering
- Chemistry
- Computer Science
- Earth and Planetary Sciences
- Energy
- Engineering
- Materials Science
- Mathematics
- Physics and Astronomy

Volume 1(32)
2021

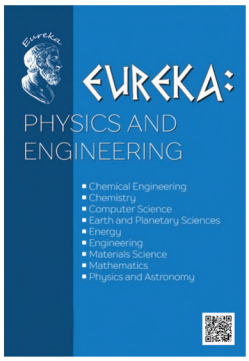

EUREKA: Physics and Engineering – scientific journal whose main aim is to publish materials allowed to see ***new discoveries at the intersection of sciences.***

- Chemical Engineering
- Chemistry
- Computer Science
- Earth and Planetary Sciences
- Energy
- Engineering
- Material Science
- Mathematics
- Physics and Astronomy
- Technology Transfer

EUREKA: Physics and Engineering
publishes 4 types of materials:
– review article,
– progress reports,
– original Research Article,
– reports on research projects

PUBLISHER OÜ «Scientific Route»
European Union
Editorial office
«EUREKA: Physical Sciences and Engineering»
Narva mnt 7-634, Tallinn, Eesti
Harju maakond, 10117
Tel. + 372 602-7570
e-mail: info@eu-jr.eu
Website: http://eu-jr.eu

EDITORIAL BOARD

CONTENT

REVIEW: COMPARISON OF ULTRASONICALLY AIDED ZINC BENEFICIATION BY MECHANICAL FLOTATION AND COLUMN FLOTATION CELL

Ugur Ulusoy
Division of Mineral Processing
Department of Mining Engineering[1]
uulusoy@cumhuriyet.edu.tr

Hulya Kurşun
Department of Material and Metallurgical Engineering[1]
hkursun@cumhuriyet.edu.tr

[1]*Sivas Cumhuriyet University*
Sivas, Turkey, TR-58140

Abstract

Zinc is a key beneficiary of economic development for the developing countries. While the global zinc mine production in 2019 was recorded as 13 million tons, the value of zinc mined in 2019, based on zinc contained in concentrate, was about $2.1 billion. Sphalerite or zinc blende (ZnS), which is the main source of zinc, provides more than 90 % of zinc productions today. Beneficiation is usually carried out by flotation to produce marketable concentrates (45–55 % Zn). The flotation, which is the most widely used separation process at fine sizes for the concentration of low grade complex Pb-Cu-Zn ores plays an important role in the global economy. In any concentration plant employing flotation technique huge quantity of ores are being processed. Thus, any increments in the flotation recovery are important to get higher profits and to ensure that resources are utilized optimally. In this review, a comparative evaluation was made between mechanical flotation (MF) [1] and column (CF) [2] cells with or without ultrasonic pre-treatment (UP) for zinc recovery from lead-zinc-copper ore and the effect of UP on the MF and CF experiments were investigated at the optimized conditions. When compared with the optimized parameters, UP increased zinc grade and recovery for both MF and CF techniques as supported by XRD patterns. Besides, the best zinc grade and recovery was obtained by UP with CF technique. So that, sphalerite mineral can be effectively beneficiated to produce saleable zinc concentrate product and UP with CF will lead to a higher metallurgical gains and improvements to Net Smelter Return (NSR). This positive effect of ultrasound, which is safe and eco-friendly, on the zinc flotation by both mechanical cell and column cell regarding zinc grade and recovery is in good agreement with the previous published works in the literature.

Keywords: Zinc, mechanical flotation, column flotation, flotation, grade, recovery, ultrasonic treatment, XRD, cavitation.

DOI: 10.21303/2461-4262.2021.001608

1. Introduction

The economic growing of countries mostly contingent on transforming their underground wealth into advantageous commodities [3]. Zinc is one of those resources, which is a mild, shiny silvery to steel-grey metal that often occurs in the presence of other minerals of copper, lead, and silver. It is essential to modern living, and, in tonnage produced, stands fourth among all metals in world production – being exceeded only by iron, aluminum, and copper. Zinc has unique chemical characteristics such as brittle until heated above 100 °C, then becomes malleable, stops oxidation and corrosion of underlying metal when applied as a coating (galvanization) and becomes strong as steel but flexible when combined with aluminum. These make zinc an indispensable element to life and industry and zinc uses range from metal products to rubber and medicines especially automotive, machinery manufacturing, construction metals and communications. Therefore, it is a critical element in a broad sort of products including coatings, castings, alloys, mill products and chemicals and other specialist applications [4]. About three-fourths of zinc used is consumed as metal, mainly as a coating to protect iron and steel from corrosion (galvanized metal), as alloying metal to make bronze and brass, as zinc-based die casting alloy, and as rolled zinc [5]. As reported by USGS [6] Global zinc mine production in 2019 was estimated to be 13 million tons, a 4 % increase from that of 2018. It is of great significant to exploit

the low-grade zinc oxide ores and improve the utilization ratio of the zinc natural resources. Zinc minerals are generally associated with other metal minerals, the most common associations in ores being zinc-lead, lead-zinc, zinc-copper, copper-zinc, zinc-silver, or zinc only. Run-of-mine zinc-containing ores must be enriched before smelting and refining because of their low zinc content.

Sphalerite is one of the sulfide minerals (frequently found together along with galena and chalcopyrite in complex Pb-Cu-Zn ores) separated from gangue minerals by conventional flotation techniques to produce marketable zinc concentrates containing 45–55 % Zn. Since huge quantity of ores are being processed by flotation, any increments in the flotation recovery does matters and cause remarkable profits [7]. The pulp must be conditioned before flotation to make valuable mineral hydrophobic. Since conditioning has a direct impact on the pulp residence time and plant throughput, various ways of facilitating conditioning process were investigated [8–11]. One of the ways of applying ultrasonic energy into pulp is using an ultrasonic cleaning bath [12].

As it is well known, ultrasound is characterized with sound waves having frequencies greater than20 kHz [13] and it plays superior role in the mineral surface. Frequencies which are measured in thousands of cycles per second (kHz) are produced by ultrasound transducers attached to the bottom, and in some cases also the sides, of the ultrasonic cleaning bath. The transducers are excited by the unit's ultrasonic generator to produce millions of microscopic bubbles in the solution that implode on contact with parts. This implosion is known as «cavitation» [14]. while hydrodynamic cavitation is defined as a process by which bubbles are produced when the local pressure is diminished to a level that destroy a liquid-liquid or solid-liquid interface in a flowing film [15]. The ultrasonic treatment (20–40 kHz) is based on the cavitation causing hydrodynamic shear [16] and giving rise to the dispersion of aggregates [17].

The size at which a particle becomes a «fine particle» is described as the size finer than the minimum for optimal flotation recovery [18]. Two primary approaches such as increasing of the particle size and decreasing of the bubble size were used to improve the fine particle recovery in the flotation process [19]. Fine particles are best floated with small bubbles, and hydrodynamic conditions inside a mechanical flotation (MF) cell are not appropriate for fine particle flotation. Column flotation (CF) provides higher concentration, more productivity, less cost of production, and better control of plant than the conventional MF mainly due to the long retention time of the solid particles, counter current flow, contact pattern and the wash water added at the top of the froth [20–22]. Moreover, CF has an advantage in recovering of fine particles than MF due to more favorable conditions and smaller bubbles. The small bubbles can be produced by hydrodynamic cavitation [23].

In the mineral industry ultrasound has been recently utilized as a positive element in successful manner. For example, iron elimination on the silica sand can be removed with efficiency by ultrasound than by mechanical scrubbing. Moreover, the combination of ultrasound and solutions of some chemicals like water glass, soda and sodium pyrophosphate, can remove iron faster owing to the synergistic effect [24–26]. The effects of UP on the flotation studied by many researchers using different coals, ores and minerals [27–50]. It has been concluded that UP increased the flotation recovery, reduced reagents consumption, and decreased the ash content. Most of the research work in flotation has been addressed to a better understanding of the variables affecting the separation. In the recent study related to zinc flotation [51] zinc recovery from lead-zinc-copper ore was higher by CF cell than MF. Nevertheless, much remains to be done regarding comparison of the effects of UP on the MF and CF. According to the knowledge of the authors no efforts were done to compare the effect of UP by using a laboratory ultrasound bath on the zinc flotation recovery from the same ore using MF and CF except for our works [1, 2]. Therefore, the aim of this work is to review and compare the effect of UP on the MF [1] and CF [2] performances in terms of Zn grade and recovery using the same ore. By this review study let's look for the answer to some questions like which one is more effective in terms of separation recovery and zinc grade? Secondly, is ultrasound really affecting on these two different beneficiation techniques positively? In other way of saying, does ultrasonic pretreatment aid to increase

the separation recovery and zinc grade of the concentrates by mechanical flotation and column flotation using the same material.

The flotation conditions optimized for both flotation experiments were as follows: For MF tests [1], effects of Potassium Amyl Xanthate (KAX) describe it fully dosage, $CuSO_4$ dosage, 2-ethyl hexanol dosage, residence time, stirring speed, and Na_2SiO_3 dosage on MF performance were tested to hold the optimum conditions. For the effects of UP on MF tests, KAX dosage, $CuSO_4$ dosage, Aerofloat 211 dosage, Na_2SiO_3 dosage, 2-ethyl hexanol dosage, optimum flotation time and stirring speed on the MF performance were set as 90 g/t, 400 g/t, 100 g/t, 50 g/t, 15 g/t, 4 min., and 1000 rpm, respectively. The effects of each parameter on the MF tests were already described in detail by the previous study [1].

As for CF optimization tests [2], effects of KAX dosage, 2-ethyl hexanol dosage, residence time, stirring speed, Na_2SiO_3 dosage, superficial air rate, superficial wash water rate, and superficial feed rate on CF performance were tested and the fixed parameters for the effect of UP on the CF for both single and multistage zinc beneficiation were set as 400 g/t of $CuSO_4$, 100 g/t of Aerofloat 211, 15 g/t of 2-ethyl hexanol, 50 g/t of Na_2SiO_3, 90 g/t of KAX, 160 rpm of stirring speed, 0.170 cm/sec of superficial wash water rate, 0.425 cm/sec of superficial feed rate, 1.5 cm. sec of superficial air rate and 4 min. of residence time. The comparison of the ultrasonic effect on the two different flotation techniques was accomplished by using a 12-liter laboratory-scale ultrasonic cleaning bath having 40 kHz (power of 600 watt).

2. Optimization of flotation for mechanical and column cells

For comparative evaluation between MF and CF the same zinc samples [1, 2, 51] was taken from zinc feed of the selective zinc flotation circuit plant (İvrindi-Balıkesir in Turkey) and treating lead-zinc-copper complex ore containing Pb, Cu, and Zn as 3.23 %, 0.52 %, and 2.71 %, respectively. The XRD of the ore was given previously [1]. Particle size distribution (psd) of the samples used for this review is given in **Fig. 1**, which shows the whole particle size is below 74 µm. While MF experiments is shown in **Fig. 2** [1] CF tests are illustrated by **Fig. 3** [2].

Concentrate grade and recovery values at different operating conditions should be tested for inferring the optimal operating conditions for comparing flotation performance of the same ore tested for the effect of ultrasonic pretreatment on the mechanical and column cell for different conditions.

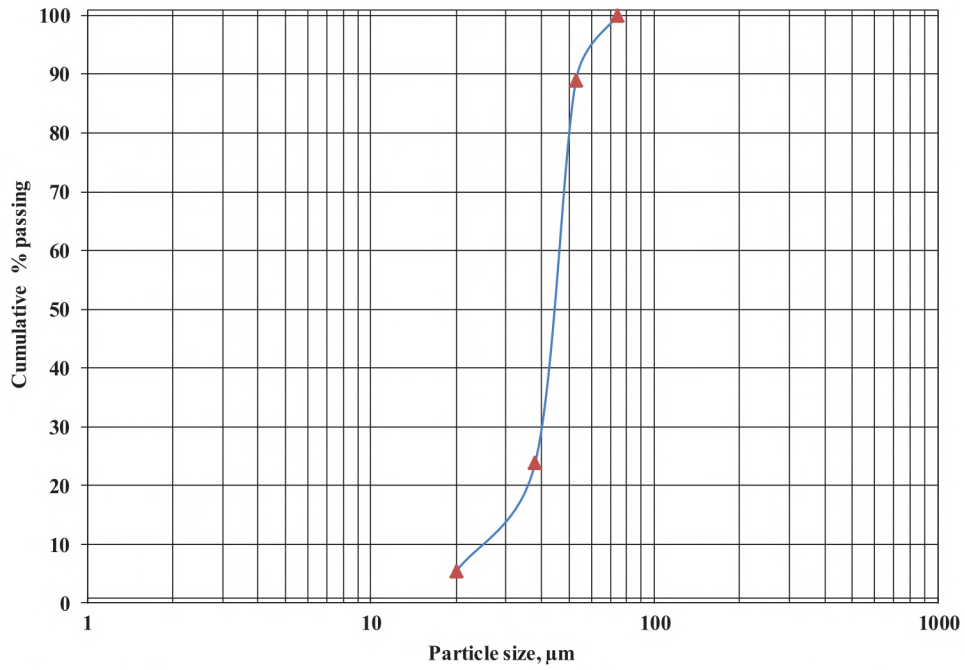

Fig. 1. Particle size distributions of the samples used in MF and CF tests (redrawn from [1, 2])

Fig. 2. Experimental setup used in MF tests with UP

Fig. 3. Experimental setup used in CF tests with UP [2]

3. Results and discussion

As shown in **Fig. 4**, the zinc grade and recovery with MF followed by UP augmented 10.21 % and 8.54 %, respectively. This result is in agreement with the previously published works [29, 37, 49].

Results of X-ray diffraction patterns of the raw ore, MF concentrate without UP and MF concentrate with UP (**Fig. 5, *a*–*d***) were also support this improvement. It should be noted that UP plays positive role on zinc content on MF since the highest sphalerite peaks were observed in MF concentrate with UP (**Fig. 5**, ***c***) whereas the lowest Quartz peaks were observed in in **Fig. 5, *c*** as clearly evident by the **Fig. 5, *d***, which represent all in one.

Since industrial flotation is a continuous and often multistage process, CF tests were also implemented by using 3 stages of batch cleaning and 3 stages of batch scavenging flotation expe-

riments using the same laboratory column cell in this work. At the optimized CF conditions [2], single stage and multiple stages of CF with UP tests were conducted. Comparing the zinc grade and recovery values by single stage CF with and without UP (**Fig. 4**), the zinc grade was raised with 7.58 units while the recovery was enhanced by 10.56 units. When 3 stages of cleaning and 3 stages of scavenging CF experiments carried out, zinc grade of the final concentrate was increased 19.91 units. On the other hand, zinc recovery was increased 4.96 units. Therefore, this result indicates that by using UP with CF sphalerite mineral can be effectively recovered for marketable zinc concentrate product. These findings are in good agreement with the previously reported studies [49, 37, 29, 52].

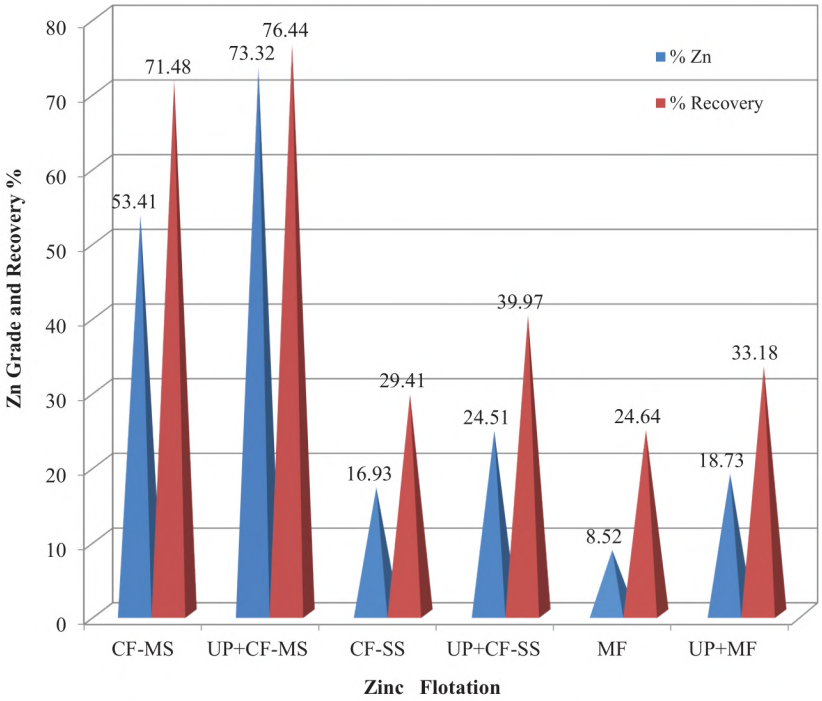

Fig. 4. Effect of UP on the performance of CF and MF in terms of zinc grade and recovery (redrawn from [1, 2]. *(Here; **CF-MS**; Multi Stage Colum Flotation, **UP+CF-MS**; Multi Stage Colum Flotation with Ultrasonic Pre-treatment, **CF-SS**; Single Stage Colum Flotation, **UP+CF-SS**; Single Stage Colum Flotation with Ultrasonic Pre-treatment, **MF**; Mechanical Flotation, **UP+MF**; Mechanical Flotation with Ultrasonic Pre-treatment)*

As shown in **Fig. 6** increase in the superficial air rate augmented the zinc recovery in CF, but diminished the zinc grade up to the values of 1.5 cm/sec. Bubbles were growth due to the coalescence (at superficial air rate values higher than 2.0 cm/sec.) intensive slurry stirring and collapsing as evidence by **Fig. 7** showing air bubble images captured at different air rates. The bubbly flow conditions, which were preferred in CF were damaged and transformed to the churn-turbulent flow conditions as large bubbles indicates worsening of flotation process as proposed by [53].

Comparison of the CF and MF results indicated that zinc grade and recovery for CF was substantially higher than MF not surprisingly for the same ore tested in this work since the main advantage of the CF cells over MF ones is higher separation performance. Besides, MF cell use agitation mechanism while in CF air bubbles are produced by air spargers connected with a compressor and CF use wash water system to wash out the hydrophilic particles entrained into the froth zone, hence preventing their recovery to the concentrate in order to increase performance and selectivity. From **Fig. 4**, the zinc grade and recovery for both CF and MF with UP were higher than the zinc grade and recovery for both CF and MF without UP when UP was applied to both CF and MF cell.

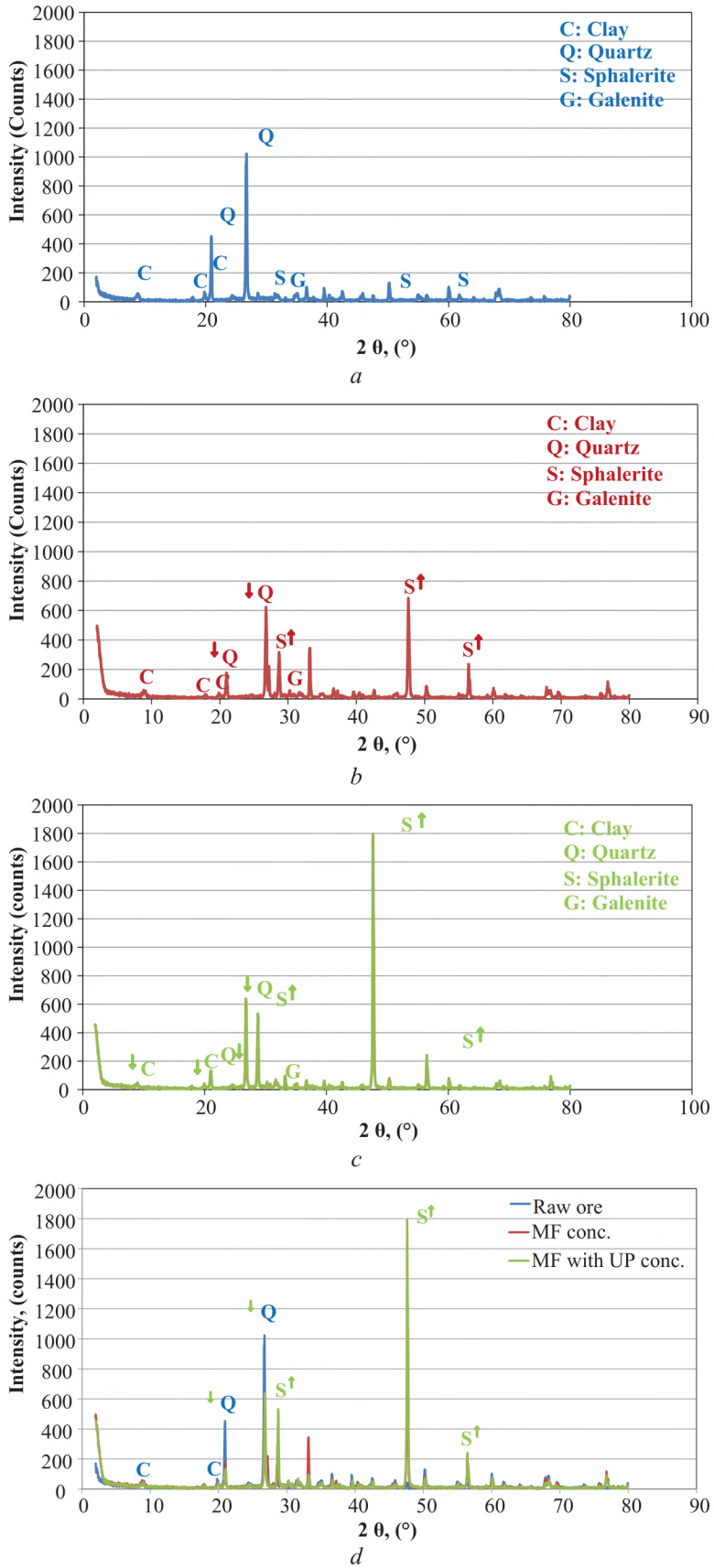

Fig. 5. XRD patterns:
a – the raw ore; *b* – concentrate of MF; *c* – concentrate of MF with UP; *d* – all in one [1]

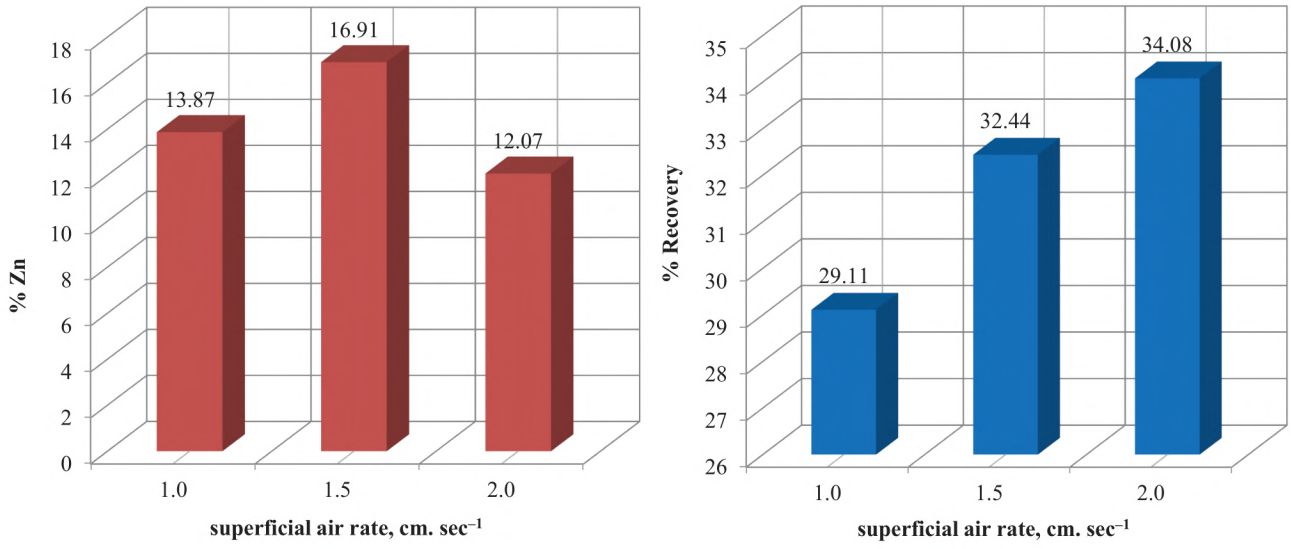

Fig. 6. Impacts of superficial air rate on the grade and recovery of zinc flotation in CF (redrawn from [2]): *a* – grade; *b* – recovery

Fig. 7. Captured images of flotation bubbles at different air rates in the CF tests without UP (modified from [2]): *a* – 0.5 cm. sec^{-1}; *b* – 1 cm. sec^{-1}; *c* – 1.5 cm. sec^{-1}; *d* – 2 cm. sec^{-1}; *e* – >2 cm. sec^{-1}

Both improvements in the zinc grade and recovery may be attributed to the dispersing effects of ultrasound, increasing adsorption of collectors on the particle surfaces. It may also be due to the hydrodynamic cavitation, which produced small bubbles [49, 37, 29, 54, 55, 28] attaching to the hydrophobic particles and leading to the agglomeration of ultrafine particles by bubble bridging, making them as if they were larger particles of higher probability of attachment to the large bubbles in a flotation cell thereby increasing contact angle, attachment forces, the bubble-particle collision efficiency and better flotation recovery [37, 15, 35]. It has found that, ultrasonic treatment was good for the adsorption of collector molecules and increased the flotation yield by making fine particles hard to stick to the bubbles surfaces to improve the selectivity of fine particles [56]. Besides, ultrasound can raise the adsorption of cavitation bubbles on the particles and enhance the hydrophobicity of coal particle surface. In addition, micro bubbles were favored to adsorb on hydrophobic particle surface, which also amended hydrophobicity and heightened the efficiency of collision/adhesion between hydrophobic particles and air bubbles for higher flotation recovery rate. It has been also reported that, transient cavitation bubbles generate more fresh and hydrophobic surfaces on the particles surfaces to become profoundly cleaned and more easily picked by flotation [57, 58].

Fig. 8 shows bubble-particle aggregates formed by attachment of the small bubbles on the hydrophobic particles. The aggregation of sphalerite mineral particles by UP owing to cavitation effect is an indication of improved flotation efficiency. It supports the improvements in flotation performance [55, 29]. Since the economic efficiency of the plant is assessed either by the net smelter return per ton of ore or the net revenue of the concentrator [59], flotation process with UP will

produce a high-grade concentrate that maximizes an economic performance index, which may be as simple as the net revenue of the plant.

Fig. 8. The bubble-particle aggregates formed by in UP at CF tests (modified from [2])

The intensity of ultrasound would affect the degree of zinc recovery. Since there are all instruments at laboratory scale, cost estimation or techno-economic evaluation for this proposed process has not been considered in this study due to the insufficient information. The use of high power and continuous-type ultrasound need to be studied because they may enhance both MF and CF process. An economic assessment of the ultrasonic pretreatment methods must be made to determine their feasibility when designing an industrial mechanical and column flotation processes.

4. Conclusions

Since CF has an advantage in recovering of fine particles than MF because of more favorable conditions and smaller bubbles. The small bubbles can be produced by using UP with CF. So, zinc grade and recovery for CF at single stage and multistage was substantially higher than MF of zinc flotation.

In fact, CF is known to provide higher concentration, more productivity, less cost of production, and better control of plant than the conventional MF owing to the long retention time of the solid particles, counter current flow, contact pattern and the wash water added at the top of the froth.

Above all, UP increased zinc grade and recovery for both MF and CF techniques as supported by XRD patterns. Considering great tonnage of ores is being processed by flotation, any increments in the flotation recovery will make noteworthy profits. Besides, UP with CF will lead to a higher metallurgical gains and improvements to Net Smelter Return (NSR).

The contribution effect of ultrasound, which is safe and eco-friendly, on the flotation performance may because of increasing dispersion, increasing adsorption of collectors and generation of more fresh and hydrophobic surfaces. So that hydrodynamic cavitation, produces small bubbles attaching to the hydrophobic particles to increase contact angle and attachment forces causing bubble-particle collision efficiency and better flotation recovery.

This review introduces UP as one of the bright and sustainable method for amending flotation of zinc ores.

Acknowledgments

Thanks are extended to the operating manager of GESOM A. Ş. for providing ore samples. The authors express appreciation to Prof. Dr. Murat Erdemoğlu and Prof. Dr. HüseyinYalçın for their help in XRD analysis and interpretation.

References

[1] Kursun, H. (2014). A Study on the Utilization of Ultrasonic Pretreatment in Zinc Flotation. Separation Science and Technology, 49 (18), 2975–2980. doi: https://doi.org/10.1080/01496395.2014.941876

[2] Kursun, H., Ulusoy, U. (2014). Zinc Recovery from a Lead–Zinc–Copper Ore by Ultrasonically Assisted Column Flotation. Particulate Science and Technology, 33 (4), 349–356. doi: https://doi.org/10.1080/02726351.2014.970314

[3] Barma, S. D. (2019). Ultrasonic-assisted coal beneficiation: A review. Ultrasonics Sonochemistry, 50, 15–35. doi: https://doi.org/10.1016/j.ultsonch.2018.08.016

[4] Renken, P. (2011). Zinc. Mining Commodity report. VSA Capital, London.

[5] Zinc Statistics and Information. Available at: https://www.usgs.gov/centers/nmic/zinc-statistics-and-information

[6] Zinc (2020). Mineral Commodity Summaries. Available at: https://pubs.usgs.gov/periodicals/mcs2020/mcs2020-zinc.pdf

[7] Koh, P., Smith, L. (2010). Experimental validation of a flotation cell model. XXV International Mineral Processing Congress (IMPC) 2010 Proceedings. Brisbane.

[8] Stassen, F. J. N. (1991). Conditioning in the flotation of gold, uranium oxide and pyrite. Journal of the Southern African Institute of Mining and Metallurgy, 91 (5), 169–174.

[9] Bulatovic, S. M., Salter, R. S. (1989). High intensity conditioning – a new approach to improving flotation of mineral slimes. Processing of Complex Ores, 169–181. doi: https://doi.org/10.1016/b978-0-08-037283-9.50020-2

[10] Rubio, J., Brum, I. (1994). The conditioning effect on the flotation of copper/molybdenum mineral particles. In Proceedings Southern Hemisphere Meeting on Mineral Technology, 4, Concepción-Chile, Proceedings, 2, 295–308.

[11] Aldrich, C., Feng, D. (1999). Effect of ultrasonic preconditioning of pulp on the flotation of sulphide ores. Minerals Engineering, 12 (6), 701–707. doi: https://doi.org/10.1016/s0892-6875(99)00053-9

[12] Teipel, U., Leisinger, K., Mikonsaari, I. (2004). Comminution of crystalline material by ultrasonics. International Journal of Mineral Processing, 74, S183–S190. doi: https://doi.org/10.1016/j.minpro.2004.07.011

[13] Leonelli, C., Mason, T. J. (2010). Microwave and ultrasonic processing: Now a realistic option for industry. Chemical Engineering and Processing: Process Intensification, 49 (9), 885–900. doi: https://doi.org/10.1016/j.cep.2010.05.006

[14] 5 Key Points to Selecting the Correct Ultrasonic Cleaner Size. Available at: http://www.tovatech.com/ultrasonic-cleaner/how-ultrasonics-works.php

[15] Zhou, Z. A., Xu, Z., Finch, J. A., Hu, H., Rao, S. R. (1997). Role of hydrodynamic cavitation in fine particle flotation. International Journal of Mineral Processing, 51 (1-4), 139–149. doi: https://doi.org/10.1016/s0301-7516(97)00026-4

[16] Khanal, S. K., Grewell, D., Sung, S., van Leeuwen, J. (Hans) (2007). Ultrasound Applications in Wastewater Sludge Pretreatment: A Review. Critical Reviews in Environmental Science and Technology, 37 (4), 277–313. doi: https://doi.org/10.1080/10643380600860249

[17] Basedow, A. M., Ebert, K. H. (1977). Ultrasonic degradation of polymers in solution. Advances in Polymer Science, 83–148. doi: https://doi.org/10.1007/3-540-07942-4_6

[18] Subrahmanyam, T. V., Forssberg, K. S. E. (1990). Fine particles processing: shear-flocculation and carrier flotation – a review. International Journal of Mineral Processing, 30 (3-4), 265–286. doi: https://doi.org/10.1016/0301-7516(90)90019-u

[19] Song, S., Lopez-Valdivieso, A., Reyes-Bahena, J. L., Lara-Valenzuela, C. (2001). Floc flotation of galena and sphalerite fines. Minerals Engineering, 14 (1), 87–98. doi: https://doi.org/10.1016/s0892-6875(00)00162-x

[20] Finch, J. A., Dobby, G. S. (1990). Column flotation. Oxford: Pergamon Press.

[21] Somasundaran, P. (1986). An Overview of the Ultrafine Problem. Mineral Processing at a Crossroads, 1–36. doi: https://doi.org/10.1007/978-94-009-4476-3_1

[22] Kawatra, S. K., Eisele, T. C. (1987). Column Flotation of Coal. In Fine Coal Processing, Klimpel, Noyes, Park Ridge, New Jersey, 414–426.

[23] Demers, I. (2005). Enhancing fine particle recovery in flotation and its potential application to the environmental desulphurization process. University of Quebec.

[24] Farmer, A. D., Collings, A. F., Jameson, G. J. (2000). Effect of ultrasound on surface cleaning of silica particles. International Journal of Mineral Processing, 60 (2), 101–113. doi: https://doi.org/10.1016/s0301-7516(00)00009-0

[25] Zhao, H. L., Wang, D. X., Cai, Y. X., Zhang, F. C. (2007). Removal of iron from silica sand by surface cleaning using power ultrasound. Minerals Engineering, 20 (8), 816–818. doi: https://doi.org/10.1016/j.mineng.2006.10.005

[26] Farmer, A. D., Collings, A. F., Jameson, G. J. (2000). The application of power ultrasound to the surface cleaning of silica and heavy mineral sands. Ultrasonics Sonochemistry, 7 (4), 243–247. doi: https://doi.org/10.1016/s1350-4177(00)00057-2

[27] Ślączka, A. (1987). Effects of an ultrasonic field on the flotation selectivity of barite from a barite-fluorite-quartz ore. International Journal of Mineral Processing, 20 (3-4), 193–210. doi: https://doi.org/10.1016/0301-7516(87)90066-4

[28] Gurpinar, G., Sonmez, E., Bozkurt, V. (2004). Effect of ultrasonic treatment on flotation of calcite, barite and quartz. Mineral Processing and Extractive Metallurgy, 113 (2), 91–95. doi: https://doi.org/10.1179/037195504225005796

[29] De F. Gontijo, C., Fornasiero, D., Ralston, J. (2008). The Limits of Fine and Coarse Particle Flotation. The Canadian Journal of Chemical Engineering, 85 (5), 739–747. doi: https://doi.org/10.1002/cjce.5450850519

[30] Celik, M. S. (1989). Effect of Ultrasonic Treatment on the Floatability of Coal and Galena. Separation Science and Technology, 24 (14), 1159–1166. doi: https://doi.org/10.1080/01496398908049894

[31] Feng, D., Aldrich, C. (2004). Effect of Ultrasonication on the Flotation of Talc. Industrial & Engineering Chemistry Research, 43 (15), 4422–4427. doi: https://doi.org/10.1021/ie034057g

[32] Ozkan, S. G. (2002). Beneficiation of magnesite slimes with ultrasonic treatment. Minerals Engineering, 15 (1-2), 99–101. doi: https://doi.org/10.1016/s0892-6875(01)00205-9

[33] Franko, J., Klima, M. S. (2002). Application of ultrasonics to enhance wet-drum magnetic separator performance. Mining, Metallurgy & Exploration, 19 (1), 17–20. doi: https://doi.org/10.1007/bf03402895

[34] Pandey, J. C., Sinha, M., Raj, M. (2010). Reducing alumina, silica and phosphorous in iron ore by high intensity power ultrasound. Ironmaking & Steelmaking, 37 (8), 583–589. doi: https://doi.org/10.1179/030192310x12731438632083

[35] Misra, M., Raichur, A. M., Lan, A. P. (2003). Improved flotation of arsenopyrite by ultrasonic pretreatment. Mining, Metallurgy & Exploration, 20 (2), 93–97. doi: https://doi.org/10.1007/bf03403138

[36] Zhou, Z. A. (1996). Gas nucleation and cavitation in flotation. McGill University.

[37] Zhou, Z. A., Xu, Z., Finch, J. A. (1994). On the role of cavitation in particle collection during flotation - a critical review. Minerals Engineering, 7 (9), 1073–1084. doi: https://doi.org/10.1016/0892-6875(94)00053-0

[38] Zhou, Z. A., Xu, Z., Finch, J. A. (1995). Fundamental study of cavitation in flotation. In: XIX International Mineral Processing Congress. Vol. 3. San Francisco, 93–97.

[39] Cilek, E. C., Ozgen, S. (2010). Improvement of the Flotation Selectivity in a Mechanical Flotation Cell by Ultrasound. Separation Science and Technology, 45 (4), 572–579. doi: https://doi.org/10.1080/01496390903484966

[40] Nicol, S. K., Engel, M. D., Kee Chye Teh. (1986). Fine-particle flotation in an acoustic field. International Journal of Mineral Processing, 17 (1-2), 143–150. doi: https://doi.org/10.1016/0301-7516(86)90052-9

[41] Buttermore, W. H., Slomka, B. J. (1991). The effect of sonic treatment on the flotability of oxidized coal. International Journal of Mineral Processing, 32 (3-4), 251–257. doi: https://doi.org/10.1016/0301-7516(91)90071-p

[42] Attalla, M., Chao, C., Nicol, S. K. (2000). The role of cavitation in coal flotation. In Proc. of the 8th Australian Coal Preparation Conference, Port Stephens, NSW. Australian Coal Preparation Society, 337–350.

[43] Jun, H., Dian-Zuo, W., Yong-Ping, H. (2002). Research on coal flotation by co-action of reagents and ultrasonic wave treatment. Journal of China University of Mining & Technology, 31 (2), 186–189.

[44] Ozkan, S. G., Kuyumcu, H. Z. (2006). Investigation of mechanism of ultrasound on coal flotation. International Journal of Mineral Processing, 81 (3), 201–203. doi: https://doi.org/10.1016/j.minpro.2006.07.011

[45] Ozkan, Ş. G., Kuyumcu, H. Z. (2007). Design of a flotation cell equipped with ultrasound transducers to enhance coal flotation. Ultrasonics Sonochemistry, 14 (5), 639–645. doi: https://doi.org/10.1016/j.ultsonch.2006.10.001

[46] Kang, W., Xun, H., Hu, J. (2008). Study of the effect of ultrasonic treatment on the surface composition and the flotation performance of high-sulfur coal. Fuel Processing Technology, 89 (12), 1337–1344. doi: https://doi.org/10.1016/j.fuproc.2008.06.003

[47] Ozkan, S. G. (2012). Effects of simultaneous ultrasonic treatment on flotation of hard coal slimes. Fuel, 93, 576–580. doi: https://doi.org/10.1016/j.fuel.2011.10.032

[48] Tao, Y., Liu, J., Yu, S., Tao, D. (2006). Picobubble Enhanced Fine Coal Flotation. Separation Science and Technology, 41 (16), 3597–3607. doi: https://doi.org/10.1080/01496390600957249

[49] Qi, B. C., Aldrich, C. (2002). Effect of ultrasonic treatment on zinc removal from hydroxide precipitates by dissolved air flotation. Minerals Engineering, 15 (12), 1105–1111. doi: https://doi.org/10.1016/s0892-6875(02)00261-3

[50] Feng, D., Aldrich, C. (2005). Effect of Preconditioning on the Flotation of Coal. Chemical Engineering Communications, 192 (7), 972–983. doi: https://doi.org/10.1080/009864490521534

[51] Kursun, H., Ulusoy, U. (2012). Zinc Recovery From Lead–Zinc–Copper Complex Ores by Using Column Flotation. Mineral Processing and Extractive Metallurgy Review, 33 (5), 327–338. doi: https://doi.org/10.1080/08827508.2011.601479

[52] Gungoren, C., Ozdemir, O., Ozkan, S. G. (2017). Effects of temperature during ultrasonic conditioning in quartz-amine flotation. Physicochemical Problems of Mineral Processing, 53 (2), 687−698. doi: http://doi.org/10.5277/ppmp170201

[53] Burstein, M., Filippov, L. (2010). Scale-up of Flotation Processes. Publication Number: CSRCR2010-01. Computational Science Research Center, San Diego State University, San Diego.

[54] Oliveira, H., Azevedo, A., Rubio, J. (2018). Nanobubbles generation in a high-rate hydrodynamic cavitation tube. Minerals Engineering, 116, 32–34. doi: https://doi.org/10.1016/j.mineng.2017.10.020

[55] Zhou, Z. A., Xu, Z., Finch, J. A., Masliyah, J. H., Chow, R. S. (2009). On the role of cavitation in particle collection in flotation – A critical review. II. Minerals Engineering, 22 (5), 419–433. doi: https://doi.org/10.1016/j.mineng.2008.12.010

[56] Mao, Y., Peng, Y., Bu, X., Xie, G., Wu, E., Xia, W. (2018). Effect of ultrasound on the true flotation of lignite and its entrainment behavior. Energy Sources, Part A: Recovery, Utilization, and Environmental Effects, 40 (8), 940–950. doi: https://doi.org/10.1080/15567036.2018.1466009

[57] Chen, Y., Truong, V. N. T., Bu, X., Xie, G. (2020). A review of effects and applications of ultrasound in mineral flotation. Ultrasonics Sonochemistry, 60, 104739. doi: https://doi.org/10.1016/j.ultsonch.2019.104739

[58] Zheng, C., Ru, Y., Xu, M., Zhen, K., Zhang, H. (2018). Effects of ultrasonic pretreatment on the flotation performance and surface properties of coking middlings. Energy Sources, Part A: Recovery, Utilization, and Environmental Effects, 40 (6), 734–741. doi: https://doi.org/10.1080/15567036.2018.1457740

[59] Sosa-Blanco, C., Hodouin, D., Bazin, C., Lara-Valenzuela, C., Salazar, J. (2000). Economic optimisation of a flotation plant through grinding circuit tuning. Minerals Engineering, 13 (10-11), 999–1018. doi: https://doi.org/10.1016/s0892-6875(00)00086-8

Received date 22.11.2020
Accepted date 15.01.2021
Published date 29.01.2021

COMPARISON OF THE PARAMETERS OF SIGNALS WITH EXTERNAL ILLUMINATION FOR SUPERVISION OF THE AREA FOR THE PROTECTION OF IMPORTANT STATE OBJECTS

Stanislav Horielyshev
Scientific and Research Center of Service and Military Activities of the National Guard of Ukraine[1]
port_6633@ukr.net

Igor Boikov
Department of Armoured Vehicles[1]
biv543@ukr.net

Pavlo Volkov
Adjunct doctoral and adjunct[1]
strong81007@gmail.com

Andrii Poberezhnyi
Scientific Research Center of Service and Military Activities of the National Guard of Ukraine[1]
fix086@ukr.net

Aleksandr Kondratenko
Department of Armored Vehicles[1]
apko_ko@ukr.net

[1]*National Academy of the National Guard of Ukraine*
3 Zakhysnykiv Ukrainy sq., Kharkiv, Ukraine, 61001

Abstract

In modern conditions, it becomes necessary to create security systems, surveillance systems, anti-terrorist systems that carry out covert detection and surveillance of small-sized ground objects, including biological ones.

Traditionally used single-position radars are ineffective in conditions of a large number of reflections that interfere with and low speed of movement of detected objects (people). The use of several such radars is impractical due to their rather high complexity and cost. In addition, it is impossible to ensure the secrecy of such systems. The construction of radar surveillance systems in the form of semi-active bistatic, including educational, radar systems is promising for the described conditions. One of the important issues in the construction of semi-active bistatic systems is the substantiation of the parameters of external illumination signals and the assessment of the attainable characteristics of such systems when using them.

The analysis and definition of the requirements for the characteristics of the illumination signals is carried out. In addition, consider the features of using signals from modern emitting systems in semi-active radars. The basic parameters of the signals are given – the bandwidth, the pulse duration (spectrum width), the power at the transmitter output, the frequency range in which the system operates. The advantages and disadvantages of semi-active radar stations (SA RS), which use such signals, are described.

Variants of semi-active bistatic systems with external illumination are determined. The widespread use of modern digital language and telecommunication systems provides the SA RS with effective illumination signals with good correlation properties, which makes it possible to obtain the necessary technical characteristics in a variety of application conditions.

Keywords: semi-active radars, illumination signal, uncertainty function, biological objects, covert surveillance.

DOI: 10.21303/2461-4262.2021.001607

1. Introduction

The planet's surface is surrounded by a multitude of radio signals for various purposes: radio broadcasting, cellular communications, television, satellite navigation signals, radio relay signals, and the like. The transmission of the listed signals is carried out via wireless communication

channels, as a result of which, when the signal propagates, they are reflected from many objects on the route, including from ground or targets close to them. Therefore, signals from known sources can be used to obtain radar information in semi-active radar stations (SA RS).

The common disadvantages of all classic radars include the detection of their operation by the enemy at ranges significantly exceeding the range of these radars. In addition, there is a great tendency for them to operate by means of electronic suppression of the enemy. Therefore, radars built on the principle of semi-active bistatic radar are of considerable interest in modern conditions.

In addition, special attention is paid to radars designed to detect small-sized objects, including biological ones, in open, heavily rugged or wooded areas. Such a task arises when creating security systems, combat observation systems, and anti-terrorist systems.

To create such systems, various physical effects and methods are used [1]: video and radar surveillance, perimeter security systems, security and fire alarm systems, access control systems. Each system has its own advantages and disadvantages related to the environment, weather conditions, and time of day.

Thus, the solution of problems associated with the research and development of SA RS for detecting ground targets is of great scientific importance. The solutions obtained will make it possible to use the SA RS for solving problems of covert detection, determining the location and classifying ground objects in conditions of various types of interference. This determines the relevance of the article, which examines the main factors affecting the range of the system, the advantages and disadvantages of illumination signals that are used in the SA RS.

Analysis of scientific literature shows that the use of the principles of spaced apart (semi-active, bistatic) radar for solving the problem of detecting targets, in most air targets, is devoted to a large number of scientific developments. So in works [2–5], the issues of application of classical spaced apart, including bistatic, systems for detecting air, aerospace objects, including ballistic missiles in the active phase of flight, are considered. The principles of construction are given and the capabilities of promising multi-position radar systems (MPRS) of air defense (AD), which will allow solving qualitatively new tasks for covert observation and control of airspace, are assessed.

In works [6, 7], the issues of the features of construction of bistatic systems of semi-active location in the radiation field of cellular communication systems, radio broadcasting and television of ground and space-based systems are highlighted. In [6], this approach is used to detect low-altitude radar objects, and in [7] – objects on the sea surface.

However, all of the above works did not touch upon the issues of identifying ground targets, let alone biological ones. And only in the last 3...5 years, work began to appear on the application of spaced-apart radar methods for observing small-sized objects near or on the Earth's surface [8, 9]. In these works, more attention is paid to the influence of the underlying earth's surface, as one of the sources of signal reflection.

In works [10, 11], the principles of construction and the issues of practical implementation of systems of semi-active radar airborne objects using illumination signals from external sources are proposed. In addition, in these works, the prospects for the SA RS use for the protection of important objects and monitoring of the territory are considered. Generally speaking, the issue of illumination of radar objects has always been in the field of vision of developers. For example, transmitters of systems for various purposes [12–15], including space-based ones [16], were used as illumination sources.

Radars for detecting biological objects appeared as a result of developments at the intersection of radiophysics and biology. Papers [17–24] describe in detail ground-based radars, built according to the classical principle of active radar, according to which the transmitter-receiver operates on a common antenna. In these works, the issue of secrecy of the functioning of the system is not discussed at all, as well as there is no information about the SA RS, which can be used for covert observation of the security zone of important state facilities.

The use of semi-active radar biological objects was touched upon in [25, 26]. In them, consider possible ways to implement the observation of biological objects using semi-active bistatic radar methods. However, it has been improved not to consider the features of using the signals of modern radiating systems in semi-active radars.

All this allows to assert that it is expedient to conduct a study devoted to the analysis of the possibility of using the methods of semi-active spaced radar of biological objects for the organization of covert surveillance under any weather conditions in the security system of important state facilities.

The aim of research is to analyze the peculiarities of using signals from modern emitting systems in semi-active radars for monitoring biological objects.

To achieve the aim, the following objectives are set:

– analysis and definition of requirements for the characteristics of signals that can be used as those that highlight;

– selection of the illumination source and assessment of the attainable characteristics and parameters of semi-active bistatic radar stations.

2. Materials on the features of using signals from modern emitting systems in semi-active radars for monitoring biological objects, and methods of their selection

2. 1. Determination of the requirements for the characteristics of signals used in semi-active radar systems

Traditionally used single-position (monostatic) radars for detecting moving objects in conditions of a large number of reflections that interfere with and a low speed of movement of vivid objects (people) are ineffective. The use of several such radars is impractical due to their rather high complexity and cost. In addition, it is impossible to ensure the secrecy of the operation of such detection systems, which is an important condition for radar surveillance.

The construction of radar surveillance systems in the form of bistatic [4, 5], including educational, radar systems, is promising for the described conditions.

Of particular interest is the use of transmitters external to the planned radar system as a source of illumination. Such transmitters can be a ground-based and space-based radio and television transmission center operating with analog and digital (which is better) signals, radio navigation systems transmitters, cellular communication systems and radio relay transmitters, etc. In this case, the new system acquires undeniable advantages:

– expensive transmitting device of the locator is excluded, since «free» radiation of industrial systems for other purposes is used;

– as a consequence of the first, the power consumption of the entire system is significantly reduced, since the main consumer is the transmitter;

– almost complete secrecy of the functioning of the new system is ensured, since the radiation of a specialized transmitter is excluded;

– a significant (almost all) part of the constituent elements of the new system can be built on mastered and such widely produced industrial products, and also significantly reduces the cost of developing the system.

It should be noted that the proposed means and methods for solving the problems of detecting an intruder by means of radar by no means cancel the means and complexes that have been created and are in service, but only increase their capabilities.

For use in semi-active radar systems, the signals from the above sources must have the following characteristics:

– signal must have characteristics that allow detecting targets and evaluating their parameters; for sufficient time resolution, signals must have an appropriate spectrum width;

– transmitters of systems which signals are used in a semi-active radio surveillance system must have antennas with a wide radiation pattern;

– placement of transmitters and the mode of their radiation should provide illumination of a given area with sufficient power;

– coordinates of the source of radio emission must be known.

In most cases, there are no difficulties in meeting these requirements. Thus, in order to ensure the characteristics of the signals that are illuminated, the problem arises of choosing a illumination source for a particular system. Let's consider the main characteristics of the emitted signals in more detail.

2. 2. Assessment of the achievable characteristics and parameters of various sources of illumination signal used in bistatic radar of biological objects

The potential characteristics of on-board radar substantially depend on the type of illumination signal used, namely, on the structure of its uncertainty function (UF). The width of the main UF peak determines the signal resolution in terms of range and speed: the narrower the peak, the higher the resolution. The UF side lobes (SL) mask a weak signal when it is detected against a strong background. Side lances create parameter measurement ambiguity.

Therefore, one should strive to ensure that the main UF peak was as narrow as possible along both axes, the SL level was as low, and the side spears were outside the working area in terms of range and radial velocity.

Illumination transmitters must have a coverage area, covering the area of finding potential targets, continuous (up to round-the-clock) radiation mode and a sufficiently high power. These requirements are best met by signals from terrestrial radio and television broadcasting systems.

Less explored is the use of satellite (language, navigation, communication) and terrestrial telecommunication systems (microwave communication lines, mobile telephony, Wireless Fidelity (Wi-Fi), Worldwide Interoperability for Microwave Access (WiMAX)). This is due to the fact that such semi-active radar systems have less power at the receiving point, they can be more focused and provides less availability.

Analog broadcasting is conducted in the meter wave range at frequencies of 66...74 MHz (ultrashort waves (USW)) and 88...108 MHz (Frequency Modulation (FM)). The signal spectrum is nominally about 50 kHz. However, since the spectrum of the frequency-modulated signal is theoretically infinite, in reality the signal occupies a bandwidth of more than 50 kHz, being limited by components that are sufficiently large in power, the spectrum is considered to be up to 190 kHz [11]. A signal bandwidth of 50 kHz corresponds to a potentially observable resolution in MPRS of 3 km. For observation of ground targets, such a resolution is unacceptable, therefore, it is not possible to consider such a signal (how it illuminates) further.

Analog television occupies frequencies of 48...100 MHz (1...5 TB channels), 174...230 MHz (6...12 channels), 470...790 MHz (21...60th channels). **Fig. 1** shows the spectrum of analog television, consisting of a luminance signal, a color signal, and analog and digital audio. The bandwidth of the broad of them, the luminance signal, is 5.5 MHz, which corresponds to a resolution of 27 m [9].

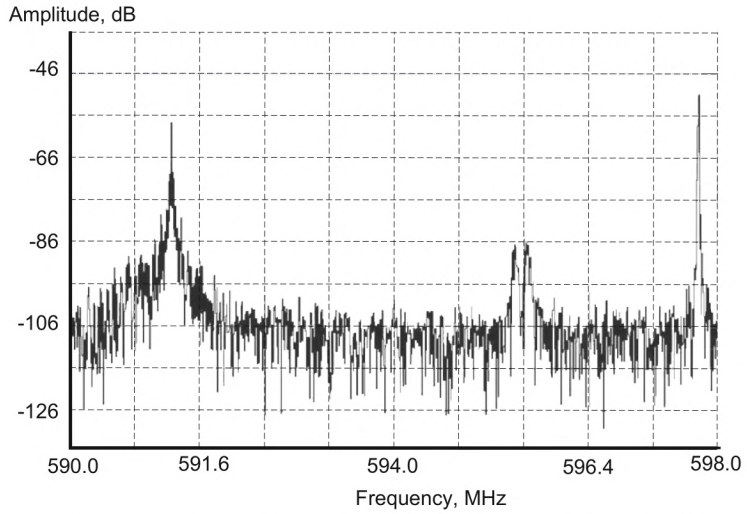

Fig. 1. Spectrum of analog TV signal. Frequency 591.25 MHz – luminance signal 595.6 MHz – color-difference signals; 597.75 MHz – sound signal

It should be noted that the authors of [9] used a band of 5.5 MHz, which is not true – the band of the brightness signal at the half power level (**Fig. 1**) does not exceed 150...200 kHz.

The power of the transmitters can reach 1 MW of effective isotropically emitted power, provides a power flux density of 51 dBW/m^2 at a distance of 100 km (in line of sight and in the

absence of losses along the propagation path). The presence of sync signals following 64 μs leads to an uncertainty in the range measurement, which is 9.6 km.

Now Ukraine has switched to digital TV broadcasting in the T2 standard, the signal bandwidth is 8 MHz.

Digital signals of terrestrial broadcasting standards Digital Video Broadcasting – Terrestrial (DVB-T) (television) and Digital Audio Broadcasting (DAB) (radio) are close to noise-like. Such digital signals have a close-to-rectangular spectrum, providing a lower level of the UF power supply in comparison with analog signals. **Fig. 2, *a*** shows the spectrum, and **Fig. 2, *b*** – SL signal of Digital Video Broadcasting – Second Generation Terrestrial (DVB-T2). Other important advantages of digital signals are wide bandwidth (that is, better range resolution) and independence of their properties from the plot.

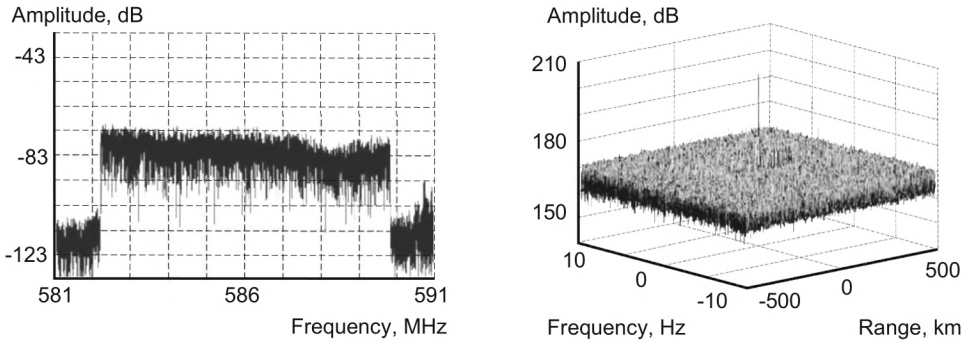

a *b*

Fig. 2. Signal of terrestrial broadcasting of DVB-T standards:
a – spectrum of DVB-T2 signal; *b* – ambiguity function of DVB-T2 signal

The combination of these advantages makes the use of digital signals predominant over analog signals, despite the lower power and complex processing.

The DAB digital terrestrial broadcasting standard uses frequencies in the 200...250 MHz range, the transmitter power is about 1 kW, which is significantly lower than in similar FM transmitters [7].

Table 1 shows the parameters of one of the DVB-T2 signals in 8 k mode.

Table 1

Parameters of DVB-T2 signal in 8k mode

Frequency, MHz	Maximum range resolution, m	Effective spectrum width, MHz	UF SL maximum power supply level, dB
583	20	7.61	–26.3

To transmit digital signals, television channels from 6 to 12 and from 21 to 69 can be used. Usually, one or two channels are allocated for broadcasting the DVB-T2 standard, each of which transmits the so-called multiplex, consisting of eight language TV channels and several radio channels ... Typical transmitter power for this standard is 8 kW.

Now, digital terrestrial television signals are considered by specialists as the main ones for use in bistatic radar systems. Its advantages:

– good UF properties (low SL power, high range resolution due to a wide spectrum, independence of signal properties from message content, that is, stability of MPRS characteristics);

– high availability due to the development of terrestrial broadcasting systems.

As the main disadvantage, let's note the relatively low power of the transmitters, as a result of the shorter operating range compared to analog systems. Note also that information on the use of these signals for bistatic location of ground targets is extremely limited.

The technical solutions used in the Digital Radio Mondiale (DRM) digital broadcasting system ensure high stability of signal reception in the presence of adverse influencing factors

in the transmission channels (interference, fading, multipath propagation, etc.). This allows for high-quality signal reception in stationary and mobile conditions, as well as in cars or other moving objects [10]. In the DRM system, broadcasting is usually carried out in a 10 kHz band, which clearly does not satisfy the range resolution.

Short-wavelength (SW) language transmitters emit more power than stations in other bands. A typical value of the energy potential of a SW radio station ($P_t \cdot G_t$) is 50 MW [12] (P_t – the average transmitter power, G_t) – the antenna gain).

Cellular telephone networks Global System for Mobile Communications (GSM) operate at frequencies of 900, 1800 MHz and higher. The 25 MHz bandwidth for a single station is divided into 125 channels of 200 kHz, which is the illumination signal bandwidth [13]. Each of the carriers is divided into 8 time slots with a duration of 577 μs. The transmitter power, depending on the class (from 1 to 5), is from 50 to 0.8 W.

Thus, GSM cellular communication provides MPRS with better resolution than FM broadcasting, but worse than digital TV. In addition, the frequency is allocated to the subscriber dynamically, so this particular station at the moment and at a particular frequency may not emit a signal. For this reason, mobile networks do not provide full availability of the illumination field.

In 3G networks, the signal frequency is about 2 GHz, the nominal frequency distance between channels is 5 MHz. Modulation with an effective bandwidth of 3.84 MHz, which can already find application in on-board radars.

Antennas of base station transmitters have a sector of 120° (there can be one, two or three antennas), the radiation elevation angle is directed downward to exclude radiation into the upper hemisphere. The points are separated by an average of 10 km, the radiated power is about 100 W, in cities, towers are installed more often, and the power is made half as low. The main development trend is to install transmitters of lower power, but more often.

GSM disadvantages – relatively low power and availability, mediocre signal properties in comparison with other digital standards; the advantage is a large coverage area. Cellular signals are still rarely used in bistatic locations, the most famous is the Celldar system.

Wi-Fi wireless access network is a family of standards for transmission of digital data streams over radio channels. Wi-Fi technology is widely used to create wireless networks that provide Internet access in a wide variety of environments.

The main advantages of using Wi-Fi transmitter signals in MPRS are high range resolution, provided by a wide signal bandwidth, large coverage area and high availability. According to experts, Wi-Fi is ideal for creating surveillance systems over short distances (tens to hundreds of meters).

Real signal bandwidths for Direct Sequence Spread Spectrum (DSSS) are about 11 MHz for Orthogonal Frequency-Division Multiplexing (ODFM) – about 17 MHz, which provides a resolution of 13 and 9 m, respectively.

When using Wi-Fi in the radar scheme, the following technical difficulties arise. First of all, the UF has a rather unfavorable structure – a high SL and local peaks, which leads to masking of weak reflections and range limitations. To overcome this effect, special processing methods should be used.

There are other problems in the construction of MPRS Wi-Fi. Many devices operate in the 2.4 GHz band, for example, they support another standard for wireless data transmission, the Bluetooth standard, or microwave ovens.

Let's note that such systems have a fairly short range (tens to hundreds of meters) and are tied to certain zones where Wi-Fi is present. However, if necessary, the access point can be additionally placed in the desired place to provide the required range. In the MPRS, a direct signal is needed. Two options are possible here [25]:

– in the first, a separate direct signal channel is created, and in a system with Wi-Fi, taking into account the locality of the observation area, it is possible to provide a sufficiently small distance between the transmitter and receiver;

– in the second, the direct signal is separated from the signals received in the reflected channel, which is the only one.

Further processing corresponds to the coherent MPRS – rejection of the direct signal from the reflected channel, calculation of a two-dimensional FN, target detection and construction of the trajectory of the observed object.

WiMAX wireless access network provides significantly higher efficiency, wide signal bandwidth and good availability [7]. The protection zone of one WiMAX network intermediary can reach 50 km directly, but significantly depends on the channel mode. In general, the standard provides for operation in the frequency range 2...11 GHz with bands from 1.25 to 20 MHz.

Satellite radio systems can be created in three categories: low-orbit (LO) – altitude 300...1000 km, medium-orbit (MO) – altitude 21000 km and geostationary (GEO) – altitude 35786 km. **Table 2** shows the parameters of some satellite sources of the illumination signal [16].

Table 2

Parameters of satellite signal of illumination sources

Type	Name	Orbit	Frequency range, MHz	Power flux density, dBW/m^2
Radar	Radarsat-2	LO	3400…7075	–53
Communication	DVB-S (Astra)	GEO	1930…2700	–111
	DVB-SH			–97
	Inmarsat-4			–95
	Thuraya		1452…1710	–118...–106
	Iridium	LO	1930…2700	–108
	Globalstar			–97
Navigational	Global Positioning System (GPS)	MO	1452…1710	–130
	ГЛОНАСС			–129...–131
	Galileo			–128

Geostationary satellites, constantly being above the same point, provide availability close to unity, but have a lower power density compared to LO.

The prospects for the use of signals in terrestrial on-board radars from relatively new space systems of digital mobile television broadcasting look more optimistic. These systems are designed to work with mobile users who can't use large antenna systems. Signals of significantly higher power are used in these systems than for stationary devices. In addition, such systems provide adequate coverage and availability.

In the future, it is on these satellites that circuit solutions remain traditional.

Among these systems are EutelsatW2A and Inmarsat 1–4 EMEA, which are available in Europe. Some parameters of the satellites Eutelsat and Inmarsat [25] are given in **Table 3**.

Table 3

Parameters of Eutelsat and Inmarsat satellites

Parameter	EutelsatW2A	Inmarsat 1–4
Latitude/Longitude	0.01° N/10.05° E	0°/25.12° E
Height, km	35 840	35 800
Power flux density, dBW/m^2	72	67
Carrier frequency, GHz	2.17	1.50
Signal bandwidth, MHz	2	0.2
Coverage area	Europe	Europe, Africa

Computer simulations carried out in [15] showed that in an MPRS using these illumination signals, one can expect an aircraft to be detected at ranges of up to 50 km (Inmarsat) and 90 km (Eutelsat).

Simulation parameters: effective target scattering area 13 dBm, antenna gain 21 dB, accumulation time 1 s, receiver noise level 5 dB.

According to the currently generally accepted point of view, given the noted shortcomings, it is still difficult to use space-based illumination transmitters to solve traditional radar problems. The issues of using space illumination for locating ground targets require further consideration.

The materials [11] provide a generalized material on diversity systems using signals from existing broadcasting and television stations as those that are probed. These data are given in **Table 4**.

The energy characteristics of the illumination signal sources are collected from various sources and are given in **Table 5**.

Table 4

Parameters of signals of broadcasting and television stations

Signal	Range solution, km	Side lobe level in range, dB	Side lobe level by velocity, dB
Language (FM)	16.5	–19.1	–46.5
Music (FM), classical/rock	5.8/6.55	–23.9/–12.0	–32.5/–26.0
Analog TV	9.61	–0.2	–9.1
Digital television	1.72	–18.5	–34.6
GSM 900/1800	1.8/2.62	–9.3/–6.9	–47/–44

Table 5

Energy characteristics of illumination signals

Signal source	Frequency, MHz	Band, MHz	Power, kWt
FM and USW	66…108	0.003…0.02	0.1…4
Analog TV	50…800	0.1…0.2	up to 50
Cellular GSM	900, 1800	up to 25	0.02
3G communication systems	1920, 2110	5	0.02
Digital TV	174…834	8	up to 10

In general, to determine the energy potential of a particular illumination option, one needs estimation calculations with averaged initial data.

3. Results of research on the principles of using bistatic radar for solving the problem of detecting biological objects and their discussion

Studies have shown that when observing ground targets, the resolution in a system with an analog broadcasting signal is unacceptable, therefore such a signal (which illuminates) is not considered.

The presence of sync signals in analog television transmitters following 64 μs leads to the appearance of an uncertainty in the range measurement, which is 9.6 km. In addition, the resolution for observing biological objects is also insufficient – such signals are impractical to use.

Digital signals of terrestrial broadcasting are close to noise-like ones, therefore, a low level of UF SL, better range resolution and independence of properties from the plot are provided. The combination of these advantages makes the use of digital signals preferable, despite the lower power and more complex processing.

Despite the large coverage area, cellular signals are still rarely used in bistatic locations due to the relatively low power and availability, as well as mediocre signal properties compared to other digital standards.

Signals of Wi-Fi and WiMAX wireless access networks provide high range resolution due to wide signal bandwidth, large coverage area, high availability. But a high SL level and local peaks lead to masking of weak reflections and range limitations when working on ground targets.

For well-known reasons, low- and mid-orbit satellites are not widely used in MPRS. According to the currently generally accepted point of view, given the noted shortcomings, it is still difficult to use space-based MPRS to solve traditional radar problems. The prospects for using signals from relatively new space systems of digital mobile television broadcasting look optimistic. The issues of using space half-light for locating ground targets require further consideration. Among the organizations dealing with these issues, there are mainly universities and scientific units of the military departments.

The peculiarities of the results obtained are in the proof of the presence of various radio devices among the emissions that can be used to solve the problem of detecting biological objects (intruders) in the observation or protection zone, including especially important objects.

Among the limitations of the applicability of the results, it should be noted that only the upper estimates are valid, that is, the potential capabilities of a particular observation system using bistatic radar methods. In the future, these restrictions can be removed by a detailed study of the systems' performance under conditions of action of various kinds of obstacles of natural and artificial origin.

In further research, one will have to face certain difficulties of a mathematical (transition to non-stationary processes) and experimental character. The latter is explained by the lack of adequate funding for the purchase of the necessary equipment and equipment.

4. Conclusions

1. Research of passive coherent systems with illumination signals of USW range of digital television is carried out in the USA, Great Britain, Russia, France, Germany, Poland, Norway, South Africa, China, Iran and other countries. This can be explained both by the high expected technical characteristics of coherent SA RS of this range (due to the properties of the signal), and by the simplicity and low cost of the design (in comparison with other USW radars). And now the most popular USW range, and in it – illumination signals from digital television.

Such plants have a number of advantages: lower cost of production, placement and operation; absence of harmful effects on the environment and interference with other radio-technical devices; almost complete secrecy; they do not need separate frequencies. The characteristic features of the SA RS determine the high potential of their application for the protection of important objects, monitoring of perimeters and territories, including with the creation of a surface radar field.

2. As a result of the research carried out, it was found that SA RS using illumination signals from third-party sources are considered promising means of detecting and tracking ground, including biological, objects. For further research, let's leave three options for bistatic systems with external illumination – a ground transmitter with a digital signal of the T2 format, a space transmitter with a digital signal, and a transmitter for a cellular communication system. In other ranges of work on semi-active coherent location is less.

It is the choice of one of the listed illumination signals that is the first step for further scientific research to justify the SA RS structure for the protection of important objects, monitoring the perimeters, their construction and implementation into a prototype.

The widespread use of modern digital language and telecommunication systems provides the SA RS with effective illumination signals with good correlation properties, which makes it possible to obtain the necessary technical characteristics in a wide variety of application conditions.

References

[1] Magauenov, R. G. (2004). Sistemy ohrannoy signalizatsii: osnovy teorii i printsipy postroeniya. Moscow: Goryachaya liniya – Telekom, 494. Available at: https://www.techbook.ru/book.php?id_book=946

[2] Kondratenko, A. P. (2002). Rol' i mesto netraditsionnoy radiolokatsii v sisteme kontrolya vozdushnogo prostranstva. Zbirnyk naukovykh prats KhVU, 1 (39), 87–90.

[3] Anoshkin, I. M. (2007). Zarubezhnye mnogopozitsionnye sistemy radiolokatsii skrytogo kontrolya vozdushnogo prostranstva. Nauka i voennaya bezopasnost', 1, 28–33. Available at: http://militaryarticle.ru/nauka-i-voennaya-bezopasnost/2007/11986-zarubezhnye-mnogopozicionnye-radiolokacionnye

[4] Kulpa, K. (2014). Passive Radar. Radar Symposium 2014. KACST, Riyadh Saudi Arabia. Available at: https://slideplayer.com/slide/3432556/

[5] Griffiths, H. (2013). Bistatic and Multistatic Radar. IEEE AESS Distinguished Lecture. ETH Zurich, 78. Available at: https://pdfs.semanticscholar.org/3f61/fe08e00103aa8c17425c386d47a99cc40d64.pdf

[6] Demidyuk, A., Demidyuk, E. (2013). Skrytiy «Rubezh» vozdushnogo kontrolya. Novye resheniya staryh problem malovysotnoy lokatsii. Voenno-promyshlennyy kur'er, 45 (513). Available at: http://vpk-news.ru/articles/18242

[7] Chetty, K., Woodbridge, K., Guo, H., Smith, G. E. (2010). Passive bistatic WiMAX radar for marine surveillance. 2010 IEEE Radar Conference. doi: https://doi.org/10.1109/radar.2010.5494627

[8] Kovalev, A. N., Kovalev, F. N. (2014). Statistical characteristics of target location finding error in bistatic forward scattering radars. Radioelectronics and communications systems, 57 (3), 3–9. doi: https://doi.org/10.20535/s0021347014030017

[9] Barhatov, A. V., Verem'ev, V. I., Vorob'ev, E. N. et. al. (2016). Passivnaya kogerentnaya radiolokatsiya. Sankt-Peterburg: Izdatel'stvo «LETI», 162. Availableat: https://search.rsl.ru/ru/record/01008926589

[10] Kutuzov, V. M., Barhatov, A. V., Bezuglov, A. V., Verem'ev, V. I., Konovalov, A. A., Kovalev, D. A. (2012). Osnovy proektirovaniya mnogopozitsionnyh dekametrovyh RLS prostranstvennoy volny. Sankt-Peterburg: Izdatel'stvo «LETI», 191. Available at: http://letiizdat.ru/izdaniya/nauchno-tehnicheskaya-literatura/monografii/2012/osnovy-proektirovaniya

[11] Griffiths, H. D. (2009). Passive bistatic radar and waveform diversity. Lecture Series Paper 3, Waveform Diversity for Advanced Radar Systems, NATO Science and Technology Organization, RTO Educational Notes. RTO-EN-SET-119 (2009). Available at: https://apps.dtic.mil/dtic/tr/fulltext/u2/a567763.pdf

[12] Thomas, J. M., Baker, C. J., Griffiths, H. D. (2007). DRM signals for HF passive bistatic radar. IET International Conference on Radar Systems 2007. doi: https://doi.org/10.1049/cp:20070642

[13] Tan, D. K. P., Sun, H., Lu, Y., Liu, W. (2003). Feasibility analysis of GSM signal for passive radar. Proceedings of the 2003 IEEE Radar Conference (Cat. No. 03CH37474). doi: https://doi.org/10.1109/nrc.2003.1203436

[14] Sutcuoglu, O., Hassoy, B. (2013). Airborne passive radar application: Interactions with space. 2013 6th International Conference on Recent Advances in Space Technologies (RAST). doi: https://doi.org/10.1109/rast.2013.6581190

[15] Cristallini, D., Caruso, M., Falcone, P., Langellotti, D., Bongioanni, C., Colone, F. et. al. (2010). Space-based passive radar enabled by the new generation of geostationary broadcast satellites. 2010 IEEE Aerospace Conference. doi: https://doi.org/10.1109/aero.2010.5446694

[16] Griffiths, H. D., Baker, C. J., Baubert, J., Kitchen, N., Treagust, M. (2002). Bistatic radar using satellite-borne illuminators. RADAR 2002. doi: https://doi.org/10.1109/radar.2002.1174642

[17] Malinin, M. (2016). Osnovnye napravleniya razvitiya za rubezhom radiolokatsionnyh stantsiy razvedki nazemnyh dvizhushchihsya tseley. Zarubezhnoe voennoe obozrenie, 11, 47–53. Available at: http://factmil.com/publ/strana/velikobritanija/osnovnye_napravlenija_razvitija_za_rubezhom_radiolokacionnykh_stancij_razvedki_nazemnykh_dvizhushhikhsja_celej_2016/9-1-0-1076

[18] Mobile complex of surface recognition and ECM «JAB». Available at: http://ust.com.ua/en/mobile-complex-of-surface-recognition-and-ecm-jab/

[19] Radiolokatsionniy kompleks ohrany obektov. Available at: http://www.umirs.ru/catalog/stationary_complex/radiolokatsionnyy-kompleks-okhrany-obektov/

[20] Mosalev, V. (2000). Stantsii radiolokatsiy razvedki nazemnyh dvizhushchihsya tseley. Zarubezhnoe voennoe obozrenie, 10, 20–22. Available at: http://militaryarticle.ru/zarubezhnoe-voennoe-obozrenie/2000-zvo/6678-radiolokacionnye-stancii-razvedki-nazemnyh

[21] Zaytsev, N. A., Platov, A. V., Potapov, V. A. (2014). Radiolokatsionnye stantsii razvedki nazemnyh dvizhushchihsya tseley. Sovremenniy uroven' i osnovnye napravleniya razvitiya. Vestnik Kontserna PVO «Almaz-Antey», 1, 41–44. Available at: http://www.npostrela.com/upload/Antey.pdf

[22] Radar «BARSUK-A». Available at: http://ust.com.ua/en/item/radar-barsuk-a/

[23] Radiolokator «LC 111» (Lis-1). Available at: http://www.bnti.ru/des.asp?itm=5258&tbl=19.01.02

[24] Radar-obnaruzhitel' lyudey za pregradami «RO-400». Available at: http://www.bnti.ru/des.asp?itm=5053&tbl=02.03.03

[25] Kondratenko, O. P. (2018). Use of methods of the bioradar-location for observation of biological objects. The Collection of Scientific Works of the National Academy of the National Guard of Ukraine, 1 (31), 19–26. Available at: http://znp.nangu.edu.ua/article/view/138489/164858

[26] Abramov, A. V., Anishchenko, L. N., Amosova, A. I. (2018). Bioradiolokatsiya. Moscow: MGTU im. Baumana, 396. Available at: https://obuchalka.org/20181025104763/bioradiolokaciya-abramov-a-v-2018.html

Received date 16.10.2020
Accepted date 05.01.2021
Published date 29.01.2021

MODELING THE PROTECTION OF PERSONAL DATA FROM TRUST AND THE AMOUNT OF INFORMATION ON SOCIAL NETWORKS

Serhii Yevseiev
Department of Cyber Security and Information Technology
Simon Kuznets Kharkiv National University of Economics
9-A Nauky ave., Kharkiv, Ukraine, 61166
serhii.yevseiev@hneu.net

Oleksandr Laptiev
Department of Information and Cybersecurity Systems
State University of Telecommunications
7 Solomenska str., Kyiv, Ukraine, 03110
alaptev64@ukr.net

Sergii Lazarenko
Department of Information Security[1]
zzi.lazarenko@nau.edu.ua

Anna Korchenko
Department of IT-Security[1]
annakor@ukr.net

Iryna Manzhul
Special departament No. 2
National Academy of the Security Service of Ukraine
22 Maksimovich str., Kyiv, Ukraine, 03022
vassa00@ukr.net

[1]*National Aviation University*
1 Liubomyra Huzara ave., Kyiv, Ukraine, 03058

Abstract

The article analyzes the parameters of social networks. The analysis is performed to identify critical threats. Threats may lead to leakage or damage to personal data. The complexity of this issue lies in the ever-increasing volume of data. Analysts note that the main causes of incidents in Internet resources are related to the action of the human factor, the mass hacking of IoT devices and cloud services. This problem is especially exacerbated by the strengthening of the digital humanistic nature of education, the growing role of social networks in human life in general. Therefore, the issue of personal information protection is constantly growing. To address this issue, let's propose a method of assessing the dependence of personal data protection on the amount of information in the system and trust in social networks. The method is based on a mathematical model to determine the protection of personal data from trust in social networks. Based on the results of the proposed model, modeling was performed for different types of changes in confidence parameters and the amount of information in the system.

As a result of mathematical modeling in the MatLab environment, graphical materials were obtained, which showed that the protection of personal data increases with increasing factors of trust in information. The dependence of personal data protection on trust is proportional to other data protection parameters. The protection of personal data is growing from growing factors of trust in information.

Mathematical modeling of the proposed models of dependence of personal data protection on trust confirmed the reliability of the developed model and proved that the protection of personal data is proportional to reliability and trust.

Keywords: social network, protection, user, parameter, transfer, information, metric, density, cycle.

DOI: 10.21303/2461-4262.2021.001615

1. Introduction

In today's world, information needs reliable protection: from unauthorized access and distribution, accidental deletion or alteration. All developed European countries are concerned about

the problem of information security, as well as the protection of personal data of citizens. This is due to the fact that informatization and digitization of information have become widespread in all areas of human activity, including the storage of personal and work data.

Social networks are one of the main methods of communication, search for connections and exchange of both publicly available and confidential information. Social networks make up an ever-growing share of shared networks. The network itself acquires new properties, acting as an independent factor.

Because information in the global network exists outside of space and time, the network itself becomes an active agent of influence on the person, keeping, above all, large amounts of data publicly available. In recent years, the vision of the problem of cybersecurity has begun to change significantly, as people increasingly cease to be the subject of cybercrime, becoming an object in itself, and not only its financial and economic interests and capabilities.

This problem is especially exacerbated by the strengthening of the digital humanistic nature of education, the growing role of social networks in human life in general.

The protection of personal data in today's information life is perhaps the most important aspect in meeting the safe use of all the capabilities of current technologies. Therefore, the problem of studying the parameters of social networks for their further use in solving problems of information and personal data protection is very relevant.

2. Literature review and problem statement

The exchange of structural and thematic data potentially allows the use of social networks to address a wide range of information security issues.

In [1] discusses social networks that can track user actions and control data for future use. A study of 45 social networks found that approximately 90 % of sites unreasonably require personal information to, for example, allow permission to join them; 85 % of sites do not use standard encryption protocols to protect data from cybercrime attacks; 72 % of sites transfer information about users to third parties.

In [2] the standards, attributes and characteristics of the profile are considered and a method of detecting signs of public opinion manipulation in social networks based on the construction of information security profiles of social Internet services, based on gradient boosting of binary trees, which automates early detection procedures.

In [3–5] it is indicated that the dissemination of personal data through social networks is much faster than in real life. It is most dangerous when personal information comes to people for whom it is not intended. Social media users are often unaware that they can change personal privacy settings to protect their data.

In [6, 7] the mechanism of application of correlation of potential crisis situations for an estimation of average and total level of criticality of a current situation in information sphere is considered. The mechanism is based on methods of expert evaluation and fuzzy logic. A correlation mechanism is proposed to determine the correlation coefficient of each dependent identification of potential crisis situations with the main one, which determines the interdependencies between them. The obtained correlation coefficients can be used to calculate the average and total levels of criticality of a situation that has arisen under the influence of several interrelated and simultaneous potential crisis situations. Only information correlation problems are considered.

In [8, 9] developed a structural-parametric model of information security risk assessment system which, due to the structural components of subsystems, the formation of primary and secondary data, as well as their components modules of initialization of input data, formation and conversion of reference values, weighing evaluation parameters and their adjustment, risk assessment and report generation, which implement the proposed methods, assessment based on databases of vulnerabilities, incrementing and decrementing the order of linguistic variables, allows for high flexibility and convenience in assessing information security risks without the participation of experts in the subject area. But only the problems of information security, which are presented in local databases, are considered.

In [10] the qualitative-quantitative method of analysis and assessment of information security risks by modifying the procedures for determining many parameters of risk assessment and

assessment of current values of parameters with the possibility of integrating the values of indicators presented in the relevant databases. To do this, it is proposed to use appropriate databases of vulnerabilities, which present their quantitative estimates. In [14], only information security issues are considered, which are presented in the databases of CVSS (Common Vulnerability Scoring System is the framework for rating the severity of security) indicators.

In [11, 12] the methodology of construction of the system of information security of banking information in automated banking systems (ABS) is considered, which is based on the first proposed three-level model of strategic management of information technology security. In [13] only information security problems are considered, without taking into account technical problems.

In addition, in the literature, the study of certain issues of this issue at different times paid attention to such specialists. Consideration of this issue is carried out by prominent.

The aim of the article is to study the whole set of parameters of threats in social networks from the loss of trust between users for their further use in solving problems of information and data protection.

3. Formulation of the problem

The exchange of personal data potentially allows the use of social networks to solve a wide range of information problems, but there is a problem of data protection. Therefore, the question of developing new mathematical models for assessing the dependence of personal data protection on trust and the amount of information on social networks is very relevant.

The aim of this research is to develop a new mathematical model for estimating the dependence of personal data protection on trust and the amount of information on social networks.

4. The main section

In the classical approach to the problem of personal data protection, there are many threats of loss of trust between users, which can be represented as a function:

$$T_i = F(\left[D_j, D_n, D_m, D_k \right]), \tag{1}$$

where T_i – the set of threats of loss of trust between users; D_j – trust in the provision of services (a person trusts the party in the provision of quality services or resources by the provider); D_n – delegation trust describes the trust in the user (representative), who acts and makes decisions on behalf of the party he trusts; D_m – access trust describes the trust on the part (provider) to the user who is granted access to resources. This is access control. Used in authentication systems; D_k – contextual trust determines the degree of faith of the participant in the necessary systems and institutional mechanisms that support transactions and ensure network security [15–17].

Loss of such a quality as trust is a process that has a time interval. Denote the amount of information in the system – I. The flow of information outside the information system through $\mathrm{d}I$, the rate of change of this flow – $\mathrm{d}I/\mathrm{d}t$. It is logical that if the flow and the rate of change of flow are zero, then there is no leakage of information:

$$\mathrm{d}I = 0;\ \frac{\mathrm{d}I}{\mathrm{d}t} = 0. \tag{2}$$

Leakage of information depends on the security of the system and the measures taken to neutralize threats to the security of personal data [18–21].

Let Z be an indicator of information system security. Let's make the equation:

$$\begin{cases} \dfrac{\mathrm{d}I}{\mathrm{d}t} = Z_p Z + (C_v + C_k) I - L_2(I_0^2 \sin^2 \omega t) - L_3(I_0^3 \sin^3 \omega t) - \ldots; \\ \dfrac{\mathrm{d}Z}{\mathrm{d}t} = D_i - I(C_{d1} + C_{d2}) - K_2(Z_0^2 \sin^2 \omega t) - K_3(Z_0^3 \sin^3 \omega t) - \ldots . \end{cases} \tag{3}$$

To solve the system of equations (3) let's write system (4) in the form:

$$\begin{cases} \dfrac{\mathrm{d}I}{\mathrm{d}t} = \alpha Z + \beta_1 I - \sum\limits_{k=2}^{\infty} L_k I_0^k \sin^k \omega t; \\ \dfrac{\mathrm{d}Z}{\mathrm{d}t} = \beta_2 I + \gamma - \sum\limits_{k=2}^{\infty} K_k Z_0^k \sin^k \omega t, \end{cases} \tag{4}$$

where $\alpha = Z_p,\ \beta_1 = C_v + C_K,\ \beta_2 = -\left(C_{d2} + C_{d1}\right),\ \gamma = D_i.$

Next, let's use the exclusion method:

$$\frac{\mathrm{d}Z}{\mathrm{d}t} = \beta_2 I + \gamma - \sum_{k=2}^{\infty} K_k Z_0^k \sin^k \omega t \Rightarrow I = \frac{1}{\beta_2}\left(\frac{dZ}{dt} - \gamma + \sum_{k=2}^{\infty} K_k Z_0^k \sin^k \omega t\right),$$

then:

$$\frac{\mathrm{d}I}{\mathrm{d}t} = \frac{1}{\beta_2}\left(\frac{d^2Z}{dt^2} + \frac{1}{\omega}\sum_{k=2}^{\infty}\left(kK_k Z_0^k \sin^{k-1}\omega t \cos\omega t\right)\right). \tag{5}$$

Substitute in the first equation of the system:

$$\frac{1}{\beta_2}\left(\frac{\mathrm{d}^2Z}{\mathrm{d}t^2} + \frac{1}{\omega}\sum_{k=2}^{\infty}\left(kK_k Z_0^k \sin^{k-1}\omega t \cos\omega t\right)\right) =$$

$$= \alpha Z + \frac{\beta_1}{\beta_2}\left(\frac{\mathrm{d}Z}{\mathrm{d}t} - \gamma + \sum_{k=2}^{\infty} K_k Z_0^k \sin^k \omega t\right) - \sum_{k=2}^{\infty} L_k I_0^k \sin^k \omega t. \tag{6}$$

Or

$$\frac{\mathrm{d}^2Z}{\mathrm{d}t^2} - \beta_1\frac{\mathrm{d}Z}{\mathrm{d}t} - \alpha\beta_2 Z = -\frac{1}{\omega}\sum_{k=2}^{\infty}\left(kK_k Z_0^k \sin^{k-1}\omega t \cos\omega t\right) - \beta_1\gamma +$$

$$+ \beta_1\sum_{k=2}^{\infty} K_k Z_0^k \sin^k \omega t - \beta_2\sum_{k=2}^{\infty} L_k I_0^k \sin^k \omega t. \tag{7}$$

Find the solution of the corresponding equation:

$$Z'' - \beta_1 Z' - \alpha\beta_2 Z = 0. \tag{8}$$

The characteristic equation has the form:

$$\lambda^2 - \beta_1\lambda - \alpha\beta_2 = 0.$$

Let's consider only the case for a positive discriminant of this equation:

$$D = \beta_1^2 + 4\alpha\beta_2 > 0 \Rightarrow \lambda_{1,2} = \frac{\beta_1 \pm \sqrt{\beta_1^2 + 4\alpha\beta_2}}{2}.$$

And

$$Z_{\text{одн}}(t) = c_1 e^{\frac{\beta_1 + \sqrt{\beta_1^2 + 4\alpha\beta_2}}{2}t} + c_2 e^{\frac{\beta_1 - \sqrt{\beta_1^2 + 4\alpha\beta_2}}{2}t} \tag{9}$$

– general solution of the equation.

To find the general solution of the inhomogeneous equation let's use the method of variation of arbitrary constants:

$$Z_{\text{одн}}(t) = c_1(t)e^{\frac{\beta_1+\sqrt{\beta_1^2+4\alpha\beta_2}}{2}t} + c_2(t)e^{\frac{\beta_1-\sqrt{\beta_1^2+4\alpha\beta_2}}{2}t}, \tag{10}$$

where $c_1'(t), c_2'(t)$ will be found from the system:

$$\begin{cases} c_1'(t)e^{\frac{\beta_1+\sqrt{\beta_1^2+4\alpha\beta_2}}{2}t} + c_2'(t)e^{\frac{\beta_1-\sqrt{\beta_1^2+4\alpha\beta_2}}{2}t} = 0, \\ c_1'(t)\dfrac{\beta_1+\sqrt{\beta_1^2+4\alpha\beta_2}}{2}e^{\frac{\beta_1+\sqrt{\beta_1^2+4\alpha\beta_2}}{2}t} + c_2'(t)\dfrac{\beta_1-\sqrt{\beta_1^2+4\alpha\beta_2}}{2}e^{\frac{\beta_1-\sqrt{\beta_1^2+4\alpha\beta_2}}{2}t} = N(t), \end{cases} \tag{11}$$

where

$$N(t) = -\frac{1}{\omega}\sum_{k=2}^{\infty}\left(kK_kZ_0^k\sin^{k-1}\omega t\cos\omega t\right) - \beta_1\gamma + \beta_1\sum_{k=2}^{\infty}K_kZ_0^k\sin^k\omega t - \beta_2\sum_{k=2}^{\infty}L_kI_0^k\sin^k\omega t. \tag{12}$$

Let's get:

$$c_1'(t)e^{\frac{\beta_1+\sqrt{\beta_1^2+4\alpha\beta_2}}{2}t} = -c_2'(t)e^{\frac{\beta_1-\sqrt{\beta_1^2+4\alpha\beta_2}}{2}t} \Rightarrow$$

$$\Rightarrow c_2'(t)e^{\frac{\beta_1-\sqrt{\beta_1^2+4\alpha\beta_2}}{2}t}\left(-\frac{\beta_1+\sqrt{\beta_1^2+4\alpha\beta_2}}{2}+\frac{\beta_1-\sqrt{\beta_1^2+4\alpha\beta_2}}{2}\right) = N(t), \tag{13}$$

or

$$c_2'(t)e^{\frac{\beta_1-\sqrt{\beta_1^2+4\alpha\beta_2}}{2}t}\sqrt{\beta_1^2+4\alpha\beta_2} = -N(t). \tag{14}$$

Then:

$$c_2(t) = -\frac{1}{\sqrt{\beta_1^2+4\alpha\beta_2}}\int N(t)e^{\frac{-\beta_1+\sqrt{\beta_1^2+4\alpha\beta_2}}{2}t}\mathrm{d}t. \tag{15}$$

And

$$c_1(t) = \frac{1}{\sqrt{\beta_1^2+4\alpha\beta_2}}\int N(t)e^{\frac{-\beta_1-\sqrt{\beta_1^2+4\alpha\beta_2}}{2}t}\mathrm{d}t. \tag{16}$$

The mathematical model in the final form will look like:

$$Z(t) = \frac{e^{\frac{\beta_1+\sqrt{\beta_1^2+4\alpha\beta_2}}{2}t}}{\sqrt{\beta_1^2+4\alpha\beta_2}}\int N(t)e^{\frac{-\beta_1-\sqrt{\beta_1^2+4\alpha\beta_2}}{2}t}\mathrm{d}t - \frac{e^{\frac{\beta_1-\sqrt{\beta_1^2+4\alpha\beta_2}}{2}t}}{\sqrt{\beta_1^2+4\alpha\beta_2}}\int N(t)e^{\frac{-\beta_1+\sqrt{\beta_1^2+4\alpha\beta_2}}{2}t}\mathrm{d}t. \tag{17}$$

In general, results are obtained in general: the dependence of personal data protection on trust is proportional to the constant parameters of protection.

In order to confirm the obtained results, let's perform modeling in the MatLab environment.

In **Fig. 1**, the dependence of personal data protection (in relative units) on the amount of information in the system is the main parameter, and the parameter of trust in information.

In **Fig. 2**, the dependence of personal data protection (in relative units) on the parameter of trust in information is the main parameter and the amount of information in the system.

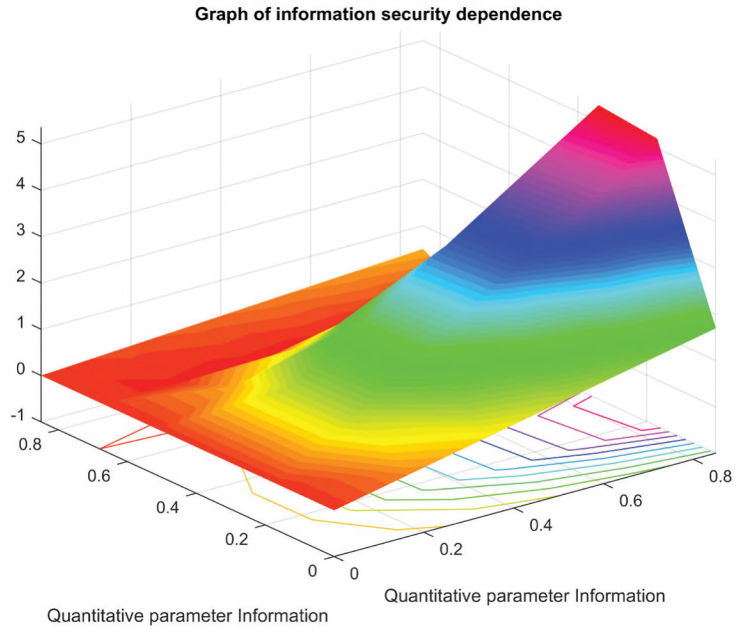

Fig. 1. Dependence of personal data protection on the growth of information in the system

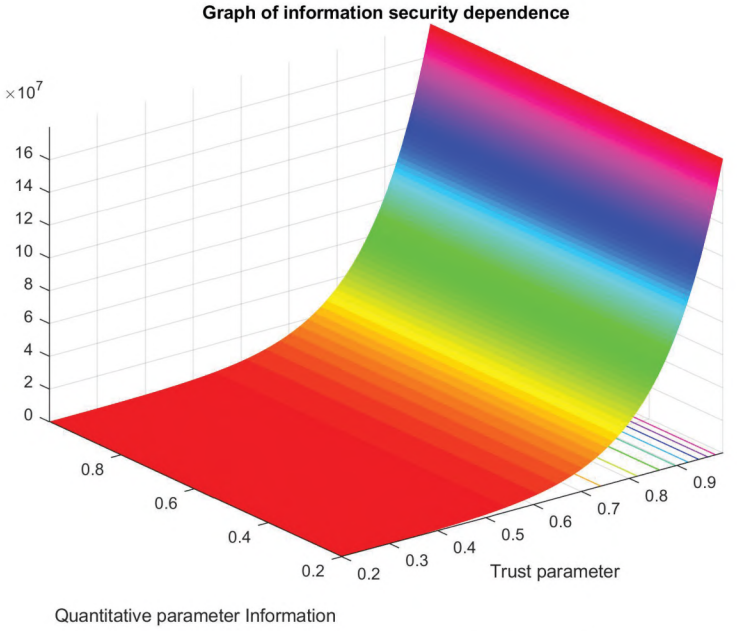

Fig. 2. Dependence of personal data protection on trust between users

As it is possible to see from the simulation results, the protection of personal data directly depends on the amount of information and the parameters of trust in this information. The protection of personal data increases with the amount of reliable information and the amount of general information, which fully confirms the accuracy of the proposed method of assessing the protection of personal data.

5. Discussion of experimental results

The peculiarity of the method is that in addition to estimating the amount of information in the system, we use the rate of change of information flow, or rather the rate of leakage of information outside the information system of personal data exchange.

When there is no information leakage, the information leakage rate is also zero. The occurrence of information leakage directly depends on the information security indicator.

The resulting system consists of two equations. One equation is the dependence of the information security indicator, the second is the dependence of the amount of information leakage on the information security parameters.

The solution of these differential equations shows the dependences of the parameters of information protection from information leakage.

An additional feature of the proposed method is using the parameter of trust in personal information and the quantitative parameter of information leakage.

But this feature is based on the accepted restrictions. It isn't taking into account the more detailed parameters of personal data protection, which in some cases may lead to an error in determining data protection.

Mathematical modeling of the proposed model proved that the protection of personal data is proportional to the reliability and trust with constant protection parameters.

The results of mathematical modeling have shown that with the increase of its quantity in the system, the trust in the information decreases, not according to the linear, but practically according to the exposition law. The simulation results showed that the confidence in the information after reaching a relative confidence factor of 0.45, is significantly reduced, which requires taking into account the greater parameters of information security.

Additional confirmation of the simulation results is shown in **Fig. 2**. The graphical results prove the statement that the confidence parameter in relative units from 0.85 to 0.99 has little effect on the parameter of increasing the amount of reliable information received.

In general, the protection of personal data increases with increasing trust parameters. This proves the adequacy of the model and is quite a favorable result.

Further development of the proposed method is a more detailed consideration of the parameters of information security.

6. Conclusions

A method for assessing the dependence of personal data protection on the amount of information in the system and trust in social networks is proposed.

Simulations for various types of changes in trust parameters and the amount of information in the system are conducted. All variants of solving the equation near the steady state of the system proved that, based on the conditions of the ratio of dissipation and natural frequency of confidence, and the attenuation of the latter to a certain value is carried out periodically, with decaying amplitude, or exponentially decaying law.

The obtained graphic materials fully showed that the protection of personal data increases with increasing factors of trust in information. Dependence of protection of personal data on trust is proportional at constant other parameters of protection.

The simulation results showed that the trust in information after reaching a relative confidence factor of 0.45, is significantly reduced, which requires taking into account the greater parameters of information security. When the parameters of trust in relative units from 0.85 to 0.99, the quantitative parameter of information has little effect on the parameter of increasing the amount of reliable information.

With the growth of the amount of information in the system and trust in information, the overall rate of information protection in modeling by the proposed method increases by 9 % than modeling by old methods, which is a quite acceptable result.

References

[1] Perera, R., Nand, P. (2017). Recent Advances in Natural Language Generation: A Survey and Classification of the Empirical Literature. Computing and Informatics, 36 (1), 1–32. doi: https://doi.org/10.4149/cai_2017_1_1

[2] Kravchenko, Y., Leshchenko, O., Dakhno, N., Trush, O., Makhovych, O. (2019). Evaluating the Effectiveness of Cloud Services. 2019 IEEE International Conference on Advanced Trends in Information Theory (ATIT). doi: https://doi.org/10.1109/atit49449.2019.9030430

[3] Pennington, J., Socher, R., Manning, C. (2014). Glove: Global Vectors for Word Representation. Proceedings of the 2014 Conference on Empirical Methods in Natural Language Processing (EMNLP). doi: https://doi.org/10.3115/v1/d14-1162

[4] Kiros, R., Zhu, Y., Salakhutdinov, R. R. (2016). Skip-thought vectors. Advances in Neural Information Processing Systems, 3276–3284.

[5] Duchnovska, K. K. (2015). Formation of the research dynamic vector space. Shtuchnyi intelekt, 3-4, 28–36.

[6] Barabash, O. V., Shevchenko, H. V., Dakhno, N. B., Open'ko, P. V., Kopiika, O. V. (2019). Target Programming with Multi-criterial Restrictions Application to the Defense Budget Optimization. Advances in Military Technology, 14 (2), 213–229.

[7] Kreines, E. M., Kreines, M. G. (2016). Control model for the alignment of the quality assessment of scientific documents based on the analysis of content-related context. Journal of Computer and Systems Sciences International, 55 (6), 938–947. doi: https://doi.org/10.1134/s1064230716050099

[8] Musienko, A. P., Serdyuk, A. S. (2013). Lebesgue-type inequalities for the de la Valée-Poussin sums on sets of analytic functions. Ukrainian Mathematical Journal, 65 (4), 575–592. doi: https://doi.org/10.1007/s11253-013-0796-4

[9] Musienko, A. P., Serdyuk, A. S. (2013). Lebesgue-type inequalities for the de la Vallée-poussin sums on sets of entire functions. Ukrainian Mathematical Journal, 65 (5), 709–722. doi: https://doi.org/10.1007/s11253-013-0808-4

[10] Grigoryan, D. S. (2012). Kogerentnaya obrabotka dannyh v zadachah spektral'nogo analiza radiolokatsionnyh signalov so sverhrazresheniem. Zhurnal Radioelektroniki, 3. Available at: http://jre.cplire.ru/jre/mar12/1/text.pdf

[11] Yevseiev, S., Korolyov, R., Tkachov, A., Laptiev, O., Opirskyy, I., Soloviova, O. (2020). Modification of the algorithm (OFM) S-box, which provides increasing crypto resistance in the post-quantum period. International Journal of Advanced Trends in Computer Science and Engineering (IJATCSE), 9 (5), 8725–8729. doi: https://doi.org/10.30534/ijatcse/2020/261952020

[12] Bakiko, V. N., Popovych, P. V., Shvaichenko, V. B. (2018). Estimation of noise immunity of the communication channel under the influence of random interference. Visnyk Natsionalnoho tekhnichnoho universytetu "KhPI". Seriya: Tekhnika ta elektrofizyka vysokykh napruh, 14, 7–10.

[13] Milov, O., Yevseiev, S., Ivanchenko, Y., Milevskyi, S., Nesterov, O., Puchkov, O. et. al. (2019). Development of the model of the antagonistic agents behavior under a cyber conflict. Eastern-European Journal of Enterprise Technologies, 4 (9 (100)), 6–19. doi: https://doi.org/10.15587/1729-4061.2019.175978

[14] Berkman, L., Barabash, O., Tkachenko, O., Musienko, A., Laptiev, O., Salanda, I. (2020). The Intelligent Control System for infocommunication networks. International Journal of Emerging Trends in Engineering Research, 8 (5), 1920–1925. doi: https://doi.org/10.30534/ijeter/2020/73852020

[15] Laptiev, O., Shuklin, G., Hohonianc, S., Zidan, A., Salanda, I. (2019). Dynamic Model of Cyber Defense Diagnostics of Information Systems With The Use of Fuzzy Technologies. 2019 IEEE International Conference on Advanced Trends in Information Theory (ATIT). doi: https://doi.org/10.1109/atit49449.2019.9030465

[16] Srivastav, S., Gupta, S. (2020). Results with Matlab coding of Middle Graph of Cycle and its related graphs in context of Sum Divisor Cordial. International Journal of Emerging Trends in Engineering Research, 8 (2), 398–401. doi: https://doi.org/10.30534/ijeter/2020/26822020

[17] Africa, A. D. M., Bulda, L. R., Marasigan, M. Z., Navarro, I. (2020). Binary Phase Shift Keying Simulation with MATLAB and SIMULINK. International Journal of Emerging Trends in Engineering Research, 8 (2), 288–294. doi: https://doi.org/10.30534/ijeter/2020/08822020

[18] Mashkov, O. A., Sobchuk, V. V., Barabash, O. V., Dakhno, N. B. et. al. (2019). Improvement of variational-gradient method in dynamical systems of automated control for integro-differential models. Mathematical Modeling and Computing, 6 (2), 344–357. doi: https://doi.org/10.23939/mmc2019.02.344

[19] Barabash, O., Dakhno, N., Shevchenko, H., Sobchuk, V. (2018). Integro-Differential Models of Decision Support Systems for Controlling Unmanned Aerial Vehicles on the Basis of Modified Gradient Method. 2018 IEEE 5th International Conference on Methods and Systems of Navigation and Motion Control (MSNMC), 94–97. doi: https://doi.org/10.1109/MSNMC.2018.8576310

[20] Barabash, O., Laptiev, O., Tkachev, V., Maystrov, O., Krasikov, O., Polovinkin, I. (2020). The Indirect method of obtaining Estimates of the Parameters of Radio Signals of covert means of obtaining Information. International Journal of Emerging Trends in Engineering Research (IJETER), 8 (8), 4133–4139. doi: https://doi.org/10.30534/ijeter/2020/17882020

[21] Rakushev, M., Permiakov, O., Lavrinchuk, O., Tarasenko, S., Kovbasiuk, S., Kravchenko, Y. (2019). Numerical Method of Integration on the Basis of Multidimensional Differential-Taylor Transformations. 2019 IEEE International Scientific-Practical Conference Problems of Infocommunications, Science and Technology (PIC S&T). doi: https://doi.org/10.1109/picst47496.2019.9061339

Received date 11.11.2020
Accepted date 12.01.2021
Published date 29.01.2021

Original Research Article: full paper

(2021), «EUREKA: Physics and Engineering»
Number 1

ADVANCED ENCRYPTION STANDARD USING FPGA OVERNETWORK

Hind Ali Abdul Hasan
Department of Laser & Optoelectronics Engineering
Alkut College University
Kut, Wasit, Iraq, 50001
hind.ali@alkutcollege.edu.iq

Safaa Maijd Mohammed
Department of Medical Instrumentation
Al-Farahidi University
Alqadisyiah, Qatr al-nada street, Baghdad, Iraq, 10011
Safa.suffi33@gmail.com

Noor Hayder Abdul Ameer
Department of Computer
University of Technology
Al-Sinaa street, Baghdad, Iraq, 10066
110048@uotechnology.edu.iq

Abstract

The increase number of eavesdropping or cracker to attack the information and hack the privacy of people. So, the essential issue is making system capable of ciphering information with rapid speed. Due to the advance in computer eavesdropping and cracker that made them to analysis the way of ciphering in rapid speed way. The development in the computer especially in the rapid processer in the last decade create the breaching of any system is a matter of time. Owing to most of breaching ways are based on analysis of system that requireы to be breached and to try brute force on that system to crack it. However, the lacking of influential processers that are capable of breaching system since earlier processors are limit to number of instructions. It can be done in second, which was not sufficient trying to break the system using brute force. In addition, the time required is far away from getting valuable messages in the time that needed. So, the research gives the focus on performing rapid system for ciphering the information rapidly and changing the ciphering every few milliseconds. The changing of ciphering in every millisecond helps system form preventing the eavesdropping and cracker from imposing brute force on the system and hacking the messages and images. The system that created is based on Advanced Encryption Standard (AES), which is it very best performing algorithm in ciphering and deciphering since it doesn't need complex mathematical formula. The research is about designing system that capable of performing AES by using high processer designed on Field programmable gate Area (FPGA). The ciphering of AES using FPGA helps minimize the time required to cipher the information. Also, the research will focus on ciphering and deciphering of images by AES using FPGA.

Keywords: FPGA, Advanced Encryption Standard, VHDL, security by AES, 256-AES , encryption by AES.

DOI: 10.21303/2461-4262.2021.001613

1. Introduction

The evolution that happens in the computer and the rapid processer that occur during the last decade make the breaching of any system is a matter of time [1]. Due most of breaching ways are based on analysis of system that need to be breached and to try brute force on that system to crack it [2, 3]. However, the lacking of powerful processers that are capable of breaching system since pervious processors are limit to number of instructions. It can be done in second, which was not sufficient trying to break the system using brute force [4]. In addition, the time required is far away from getting valuable messages in the time that needed [5, 6]. Due to these reasons, the research gives the focus on performing rapid system that capable of ciphering the information in rapid way and changing the ciphering every few milliseconds [7, 8]. The changing of ciphering in every millisecond helps system form preventing the eavesdropping and cracker from imposing brute force on the system and hacking the messages and images [9].

National Institute of standards and technology (NIST) used the Advanced Encryption Standard (AES) as a replacement for 3DES and IDES which was the most used for ciphering in

their time. The difference in the way of the AES than the 3DES and IDES is that AES is not based on Feistel Structure. The advantage of this structure is that AES can perform the whole block of data in single matrix [9].

The system that created is based on AES, which is it very best performing algorithm in ciphering and deciphering since it doesn't need complex mathematical formula [3, 10]. And it has flexibility in use because of it can used in ciphering message or images [10, 11]. Also, the AES is chosen based on preforming of the algorithm. It was the top on security scoreboard during the two previous decades. The evolution of this algorithm that develops pervious these years to became the best ciphering ways in network and banking security [12].

The system that created in this research is AES using the FPGA. The FPGA is device that capable of designing processer that capable of performing special algorithm based on the program that injected in the FPGA. The special processer that design in FPGA is capable of performing AES on images and message depending on the way that needed in attach that insert to the FPGA as input [13]. The FPGA is rapid the time that required to ciphering any text message in microsecond and enhanced the AES by ciphering and deciphering time required. Due to capability of parallel processing on FPGA [14]. The FPGA gives the opportunity to changing the ciphering ever millisecond in rapid ways since it only required a microsecond to cipher or decipher any messages [10]. This will help in sending information through the network will never be breaching due to rapid changing of ciphering.

A Huge amount of application of AES algorithm used because its ability in cipher data and invincible to break and the flexibility in usage [15, 16]. Also, it doesn't require massive amount of resources and that made it powerful in ciphering and deciphering. The AES consisting of four element or steps as shown in **Fig. 1 [**17].

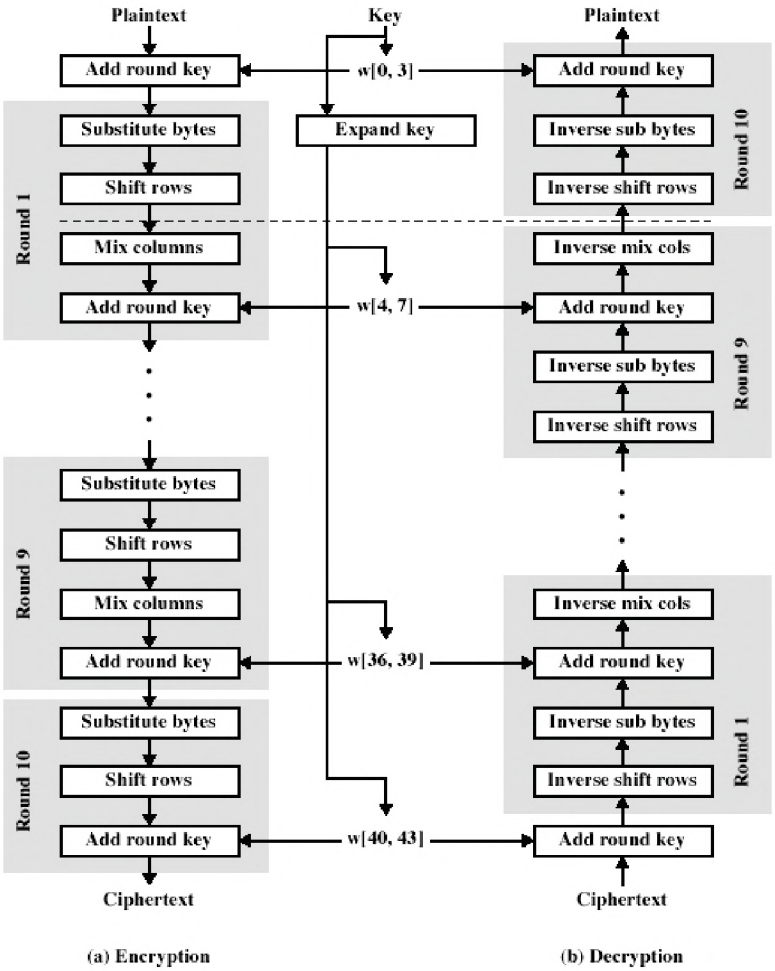

Fig. 1. The Overall structure of AES

As shown in the **Fig. 1** each round consist from various steps which these steps are **SubBytes**, which used to divide the bytes of messages into pieces in order to encrypt this message and exchange each pixel that want to be ciphering with value that located in S-Box. On the other hand, the second steps are **ShiftRows**, which will shift each row in amount that may be different from others row in the message or images. The last but not least step is **MixColumns** that will mix four bytes of each column and it will explain later in ciphering section. The last step is **ADDRoundKeys**. This step is used to add key in every round of the ciphering process. These steps are power of AES since it very complex and truck steps that made to create the mighty of AES algorithm.

2. AES with FPGA

The AES composed from four steps as mentioned before and can be shown in **Fig. 2**. As the initial step, the AES algorithm is subject to the data needed to be ciphering. It will deter the step if the data is required to be cipher as plane text for first operation for changing the plain text to state array [15]. Otherwise, if the data is consist from image it will not require to make array state since the images will represent as array state. This research uses 256×256 images for ciphering and deciphering. The first deterring of program is not needed since the images are represented as array. That means the image will go to the following process which will substitute all pixels with a value located in S-Box that corresponding to its location. The S-Box is constructed from 16×16 array. The number of values that S-Box consisted is 256 values and each one of these values are different from others in the same matrix that needed to be ciphered.

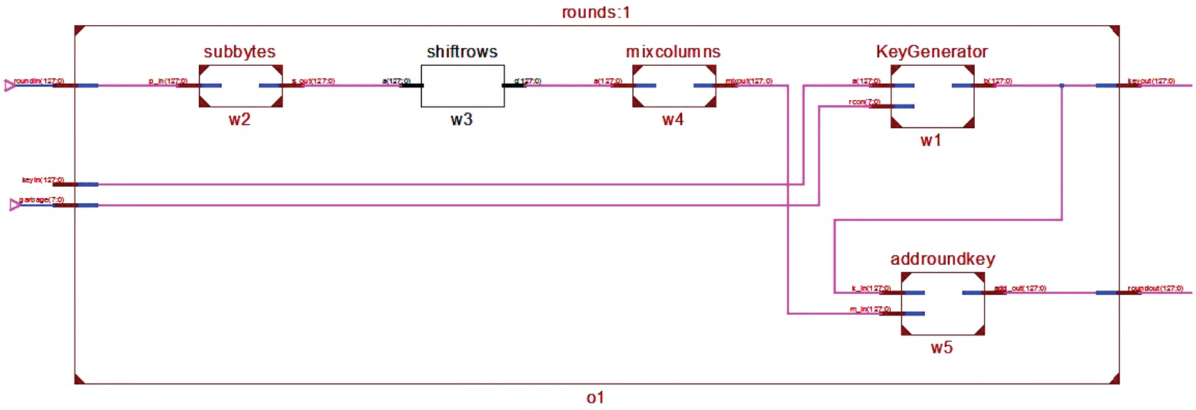

Fig. 2. AES Steps

The second step is simply substitution of every pixel in array with value that corresponding to the value in S-Box. Since the S-Box is an array and this size of this array is 16 by 16. The S-Box contains 256 values in it and each value is different from other that located in the same matrix. The operation of substitution of pixels in array with its corresponding value in S-Box can be shown in **Fig. 3**.

ShiftRows will be the Second step after complete the substitution of all pixel in array with its corresponding pixel in S-Box. The ShiftRows as its name mean that shifting all rows in the state array to the left. The shifting will be differ from row to row in the same state array matrix and the shifting will depends on their location. The shifting process based on Anti-Clock wise and the shifting process can be shown in **Fig. 4**.

In last step but not least the MixColumn, from its name its transform columns. The MixColumn will divide every column into 4 bytes block and each block will be transformed into polynomials equation by Galois function GF(2^8). These polynomial equation will be multiplied by its modulo $x^8+x^4+x^3+x^1+x^0$ as shown in **Fig. 5** [18].

Then the last step will applied which is KeyGenerate and AddRoundKey. This step is first generate key for XORed the 16 bytes of the key generated with its corresponding 16 bytes of array of image. The key is generated based on the schedule of the algorithm. **Fig. 6** shows the AddRoundKey process. Finally, when all these steps applied on the state array. The steps will repeat again for 10 more round on state array to encrypt the system as shown in **Fig. 7**.

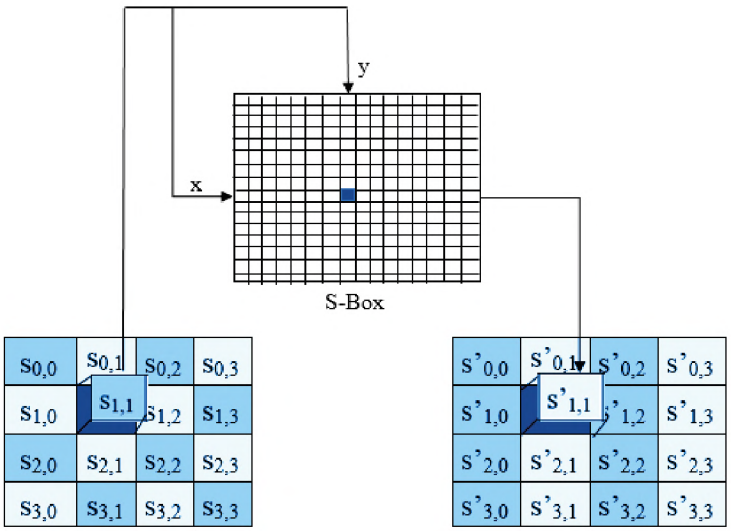

Fig. 3. Transformation of pixel [17]

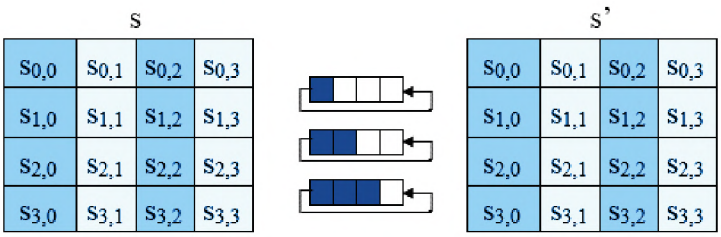

Fig. 4. ShiftRows processing

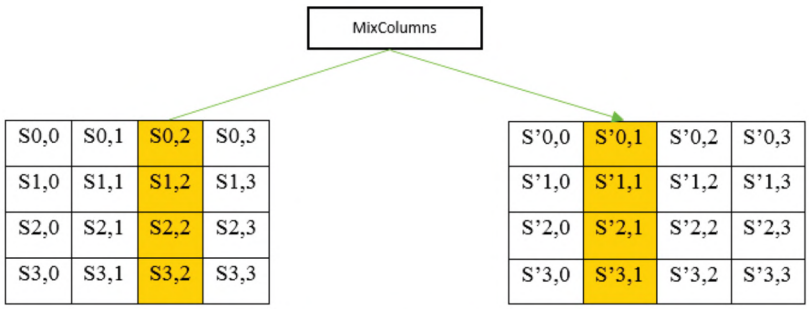

Fig. 5. Mix column transformation [19]

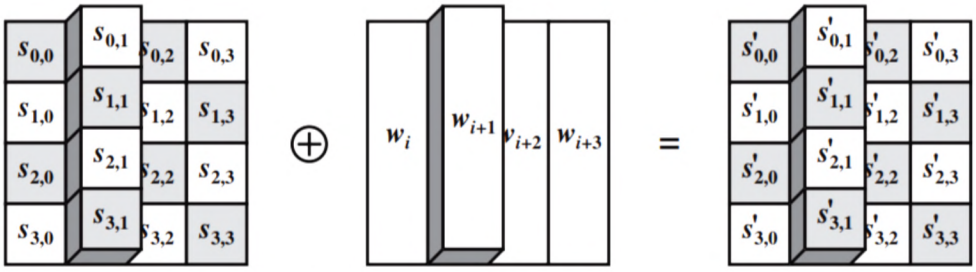

Fig. 6. Round Key transformation

The deciphering process will be as reverse to the steps of ciphering. It will start with AddRoundKey and back to all previous round. Then, this step completes the results of first round will be input to inverse of MixColumn. MixColumn will return each 4 byte to its original results by multiply each 4 bytes with module of GF(8) equation. Then the results of this will go to the third step. The Shift Row will shift return the offset of each row to its position. Once all rows return to its

order and location before Shifting Row. The final step will be applied when Sub Byte will return each value of the state to its real value based on the S-Box. The results of Sub Byte will be the original images or the plain text.

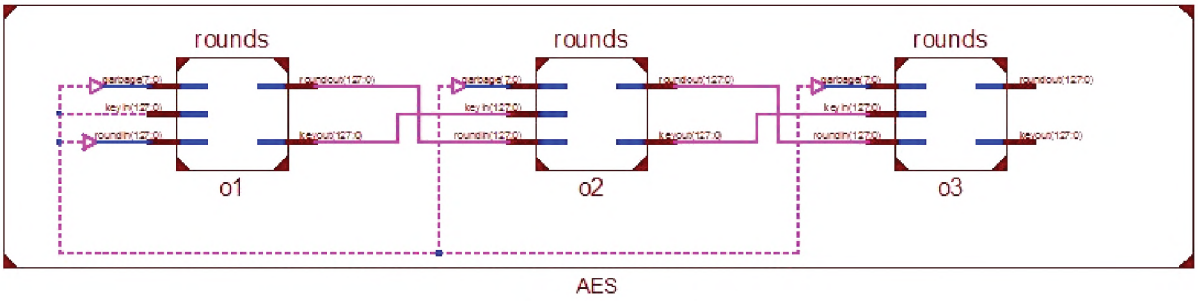

Fig. 7. Three Rounds of AES

3. Material and methods

Spartan 3AN is used for the implementation of the proposed algorithm as the device to implement the algorithm and has been programmed using Very High-level Design Language (VHDL). VHD L is used in this project for configuring and applying the AES algorithm in the FPGA. This language is one of the most famous languages that used in programming and configurable the FPGA. As known FPGA is very complicated devices specially in coding and working while in contrast it gives great results compare to other devices in the same field. The VHDL is used in Synthesis, simulation and generating the programmable file code for each structure and sections of AES algorithm in the FPGA and it can be shown in **Fig. 7.** The flexibility of fully utilizing and programing FPGA to achieve great results in ciphering and deciphering of AES in FPGA is noted.

4. Results

Rapid ciphering of information is most important in our days since the evolution of massive information need ciphering to transmit to their recipient. However, the using of FPGA help to improve of rapid ciphering of Image using AES. The combination of AES algorithm requires massive resource and injected on FPGA help to rapid ciphering of images. The time required to cipher 256×256 image is only 20 nanoseconds as shown in **Fig. 8**. This time is very helpful since it can cipher and decipher multiple images with no time.

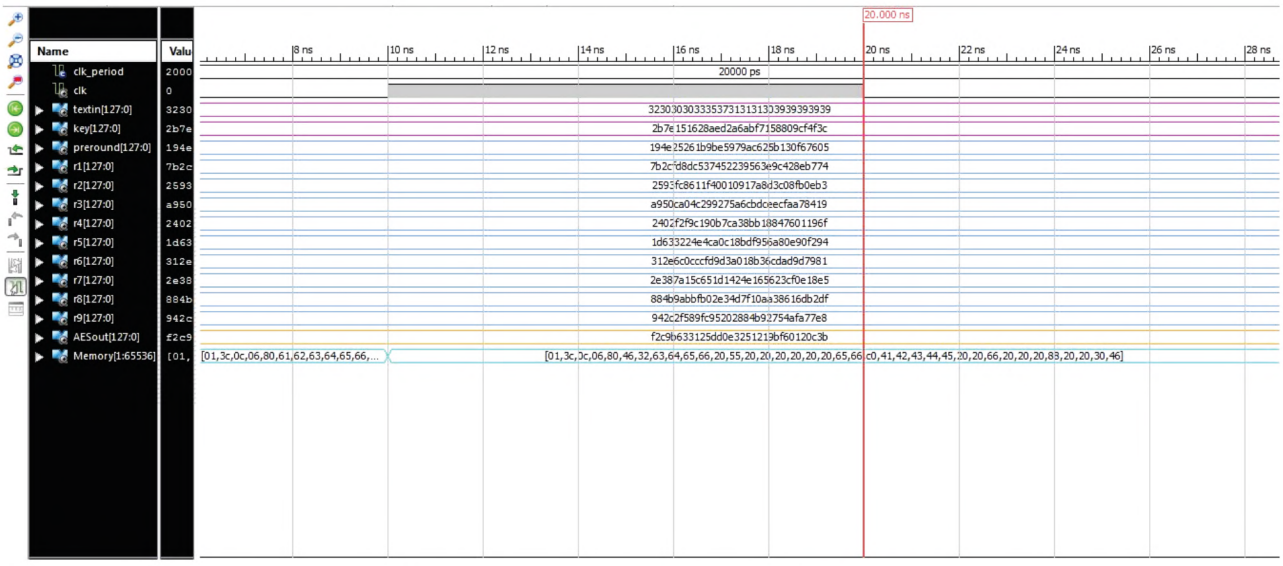

Fig. 8. Time required to cipher 256×256 image

Also, the resources of AES that toke from the FPGA resource are small as shown in **Table 1**. The FPGA that used in this experiment is Spartan 3AN and a frequency. The FPGA faster the operation of ciphering of image since it used parallel processing that means perform multiple tasks in same time if none of these tasks related to each other. The AES algorithm took the advantage of FPGA since most of their procedure is not related to each other. The resource that allocated in FPGA when injecting AES on it is explained as shown below.

Table 1
Adopted FPGA Resources

Logic Utilization	Used	Available	Utilization
Number of Slices	2000	5888	34 %
Number of Slice Flip Flops	812	11776	7 %
Number of 4 input LUTs	950	11776	8 %
Number of bonded IOBs	12	372	3 %
Number of GCLKs	1	24	4 %

In addition, the program is used to changing the ciphering with every millisecond. It will allow to give more confidently to the system and this will not be happening if the FPGA not here. The proposed is compared with different algorithm and different types of FPGA devices and these different algorithms are used different types of approach to encryptions data. However, the results that have been taken from this proposed algorithm is more greats than other as shown in **Table 2.** The table shows that all the proposed approach used 128 bits for ciphering compare to 256 bits which is more security and more reliable than other methods. However, this cost the proposed approach more time than other for ciphering due to the large size of the algorithm. Also, the results shows that the number of slices that is used is small compared to other since the algorithm used 256 bits types of algorithm compared to 128 bits for other methods. Also, it can be shown that the throughput of the algorithm is less than Harshali Zodpe and Ashok Sapkal due to two facts the first they used faster FPGA devices so the throughput is faster the other is that the algorithm used 256 bits in ciphering compared to 128 bits in the other methods.

Table 2
Comparative between different types AES approach [20]

Design	Device	Bit width (bits)	No. of Slices	Throughput (Gbps)
Proposed	Spartan 3 AN	256	2000	4.23
Wang and Ha	XC6VLX240T	128	15,612	1.88
Qiang et al.	XC4VLX60	128	1975	2.06
Harshali Zodpe and Ashok Sapkal	XC7VX690T	128	4089	6.34

5. Discussion of experimental results

Defending the data is the most important as for world international or personal to saves data. Every year many algorithms are either formed or add new features to the previous algorithms to enhance the security of algorithms. This research used the most effective algorithm which is AES. FPGA is used in this research for speed-up the process of the algorithm and had made major effect to the speed of the algorithm with only 20 ns for complete the ciphering of nine round. The algorithm used the 256 bits for ciphering which is great enhancement in the security to cipher text due to the fact the eavesdropping needs more time to deciphering and more

sophisticated computer to break the system compared to 64 or 128 AES algorithm. There is no limitation in 256 AES algorithm in this research due to using the FPGA for ciphering and deciphering since the FPGA used the parallel processing that allow to perform multiply process in the same and this save time for performing the 256-AES. However, without the FPGA used 256-AES for ciphering and deciphering is bit slower since it required more process for ciphering than other 64 or 128 AES algorithm. The enhanced for this research is to use on high quality image and tried to compress the image and also tried to used multiple single processors like using multiple raspberry-pi or Arduino to provide the same results like FPGA.

6. Conclusion

The massive resource of information increases in every day the advance of the computers that used by eavesdropping to attack these data. It gives the essentiality to find way to rapid ciphering and to changing ciphering from time to time to make it invincible to eavesdropping to hack system. This done by union the FPGA and AES since the AES has the best scoring in security scoreboard and FPGA is special device. It allows to create special processor to do the AES operations. The FPGA help in festering the ciphering of AES in only 20 nanoseconds for image sized 256×256 pixels. And this done due to the ability of FPGA in performing the parallel processing and support of the AES algorithm to work in parallel. The next steps in this research will applied the algorithm on larger image size and to perform the algorithm on other devices to like Raspberry Pi and Arduino in parallel mode.

References

[1] Ekert, A. K., Huttner, B., Palma, G. M., Peres, A. (1994). Eavesdropping on quantum-cryptographical systems. Physical Review A, 50 (2), 1047–1056. doi: https://doi.org/10.1103/physreva.50.1047

[2] Omran, S. S., Al-Hillali, A. A. (2015). Quarter of Iris Region Recognition Using the RED Algorithm. 2015 17th UKSim-AMSS International Conference on Modelling and Simulation (UKSim). doi: https://doi.org/10.1109/uksim.2015.70

[3] Babitha M.P., Babu, K. R. R. (2016). Secure cloud storage using AES encryption. 2016 International Conference on Automatic Control and Dynamic Optimization Techniques (ICACDOT). doi: https://doi.org/10.1109/icacdot.2016.7877709

[4] Barriga, L., Blom, R., Gehrmann, C.,Naslund, M. (2000). Communications security in an all-IP world. Ericsson review, 2, 96–107.

[5] Nishikawa, N., Amano, H., Iwai, K. (2017). Implementation of Bitsliced AES Encryption on CUDA-Enabled GPU. Lecture Notes in Computer Science, 273–287. doi: https://doi.org/10.1007/978-3-319-64701-2_20

[6] Abdullah, A. M. (2017). Advanced encryption standard (AES) algorithm to encrypt and decrypt data. Cryptography and Network Security.

[7] Maharjan, R., Shrestha, A. K., Basnet, R. (2019). Image Steganography: Protection of Digital Properties against Eavesdropping.arXiv.org. Available at: https://arxiv.org/abs/1909.04685

[8] Peake, T. M. (2005). Eavesdropping in communication networks. Animal Communication Networks, 13–37. doi: https://doi.org/10.1017/cbo9780511610363.004

[9] Alanazi, H. O., Zaidan, B. B., Zaidan, A. A., Jalab, H. A., Shabbir, M., Al-Nabhani, Y. (2010). New Comparative Study Between DES, 3DES and AES within Nine Factors. Journal of Computing, 2(3), 152–157.

[10] Stallings, W. (2011). Cryptography and Network Security Principles and Practice.Prentice Hall.

[11] Ueno, R., Morioka, S., Homma, N., Aoki, T. (2016). A High Throughput/Gate AES Hardware Architecture by Compressing Encryption and Decryption Datapaths. Cryptographic Hardware and Embedded Systems – CHES 2016, 538–558. doi: https://doi.org/10.1007/978-3-662-53140-2_26

[12] Banik, S., Bogdanov, A., Regazzoni, F. (2017). Compact circuits for combined AES encryption/decryption. Journal of Cryptographic Engineering, 9 (1), 69–83. doi: https://doi.org/10.1007/s13389-017-0176-3

[13] Jumma, L. F.,Omran, S. S. (2018). Design of Superscalar SHA-1 & SHA-2 MIPS Processor Using FPGA. Association of Arab Universities Journal of Engineering Sciences, 25(3), 88–99.

[14] Omran, S. S., Al-Hilali, A. A. (2018). Comparative Study Between Different Rectangle Iris Templates. 2018 International Conference on Advanced Science and Engineering (ICOASE). doi: https://doi.org/10.1109/icoase.2018.8548913

[15] Al-Hilali, A. A., Jumma, L. F., Amory, I. A. (2019). High-Quality Image Security Implementation Using 128-Bit Based on Advanced Encryption Standard algorithm. Journal of Southwest Jiaotong University, 54 (6). doi: https://doi.org/10.35741/issn.0258-2724.54.6.32

[16] Çavuşoğlu, Ü., Kaçar, S., Zengin, A., Pehlivan, I. (2018). A novel hybrid encryption algorithm based on chaos and S-AES algorithm. Nonlinear Dynamics, 92 (4), 1745–1759. doi: https://doi.org/10.1007/s11071-018-4159-4

[17] Messerges, T. S. (2001). Securing the AES Finalists Against Power Analysis Attacks. Fast Software Encryption, 150–164. doi: https://doi.org/10.1007/3-540-44706-7_11

[18] Elsherif, S., Mostafa, G., Farrag, S., Alexan, W. (2019). Secure Message Embedding in 3D Images. 2019 International Conference on Innovative Trends in Computer Engineering (ITCE). doi: https://doi.org/10.1109/itce.2019.8646685

[19] Al-Fedaghi, S., Alsulaimi, M. (2018). Privacy Thinging Applied to the Processing Cycle of Bank Cheques. 2018 3rd International Conference on System Reliability and Safety (ICSRS). doi: https://doi.org/10.1109/icsrs.2018.8688874

[20] Zodpe, H., Sapkal, A. (2020). An efficient AES implementation using FPGA with enhanced security features. Journal of King Saud University – Engineering Sciences, 32 (2), 115–122. doi: https://doi.org/10.1016/j.jksues.2018.07.002

Received date 16.08.2020
Accepted date 25.01.2021
Published date 29.01.2021

Original Research Article: full paper

(2021), «EUREKA: Physics and Engineering»
Number 1

A DEEP LEARNING MODEL IMPLEMENTATION BASED ON RSSI FINGERPRINTING FOR LORA-BASED INDOOR LOCALIZATION

Irsan Taufik Ali
Department of Electrical Engineering[1]
irsan.taufik@ui.ac.id

Abdul Muis
Department of Electrical Engineering[1]
muis@ui.ac.id

Riri Fitri Sari
Department of Electrical Engineering[1]
riri@ui.ac.id

[1]*Universitas Indonesia*
Depok, Indonesia, 16424

Abstract

LoRa technology has received a lot of attention in the last few years. Numerous success stories about using LoRa technology for the Internet of Things in various implementations. Several studies have found that the use of LoRa technology has the opportunity to be implemented in indoor-based applications. LoRa technology is found more stable and is more resilient to environmental changes. Environmental change of the indoor is a major problem to maintain accuracy in position prediction, especially in the use of Received Signal Strength (RSS) fingerprints as a reference database. The variety of approaches to solving accuracy problems continues to improve as the need for indoor localization applications increases. Deep learning approaches as a solution for the use of fingerprints in indoor localization have been carried out in several studies with various novelties offered. Let's introduce a combination of the use of LoRa technology's excellence with a deep learning method that uses all variations of measurement results of RSS values at each position as a natural feature of the indoor condition as a fingerprint. All of these features are used for training in-deep learning methods. It is DeepFi-LoRaIn which illustrates a new technique for using the fingerprint data of the LoRa device's RSS device on indoor localization using deep learning methods. This method is used to find out how accurate the model produced by the training process is to predict the position in a dynamic environment. The scenario used to evaluate the model is by giving interference to the RSS value received at each anchor node. The model produced through training was found to have good accuracy in predicting the position even in conditions of interference with several anchor nodes. Based on the test results, DeepFi-LoRaIn Technique can be a solution to cope with changing environmental conditions in indoor localization.

Keywords: Internet of Things, LoRa, Indoor Localization, RSSI Fingerprinting, Deep Learning.

DOI: 10.21303/2461-4262.2021.001620

1. Introduction

In recent years several studies have been carried out to solve the problem of Indoor localization with varying degrees of accuracy. The proposed indoor positioning system uses a variety of technologies such as Radio Frequency Identification (RFID), WiFi, Bluetooth Low Energy (BLE), Zigbee, Ultra-Wideband (UWB), Visible Light Communication (VLC) as well as vision-based technology. A few years ago the use of Low Power Wide Area (LPWA) LoRa technology was widely used to localize applications. LoRa is generally projected for outdoor applications. LoRa is generally projected for outdoor applications. Many publications have reported successful implementation of LoRa in a variety of outdoor applications including [1–4]. The LoRa property can also be used for indoor scenarios as in [5, 6] including for localization applications [7–9].

In general, regional characteristics and obstacles greatly affect the propagation of telecommunications signal waves regardless of technology. The density, height of buildings, environmental conditions, and contours of the area greatly affect the use of Internet of Things Technology such as LoRa for indoor localization applications. Sadowski et al [10] found that LoRa has a poor performance for indoor localization however on the other side diverse the development of IoT LoRa technology was found to have some advantages as an alternative wireless-based technology.

In other research Islam et al. [7]. LoRa technology was found to be more stable than WiFi and BLE and is more resilient to environmental changes. LoRa operates in the sub-GHz band, which makes it obtain more penetration capability so it is more resistant to noise and multipath so that LoRa becomes the best choice for indoor localization in large rooms and high rise buildings. In a recent 2020 study, Anjum et al. [11] chose LoRa as a device in the positioning system and it was found that LoRa could be a viable solution for the Indoor localization system. Diverse results were obtained from various studies in the use of LoRa in indoor locations. Here it is possible to see that there are many opportunities to improve LoRa performance in indoor locations. With the right approach, this property makes LoRa a promising choice for indoor localization systems.

One popular approach to indoor localization systems is the use of radiofrequency fingerprinting such as WiFi. Fingerprinting is a localization technique used for positioning based on the measurement of Received Signal Strength Intensity (RSSI) on several wireless access points. Positioning is based on a fingerprinting database as a reference containing RSS values that represent each position in the room. Fingerprinting based localization generally consists of two basic phases [12]. First, is the off-line phase, which is also called the training phase, and second, is the on-line phase, which is also called the test phase. In the off-line training stage, machine learning methods can be used to train and store fingerprints that contain all RSS data. Such machine learning methods not only to reduce computational complexity but also to gain core features in RSS for better localization performance. K-nearest-neighbor (KNN) algorithm, artificial neural network, and supporting vector machines, as a popular machine learning method that has been applied for fingerprinting-based indoor localization fingerprinting [13, 14].

Indoor localization systems use RSS data as fingerprint information [15] because of the simplicity of RSS operation and low hardware requirements. However, there are two disadvantages to the RSS method. First, the RSS data collected will be different for the same position from time to time due to the influence of various transmission conditions in the indoor environment. Changes in environmental conditions in a room such as changes in the location and addition of furniture, the addition of other equipment as well as changes in room partitions are a problem in the application of indoor localization. Changes in these conditions will greatly affect variations in RSS data obtained so that it can cause significant errors in positioning [16], especially in the use of fingerprint techniques for indoor localization. In general, there are three main problem formulations captured in the description of the above mention problem:

1. How to reduce the influence of changes in environmental conditions that are dynamic to minimize a very significant difference between the RRS value obtained at the off-line training stage with the RSS value obtained at the testing stage.

2. What is the right solution to address variations in RSS values that will occur in the use of fingerprinting techniques for indoor localization?

3. How to minimize positioning errors caused by variations in RSS value differences in each position due to dynamic environmental conditions.

The following studies have been conducted to overcome the dynamic environmental conditions in indoor localization.

In paper [17] Seong et al. proposed a new database creation method based on the Log-distance Path loss Model to delete RSSI data from unnecessary Wi-Fi, and produce an Access Point (AP) database that can be updated depending on changes in the indoor environment. The proposed algorithm has a higher position resolution than the existing fingerprinting and can improve positioning accuracy due to low dependence on the reference point. To develop the database, the AP signal is not regularly filtered by using Hausdorff distance. There is an opinion that this is not necessary, by using the method of deepening the data of abnormal measurement results can enrich the features of a position that will be the main source of learning at the training stage.

Luo et al. [18] using autonomous robots that patrol the path that has been determined to detect changes in the environment and continue to collect RSS measurement data and map it as a solution. RSS and map measurements are used to build and update databases. Position detection accuracy is maintained by always updating the fingerprinting database if environmental changes are detected. This research was conducted in a simulation with controlled change scenarios and in a limited environment.

Let's offer a different technique to cope with changes in dynamic environments without continuously updating when conditions change. The idea is quite simple, namely by recording all

variations of RSS measurement results in each position. Let's make variations of the measurement results as patterns of disturbance in the room that will be included in off-line training. Disturbances can be caused by many factors such as interference, attenuation of multipath, reflection, deflection, diffraction, and channel fading. Our study does not discuss in detail the types of disturbances that cause variations in RSS measurement results in one position. Let's consider these variations to be natural features of important environmental conditions as a source of learning. This paper contributes to overcoming the problems outlined above. In this paper, let's use the term DeepFi-LoRaIn to describe the use of LoRa device fingerprinting RSS data in indoor localization using the deep learning method. Some of these contributions are as follows:

1. Using LoRa technology as an option for indoor localization systems with good penetration capability so that it is more resistant to noise and multipath, resulting in a more stable RSS measurement value.

2. Using variations in the measurement results of RSS values in a position as a natural feature of the condition of the room without normalizing the data as a fingerprinting database. All of these features are used for training on deep learning methods.

3. Using a deep learning approach to solve the problem of changing environmental conditions to see the accuracy of position predictions.

4. Conduct testing of models that have been trained to be able to predict position in natural conditions using a variety Scenarios of RSS values and changes in the value of RSS in some Anchor Node (AN) that does not exist at the training stage.

The rest of the paper is outlined as follows. Related works are presented in Section 2. In Section 3 let's present the proposed system Deep-Fi LoRaIn. The result and validation are presented in Section 4. Discussion of experimental results is presented in Section 5. Finally, Section 6 shows the conclusion.

2. Related Work

Several studies have been conducted to improve the accuracy of positioning in the indoor localization system. Changes in the dynamic indoor environment are a challenge for researchers to maintain accuracy in positioning, especially in the use of fingerprinting RSS as a reference database. Some of the following research has tried to overcome the problems that have been stated previously.

Long-time before other studies were carried out in 2005 the paper [19] initiated a basic theory and developed an algorithm to build a localization and tracking system in a room with Zero-configuration. The technique introduced can produce a reliable system to support service and location-based network management. The localization algorithm takes input in the form of an on-line measurement of the Received Signal Strength (RSS) between the client and the adjacent AP, to estimate the client's location. Online RSS measurements between AP 802.11 are used to capture in real-time the effects of multi-path RF on temperature and humidity variations, opening and closing doors, furniture relocation, and human mobility during RSS measurements. This technique is also quite responsive to environmental dynamics because the impact of changes in physical characteristics has been explicitly found in the mapping between RSS value and actual geographical distance. This rationale is used as a reference in our research. Characteristics of environmental changes that affect variations in RSS values are the main features that represent natural conditions at a point. Variation of features is needed as a source of training in the proposed deep learning method.

A deep learning approach as a solution to the use of fingerprinting on indoor localization has been conducted in several studies with a variety of novelty offered. Some studies use Channel State Information (CSI) as Wi-Fi signal fingerprinting data and other studies use RSSI as fingerprinting. Wang et al. [13], produced a novelty using the deep learning method in the Indoor localization system. Indoor fingerprinting uses CSI which is trained using a deep learning approach called Deep learning fingerprinting (DeepFi). The DeepFi system architecture includes an off-line training phase and an online localization phase. In the off-line training stage, deep learning is used to train all deep network weights as fingerprints. Besides, the greedy learning algorithm is used to train each layer to reduce complexity. In the on-line localization phase, the probabilistic method is used based on the radial basis function to obtain an approximate location. The experimental results are presented to confirm that DeepFi can effectively reduce location errors compared to the previous

three methods namely FIFS [20], Horus [21], and Maximum Likehood [22]. The results obtained that DeepFi is more accurate in predicting the location of a device compared to the FIFS, Horus, and Maximum Likehood methods. Let's also use the term DeepFi in the development of research-based on RSSI fingerprinting data on LoRa devices – DeepFi-LoRaIn.

The use of CSI was also followed by researchers [23], but by using an integrated approach. The approach consists of three stages. First, using the Local Outlier Factor (LOF), the anomaly detection algorithm is used to correct abnormal data. Second, in the training phase, 3 DNN models were trained to classify fingerprint regions using CSI data that was processed from 3 antennas. Third, in the testing phase, a model fusion method called the Group Method of Data Handling (GMDH) was adopted to integrate 3 prediction results of several models and provide final position results. Test-bed experiments are carried out in empty corridors, and the final position accuracy reaches at least 97 %.

The CellinDeep in research [24] used a deep learning approach to Android-based cellular communication for indoor localization. The system produces this accuracy better than other cellular-based indoor systems at least 350 %. CellinDeep produces savings of at least 93.45 % power compared to WiFi-based techniques. Paper [25] used deep learning methods that focus even more on design problems including the influence of different hyperparameters, avoiding overfitting, and training algorithms. Some things done in the paper are used as references, such as the determination of several hyperparameters that are proven to be able to improve the optimization and accuracy of a model in the training and prediction process. Other guidelines [26] derived from several experiments that were carried out widely are also used as a reference for solving problems. The use of Python in Tensorflow along with Keras modules as a deep learning framework makes it easy for us to solve problems in deep learning in indoor localization as in previous studies [25, 27].

3. Proposed System Deep-Fi LoRaIn

The method used in this study is to combine the use of devices and simulations. The device used is the LoRa device to obtain RSS values at each position and NS3 simulators to simulate the LoRa network and Tensorflow Keras is used to simulate the process of deep learning and position prediction test. Following **Fig. 1** shows the overall research flow.

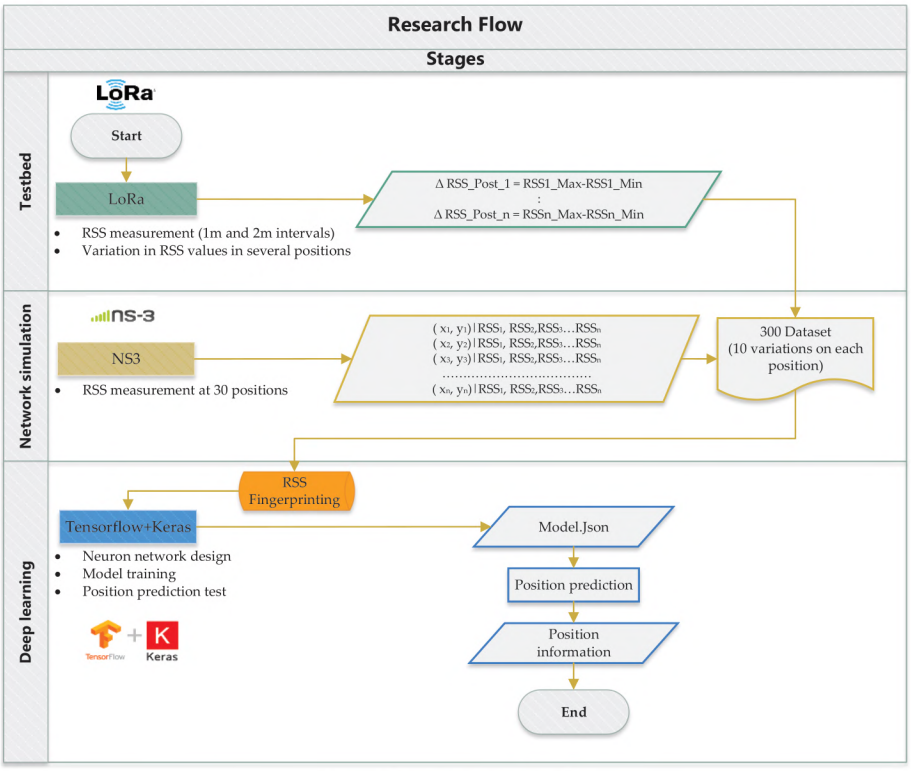

Fig. 1. Research flow chart

The research flow is divided based on the three stapes, The first step measuring RSS using a testbed, the second stage measuring RSSI at 30 positions using network simulation and the third stage is designing a neural network architecture. Detail of the flow of the research is described in the following stages as shown in **Fig. 1**.

3. 1. RSS measurement using testbed

Testbed was conducted to determine the RSSI characteristics of LoRa devices in a room and find variations in RSS values in several positions. This variation of RSS values will then be used to form a dataset that will be used in training. To obtain the existing pattern of disturbances in the room such as interference, attenuation of multipath, reflection, deflection, diffraction, and channel fading using data obtained based on direct measurements in the room using a testbed. During testing, let's used the ESP32 LoRa SX1278 device as an anchor node and as a tracked node. LoRa device specification is shown in **Table 1**.

Table 1
LoRa device specification

Parameter	LoRa Value
Radio	SX1278
Frequency band	433 MHz
Anchor height	2 m
Tracked node height	1.5 m
Radiation pattern	Omnidirectional
Sensitivity	–148 dBm, +20 dBm

The room size is 11 meters long and 7 meters wide. The building wall material is made of 70 % Concrete board and 30 % glass with a thickness of 0.75 cm. The ceiling is made of plasterboard with a thickness of 0.5 cm. In the room, there are 28 cubical tables with particle board material with a thickness of 2 cm and a thin steel storage cabinet with a thickness of 1.5 mm.

RSS measurement is conducted using 1 device as the anchor node and 1 device as tracked nodes. The measurement scenario is done by shifting the tracked node away from the anchor node at the intervals of 1 meter and 2 meters in the line-of-sight. Measurements are made in several points and then recorded in the database using a computer as a data logger. Measurements are made at each point every 2 seconds with a duration of 2 minutes for each position as shown in **Fig. 2**.

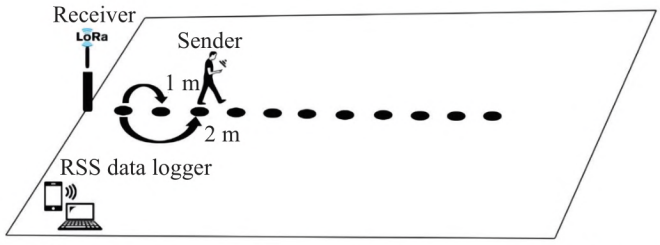

Fig. 2. RSS measurement position testbed in the interval of 1 m and 2 m

RSS characteristics obtained from the results of simulation and testbed measurements are used to find variations in RSS values at one point caused by disturbances that occur in the room. RSS measurement results are processed using spreadsheets to determine the amount of data variation as well as the range of data for the highest and lowest RSS values which are delta changes in RSS values found at each position at the time of measurement.

3. 2. Measure RSSI at 30 positions using network simulation

Network simulations using NS3 are performed to measure RSS at 30 positions based on values received at 4 anchor nodes. RSS values generated through simulation are fixed values that

represent each position. The results of this measurement are further extended using a variation pattern of values obtained in the measurement using the testbed so that each position has 10 variations of the measurement results. The total dataset generated is as much as 300 RSS fingerprinting data. The dataset in the form of RSS fingerprinting was obtained from simulations using NS-3 with a scenario of 4 anchor nodes positions in each corner of the room measuring 11X7 m. The collection of RSS values uses a node that functions as a tracked node that is positioned at 30 different points scattered in the room as shown in **Fig. 3.**

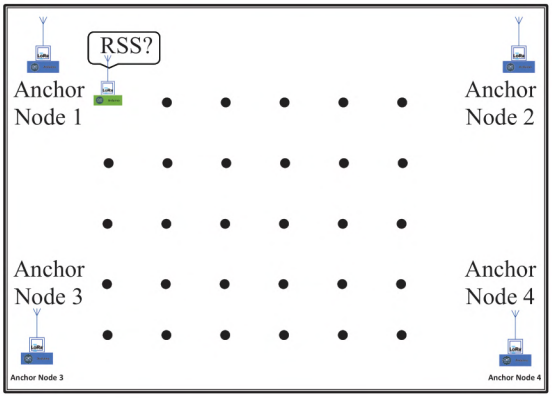

Fig. 3. RSS Fingerprint position for 30 different locations

Furthermore, the amount of RSS value sent from the tracked node will be read at each anchor node as a fingerprinting database. For communication between LoRa nodes using 433 MHz frequency with a 14 dBm sending signal strength with spreading factor 7. Tensorflow Keras simulations are used for several processes. First, to design a neuron network architecture along with hyperparameter. Second, conduct training on the fingerprinting dataset to produce the most optimal model. Third, it is used for testing in predicting position using the optimal model.

3. 3. System architecture

This section will explain system architecture in general As shown in **Fig. 4**. The system uses LoRa devices as sender and receiver, 4 devices as an anchor node, and 1 device as a tracked node. The system is divided into 2 stages: the off-line phase, which is called the training phase, and second, the on-line phase, which is called the test phase. The training phase is carried out to construct a database based on survey data related to RSS feeds in several positions. At this stage, a comprehensive location survey is performed to record fingerprints of the RSS magnitude of each anchor node at the target tracked node location. During the location survey, the collector must stand in each training position and do RSS scans for several at different positions. RSS value is collected at each position as a reference point in the database.

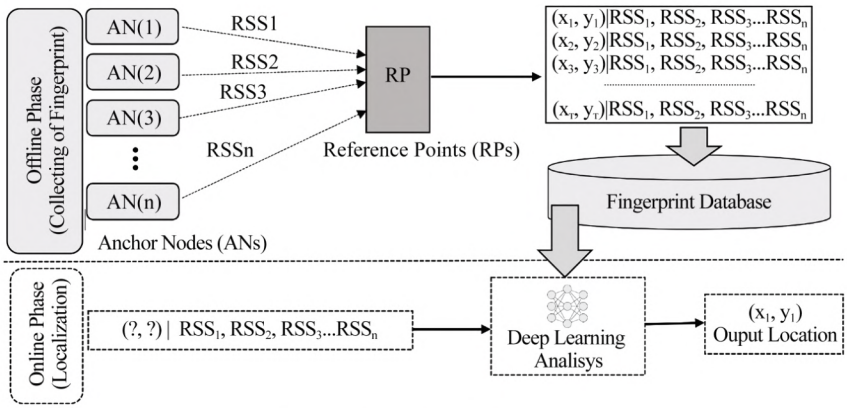

Fig. 4. System architecture

The LoRa end-device sends an uplink packet to the server. The server receives the packet and measures the RSSI value. These values are stored in a database and fingerprint maps are generated from RSSI data for the service area. In the online phase, the LoRa end-device sends an uplink packet containing RSSI information to the Server. RSSI data is sent to the position server from the position of the end device for identification.

A. Neuron Architecture

Hyperparameter is a variable that greatly affects the model output. Hyperparameter learning consists of the number of layers, the number of neurons in each layer, the choice of nonlinearity parameters, the learning rate, batch size, etc. The choice of hyperparameter is an important problem in learning. Until now, there is currently almost no integrated theory to choose the parameters correctly. However, some research experiments can be used as a reference as in the paper that has been reviewed previously, although not all hyperparameters are discussed in this paper. In this section, let's discuss how to improve the performance of deep learning networks and how to set deep learning hyperparameters. Let's focus on the parameters that affect the results of the training, to find the most accurate model.

a. Activation function

In the process of building a neural network, one of the choices is what activation function to use in the hidden layer as well as at the output layer of the network. The activation function decides whether a neuron should be activated or not by calculating the weighted sum and further adding bias with it. The purpose of the activation function is to introduce non-linearity into the output of a neuron. The neural network has neurons that work in correspondence of weight, bias, and their respective activation function. In a neural network, it would update the weights and biases of the neurons based on the error at the output. This process is known as back-propagation. Activation functions make the back-propagation possible since the gradients are supplied along with the error to update the weights and biases. As the name implies, the activation function functions to determine whether the neuron must be «active» or not based on the weighted sum of the input. In general, there are 2 types of activation functions, Linear and Non-Linear Activation functions. Let's use non-linear functions namely sigmoid and Relu. There are many other activation functions however, the functions mentioned above are functions that are used in this case.

The sigmoid activation or is also called a logistic function has been the default choice for activation functions for a long time. The sigmoid function is the continuous activation function most commonly used to classify 2 classes or groups of data. The Sigmoid function has a range from 0 to 1.

In hidden units, the nonlinear activation function $h(.)$ Used is the logistic sigmoid function, as follows [28]:

$$z_J = h\left(a_J\right) = \tanh\left(a_J\right), \tag{1}$$

the quantities a_J known as activations, where

$$\tanh(a) = \frac{(e^a - e^{(-a)})}{(e^a + e^{(-a)})} \tag{2}$$

a sum-of-squares error, in which the output units have linear activation functions, so that At output units, for regression problems, the usual activation function used is the identity function [28]:

$$y_k = a_k. \tag{3}$$

For classification problems, the usual activation function used is a logistical sigmoid function, i. e.:

$$y_k = \sigma(a_k), \tag{4}$$

where

$$\sigma(a) = \frac{1}{1+e^{-a}}. \tag{5}$$

The ReLU function is the most popular function currently used with several success stories in terms of image recognition and voice recognition. Basically, ReLU does a «threshold» from 0 to infinity. ReLU can also cover up weaknesses held by Sigmoid and Tanh. It is known that the Rectified Linear Unit (ReLU), is formulated as a function [29]

$$f(x) = \max(0, x). \tag{6}$$

b. Learning rate

The use of learning rate parameters has an important influence on the time needed to achieve the desired target. Will slowly optimize the value of weight changes and produce smaller errors. The learning rate variable states a constant that is between 0.1–0.9. This value shows the speed of learning from the network. If the learning rate used is too small then too many epochs are needed to achieve the desired target value, causing the training process to take a long time. The greater the value of learning rate is used, the network training process will be faster, but if it is too large it will cause the network to become unstable and cause repeated error values back and forth between certain values, thus preventing errors from reaching the expected target. Therefore the selection of the value of the variable learning rate must be as optimal as possible to obtain a fast training process [30].

c. Adam optimization

Adam (Adaptive Moment Estimation) is a first-order stochastic-based optimization algorithm of stochastic objective functions, based on adaptive estimates of low-order moments that can be used instead of the classical stochastic gradient descent procedure to update the network weight iteratively based on training data. Adam is currently a popular algorithm in the field of deep learning because it achieves good results quickly. Empirical results show that Adam works well in practice and is better than other stochastic optimization methods. Adam is relatively easy to configure where the default configuration parameters work well in most problems. In several papers [31, 32], Adam is recommended as an optimization algorithm used for deep learning applications. Adam keeps an exponentially decaying average of past gradients m_t. m_t and v_t are values of the first moment which is the Mean and the second moment which is the uncentered variance of the gradients respectively [33]. The formulas for the first Moment (mean) and the second moment (the variance) of the Gradients. Where β_1 and β_2 is Exponential decay rates:

$$\hat{m}_t = \frac{m_t}{1-\beta_1^t}, \tag{7}$$

$$\hat{v}_t = \frac{v_t}{1-\beta_2^t}. \tag{8}$$

Then the final formula for the parameter update is:

$$\theta_{t+1} = \theta_t - \frac{\eta}{\sqrt{\hat{v}_t + \epsilon}} \hat{m}_t, \tag{9}$$

where θ_t is updated parameters.

d. Number of layers

Bengio et al. [26], suggests the use of a higher number of hidden neuron layers to provide significant expressive power. A large number of hidden layers provide more capacity for more complex function models with weaknesses that are difficult in the training process. For regression and classification tasks, and not learning representations, it is also recommended to use the same layer size rather than decreasing or increasing the number of layers. The fully-connected layer is the layer in which all the activation neurons from the previous layer are all connected with neurons in the next layer as well as ordinary artificial neural networks. Every activation from the previous layer needs to be converted into one-dimensional data before it can be connected to all neurons in the Fully-connected layer. The difference between the fully-connected layer and the ordinary convolution layer

is that the neurons in the convolution layer are connected only to certain regions of the input, while the fully-connected layer has a whole connected neuron. However, the two layers still operate the dot product, so the function is not so different. The neural network configuration is shown in **Fig. 5.**

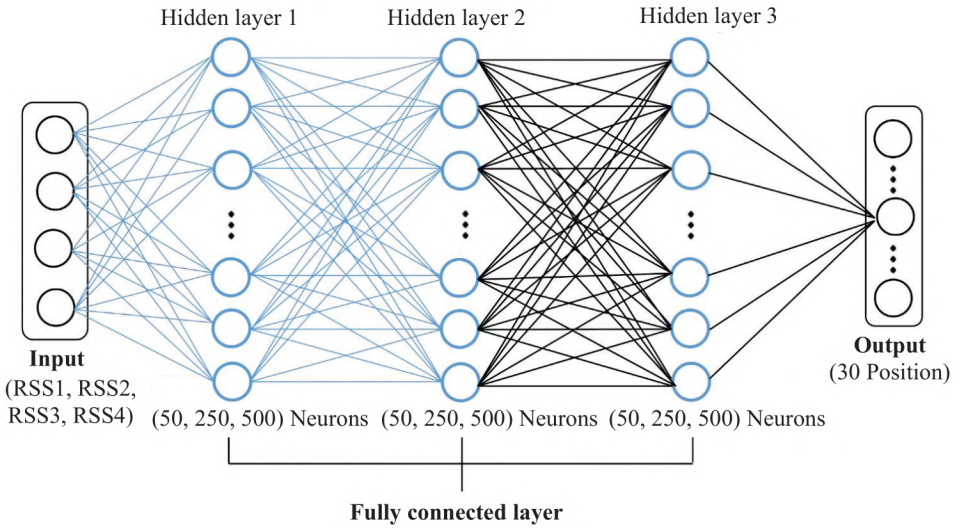

Fig. 5. Neural network configuration

Recommendations from some of the above experimental results are used as a reference to determine hyperparameter in this paper. Let's propose to use three hidden layer neural networks that are fully connected by changing the number of neurons in each hidden layer during training. All hidden layers are equipped with the ReLU non-linearity activation function and for output using the Sigmoid activation function. For the output layer, let's use a dropout layer with a 50 percent reduction rate. Its weight is initialized by using the random procedure suggested by [34]. Neural networks are trained using Adam's algorithm with a learning rate of 0.001, batch size 8. Training data uses 70 % of the 300 data available on the datasets while the test data uses 30 % of the 300 data available on the datasets. Input is the RSSI value obtained from 4 different anchor nodes. The output is an approximate location with 30 labels in a multi-categorical format that represents each position. The following **Table 2** shows the parameters used.

Table 2
Parameter Set Up

Parameter	Parameter Value
Model type	Sequential
Hidden layer (Activation)	ReLu
Output layer (Activation)	Sigmoid
Hidden layer number	3
Neuron number	50, 250, 500 fully connected layer
Optimizer	Adam
Data set size	300
Data training	70 %
Data test	30 %
Learning rate	0.001
Batch size	8
Epochs	100, 125, 150, 200, 250

The main objective of the training stage is to find the best model with the highest accuracy, which will then be used as a reference to determine the position at the testing stage. In this scenario,

the training is repeated to find the best model. At each parameter switch, the number of neurons and epochs is set with different values. For the parameter number of neurons using 3 different values, namely 50, 250, and 500 neurons with all layers connected. Epochs parameter uses 5 different values namely, 100, 125, 150, 200, and 250 number of epochs. The results of the training model will be discussed in result and validation in the next session.

B. Testing Scenarios

The dataset used is in the form of a fingerprint database which is the result of RSS measurements using the previous NS-3 simulation stage. The determination of variations in data features is done randomly uses on RSS values of 30 positions that have been obtained on measurements using NS-3. The range of variations in RSS value generated refers to the delta values obtained in the measurement using the testbed. Each position produces 10 variations of RSS values, resulting in 300 datasets of RSS values from 30 positions on the 4 anchors.

The test stage for predicting the position consists of 4 scenarios. The first scenario is called variable position testing which aims to measure the accuracy of the prediction results of each feature variation that each position has. In this test, the RSS input values are taken randomly from various features representing the 30 available positions from the RSS fingerprinting dataset.

The second scenario is called an adaptive test which aims to measure the accuracy of prediction of positions if there is a change in the indoor environment. Adaptive testing consists of 3 scenarios namely the scenario of changes in the value of RSS on 1 anchor node, 2 anchor nodes, and 3 anchor nodes at each position randomly. Changing the RSS value is done to simulate interference with the environment that can occur when predicting position. Disturbances can change the measurement results of RSS values at certain anchor nodes.

4. Result and Validation

4. 1. Training model result

Based on the results of several pieces of training using a combination of different numbers of neurons and epochs, let's obtain varying model accuracy values as shown in **Table 3** below.

Training using 50 neurons; the number of epochs 100 produces an accuracy value of the model 84.44 %, the number of epochs 125 has an accuracy of the model 86.67 %, the number of epochs 150 obtains an accuracy value of the model 84.44 %, the number of epochs 200 gets an accuracy value of the model 87.78 % and the accuracy of the model the highest is 90 % on the number of epochs 250.

Furthermore, training uses 250 neurons; the number of epochs 100 obtained the accuracy value of the model 81.11 %, the number of epochs 125 resulted in the accuracy of the model 83.33 %, the number of epochs 150 obtained the accuracy value of the model 85.56 %, the number of epochs 200 obtained the accuracy value of the model 87.78 % and the accuracy value of the model the highest was obtained on epochs 250 with a model accuracy value of 88.89 %.

The training uses 500 neurons; the number of epochs 100 produces an accuracy value of the model 82.22 %, the number of epochs 125 obtained the accuracy of the model 85.56 %, the number of epochs 150 the accuracy value of the model is 84.44 %, the number of epochs 200 gets the accuracy value of the model 87.78 % and the accuracy value of the model the number of epochs 250 is 92.22 %. From the overall results of the training, the highest accuracy model obtained on the use of the number of 500 neurons on epochs 250 was 92.22 %.

Table 3

Training model accuracy

Epochs	Model Accuracy (%)		
	50 Neurons	250 Neurons	500 Neurons
100	84.44	81.11	82.22
125	86.67	83.33	85.56
150	84.44	85.56	85.56
200	87.78	87.78	90.00
250	90.00	88.89	92.22

In **Fig. 6** it is possible to see a graph of the highest model training results with an accuracy of 92.22 % using 500 neurons and 250 epochs. In the graph, it is possible to see the results of the training model that shows that there is no overfitting where the accuracy value obtained during training does not exceed the accuracy value obtained during training.

Fig. 7 shows a graph of the loss model where the amount of the loss value obtained in testing is below the loss value during training. This model is the best model obtained from the overall results of the training model used as a reference to predict the position at a later stage.

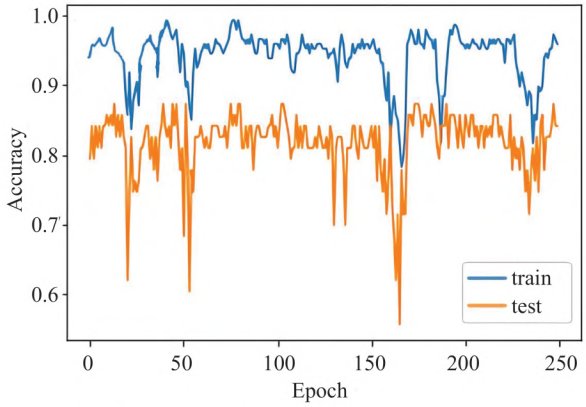

Fig. 6. Result of validation of the training model

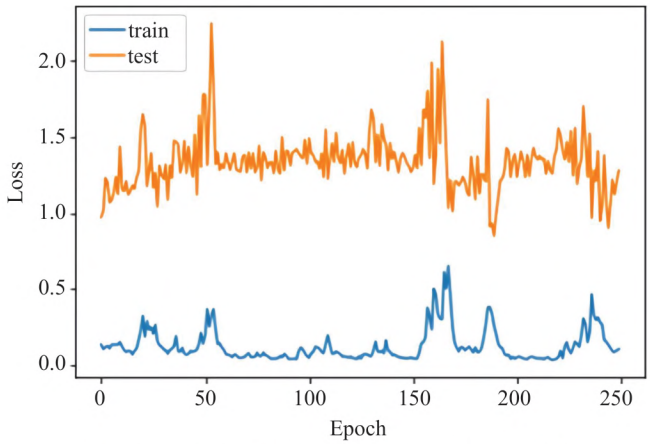

Fig. 7. Result of validation of the loss model

4. 2. Varied positions testing results

In the varied position testing stages, the input RSS values at 4 AN that have been randomly selected from each position. The test produces predictive results that correspond to 30 actual positions as shown in **Table 4**.

Table 4

Prediction result of 30 positions for Varied position test and

Input (RSS1,RSS2,RSS3,RSS4)	Real Position	Predict Position
1	2	3
[–39.0871,–54.1477,–62.7648,–65.0123]	1	1
[–42.8357,–54.3426,–62.9856,–64.6272]	2	2
[–46.9621,–53.7561,–64.4561,–62.8952]	3	3
[–51.8922,–46.9673,–61.3546,–63.5343]	4	4
[–54.5921,–42.5249,–63.6538,–63.2173]	5	5

Continuation of Table 4

1	2	3
[–56.2007,–37.1931,–64.6808,–62.7425]	6	6
[–48.1532,–58.1024,–58.1733,–63.1034]	7	7
[–48.7533,–54.9862,–60.3752,–61.7533]	8	8
[–51.8532,–53.2734,–60.8533,–61.4732]	9	9
[–52.8637,–52.8543,–62.8632,–61.8656]	10	10
[–56.3754,–50.6482,–62.7563,–62.1064]	11	11
[–56.5783,–48.3858,–63.2738,–58.2567]	12	12
[–54.6392,–58.8634,–55.5383,–59.6374]	13	13
[–54.1073,–58.8536,–57.5993,–56.1274]	14	14
[–55.6499,–56.8695,–57.4759,–58.4178]	15	15
[–55.1962,–54.3759,–59.9853,–58.1652]	16	16
[–58.7353,–54.9637,–58.8263,–57.1823]	17	17
[–60.1938,–52.5638,–61.2933,–57.2034]	18	18
[–59.0723,–60.9722,–52.1733,–57.5743]	19	19
[–58.8653,–60.1062,–52.9724,–56.0363]	20	20
[–59.9627,–58.9366,–53.6428,–55.7453]	21	21
[–59.8714,–59.1291,–55.2549,–53.6468]	22	22
[–60.9632,–58.2134,–56.1633,–52.9833]	23	23
[–62.3647,–59.4629,–59.3562,–52.4728]	24	24
[–61.3849,–63.7005,–43.1623,–56.7086]	25	25
[–61.9673,–63.9763,–47.1734,–53.8364]	26	26
[–61.1635,–62.9634,–49.9534,–52.9534]	27	27
[–61.9726,–62.4838,–51.5368,–48.8253]	28	28
[–64.1834,–62.1723,–55.4738,–46.8356]	29	29
[–63.2739,–61.8364,–56.1836,–43.9673]	30	30

The 30 input RSS values that are used represent 30 positions at the test stage resulting in the exact position prediction results corresponding to the actual position. As represented in **Fig. 8.**

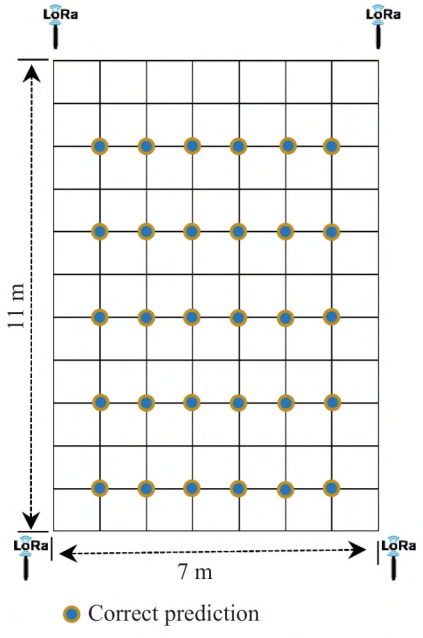

Fig. 8. Prediction result of 30 positions for varied position testing

Prediction results for positions 1 to 30 are very much in line with the actual position. These results indicate that the model obtained from the training results functions optimally as a reference at the prediction stage.

4. 3. Adaptive 1 node test result

In the adaptive 1 node test, the changes in RSS values in several AN positions do not significantly influence the predicted results. A prediction error occurred at 4 points out of 30 test points. The test result data can be seen in the following **Table 5**.

Table 5

Prediction result of 30 positions for adaptive test

Input (RSS1,RSS2,RSS3,RSS4)	Real Position	Predict Position
[–39.0871, –54.1477, –60.5478, –65.0123]	1	1
[–40.8647, –54.3426, –62.9856, –64.6272]	2	1
[–46.9621, –50.7685, –64.4561, –62.8952]	3	3
[–51.8922, –46.9673, –61.3546, –55.8673]	4	11
[–54.5921, –42.5249, –63.6538, –63.2173]	5	5
[–56.2007, –37.1931, –62.7332, –62.7425]	6	6
[–48.1532, –55.8757, –58.1733, –63.1034]	7	7
[–48.7533, –54.9862, –60.3752, –59.1857]	8	8
[–52.3569, –53.2734, –60.8533, –61.4732]	9	9
[–52.8637, –52.8543, –62.8632, –62.7356]	10	10
[–57.9563, –50.6482, –62.7563, –62.1064]	11	11
[–56.5783, –48.3858, –60.8686, –58.2567]	12	12
[–54.6392, –55.875, –55.5383, –59.6374]	13	12
[–54.1073, –58.8536, –55.9636, –56.1274]	14	14
[–56.1356, –56.8695, –57.4759, –58.4178]	15	15
[–56.9866, –54.3759, –59.9853, –58.1652]	16	16
[–58.7353, –56.1345, –58.8263, –57.1823]	17	16
[–60.1938, –52.5638, –60.4736, –57.2034]	18	18
[–59.0723, –60.9722, –52.1733, –58.1355]	19	19
[–58.8653, –61.8653, –52.9724, –56.0363]	20	20
[–59.9627, –58.9366, –53.6428, –54.8674]	21	21
[–58.6537, –59.1291, –55.2549, –53.6468]	22	22
[–60.9632, –58.2134, –56.1387, –52.9833]	23	23
[–63.1698, –59.4629, –59.3562, –52.4728]	24	24
[–61.3849, –63.7005, –42.8756, –56.7086]	25	25
[–61.9673, –63.1899, –47.1734, –53.8364]	26	26
[–62.8754, –62.9634, –49.9534, –52.9534]	27	27
[–61.9726, –62.4838, –50.9532, –48.8253]	28	28
[–64.1834, –63.3861, –55.4738, –46.8356]	29	29
[–63.2739, –61.8364, –55.4637, –43.9673]	30	30

Fig. 9 exhibits 4 position prediction errors, 2 of them just shifted to the closest position, which was position 2 and position 17 prediction.

Incorrect prediction results occur when using input data in position 2, position 4, position 13, and position 17. Prediction for position 2 produces output for position 1, position 4 produces prediction output position 11, position 13 produces predictive output position 12, and position 17 produces predictive output position 16.

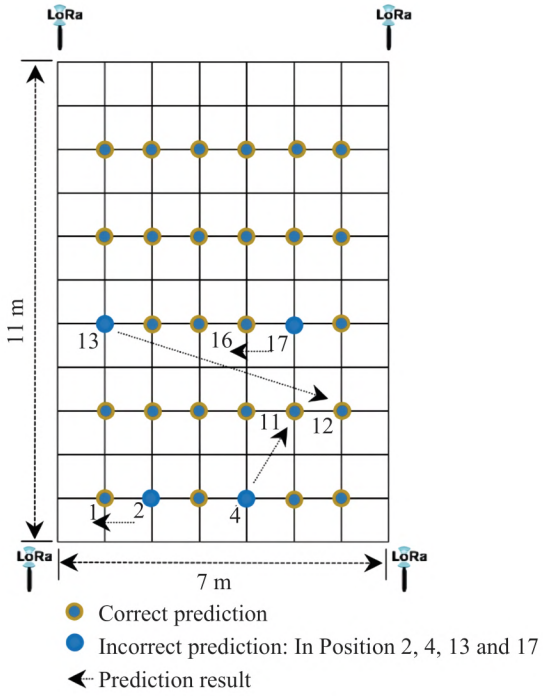

Fig. 9. Prediction result of 30 positions for adaptive 1 node test

4. 4. Adaptive 2 node test result

For adaptive 2 node testing results, prediction error increased from the previous test to 5 positions as shown in **Table 6** and **Fig. 10** below.

Table 6

Prediction result of 30 positions for adaptive 2 node test

Input (RSS1,RSS2,RSS3,RSS4)	Real Position	Predict Position
1	2	3
[–40.0426, –54.1477, –60.5478, –65.0123]	1	1
[–40.8647, –52.7537, –62.9856, –64.6272]	2	2
[–46.9621, –50.7685, –64.4561, –61.2937]	3	3
[–50.8663, –46.9673, –61.3546, –55.8673]	4	11
[–54.5921, –42.5249, –62.7384, –63.2173]	5	5
[–56.2007, –36.9371, –62.7332, –62.7425]	6	6
[–46.5362, –55.8757, –58.1733, –63.1034]	7	7
[–48.7533, –54.9862, –61.6365,-59.1857]	8	8
[–52.3569, –53.2734, –60.8533,-62.6382]	9	9
[–52.8637, –53.0635, –62.8632, –62.7356]	10	10
[–57.9563, –50.6482, –64.0737, –62.1064]	11	11
[–56.5783, –48.3858, –60.8686, –57.5352]	12	12
[–54.6392, –55.875, –54.2738, –59.6374]	13	14
[–56.8364, –58.8536, –55.9636, –56.1274]	14	14
[–56.1356, –58.0635, –57.4759, –58.4178]	15	15
[–56.9866, –54.3759, –59.9853, –60.1257]	16	16
[–58.7353, –56.1345, –61.8536, –57.1823]	17	16
[–60.1938, –52.5638, –60.4736, –58.0436]	18	18

Continuation of Table 6

1	2	3
[–59.0723, –60.9722, –52.1733, –58.1355]	19	19
[–58.8653, –61.8653, –52.9724, –58.0364]	20	20
[–58.8653, –61.8653, –52.9724, –58.0364]	21	22
[–58.6537, –61.1873, –55.2549, –53.6468]	22	22
[–62.1584, –58.2134, –56.1387, –52.9833]	23	23
[–63.1698, –60.0354, –59.3562, –52.4728]	24	24
[–61.3849, –65.6353, –42.8756, –56.7086]	25	25
[–61.9673, –63.1899, –47.1734, –56.0627]	26	26
[–62.8754, –62.9634, –49.9534, –54.0263]	27	27
[–61.9726, –63.0527, –50.9532, –48.8253]	28	28
[–64.1834, –63.3861, –55.4738, –47.9267]	29	29
[–65.0737, –61.8364, –55.4637, –43.9673]	30	29

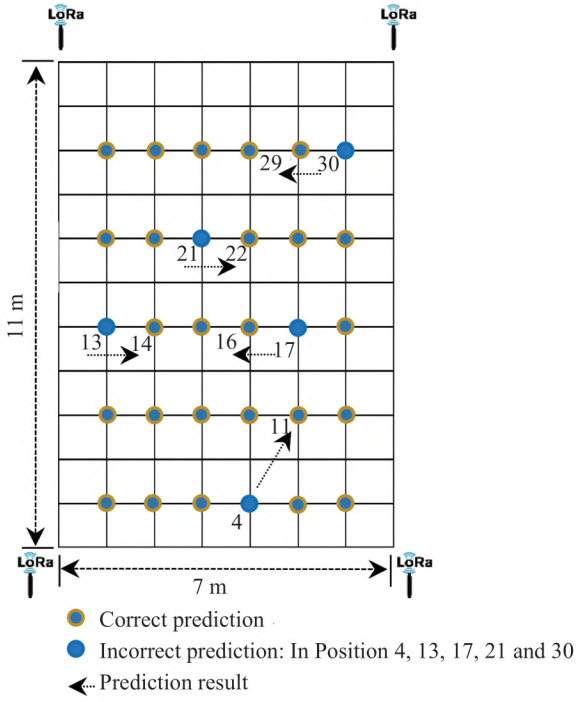

Fig. 10. Prediction result of 30 positions for adaptive 2 node test

Prediction errors occur at 5 positions namely, position 5, position 13, position 17, position 21, and position 30. Position 4 is predicted to be position 11, position 13 is predicted at the closest position is 14. At position 17 the prediction becomes position 16, Position 21 becomes position 22, and prediction result position 30 becomes position 29. From 5 prediction error results, 4 prediction positions only shift to the closest position.

4. 5. Adaptive 3 node test result

Adaptive test results for changes in 3 nodes increased from adaptive testing on 2 nodes to 9 position prediction errors. These errors can be seen in **Table 7** and **Fig. 11** below.

Prediction errors occur at 9 positions, namely, at position 4, position 8, position 13, position 17, and position 20. Furthermore, the prediction error occurs at position 21, position 22, position 28,

and position 30. For all prediction errors, 5 of them are error position predictions that also occurred in previous tests. **Fig. 11** is clearly seen from 9 prediction errors, 7 prediction errors are only shifted at the closest position, position 8 prediction becomes position 9, position 13 prediction shifts to position 14, and position 17 prediction becomes position 16. Furthermore, prediction of position 20 becomes position 19, prediction position 21 shifts to position 22, prediction of position 28 becomes position 27, and the result of the prediction of position 30 shifts to position 29. For the results of predictions that have a shift in a position somewhat far away is at position 4 and position 22. Prediction of position 4 becomes position 11 and prediction 24 shifts to position 14.

Table 7

Prediction result of 30 positions for adaptive 3 node test

Input (RSS1,RSS2,RSS3,RSS4)	Real Position	Predict Position
[–40.0426,–54.1477,–60.5478,–66.0527]	1	1
[–40.8647,–52.7537,–64.9657,–64.6272]	2	2
[–49.8546,–50.7685,–64.4561,–61.2937]	3	3
[–50.8663,–46.9673,–64.9665,–55.8673]	4	11
[–54.5921,–42.5249,–62.7384,–64.7854]	5	5
[–54.8754,–36.9371,–62.7332,–62.7425]	6	6
[–46.5362,–55.8757,–58.1733,–63.8094]	7	7
[–50.6342,–54.9862,–61.6365,–59.1857]	8	9
[–52.3569,–54.8375,–60.8533,–62.6382]	9	9
[–53.9446,–53.0635,–62.8632,–62.7356]	10	10
[–57.9563,–50.6482,–64.0737,–63.0463]	11	11
[–55.1856,–48.3858,–60.8686,–57.5352]	12	12
[–54.6392,–55.875,–54.2738,–58.9547]	13	14
[–56.8364,–58.8536,–55.9636,–56.6484]	14	14
[–56.1356,–58.0635,–57.4759,–58.8536]	15	15
[–56.9866,–54.3759,–60.1757,–60.1257]	16	16
[–56.0251,–56.1345,–61.8536,–57.1823]	17	16
[–60.5424,–52.5638,–60.4736,–58.0436]	18	18
[–59.0723,–60.4746,–52.1733,–58.1355]	19	19
[–59.0824,–59.8635,–53.1072,–55.8254]	20	19
[–60.8678,–58.9366,–55.0374,–54.8674]	21	22
[–58.6537,–61.1873,–55.2549,–55.1072]	22	14
[–62.1584,–58.2134,–56.1387,–53.9673]	23	23
[–63.1698,–60.0354,–59.3562,–53.0828]	24	24
[–63.2438,–65.6353,–42.8756,–56.7086]	25	25
[–62.0854,–63.1899,–47.1734,–56.0627]	26	26
[–62.8754,–64.8432,–49.9534,–54.0263]	27	27
[–61.9726,–63.0527,–50.9532,–51.1756]	28	27
[–65.0547,–63.3861,–55.4738,–47.9267]	29	29
[–65.0737,–61.8364,–55.4637,–45.0565]	30	29

The results of varied position test and the adaptive test showed that the model used as a predict reference to make predictions is quite adaptive to changes. Disturbance simulations do not significantly affect the predicted results. **Table 8** summarizes the final results for a varied position testing and adaptive testing.

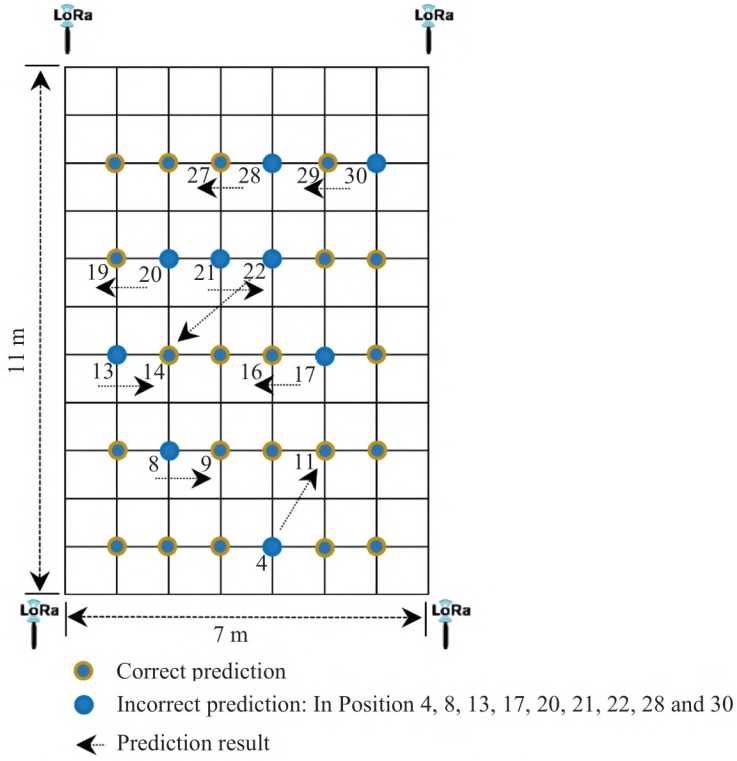

Fig. 11. Prediction result of 30 positions for adaptive 3 node test

Table 8
Accuracy of predictions

Predict Test	Incorrect	Correct	Accuracy (%)
Varied positions	0	30	100
Adaptive 1 node	4	26	86.66
Adaptive 2 node	5	25	83.33
Adaptive 3 node	9	21	70

The results of the predictions in varied position testing reach 100 % accuracy and the adaptive 1 node testing results obtained the accuracy level of 86,66 %, The 2 node adaptive test results produce an accuracy of 83.33 % and for the 3 nodes adaptive test the prediction accuracy results are obtained at 70 %. From the overall prediction results using 4 test scenarios, the average accuracy obtained is far above 50 %, which is 85 %.

5. Discussion of Experimental Results

Three main problems to be solved in this research are reducing the environmental influence on the results of RSS measurements, addressing the variability of RSS values, and positioning accuracy. Therefore, this study aims to develop techniques that can improve the ability and accuracy of object position detection for indoor localization applications in a dynamic environment. Development and optimization of the use of fingerprint techniques for indoor localization applications using a deep learning approach. The following are the results obtained from the study.

Environmental influences that cause differences in the RSS value at the time of fingerprinting data collection with the RSS value at the time of testing can be minimized by taking advantage of the LoRa device. Here the researchers see that there are still opportunities to improve LoRa performance in indoor locations. With the right approach, these properties make LoRa a promising choice for indoor localization systems.

Variation in the change in the RSS measurement value at each position due to changing environmental conditions which can serve as a feature that helps improve the training process. The right hyperparameter setting based on best practice experience produces the best model with the highest accuracy of 92.22 %, as shown in **Fig. 2**. The best model with the highest accuracy is used as a reference to obtain position prediction results with high accuracy.

The results of the position variation test and adaptive test in **Table 8** show that the deep learning approach can be a solution to address changes in environmental conditions that occur in cases of indoor localization. Referring to the results of the simulation of environmental changes carried out in the adaptive test scenario, it shows that the use of a deep learning approach is proven to be able to overcome changes in environmental conditions that occur in indoor environments with accurate predictions.

With the concept and use of simple infrastructure, this method is possible to be implemented in an Indoor Localization system. Compared to the concept applied in previous studies, the use of the DeepFi-LoRaIn concept does not require additional equipment that is always operating indoors to monitor and record changes that occur in the environment. The resulting training model is able to maintain a good accuracy of position prediction despite changing conditions in the environment.

This research was conducted with several limitations, including the use of limited space and static object detection. The future challenge is the implementation in a wider indoor environment using moving object prediction. The advantages of LoRa's reach can be used to implement indoor localization between buildings. Improved position prediction accuracy can still be improved by increasing the number of RSS fingerprint features that represent each changing environment as training data predicts the existence of immovable objects using.

6. Conclusions

The results of variation and adaptive tests showed the average accuracy obtained is 85 %, even the result of predictions in varied position testing reaches 100 % accuracy. That result showed the deep learning approach can be a solution to overcome changes in environmental conditions that occur in the case of indoor localization. Variations in changes in the measurement value of RSS in each position are caused by changes in environmental conditions that can represent the real conditions in the environment. Variations in RSS values in each position serve as features that help to improve the training process. The use of the deep learning approach is proven to be able to cope with changes in environmental conditions that occur in the indoor environment with accurate prediction accuracy. The characteristic of RSS LoRa fingerprint in indoor location is promising to be implemented due to it is relatively more stable to environmental changes with the result that is no significant shift in RSS values that are between in training stages and the prediction stages.

Acknowledgement

We thank Ministry of Research and Higher Education of Republic of Indonesia for financial support for this research under the PDD Grant number NKB-423/UN2.RST/HKP.05.00/2020.

References

[1] Harris, N., Curry, J. (2018). Development and Range Testing of a LoRaWAN System in an Urban Environment. World Academy of Science, Engineering and Technology. International Journal of Electronics and Communication Engineering, 12 (1), 47–55. 5.

[2] Nor, R. F. A. M., Zaman, F. H., Mubdi, S. (2017). Smart traffic light for congestion monitoring using LoRaWAN. 2017 IEEE 8th Control and System Graduate Research Colloquium (ICSGRC), 132–137. doi: http://doi.org/10.1109/ICSGRC.2017.8070582

[3] Mdhaffar, A., Chaari, T., Larbi, K., Jmaiel, M., Freisleben, B. (2017). IoT-based health monitoring via LoRaWAN. IEEE EUROCON 2017 – 17th International Conference on Smart Technologies, 519–524. doi: http://doi.org/10.1109/EUROCON.2017.8011165

[4] Li, L., Ren, J., Zhu, Q. (2017). On the application of LoRa LPWAN technology in Sailing Monitoring System. 2017 13th Annual Conference on Wireless On-demand Network Systems and Services (WONS), 77–80. doi: http://doi.org/10.1109/WONS.2017.7888762

[5] Ke, K.-H., Liang, Q.-W., Zeng, G.-J., Lin, J.-H., Lee, H.-C. (2017). A LoRa wireless mesh networking module for campus-scale monitoring. Proceedings of the 16th ACM/IEEE International Conference on Information Processing in Sensor Networks. doi: https://doi.org/10.1145/3055031.3055034

[6] Wixted, A. J., Kinnaird, P., Larijani, H., Tait, A., Ahmadinia, A., Strachan, N. (2016). Evaluation of LoRa and LoRaWAN for wireless sensor networks. 2016 IEEE SENSORS. doi: https://doi.org/10.1109/icsens.2016.7808712

[7] Islam, B., Islam, M. T., Kaur, J., Nirjon, S. (2019). LoRaIn: Making a Case for LoRa in Indoor Localization. 2019 IEEE International Conference on Pervasive Computing and Communications Workshops (PerCom Workshops). doi: https://doi.org/10.1109/percomw.2019.8730767

[8] Lam, K.-H., Cheung, C.-C., Lee, W.-C. (2017). LoRa-based localization systems for noisy outdoor environment. 2017 IEEE 13th International Conference on Wireless and Mobile Computing, Networking and Communications (WiMob). doi: https://doi.org/10.1109/wimob.2017.8115843

[9] Fargas, B. C., Petersen, M. N. (2017). GPS-free geolocation using LoRa in low-power WANs. 2017 Global Internet of Things Summit (GIoTS). doi: https://doi.org/10.1109/giots.2017.8016251

[10] Sadowski, S., Spachos, P. (2018). RSSI-Based Indoor Localization With the Internet of Things. IEEE Access, 6, 30149–30161. doi: https://doi.org/10.1109/access.2018.2843325

[11] Anjum, M., Khan, M. A., Hassan, S. A., Mahmood, A., Qureshi, H. K., Gidlund, M. (2020). RSSI Fingerprinting-Based Localization Using Machine Learning in LoRa Networks. IEEE Internet of Things Magazine, 3 (4), 53–59. doi: https://doi.org/10.1109/iotm.0001.2000019

[12] Bahl, P., Padmanabhan, V. N. (2000). RADAR: an in-building RF-based user location and tracking system. Proceedings IEEE INFOCOM 2000. Conference on Computer Communications. Nineteenth Annual Joint Conference of the IEEE Computer and Communications Societies (Cat. No.00CH37064). doi: https://doi.org/10.1109/infcom.2000.832252

[13] Wang, X., Gao, L., Mao, S., Pandey, S. (2017). CSI-based Fingerprinting for Indoor Localization: A Deep Learning Approach. IEEE Transactions on Vehicular Technology, 66 (1), 763–776. doi: https://doi.org/10.1109/tvt.2016.2545523

[14] Li, J., Li, Y., Ji, X. (2016). A novel method of Wi-Fi indoor localization based on channel state information. 2016 8th International Conference on Wireless Communications & Signal Processing (WCSP). doi: https://doi.org/10.1109/wcsp.2016.7752710

[15] Wang, B., Zhou, S., Liu, W., Mo, Y. (2015). Indoor Localization Based on Curve Fitting and Location Search Using Received Signal Strength. IEEE Transactions on Industrial Electronics, 62 (1), 572–582. doi: https://doi.org/10.1109/tie.2014.2327595

[16] Xiao, Y., Zhang, S., Cao, J., Wang, H., Wang, J. (2017). Exploiting distribution of channel state information for accurate wireless indoor localization. Computer Communications, 114, 73–83. doi: https://doi.org/10.1016/j.comcom.2017.10.013

[17] Seong, J.-H., Seo, D.-H. (2017). Environment Adaptive Localization Method Using Wi-Fi and Bluetooth Low Energy. Wireless Personal Communications, 99 (2), 765–778. doi: https://doi.org/10.1007/s11277-017-5151-x

[18] Luo, R. C., Hsiao, T. J. (2019). Dynamic Wireless Indoor Localization Incorporating With an Autonomous Mobile Robot Based on an Adaptive Signal Model Fingerprinting Approach. IEEE Transactions on Industrial Electronics, 66 (3), 1940–1951. doi: https://doi.org/10.1109/tie.2018.2833021

[19] Lim, H., Kung, L.-C., Hou, J. C., Luo, H. (2006). Zero-Configuration, Robust Indoor Localization: Theory and Experimentation. Proceedings IEEE INFOCOM 2006. 25TH IEEE International Conference on Computer Communications. doi: https://doi.org/10.1109/infocom.2006.223

[20] Xiao, J., Wu, K., Yi, Y., Ni, L. M. (2012). FIFS: Fine-Grained Indoor Fingerprinting System. 2012 21st International Conference on Computer Communications and Networks (ICCCN). doi: https://doi.org/10.1109/icccn.2012.6289200

[21] Youssef, M., Agrawala, A. (2005). The Horus WLAN location determination system. Proceedings of the 3rd International Conference on Mobile Systems, Applications, and Services – MobiSys '05. doi: https://doi.org/10.1145/1067170.1067193

[22] Brunato, M., Battiti, R. (2005). Statistical learning theory for location fingerprinting in wireless LANs. Computer Networks, 47 (6), 825–845. doi: https://doi.org/10.1016/j.comnet.2004.09.004

[23] Yin, Y., Song, C., Li, M., Niu, Q. (2019). A CSI-Based Indoor Fingerprinting Localization with Model Integration Approach. Sensors, 19 (13), 2998. doi: https://doi.org/10.3390/s19132998

[24] Rizk, H., Torki, M., Youssef, M. (2019). CellinDeep: Robust and Accurate Cellular-Based Indoor Localization via Deep Learning. IEEE Sensors Journal, 19 (6), 2305–2312. doi: https://doi.org/10.1109/jsen.2018.2885958

[25] Xiao, L., Behboodi, A., Mathar, R. (2017). A deep learning approach to fingerprinting indoor localization solutions. 2017 27th International Telecommunication Networks and Applications Conference (ITNAC). doi: https://doi.org/10.1109/atnac.2017.8215428

[26] Bengio, Y. (2012). Practical Recommendations for Gradient-Based Training of Deep Architectures. Neural Networks: Tricks of the Trade, 437–478. doi: https://doi.org/10.1007/978-3-642-35289-8_26

[27] Riyaz, S., Sankhe, K., Ioannidis, S., Chowdhury, K. (2018). Deep Learning Convolutional Neural Networks for Radio Identification. IEEE Communications Magazine, 56 (9), 146–152. doi: https://doi.org/10.1109/mcom.2018.1800153

[28] Bishop, C. (2006). Pattern recognition and machine learning. Springer, 738.

[29] Nair, V., Hinton, G. E. (2010). Rectified linear units improve restricted boltzmann machines. Proceedings of the Proceedings of the 27th international conference on machine learning (ICML-10).

[30] Goodfellow, I., Bengio, Y., Courville, A. (2016). Deep learning. Adaptive computation and machine learning. MIT Press.

[31] Ruder, S. (2016). An overview of gradient descent optimization algorithms. Available at: https://arxiv.org/pdf/1609.04747.pdf

[32] Hijazi, S., Kumar, R., Rowen, C. (2015). Using convolutional neural networks for image recognition. Cadence Design Systems Inc. Available at: https://ip.cadence.com/uploads/901/cnn_wp-pdf

[33] Kingma, D. P., Ba, J. (2014). Adam: A Method for Stochastic Optimization. Available at: https://arxiv.org/pdf/1412.6980.pdf

[34] He, K., Zhang, X., Ren, S., Sun, J. (2015). Delving Deep into Rectifiers: Surpassing Human-Level Performance on ImageNet Classification. 2015 IEEE International Conference on Computer Vision (ICCV). doi: https://doi.org/10.1109/iccv.2015.123

Received date 22.10.2020
Accepted date 28.01.2021
Published date 29.01.2021

Original Research Article: full paper

(2021), «EUREKA: Physics and Engineering»
Number 1

CLASSIFICATION RULE FOR DETERMINING THE TEMPERATURE REGIME OF INDUCTION GRAY CAST IRON

Iraida Stanovska
Department of Higher Mathematics and Modeling Systems[1]
stanovskairaida@gmail.com

Vasyl Duhanets
Department of Technical Service and General Technical Disciplines
State Agrarian and Technical University in Podilia
13 Shevchenko str., Kamianets-Podilskyi, Ukraine, 32300
duganec-vasil@gmail.com

Lada Prokopovych
Department of Cultural Studies, Art and Culture Philosophy Studies[1]
lada.prokopovich@gmail.com

Serhiy Yakhin
Department of Industrial Engineering
Poltava State Agrarian Academy
1/3 Skovorody str., Poltava, Ukraine, 36003
sergii.iakhin@pdaa.edu.ua

[1]*Odessa National Polytechnic University*
1 Shevchenko ave., Odessa, Ukraine, 65044

Abstract

The complexity of using instruments for measuring the technological parameters of induction melting in a continuous mode, and sometimes the impossibility of this, requires the creation of reliable indirect methods for assessing the numerical values of these parameters. This is especially important for quality control of control systems that ensure a given melting temperature regime. The paper proposes a classification rule based on parametric classification methods, which makes it possible to determine the temperature regime of induction melting based on the SiO_2 content in the slag and the distribution coefficient $K_d = SiO_2/(FeO + MnO)$.

Checking the classifying ability of the obtained rule showed that it is high, since for all the numerical data of the factor-signs, both the high-temperature and low-temperature modes were classified correctly. The restrictions on the application of the classification rule are shown, among them: the restrictions imposed by the range of variation of the values of the attribute factors, and the restrictions imposed by the small sample of the initial data, as well as the arbitrary area of their distribution in the space of the factor-attributes.

The rule is presented in a normalized form, and also converted to natural form for ease of practical use.

Application of the rule can be recommended to technologists of metallurgical production of foundries to check the compliance of the technological process operations with the specified melting regulations. It can also be used to diagnose processes or temperature control systems that determine the quality of the resulting cast iron. To do this, it is enough to substitute the actual values of SiO_2, and K_d into the classification rule. The value of the distribution coefficient K_d is calculated according to the actual data on the content of FeO and MnO in the slag.

Keywords: induction melting, high-temperature regime, low-temperature regime, slag, temperature control, factor-signs, classifying rule.

DOI: 10.21303/2461-4262.2021.001604

1. Introduction

Advances in the production of castings from high-quality cast iron, including synthetic cast iron, arouse increased interest in this structural material as promising for highly loaded parts of diesel internal combustion engines (ICE). Cast iron melting technologies are considered as an important part of the design and technological preparation for the production of internal combustion engine parts, primarily pistons, which of all engine parts operate in the most difficult conditions and determine the reliability and service life of the engine as a whole [1]. The improvement of such

technological processes is aimed at obtaining a high-quality alloy with improved mechanical characteristics, for which the cast iron melt is subjected to combined modification using the minimum amount of alloying elements [2–4]. The alloying elements used, among which Cr, Ni prevail, as well as the transition to the field of special, for example, aluminum cast irons, for the production of cast parts for internal combustion engines, allow not only to solve the problem of improving the mechanical characteristics, but also to reduce the weight and size characteristics of the parts. However, the use of combined modification and alloying technologies requires the selection of rational technological modes of melting and the maintenance of such modes throughout the entire campaign. In modern furnaces, these possibilities are often laid down at the design level. Thus, in [5] it was noted that single-circuit circulation with a downward flow of metal is expedient when alloying the metal and introducing microadditives, as well as when doping the melt with intermetallic compounds and nanopowders. This is facilitated by the concentration of power in the upper part of the crucible, which causes intense heating and turbulence of metal flows in the sub-slag layer. As a result of these processes, it becomes possible to quickly introduce and distribute alloying materials and creates favorable conditions for adjusting the chemical composition and homogenization of the bath [5].

From a structural point of view, the possibility of controlling induction furnaces is realized on the basis of methods for controlling current inverters [6]. At the same time, the author gives a number of arguments in favor of the need for a certain clarification of the term «current inverter» associated with the development of the element base of power conversion equipment. In particular, in work [6] it is noted that frequency converters for installations of induction heating and melting of metals are performed mainly in the form of systems with a pronounced direct current link, containing a single- or multiphase controlled (or uncontrolled) rectifier, a direct current link and an autonomous inverter of a given class. The DC link can include, separately or in various combinations, a filter, an active or passive clamp, a DC controller and other units made according to the corresponding schemes. Traditionally, in induction installations of medium (from hundreds of kilowatts to units of megawatts) and large (tens of megawatts) power, single-phase bridge current inverters are widely used.

The implementation on induction furnaces, within the framework of design solutions, of technological capabilities for controlling the thermal regime of melting and the dynamics of the movement of the melt stimulates the flow of oxidation-reduction processes in the bath, which provide the specified chemical composition of the alloy at the output. Thus, in works [7, 8], studies are described that are devoted to identifying the regularities of carbon transformations at high temperatures, which are characteristic of smelting ferrous alloys in induction furnaces, as the main processes to be controlled by smelting technologies. In particular, it is said that as a result of studying the process of carbon oxidation for three different brands in an environment of carbon dioxide at different temperatures, thermogravimetric analysis data were obtained, on the basis of which the equations of the process rate were determined. The resulting kinetic equations, the parameters of which are the pre-exponential factor and the activation energy of the heterogeneous reaction of carbon oxidation in a carbon dioxide medium, can be used among mathematical models in problems of melting control. A similar approach was used in [9], where the calculation of the aforementioned parameters of the kinetic equations was performed for melts doped with vanadium. It should be noted that the regulation of the thermal regime of induction melting should take into account the factor of using modifiers and a complex of alloying elements, if they are introduced in minimum quantities. This is due to the need to ensure a given value of alloy overheating as one of the essential factors for regulating the formation of microstructure [10–12], which determines the mechanical or special properties of cast iron.

The above arguments allow to speak about the importance of control and regulation of induction melting processes, in particular, using computer-integrated solutions in terms of automating these processes. Deviations from the specified melting temperature conditions caused by a malfunction of the automation system can lead to deviations in the chemical composition, microstructure and properties of cast iron. Therefore, criteria for evaluating the performance indicators of the automation equipment included in the temperature control loops are needed, which make it possible to determine the deviations from the specified melting temperature regime. A quantitative measure of such an assessment may indicate a violation of the normal functioning of the temperature control loops as a subsystem of the induction melting automation system.

2. Materials and methods of research

The study is based on the concept proposed in [13] that the composition of the slag can be used to determine the deviation of the melting temperature from normal. The schematic diagram of temperature control is shown in **Fig. 1** [14].

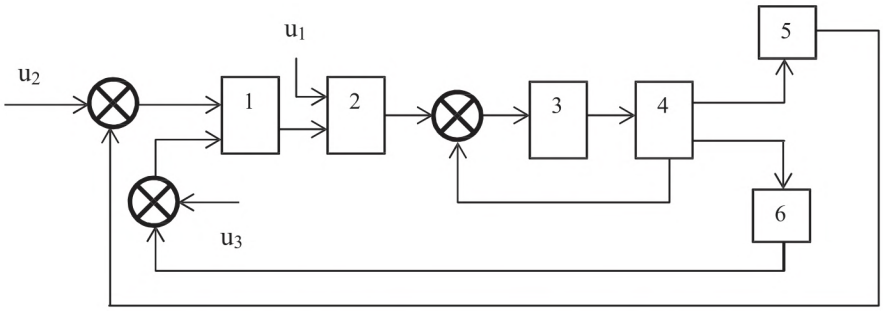

Fig. 1. Scheme for regulating the temperature regime of induction melting: 1 – thermal regime controller, 2 – setpoint setting unit for electric mode controller, 3 – electric mode controller, 4 – temperature measuring device, 5 – metal temperature sensor, 6 – lining temperature sensor, u_1 – setting the directive schedule of the electric melting mode, u_2 – setting the directive schedule of the melting temperature regime, u_3 – setting the maximum permissible lining temperature

The temperature correction mode is based on periodic monitoring of the metal temperature and continuous monitoring of the lining temperature. The thermal mode controller 1 is connected with the metal temperature sensors 5 and the lining temperature 6 and acts on the unit for setting the setpoint of the electric mode controller 2. Before melting, in 2 and 1, directive graphs of the electric (u_1) and temperature (u_2) melting modes, as well as the measurement program are introduced metal temperatures (in time or in connection with technological operations) and the maximum permissible lining temperatures (u_3).

According to the signal of the difference between the actual and the set metal temperature, the computing unit 2 calculates the parameters of the electric mode, which are automatically set and maintained by the controller of the electric mode 3. When the critical temperatures of the furnace lining are reached, unit 2 reduces the power supplied to the furnace. The temperature is measured by the device 4.

For the study, let's use data on the content of SiO_2 (%), FeO (%), MnO (%) in slags from [13]. After processing the data to check the limits of applicability of the classifying rule, the results of [15] were used, while the data were extrapolated to the low-temperature region and equations (1)–(3) were used:

$$SiO_2 = 25.302e^{0.0008T}, \quad (1)$$

$$FeO = -83.49\ln T + 613.87, \quad (2)$$

$$MnO = -19.42\ln T + 143.96, \quad (3)$$

where T – melt temperature.

Equations (1)–(3) were derived from Excel's built-in trend tool.

As a research method, the parametric method of classification was used, which has proven itself in the problems of predicting the quality of castings and materials for them [16, 17], as well as diagnostics of technological processes in metallurgical production [18, 19].

The discriminant function in this case has the form of a classifying rule:

$$y = f(x) = x^T \operatorname{cov}^{-1}(x)(m_1 - m_2), \quad (4)$$

where $y = f(x)$ – value of the discriminant function, depending on the location of the classifying point in the space of the factor-signs $x^T, \text{cov}^{-1}(x)$ – inverse matrix of the covariance, m_1, m_2 – mathematical expectations of the values of the factor-signs for classes 1 and 2, respectively, calculated by formulas (5), (6) accordingly, T denotes the transposition operation.

$$m_1 = \frac{1}{N_1}\left(\sum_{j=1}^{N_1} x_{1j} \sum_{j=1}^{N_1} x_{2j}\right)^T, \tag{5}$$

$$m_2 = \frac{1}{N_2}\left(\sum_{j=1}^{N_2} x_{1j} \sum_{j=1}^{N_2} x_{2j}\right)^T. \tag{6}$$

In formulas (5), (6), the values N_1 and N_2 denote the number of elements in classes 1 and 2, respectively.

Class covariance matrices were calculated using the formula:

$$\text{cov}(x) = \frac{1}{N_i}\sum_{j=1}^{N_i} X_i X_j^T - m_i m_i^T. \tag{7}$$

The classifying rule, which allows to check whether the melting was carried out at high-temperature mode or at low-temperature mode, in general form corresponds to equation (8):

$$x^T \text{cov}^{-1}(x)(m_1 - m_2) = \frac{1}{2}(m_1 + m_2)^T \text{cov}^{-1}(x)(m_1 - m_2). \tag{8}$$

The complete algorithm for calculating the parameters of the classifying rule is given in [13], **Table 1** shows the initial data for constructing a classifying rule.

Table 1

Experimental industrial data

Sample number	Slag composition, %							
	High temperature mode				Low temperature mode			
	SiO_2	$FeO+Fe_2O_3$	MnO	K_d	SiO_2	$FeO+Fe_2O_3$	MnO	K_d
1	56.62	20.78	1.19	0.93	39.32	40.77	1.31	2.58
2	65.38	16.82	0.93	1.11	44.55	35.92	2.27	3.68
3	76.18	7.14	2.48	1.45	47.16	31.18	1.2	8.09
4	70.85	10.12	1.22	1.67	50.17	29.4	0.75	6.25
5	69.95	9.86	0.41	2.26	53.22	23.55	1.15	6.79

SiO_2 and distribution coefficient $K_d = SiO_2/(FeO + MnO)$ were chosen as the factors. All calculations were carried out in a normalized form, in which the values of the factor-signs, denoted by x_1 and x_2, were in the range [–1; +1]. The following actual values of the attribute factors corresponded to this normalized range: SiO_2 (%) = [65.38; 76.18], K_d = [0.93; 2.26] – for the high-temperature regime, SiO_2 (%) = [39.32; 53.22], K_s = [2.58; 8.09] – for low-temperature mode. That is, the general normalized range was as follows: SiO_2 (%) = [39.32; 76.18], K_s = [0.93; 8.09].

The classification rule based on equation (8) had a general form:

$$\begin{aligned} x^{(j)} &\in Class\#1 \text{ if } y \geq y_0, \\ x^{(j)} &\in Class\#2 \text{ if } y < y_0. \end{aligned} \tag{9}$$

4. Results and discussion of research results

A classification rule is obtained, presented in a standardized form:

$$x^j \in class\#1 \text{ if } -21.8531x_1 + 31.377x_2 \geq -12.0605,$$
$$x^j \in class\#2 \text{ if } -21.8531x_1 + 31.377x_2 < -12.0605. \quad (10)$$

The left side of the inequality is from equation (4), and the distribution of this value for the selected values of the attribute factors is shown in **Fig. 2**.

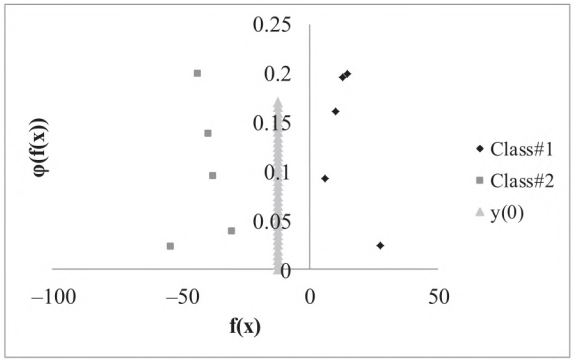

Fig. 2. Distribution of value $y = f(x)$

From **Fig. 2**, it can be seen that all experimental points are correctly distributed among classes. Therefore, the obtained rule (10) can be used to establish the melting temperature. For practical application, it is necessary to transform it to its natural form, using the ranges of variation of the values of the factor-signs selected in the normalization process. The final rule is received:

$$x^j \in class\#1 \text{ if } -21.8531\left(\frac{x_1 - 57.75}{18.43}\right) + 31.377\left(\frac{x_2 - 4.51}{3.58}\right) \geq -12.0605,$$
$$x^j \in class\#2 \text{ if } -21{,}8531\left(\frac{x_1 - 57.75}{18.43}\right) + 31.377\left(\frac{x_2 - 4.51}{3.58}\right) < -12.0605. \quad (11)$$

The results of checking the limits of applicability of the rule are given in **Table 2**. They were obtained by substituting in (11) the numerical values of the attribute factors from work [15], having previously used equations (1)–(3).

Table 2

Verification results of the classification rule

T °C	SiO_2	FeO	MnO	K_d	$y = f(x)$
High temperature mode					
1500	84.01	3.31	1.94	16	**70.39722**
1475	82.34	4.71	2.26	11.81	**35.4605**
1450	80.71	6.14	2.6	9.23	**14.88685**
1425	79.11	7.59	2.93	7.52	**1.63889**
1400	77.55	9.07	3.28	6.28	**–7.37752**
Low temperature mode					
1300	71.58	15.26	4.72	3.58	**–24.1144**
1275	70.17	16.88	5.09	3.19	**–25.8974**
1250	68.78	18.53	5.48	2.86	**–27.1734**
1225	67.42	20.22	5.87	2.58	**–28.0568**
1200	66.08	21.94	6.27	2.34	**–28.6314**

From **Table 2** it is possible to see that for both modes, rule (11) shows opposite results in relation to the determination of the temperature regime. The reason for this is that the values of the factor-signs obtained from the results of approximation and extrapolation of the results of work [15] are far beyond the variation intervals adopted in this study: SiO_2 (%) = [66.08; 84.01], K_d = [2.34; 16] (**Table 2**) in comparison with SiO_2 (%) = [39.32; 76.18], K_d = [0.93; 8.09] (**Table 1**).

Therefore, before applying rule (11), it is necessary to check whether the actual data on SiO_2 and K_d belong to the SiO_2 range (%) = [39.32; 76.18], K_d = [0.93; 8.09]. This is a limitation on the application of the resulting classification rule. Another limitation of this study is that the rule is derived from a small sample of experimental data. An increase in the sample size and optimization of the experimental data area, for example, based on artificial orthogonalization [20], would allow obtaining a more accurate result.

Therefore, the direction of further research is the collection of primary data to increase the sample size and the formation of such an area of the space of factor-signs that will allow the most accurate calculation of the parameters of the classifying rule. Expanding the range of variation in this case will make it possible to obtain classification rules for wider areas of the space of factor-signs.

5. Conclusions

The resulting classification rule allows one to determine the temperature regime of induction melting based on the SiO_2 content in the slag and the distribution coefficient $K_d = SiO_2/(FeO + MnO)$. Checking its classifying ability shows that it is high, since for all numerical data of factor-signs, all modes are classified correctly.

References

[1] Puliaiev, A., Orendarchuk, J., Penziev, P., Akimov, O., Marynenko, D., Marchenko, A. (2017). Development of a system for organizing a modular design and technological preparation for the production of cast iron pistons for internal combustion engines. Technology Audit and Production Reserves, 3 (1 (35)), 23–27. doi: https://doi.org/10.15587/2312-8372.2017.105636

[2] Akimov, O. V., Marchenko, A. P. (2008). Eksperimental'nye issledovaniya i komp'yuternoe modelirovanie materialov dlya blok-kartera DVS. Eastern-European Journal of Enterprise Technologies, 5 (1 (35)), 52–57.

[3] Demin, D. A., Pelikh, V. F., Ponomarenko, O. I. (1998). Complex alloying of grey cast iron. Litejnoe Proizvodstvo, 10, 18–19.

[4] Demin, D. A., Pelikh, V. F., Ponomarenko, O. I. (1995). Optimization of the method of adjustment of chemical composition of flake graphite iron. Litejnoe Proizvodstvo, 7-8, 42–43.

[5] Trauzel', D., Shlyukaber, Donbah, F. (2003). Realizatsiya spetsial'nyh tehnologicheskih i metallurgicheskih zadach v induktsionnyh pechah sredney chastoty. Liteyshchik Rossii, 5, 20–23.

[6] Silkin, E. (2007). Realizatsiya i sposoby upravleniya ventilyami v invertorah toka preobrazovateley chastoty dlya ustanovok induktsionnogo nagreva i plavki metallov. Silovaya elektronika, 3, 108–114.

[7] Roberts, D. G., Hodge, E. M., Harris, D. J., Stubington, J. F. (2010). Kinetics of Char Gasification with CO2 under Regime II Conditions: Effects of Temperature, Reactant, and Total Pressure. Energy & Fuels, 24 (10), 5300–5308. doi: https://doi.org/10.1021/ef100980h

[8] Kim, S. K., Park, C. Y., Park, J. Y., Lee, S., Rhu, J. H., Han, M. H. et. al. (2014). The kinetic study of catalytic low-rank coal gasification under CO2 atmosphere using MVRM. Journal of Industrial and Engineering Chemistry, 20 (1), 356–361. doi: https://doi.org/10.1016/j.jiec.2013.03.027

[9] Demin, D. A. (1998). Change in cast iron's chemical composition in inoculation with a Si-V-Mn master alloy. Litejnoe Proizvodstvo, 6, 35.

[10] Endo, M., Yanase, K. (2014). Effects of small defects, matrix structures and loading conditions on the fatigue strength of ductile cast irons. Theoretical and Applied Fracture Mechanics, 69, 34–43. doi: https://doi.org/10.1016/j.tafmec.2013.12.005

[11] Fourlakidis, V., Diószegi, A. (2014). A generic model to predict the ultimate tensile strength in pearlitic lamellar graphite iron. Materials Science and Engineering: A, 618, 161–167. doi: https://doi.org/10.1016/j.msea.2014.08.061

[12] Cheng, Y., Huang, F., Li, W., Liu, R., Li, G., Wei, J. (2016). Test research on the effects of mechanochemically activated iron tailings on the compressive strength of concrete. Construction and Building Materials, 118, 164–170. doi: https://doi.org/10.1016/j.conbuildmat.2016.05.020

[13] Demin, D. (2020). Constructing the parametric failure function of the temperature control system of induction crucible furnaces. EUREKA: Physics and Engineering, 6, 19–32. doi: https://doi.org/10.21303/2461-4262.2020.001489

[14] Shumihin, V. S., Kutuzov, V. P., Hramchenkov, A. I. et. al.; Aleksandrov, N. N. (Ed.) (1982). Vysokokachestvennye chuguny dlya otlivok. Moscow: Mashinostroenie, 222.

[15] Zavertkin, A. S. (2013). The influence of the lining's manufacturing technology and of cast iron's melting in induction furnaces on the slag forming. Novye Ogneupory (New Refractories), 1, 36–39.

[16] Ponomarenko, O., Trenev, N. (2013). Computer modeling of crystallization processes as a reserve of improving the quality of pistons of ICE. Technology Audit and Production Reserves, 6 (2 (14)), 36–40. doi: https://doi.org/10.15587/2312-8372.2013.19529

[17] Vasenko, Y. (2012). Technology for improved wear iron. Technology Audit and Production Reserves, 1 (1 (3)), 17–21. doi: https://doi.org/10.15587/2312-8372.2012.4870

[18] Aouati, M. (2018). Improving the accuracy of classifying rules for controlling the processes of deculfuration and dephosphorization of Fe-C melt. Technology Audit and Production Reserves, 2 (3 (46)), 10–18. doi: https://doi.org/10.15587/2312-8372.2019.169696

[19] Aouati, M. (2017). Parametric identification in the problem of determining the quality of dusulfusation and deposphoration processes of Fe-C alloy. Technology Audit and Production Reserves, 2 (1 (34)), 9–15. doi: https://doi.org/10.15587/2312-8372.2017.99130

[20] Demin, D. (2017). Synthesis of optimal control of technological processes based on a multialternative parametric description of the final state. Eastern-European Journal of Enterprise Technologies, 3 (4 (87)), 51–63. doi: https://doi.org/10.15587/1729-4061.2017.105294

Received date 02.12.2020
Accepted date 14.01.2021
Published date 29.01.2021

Original Research Article: full paper

(2021), «EUREKA: Physics and Engineering»
Number 1

A RESEARCH ON MULTI-OBJECTIVE OPTIMIZATION OF THE GRINDING PROCESS USING SEGMENTED GRINDING WHEEL BY TAGUCHI-DEAR METHOD

Do Duc Trung
Faculty of Mechanical Engineering[1]
doductrung@haui.edu.vn

Nhu-Tung Nguyen
Faculty of Mechanical Engineering[1]
tungnn@haui.edu.vn

Dung Hoang Tien
Faculty of Mechanical Engineering[1]
tiendung@haui.edu.vn

Ha Le Dang
Center of Mechanical Engineering[1]
danghack@gmail.com

[1]*Hanoi University of Industry*
298 Cau Dien str., Bac Tu Liem District, Hanoi, 100000

Abstract

In this study, the mutil-objective optimization was applied for the surface grinding process of SAE420 steel. The aluminum oxide grinding wheels that were grooved by 15 grooves, 18 grooves, and 20 grooves were used in the experimental process. The Taguchi method was applied to design the experimental matrix. Four input parameters that were chosen for each experiment were the number of grooves in cylinder surface of grinding wheel, workpiece velocity, feed rate, and cutting depth. Four output parameters that were measured for each experimental were the machining surface roughness, the system vibrations in the three directions (*X*, *Y*, *Z*). The DEAR technique was applied to determine the values of the input parameters to obtaine the minimum values of machining surface roughness and vibrations in three directions. By using this technique, the optimum values of grinding wheel groove number, workpiece velocity, feed-rate, cutting depth were 18 grooves, 15 m/min, 2 mm/stroke, and 0.005 mm, respectively. The verified experimental was performed by using the optimum values of input parameters. The validation results of surface roughness and vibrations in *X*, *Y*, *Z* directions were 0.826 (μm), 0.531 (μm), 0.549 (μm), and 0. 646 (μm), respectively. These results were great improved in comparing to the normal experimental results. Taguchi method and DEAR technique can be applied to improve the quality of grinding surface and reduce the vibrations of the technology system to restrain the increasing of the cutting forces in the grinding process. Finally, the research direction was also proposed in this study.

Keywords: Surface Grinding, Segmented Grinding Wheel, Taguchi, Dear, Surface Roughness, Vibration.

DOI: 10.21303/2461-4262.2021.001612

1. Introduction

Using a discontinuous grinding wheel (slotted and segmented wheel) was a promising solution in improving the efficiency of the grinding process [1, 2]. Using slotted grinding wheel could reduce the cutting heat by 40 % to 80 % compared with conventional grinding wheels [3]. Using segmented grinding wheel could reduce the cutting force by up to 30 % compared with conventional grinding wheels [4]. Both surface roughness and cutting force when using segmented grinding wheels have a smaller value than when using conventional grinding wheel [5, 6]. Some recommendations when using a slotted aluminum oxide grinding wheel have also been proposed: surface roughness will have a minimum value when the number of grooves on the grinding wheel was18 (grooves) [7], the cutting force is minimized when the grooves in the grinding wheel were 20 (grooves) [8].

Surface roughness is often a common parameter that was chosen for evaluating the efficiency of machining in general, and grinding in particular [9, 10]. Research to find the solutions to

reduce surface roughness when grinding with conventional grinding wheel has been published in many studies. However, studies on surface roughness when grinding with a segmented grinding wheel were very limited. The studies that are performed to improve the surface quality when using the segmented grinding wheel for each different material were necessary.

In the machining processes, vibration is often studied through two methods: theoretical modeling method and experimental planning method. The theoretical modeling method has a wider application ability, but the number of input parameters is quite large, it is quite difficult to implement [11]. The experimental planning method is quite easy to perform because the number of input parameters is small [12–14]. However, this method is only applicable to each specific case. The above methods are aimed to predict the vibrations, cutting force, and surface roughness in the machining process to improve the quality of machining, and reduce the time and cost of the machining process.

The vibrations of the grinding machine spindle, even in very small amplitudes, also have a significant effect on the depth of the cut of the grinding grain on the machining surface, thereby affecting grinding productivity, surface quality and influence on the uneven wear phenomenon of the grinding wheel [3, 13–15]. The spindle vibration of the grinder consists of forced and spontaneous (self-vibrating) vibrations [16]. The forced vibration is transmitted by external factors. The factors causing forced vibration can be mentioned as grinding wheel imbalance, bearing error, assembly error, etc. [17].

Self-vibrating is the vibration that occurs during grinding, which is highly dependent on the uniformity of the work material, cutting conditions, and the grinding wheel properties [13, 14]. Compared with the forced vibrations, the reduction of spontaneous vibrations is much more advantageous, this can be accomplished by changing some of the factors that affect on it, such as selection of the suitable cutting conditions, improvement of the clamp system, etc. [13, 18]. However, so far, it seems that the determination of the value of the cutting parameter to reduce the vibrations of the grinder spindle when using a segmented grinding wheel has not been mentioned by any studies. The aim of research that was presented in this paper was determination of the optimal value of several machining parameters to ensure that both surface roughness and self-vibrations are of small value.

This study selected the combination of Taguchi method and Data Envelopment Analysis based Ranking (DEAR) technique. The reason this combination method was chosen is because the experimental design according to the Taguchi method has the advantage of allowing a small number of experiments to be performed with a large number of input parameters, especially it is very suitable when having not much information of the research subjects [19–21]. The grinding process using a segmented grinding wheel is a case where there are too less information about the study subjects, so it is very suitable when using the Taguchi method to design experiments. DEAR technique showed an excellent efficiency in determining the optimal value of technology parameters in the machining processes, which has been performed in a simple methodology [22]. This method that was evaluated has been more effective than some other methods [23–25].

2. Multi-objective optimization using DEAR technique

The aim of this research was determination of the input parameters to obtain the minimum values of machining surface roughness and vibration amplitudes in *X*, *Z*, *Y* directions. The DEAR technique that was used to solve optimization problem consisted of the steps as the following [25–27].

– Determine the weights (*w*) for each response for all experiments. Weight of response is the ratio between response at any trial to the summation of all responses.

– Transform the data of response into weighted data by multiplying the observed data with its own weight.

– Divide the data as smaller the better with smaller the better.

– Treat this value as multi response performance index (*MRPI*).

$$MRPI = W_{R_a} \cdot R_a + W_{A_x} \cdot A_x + W_{A_y} \cdot A_y + W_{A_z} \cdot A_z; \quad (1)$$

$$W_{R_a} = \frac{R_a}{\sum R_a}; \quad (2)$$

$$W_{A_x} = \frac{A_x}{\sum A_x}; \quad (3)$$

$$W_{A_y} = \frac{A_y}{\sum A_y}; \quad (4)$$

$$W_{A_z} = \frac{A_z}{\sum A_z}. \quad (5)$$

For each input parameter, at any of the investigated levels that the *MRPI* is the smallest value is considered to be the best level. Subtract the maximum value of the *MPRI* from the minimum value of the *MRPI*, the input parameters that has the subtraction value of *MRPI* is the largest among the selected input parameters is considered to have the greatest influence on the output parameters [25–27].

3. Material and Method

3. 1. Experimental Machine and Grinding Wheel

The grinding machine (APSG-820/2A) that was made in Taiwan was used to perform the experimental research. The machine is capable of infinitely level adjusting the workpiece velocity and the feed-rate through the hydraulic pump system. Cutting depth is adjusted by vernier with precision of 0.005 mm (each line of vernier is 0.005 mm).

Three aluminum oxide grinding wheels that were used with the sign of WA46J7V1A. The external diameter, thickness, and hole diameter of grinding wheels were 180 mm, 31.75 mm, and 13 mm, respectively. Three grinding wheels were grooved on the cylinder surface with number of the grooves of 15, 18, and 20, respectively. Each groove was semicircle with the diameter of 12 mm as shown in **Fig. 1**.

a *b* *c*

Fig. 1. Experimental segmented grinding wheels: *a* – 15 grooves, *b* – 18 grooves, *c* – 20 grooves

To eliminate the effect of the grinding wheel wear on the output parameters, before conducting each experiment, the grinding wheel was dressed using a dressing tool with a diamond grain. The parameters of the grinding wheel dressing conditions include the wheel dressing depth of 0.01 mm, the wheel dressing feedrate of 100 mm/min, the number of wheel dressing times of 3 times.

3. 2. Experimental Workpiece

The SAE420 steel was used to conduct the experiments. This steel that was made in USA has the chemical composition as listed in **Table 1**. According several Standard, the equivalent sign of SAE420 steel are described in **Table 2**. The properties of SAE420 were described in **Table 3.** The length, width, and height of workpieces were 60 mm, 40 mm, and 10 mm, respectively as shown in **Fig. 2**.

Table 1

Chemical composition of SAE420 steel

C	Si	Mn	Cr	S
0.42	1.00	1.00	13.00	0.005

Table 2
Equivalent symbol of SAE420 steel of according several Standard

USA	Russia	Germany	Japan	France	England	Europe	Italy	Spain	China
SAE	GOST	DIN	JIS	AFNOR	BS	EN	UNI	UNE	GB
420	3X13	1.4028	SUS420J2	410F21	420S45	1.4028	GX30Cr13	F.3403	3Cr13

Table 3
The properties of SAE420 steel

Density (g/cm^3)	Electrical Resistivity (μΩcm)	Thermal Conductivity (W/m/K)	Coefficient of Thermal Expansion (μm/m/K)	Modulus of Elasticity (MPa)	Specific Heat (KJ/kg/K)	Rockwell Hardness
7.74	55	24.9	10.2	200×10^3	0.46	B88

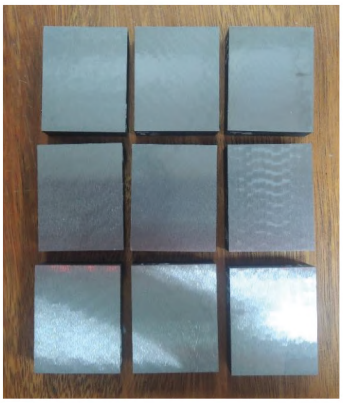

Fig. 2. Experimental workpieces

SAE420 steel that is a common steel is used for the manufacturing of the products in the shipbuilding, petroleum, chemical technology, food processing, and medical industries. etc. In the above products, many products need to be machined the important surfaces by grinding method. However, up to now, it seems that there has not been any published research on grinding this steel with a segmented grinding wheel. Therefore, the results of this study will have certain contributions to grinding technology in general and to grinding technology of this steel in particular.

3. 3. Experimental Design

In this study, the Taguchi method was applied to design the experimental matrix. Four input parameters that were chosen for each experiment were the number of grooves in cylinder surface of grinding wheel, workpiece velocity, feed-rate, and cutting depth. The experimental matrix was design by using the Minitab software, and this matrix was stored in **Table 4**.

The experimental matrix that is designed according to the Taguchi method is used in this study because this method allows to perform with many input parameters, but the required number of experiments to perform is not much. For example in this study, there are 4 input parameters, each parameter has 3 value levels, but the number of experiments is only 9. Meanwhile, if compared with the design of the experimental matrix in the form of full orthogonality with 4 input parameters, the number of experiments are 17 experiments (including 16 experimental points at the origin and at least 1 experimental point at the center). On the other hand, a prominent advantage of the experimental method according to the Taguchi method is that it is possible to select the input parameters in a qualitative form (not quantitative form). Furthermore, in the Taguchi method, the values of the input parameters also need not be followed by the rule that the value of mid-level is equal to the average of the two low and high levels. With the number of grooves in the grinding wheel are 15, 18, and 20 showing that 18 is not the average of 15 and 20, it shows that the design of the experimental matrix according to the Taguchi method is the most suitable choice in this study.

Table 4

Taguchi L9 based OA design

No.	Coded levels				Actual values			
	Z	*V*	*f*	*t*	*Z* (grooves)	*V* (m/min)	*f* (mm/stroke)	*t* (mm)
1	1	1	1	1	15	10	2	0.005
2	1	2	2	2	15	15	3	0.010
3	1	3	3	3	15	20	4	0.015
4	2	1	2	2	18	10	2	0.015
5	2	2	3	3	18	15	4	0.005
6	2	3	1	1	18	20	2	0.010
7	3	1	3	3	20	10	4	0.010
8	3	2	1	1	20	15	2	0.015
9	3	3	2	2	20	20	3	0.005

3. 4. Measurement System

MITUTOYO-Surface test SJ-210 surface roughness tester was used to measure the machining surface roughness of the workpiece. The evaluation length was fixed at 0.8 mm. The surface roughness was measured perpendicular to the cutting velocity direction and repeated three times following three repeated times of each cutting test. The average value of surface roughness that was measured three consecutive times was used for analysis and evaluation.

The vibration measurement system that included the acceleration sensor Type 4525-B-001, the data processing box, and the PULSE software was used to measure the system vibrations. For each experiment, the vibrations of system were measured simultaneously in three directions (*X*, *Y*, *Z*). The detail is illustrated in **Fig. 3**.

The accelerometer is mounted on the grinding wheel guard. In each experiment, the vibration components will be measured in a 5-second interval. During this interval time, the software on the computer will display a graph of the vibration components during the time when the grinding wheel cutting and uncutting into the workpiece. However, during data processing, only the part of the graph of vibration during the time when the grinding wheel cutting into the workpiece is used, and in each experiment, the value of the vibration components is calculated as the its average value in this stage (the stage when grinding wheel cutting into the surface of the workpiece).

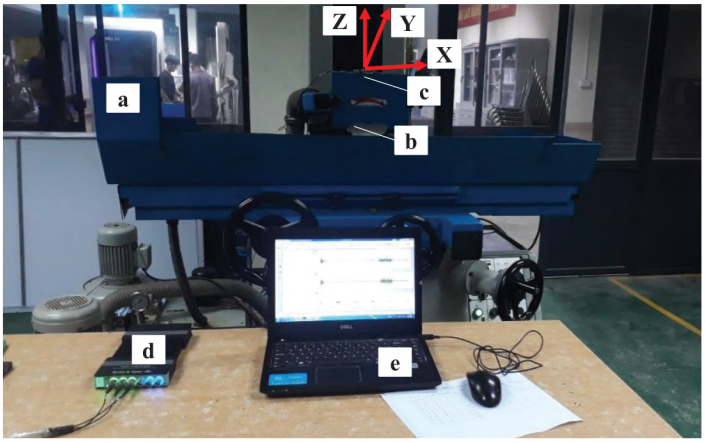

Fig. 3. Setup of vibration measurement: *a* – grinding machine; *b* – grinding wheel; *c* – aceleration sensor; *d* – data processing box; *e* – PC and software

3. 5. Machining Condition

The experiments were conducted in the grinding conditions as following:

– Grinding wheel velocity: 26 m/s.

– Cooling fluid: emulsion 10 %, overflow irrigation method, volume flow rate of 5 lit/min.

4. Results and discussions

The experiments were conducted according to the **Table 4**. The experimental results were achieved and stored in **Table 5**. The influence degrees of the input parameters (groove number on the cylinder grinding surface, workpiece velocity, feed-rate, cutting depth) on the output parameters (machining surface roughness, vibration amplitudes in *X*, *Y*, *Z* directions) were presented from **Fig. 4–7**.

Table 5

Experimental matrix and Results

No.	*Z* (grooves)	*V* (m/min)	*f* (mm/str.)	*t* (mm)	*Ra* (μm)	*Ax* (μm)	*Ay* (μm)	*Az* (μm)
1	15	10	2	0.005	0.537	0.3578	1.2138	0.3601
2	15	15	3	0.010	1.198	0.6676	2.4796	0.7057
3	15	20	4	0.015	1.542	0.7484	6.2027	1.6251
4	18	10	3	0.015	0.656	0.7042	2.0370	0.8476
5	18	15	4	0.005	1.133	0.7347	2.0523	0.9499
6	18	20	2	0.010	1.001	0.4356	1.5205	0.4845
7	20	10	4	0.010	1.983	1.8158	5.7678	1.9608
8	20	15	2	0.015	2.095	0.9331	2.8419	1.3573
9	20	20	3	0.005	2.543	0.5943	1.4069	0.7439

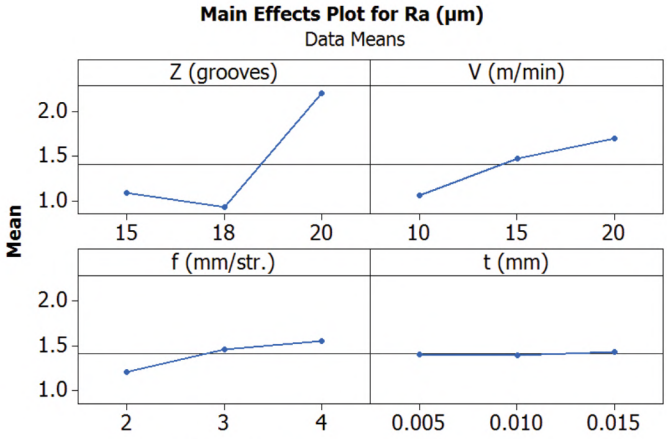

Fig. 4. Main Effect Plot for Ra

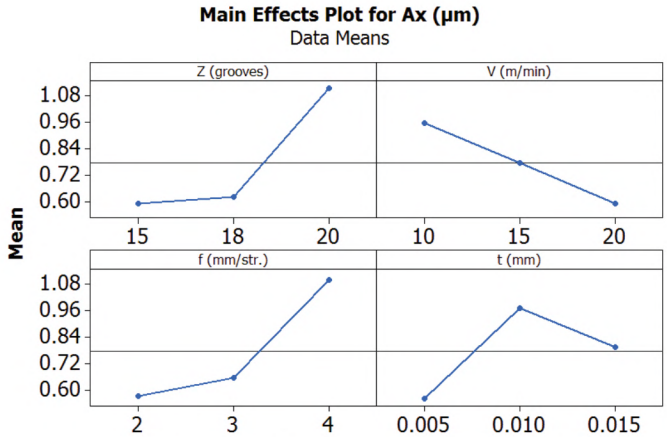

Fig. 5. Main Effect Plot for Ax

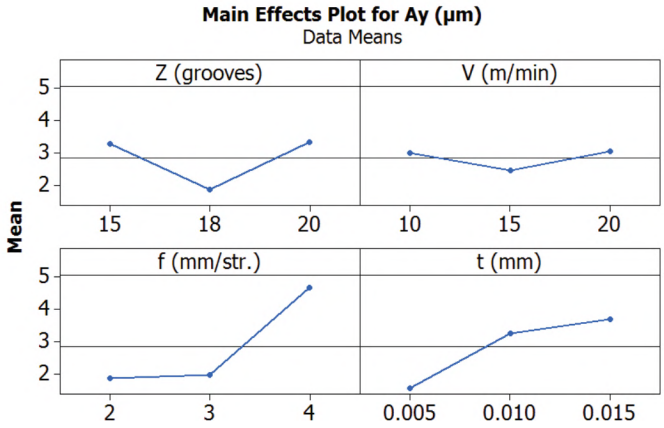

Fig. 6. Main Effect Plot for Ay

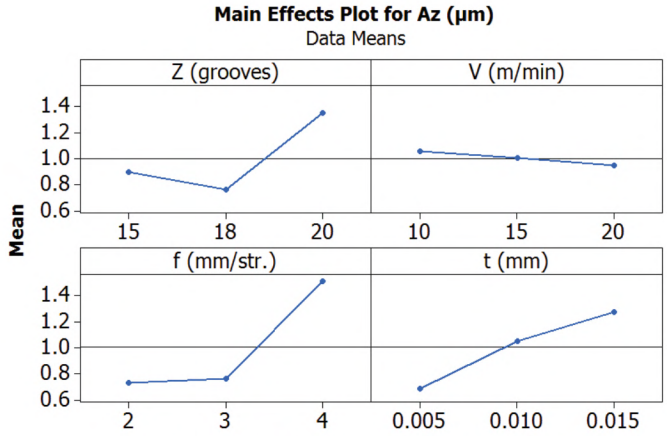

Fig. 7. Main Effect Plot for Az

The results from these figures showed that:

– the number of grooves on the cylinder surface of grinding wheel had the most influence on the machining surface roughness. This issue can be explained that when the number of the grooves changes, it makes the changes of the friction between grinding wheel and workpiece surface. It changes the level of coolant introduction into the cutting zone and also changes the chip release and heat release ability during machining. These factors change the degree of scratching of the grinding grains on the workpiece surface and change the plastic deformation on the workpiece surface, so changing the surface roughness;

– the second factor that influenced on the machining surface roughness was workpiece velocity. This phenomenon can be explained as following: when the workpiece speed changes, it will change the contact time between the workpiece surface and the grinding wheel, which changes the number of scratches of the grinding grains into the workpiece surface leading to change of surface roughness. The feed-rate and the depth of cut had a little effect on the surface roughness;

– all four input parameters that had a significant influence on the amplitude of the technology system's vibration in the *X*-direction. In which, it seems that the degrees of influence on the vibration amplitude in *X* direction increased in the order of influence of cutting depth, workpiece velocity, number of grooves, and feed-rate. This phenomenon can be explained as following: when changing the number of grooves in the grinding wheel as well changing the cutting parameters, the cutting conditions of grinding wheel into the workpiece will change, therefore influencing on the cutting force and vibration degree of the system in *X* direction;

– the feed-rate had the most influence on the system vibration amplitude in *Y* direction. The second factor that affected on the system vibration amplitude in *Y* direction was depth of cut. The number of grooves on the cylinder surface of grinding wheel and the workpiece velocity had

a little effect on the system vibration amplitude in *Y* direction. The feed-rate also had the most influence on the system vibration amplitude in *Z* direction. The second and third factors that affected on the system vibration amplitude in *Z* direction were also depth of cut and number of grooves on the cylinder surface of grinding wheel. The workpiece velocity also had a little effect on the system vibration amplitude in *Z* direction. The reason is because when changing the feed rate, it will change the «re-cut» phenomenon of the grinding wheel into the workpiece surface. While changing the cutting depth will change the depth of the cut of each grinding grain left on the workpiece surface, this will also change the «re-cut» phenomenon. These factors change the cutting forces and vibrations in the *Y*-direction;

– when using grinding wheel with 18 grooves, the machining surface roughness, *Ay*, and *Az* were smallest in comparing with the cases using grinding wheel with 15 and 20 grooves. Besides, when using grind wheel with 18 grooves, *Ax* was larger than that one when using grinding wheel with 15 grooves, but it was smaller than that one when using grinding wheel with 20 grooves. It seems that the machining surface roughness and vibration amplitudes will be obtained with small values when using the grinding wheel with 18 grooves. This problem can be understood because changing the number of grooves on the grinding wheel surface will change the contact conditions between the grinding wheel and the workpiece and change the coolant supply degree into the cutting zone, change the chip escaping phenomenon and heat escaping phenomenon when grinding, so these phenomena will influence on the plastic deformation of the machining surface, thereby affecting surface roughness and vibrating components;

– when the workpiece velocity increased, the machining surface roughness increased, but the *Ax* decreased. The workpiece velocity almost had not the influence on the *Ay* and *Az*. This point can be explained that the reason for the value of *Ax* decreased in higher workpiece velocity would be that the higher load in *X* direction increases the apparent rigidity. This factor had a litter effect on the vibrations in the other directions (*Y*, *Z* directions);

– when increasing the feed-rate, the vibration amplitude (*Ax*) increased quickly. While *Ay* and *Az* only increased when the feed-rate increased from 3 mm/stroke to 4 strokes. This is easy to understand because when the feed rate increases, in the next longitudinal stroke, the grinding wheel will have to perform the «re-cutting» process the protrusions on the workpiece surface more than the previous stroke. This causes cutting forces and vibration components to increase;

– when depth of cut increased, the vibration amplitudes in *Y* and *Z* directions (*Ay* and *Az*) increased. While *Ax* only increased when the depth of cut increased from 0.005 mm to 0.01 mm. If the cutting depth increased from 0.01 mm to 0.015 mm, *Ax* decreased. The reasons for these influence is understood that when the depth of the cut changes, the depth of the cuts of the grinding grains left on the workpiece surface change, it also changes the degree of plastic deformation of the machined materials, thereby alter cutting forces and vibrating components.

From above points of analyzed results, it seems that the degree and rule of input parameters on the machining surface roughness, system vibration amplitudes were quite complex. To determine the input parameters with minimum values of surface roughness and system vibrations, the multi-objective optimization problem should be solved. Four output parameters that were machining surface roughness, vibration amplitude in *X*, *Y*, *Z* directions were chosen as the objective functions of the multi-objective optimization problem. In this study, DEAR technique was used to solve this problem.

From the results in **Table 5**, the weight of each response and *MRPI* at each experiment were calculated and stored in **Table 6**. From the date in **Table 6**, *MRPI* of all input parameters that were calculated by sum of *MRPI* of each parameter at the corresponding level and stored in **Table 7**.

The results from **Table 7** showed that the number of grooves on the cylinder surface of grinding wheel and workpiece velocity had the smallest values of *MRPI* corresponding to the level 2. While the feed-rate and depth of cut had the smallest values of *MRPI* corresponding to the level 1. So, the optimum values of the input parameters that were groove numbers of 18 ($Z=18$ grooves), workpiece velocity of 15 m/min ($V=15$ m/min), feed-rate of 2 mm/stroke ($f=2$ stroke), and cutting depth of 0.005 mm ($t=0.005$ mm). The *MRPI* had the largest value of *Max-Min* was the feed-rate (*Max-Min* = 3.69445). So, if evaluating the grinding process through the grinding surface roughness, system vibrations in *X*, *Y*, *Z* directions, feed-rate was factor that has the most influence

on the output parameters, the second and third factor that have the effect on the output parameter were number of grooves and depth of cut. The workpiece velocity has the smallest influence on the output parameters. These results were suitable with the analyzed results that were presented in above sections 3.

Table 6

The respones weight and *MRPI* at each experiment

No.	Weight				*MRPI*
	Ra	*Ax*	*Ay*	*Az*	
1	0.04232	0.05118	0.04756	0.03986	0.11312
2	0.09442	0.09549	0.09715	0.07811	0.47289
3	0.12153	0.10704	0.24303	0.17987	2.06725
4	0.05170	0.10072	0.07981	0.09381	0.34694
5	0.08930	0.10508	0.08041	0.10514	0.44328
6	0.07889	0.06230	0.05957	0.05363	0.22268
7	0.15629	0.25972	0.22599	0.21703	2.51051
8	0.16512	0.13346	0.11135	0.15023	0.99080
9	0.20043	0.08500	0.05512	0.08234	0.69900

Table 7

Total values of *MRPI* of the input parameters at the levels

Parameters	Levels			*Max-Min*
	1	2	3	
Z	2.65326	**1.01289**	4.20032	3.18742
V	2.97057	**1.90696**	2.98893	1.08197
f	**1.32659**	1.51883	5.02105	**3.69445**
t	**1.25540**	3.20608	3.40499	2.14960

To verify the results of the optimization process, several tests were carried out in the same technology system. The optimum values of input parameters that were used in grinding tests were groove numbers of 18 grooves, workpiece velocity of 15 m/min, feed-rate of 2 mm/stroke, and cutting depth of 0.005 mm. The obtained values of averages of grinding surface roughness, vibration amplitudes in *X*, *Y*, *Z* directions were 0.826 (μm), 0.531 (μm), 0.549 (μm), and 0.646 (μm), respectively. These results were great improved in comparing to the experimental results in **Table 5**.

5. Conclusion

In this study, the combination of Taguchi method and DEAR technique that was successfully applied to determine the optimum values for multi-objective when grinding the SAE420 steel by using the segmented grinding wheel. From the achieved results, the conclusions of this study were withdrawn as following:

– the degree and rule of input parameters on the machining surface roughness, system vibration amplitudes were very complex;

– the number of grooves on the cylinder surface of grinding wheel had the most influence on the machining surface roughness. The second factor that influenced on the machining surface roughness was workpiece velocity. The feed-rate and the depth of cut had a little effect on the surface roughness;

– when using grinding wheel with 18 grooves, the machining surface roughness, *Ay*, and *Az* were smallest in comparing with the cases using grinding wheel with 15 and 20 grooves. Besides, when using grinding wheel with 18 grooves, *Ax* was larger than that one when using grinding wheel with 15 grooves, but it was smaller than that one when using grinding wheel with 20 grooves;

– feed-rate was factor that has the most influence on the output parameters, the second and third factor that have the effect on the output parameter were number of grooves and depth of cut. The workpiece velocity has the smallest influence on the output parameters;

– the optimum values of input parameters were groove number of 18 grooves, workpiece velocity of 15 m/min, feed-rate of 2 mm/stroke, and cutting depth of 0.005 mm;

– using the optimum values of input parameters, averages value of grinding surface roughness, vibration amplitudes in *X*, *Y*, *Z* directions were 0.826 (μm), 0.531 (μm), 0.549 (μm), and 0.646 (μm), respectively. These results were great improved in comparing the cases using the normal values of input parameters;

– taguchi method and DEAR technique can be applied to improve the quality of grinding surface and reduce the vibrations of the technology system. So that can be used to restrain the increasing of the cutting forces and chatter in the grinding process;

– in this study, only the number of grooves in the grinding wheel is considered, have not considered the size and shape of the grooves. Besides, other factors of the grinding process affect the output parameters such as grinding wheel dressing, cooling lubrication conditions, etc. also have not considered in this study. These are issues that need to be done in the next research to evaluate the segmented grinding wheel process in a more comprehensive way.

References

[1] Herman, W. C. (1936). Pat. No. US2032362A. Segmental grinding wheel. Available at: https://patents.google.com/patent/US2032362A/en

[2] Nguyen, T., Zhang, L. C. (2005). Modelling of the mist formation in a segmented grinding wheel system. International Journal of Machine Tools and Manufacture, 45 (1), 21–28. doi: https://doi.org/10.1016/j.ijmachtools.2004.06.019

[3] Lee, K. W., Wong, P. K., Zhang, J. H. (2000). Study on the grinding of advanced ceramics with slotted diamond wheels. Journal of Materials Processing Technology, 100 (1-3), 230–235. doi: https://doi.org/10.1016/s0924-0136(00)00403-9

[4] Jin, D. X., Meng, Z. (2004). Research for Discontinuous Grinding Wheel with Multi-Porous Grooves. Key Engineering Materials, 259-260, 117–121. doi: https://doi.org/10.4028/www.scientific.net/kem.259-260.117

[5] Fan, X., Miller, M. (2004). Force Analysis for Segmental Grinding. Proc ASPE Annual Meeting, 3–6.

[6] Handigund, P. B., Miller, M. H. (2011). Abrasive Wear and Forces in Grinding of Silicon Carbide. Michigan Technological University. Houghton, MI.

[7] Phuong, N. T., Giang, N. T. P., Dong, N. T. (2017). Research on the Affect of Technologycal Parameters on Cutting Temperature When Machining use Segmented Grinding Wheel. International Journal of Electronics Communication and Computer Engineering, 8 (3), 208–212.

[8] Phuong, N. T., Nguyen, G. P. T., Nguyen, D. T. (2017). A research on the effect of cuttıng parameters on cuttıng force ın flat grındıng usıng segmented grındıng wheel. Vietnam Journal of Science and Technology, 55 (6), 793–802. doi: https://doi.org/10.15625/2525-2518/55/6/8961

[9] Ohashi, K., Tan, K., Ashida, T., Tsukamoto, S. (2015). Quick On-Machine Measurement of Ground Surface Finish Available for Mass Production Cylindrical Grinding Processes. International Journal of Automation Technology, 9 (2), 176–183. doi: https://doi.org/10.20965/ijat.2015.p0176

[10] Takaya, Y. (2014). In-Process and On-Machine Measurement of Machining Accuracy for Process and Product Quality Management: A Review. International Journal of Automation Technology, 8 (1), 4–19. doi: https://doi.org/10.20965/ijat.2014.p0004

[11] Nguyen, N.-T., Kao, Y.-C., Dung, H. T., Trung, D. D. (2020). A Prediction Method of Dynamic Cutting Forces and Machine-Tool Vibrations When Milling by Using Ball-End Mill Cutter. Lecture Notes in Networks and Systems, 47–54. doi: https://doi.org/10.1007/978-3-030-37497-6_5

[12] Nguyen, T.-L., Nguyen, N.-T., Hoang, L. (2020). A study on the vibrations in the external cylindrical grinding process of the alloy steels. International Journal of Modern Physics B, 34 (22n24), 2040150. doi: https://doi.org/10.1142/s0217979220401505

[13] Marinescu, I. D., Hitchiner, M. P., Uhlmann, E., Rowe, W. B., Inasaki, I. (2006). Handbook of Machining with Grinding Wheels. CRC Press, 632. doi: https://doi.org/10.1201/9781420017649

[14] Malkin, S., Guo, C. (2008). Grinding technology: Theory and Applications of Machining with Abrasives. Industrial press, 372.

[15] Cao, Y., Guan, J., Li, B., Chen, X., Yang, J., Gan, C. (2013). Modeling and simulation of grinding surface topography considering wheel vibration. The International Journal of Advanced Manufacturing Technology, 66 (5-8), 937–945. doi: https://doi.org/10.1007/s00170-012-4378-7

[16] Malkin, S. (1984). Grinding of metals: Theory and application. Journal of Applied Metalworking, 3 (2), 95–109. doi: https://doi.org/10.1007/bf02833688

[17] Aini, R., Rahnejat, H., Gohar, R. (1990). A five degrees of freedom analysis of vibrations in precision spindles. International Journal of Machine Tools and Manufacture, 30 (1), 1–18. doi: https://doi.org/10.1016/0890-6955(90)90037-j

[18] Liu, T., Deng, Z., Lv, L., She, S., Liu, W., Luo, C. (2020). Experimental Analysis of Process Parameter Effects on Vibrations in the High-Speed Grinding of a Camshaft. Strojniški Vestnik – Journal of Mechanical Engineering, 66 (3), 175–183. doi: https://doi.org/10.5545/sv-jme.2019.6294

[19] Phadke, S. (1989). Quality Engineering Using Robust Design. Prentice Hall, 250.

[20] Karna, S. K., Singh, R. V., Sahai, R. (2012). Application of Taguchi Method in Indian Industry. International Journal of Emerging Technology and Advanced Engineering, 2 (11), 387–391.

[21] Karna, S. K., Sahai, R. (2012). An Overview on Taguchi Method. International Journal of Engineering and Mathematical Sciences, 1, 11–18.

[22] Manoj, M., Jinu, G. R., Muthuramalingam, T. (2018). Multi Response Optimization of AWJM Process Parameters on Machining TiB2 Particles Reinforced Al7075 Composite Using Taguchi-DEAR Methodology. Silicon, 10 (5), 2287–2293. doi: https://doi.org/10.1007/s12633-018-9763-x

[23] Muthuramalingam, T., Vasanth, S., Vinothkumar, P., Geethapriyan, T., Rabik, M. M. (2018). Multi Criteria Decision Making of Abrasive Flow Oriented Process Parameters in Abrasive Water Jet Machining Using Taguchi–DEAR Methodology. Silicon, 10 (5), 2015–2021. doi: https://doi.org/10.1007/s12633-017-9715-x

[24] Thangaraj, M., Loganathan, G. B., Atif, A., Palanisamy, S. (2019). Multi Response Optimization on Machining Titanium Alloy Using Taguchi-DEAR Analysis in Abrasive Water Jet Cutting. SAE Technical Paper Series. doi: https://doi.org/10.4271/2019-28-0070

[25] Sandeep, M. J., Manjunath, P. G. C., Chate, G. R., Parappagoudar, M. B., Daivagna, U. M. (2019). Multi Response Optimization of Green Sand Moulding Parameters Using Taguchi-DEAR Method. Applied Mechanics and Materials, 895, 1–7. doi: https://doi.org/10.4028/www.scientific.net/amm.895.1

[26] Reddy, V., Reddy, C. S. (2016). Multi Response Optimization of EDM of AA6082 Material using Taguchi- DEAR Method. International Journal of Scientific & Engineering Research, 7 (6), 215–219.

[27] Muthuramalingam, T., Vasanth, S., Mohamed, R. M., Geethapriyan, T., Ramamurthy, A. (2016). Multi reponse Optimization of EDM Process Parameters using Assignments of Weight Method. International Journal of Engineering Research & Technology, 4 (26).

Received date 18.01.2021
Accepted date 25.01.2021
Published date 29.01.2021

Original Research Article: full paper

(2021), «EUREKA: Physics and Engineering»
Number 1

ANALYSIS OF THE CONDITION OF A PIPE FIXED IN A CLAMPING DEVICE

Emin Musa Afandiyev
Department of Industrial engineering[1]
ertef4@gmail.com

Mahammadali Nuraddin Nuriyev
Department of Industrial engineering[1]
mehman62@mail.ru

[1]*Azerbaijan State Economic University (UNEC),*
6 Istiglaliyyat str., Baku, Azerbaijan, AZ 1001

Abstract

Due to the fact that clamping devices are widely used in various industries, the requirements for the operation of such devices are constantly increasing. This is due to an increase in the general requirements for processing accuracy, as well as an increase in the forces acting on the clamped part. The reliability of these devices when working with thin-walled cylindrical parts is of great importance.

Thin-walled cylinders used in mechanical engineering are subject to significant loads. With prolonged exposure to loads from clamping forces, as well as from axial tensile forces, plastic deformations of cylindrical parts occur. In the oil and gas industry, when clamping drill and casing pipes in some areas in the capture zone, stresses exceed the yield strength. Multiple clamping of the pipe will reduce the pipe wall in the gripping area, which causes premature pipe failure. Therefore, increasing the holding capacity of clamping mechanisms is relevant.

Analysis of broken drill pipes, which have been operating in wedge grips for a long time, showed that in most cases the pipes undergo plastic deformation caused by damage to the pipe surface by the teeth of the ram. To clarify the actual conditions of loading the pipe and the possibilities of increasing the capacity of the clamping devices, studies of the contact pressures in the clamping zone were carried out.

A new pipe clamping chuck is also presented, which provides a sufficiently high reliability of fastening of cylindrical parts.

Keywords: pipe, load, stress, deformation, holding capacity, cartridge, clamp, paper gauge.

DOI: 10.21303/2461-4262.2021.001587

1. Introduction

A feature of the operation of thin-walled cylindrical parts, in particular, drill pipes, is the susceptibility to significant deformations during the process of being gripped by clamping mechanisms. As a rule, the clamping forces are applied multiple times in the same area of the pipe. In this case, the compressive stresses can exceed the yield strength of the pipe metal. This results in local plastic deformations in the gripping zone of the pipe in the clamping mechanism. The shape and dimensions of the elements of the clamping mechanisms also have a significant effect on the nature of the pipe deformations and stresses, as well as the holding capacity of the clamping devices. This is due to the nature of the distribution of contact pressures on the surfaces of the parts of the clamping device.

With long-term operation of pipes under these conditions, such deformations lead to a thinning of the pipe wall, which creates the danger of breaking the pipe string. Drill string breakage accidents require high costs to retrieve the string or lead to abandonment of the well. The oil and gas industry is constantly experiencing a need to improve the quality of drilling equipment, especially drill and casing pipes. This is due to the high labor intensity and energy consumption of oil and gas production. Improving the quality of drilling equipment is aimed at extending the service life of pipes in order to eliminate the possibility of emergencies. This explains the relevance of the presented work.

Investigation of the distribution of contact pressures on the surfaces of parts of the clamping device, which affect the state of the pipe and the holding capacity of the clamping devices, is an important task for the oil and gas production, machine building and other industries.

Reliability and durability of clamping devices when working with thin-walled cylindrical parts is of great importance, both in mechanical engineering and in the oil and gas industry. Therefore, the study of issues of increasing the holding capacity of clamping mechanisms is an important task.

2. Literature review and problem statement

Requirements for the quality of drill pipes are due to the high labor and energy consumption of oil production. Improving the quality of drilling equipment, in particular, clamping mechanisms, extends the service life of drill pipes in order to eliminate the possibility of emergencies. Work in this direction is of great practical importance.

In work [1], some technological methods for improving the quality of pipes are considered, as well as design features of some clamping devices used in round-trip operations when drilling wells. However, no attention has been paid to damage to the pipe surface by clamping jaws.

In work [2] it is shown that pipe damage during tripping operations occurs mainly from the action of clamping jaws. The condition of the pipe in the clamping device is also influenced by various factors, such as clamping force, radial and axial loads, column mass. It is noted that the most uniform distribution of forces along the teeth of the clamping jaws is provided by an oblique intersecting notch, which gives a high holding capacity of the clamping devices.

Drill-pipe clamping mechanisms have also been investigated by the American Petroleum Institute (API). In the API standards, it is noted that deformations of drill pipes occur due to cuts on their surface, which are left by teeth of wedge rams or drill tongs [3].

Work [4] is devoted to the study of thin-walled cylindrical parts. The paper considers external factors affecting the stress state of a cylindrical part. The adhesion coefficients in the clamping devices were analyzed. Methods for improving the design of their elements are proposed in order to increase the adhesion coefficients. However, not all influencing factors are taken into account.

The paper [5] describes the properties of paper used as a sensor when measuring contact pressures.

In works [6, 7] external factors influencing the stress state of the pipe are considered. The coefficients of adhesion in the clamping devices are analyzed. Methods for improving the design of their elements are proposed in order to increase the adhesion coefficients.

In work [8] it is shown to what deformations the pipe is subject during operation. The processes of material creep are considered, which can be, as a consequence of stress relaxation under sufficiently long exposure to high stresses. These processes, considered in the work, show that in order to increase the holding capacity of the clamping mechanisms, it is necessary to comprehensively study all the factors affecting the deformation of the drill pipe during tripping operations.

In the material [9], a new pipe clamping chuck is presented, which provides reliable pipe clamping during processing.

In other works, the influence of structural elements of clamping devices on the stress state and deformation of the pipe has also been investigated, and recommendations are given for improving their design in order to increase the holding capacity [10, 11].

In the literature presented, insufficient attention is paid to recommendations for reducing stresses and deformations when fastening thin-walled cylindrical and other similar parts in clamping devices. There are practically no dependencies for engineering calculations and analysis of loading schemes.

3. The aim and objectives of research

The aim of this research is to identify the nature of the distribution of contact pressures on the surfaces of the parts of the wedge-clamping mechanism and its effect on the loads acting on the pipe. The equalization of the distribution of the load on the pipe helps to reduce deformations of the drill pipes during tripping operations and to increase the holding capacity of the clamping devices.

For this aim, it is necessary to solve the following objectives:

– to determine the nature of the distribution of the contact load from the axial force along the wedges and clamping jaws to reduce pipe deformation;

– to determine the possibility of ensuring high reliability of clamping of the processed cylindrical parts using a new design of the clumping device.

4. Study of factors affecting the state of the pipe in the clamping mechanism

4. 1. The nature of the distribution of contact pressures on the surfaces of wedges and clamping jaws

The working condition of drill pipes and their permissible weight during tripping operations depends on the design of the clamping device. This is due to the nature of the distribution of the loads that are created by this device.

In studies of the nature of the distribution of contact pressures, the method of prints was applied, based on the change in the transparency of the paper as a result of its squeezing. In the experiment, let's use high quality writing paper withstanding pressures in the range of 0–500 MPa, the optical non-uniformity of which does not exceed 1.5 μA [5].

When analyzing contact pressures in this way, special friction conditions are created between surfaces. In this case, the frictional forces have a great influence on the horizontal and shear stresses. At the same time, such influence on the distribution of contact pressures is small. Therefore, when studying the distribution of contact pressures, the dynamics of friction can be neglected. The experiments were carried out on a specially designed stand (**Fig. 1**), equipped with hydraulic jacks, which simulates the operation of the clamping device during hoisting operations.

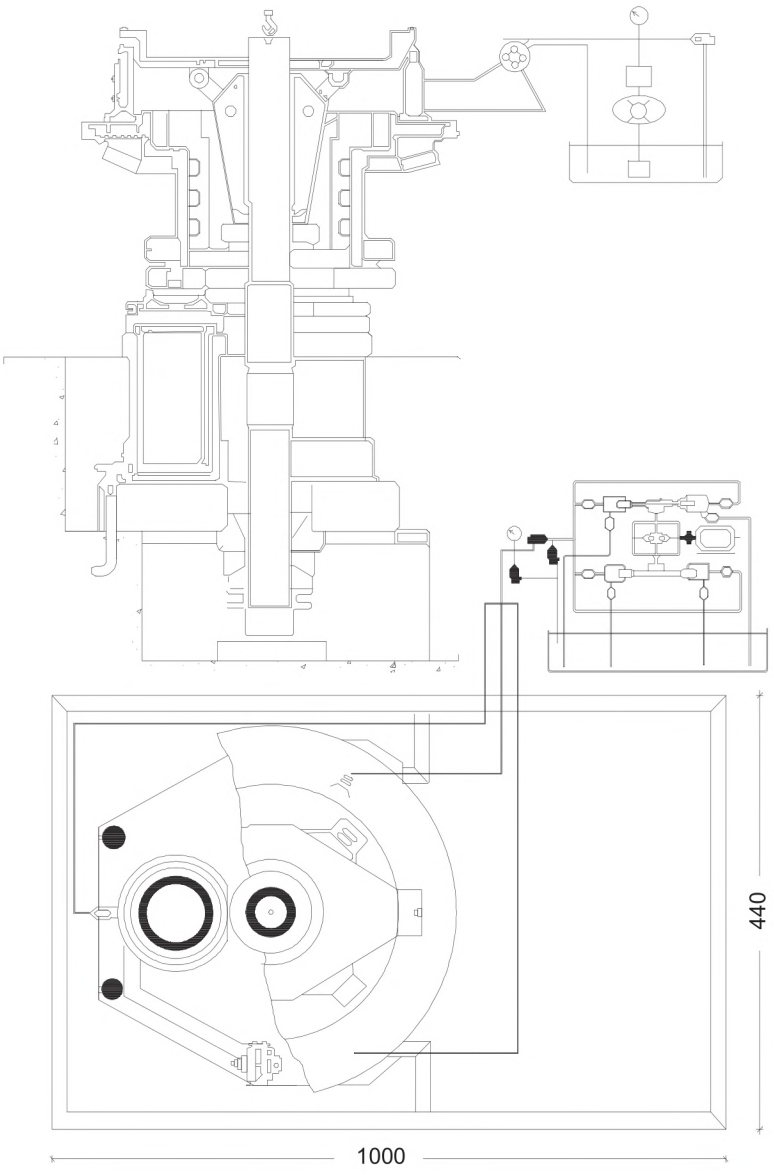

Fig. 1. Hydraulic stand

The stand is installed in a concrete pit 1.8 m deep, 2.2 m and 1.2 m in size. On the ledge of the foundation, a plate with a thickness of 180 mm is installed and fixed with four anchor bolts, which serves as the base of the stand. There are 3 cylinders of the GDZ-300 jack on the plate. On the pistons of the jack, 3 feet with spherical heads are installed, forming a hinge joint. The plate prevents the heels from moving relative to the head.

A plate is installed on the projections of the spherical heads, on which the rotor table is laid. The main parts of the wedge gripper are installed in the rotor table. The working pressure is created by the pumping unit of the hydraulic jack GDZ-300. The working fluid of the jack is Industrial oil 30.

After reaching the required effort, the pumping unit is turned off. To relieve the load, the drain valve opens and the oil returns to the tank.

The stand is capable of creating a longitudinal axial load on the pipe up to 450 tons. As an experimental sample, let's use a branch pipe from a drill pipe with a diameter of 141 mm and a wall thickness of 10 mm made of steel of strength group E.

The object of research were wedges and liners, as well as clamping jaws with an inner cylindrical surface. Standard A4 size paper sheets were placed between the wedge and the liner under the wedge support plane; between the wedge and dies; as well as between the ends of adjacent dies (**Fig. 2**). In all cases, a sheet of paper, which is actually a contact pressure sensor, was placed between two sheets of paper of the same brand to protect against impurities.

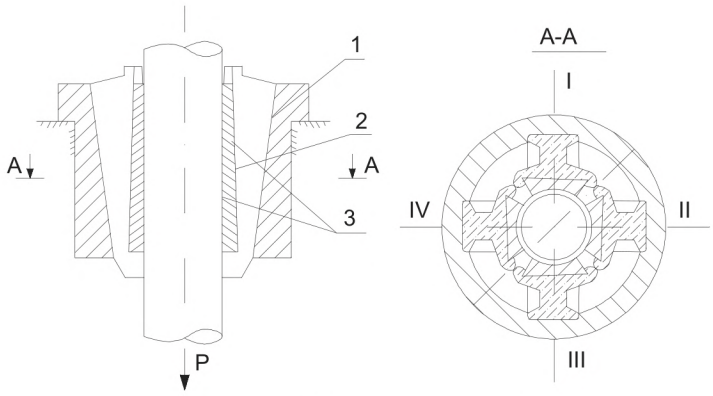

Fig. 2. Location of the pipe in the wedge grip

The surfaces of the clamping unit that come in contact with the paper sensors were thoroughly cleaned of grease. Considering that the lack of lubrication could lead to seizure on the wedge bearing surfaces, paper sensors were placed under each wedge in turn, and the bearing planes of the remaining wedges were coated with graphite grease.

The axial tensile force **P** in each experiment was adjusted to 10 kN. After reaching the specified load, the installation was unloaded, the paper gauges were released, and the contact pressures were measured on all surfaces (**Fig. 3**). Measurements were taken immediately after unloading, considering that paper probes can induce stress relaxation.

It has been experimentally established that the pressures on the supporting surfaces of the wedges are unevenly distributed. In particular, contact pressures of up to 300 MPa are noted in the lower layers of the support plane, as well as in the lower parts of the surfaces of the backs of the lower jaw. The highest pressures are noted at the ends of the lower jaw, which takes up the entire axial load. The ends of the middle and upper jaws are practically unloaded.

Due to the fact that the load on each wedge was the same, the dynamics was not taken into account here. The results were recorded after reaching the specified load and clearly reflected on the paper sensors due to the change in density. This made it possible to obtain a clear picture of the distribution of contact pressures on the surfaces of the clamping device elements.

Uneven pressure distribution is a consequence of the influence of the design features of the clamping mechanism, as well as some technological factors, such as manufacturing and assembly accuracy, the macro geometry of contact surfaces, etc. As a result of the uneven pressure distri-

bution, contact and volumetric deformations of the pipe significantly increase. This can lead to its premature failure. It is possible to reduce the unevenness of the pressure distribution by using self-aligning wedges and dies with an oblique intersecting notch [4].

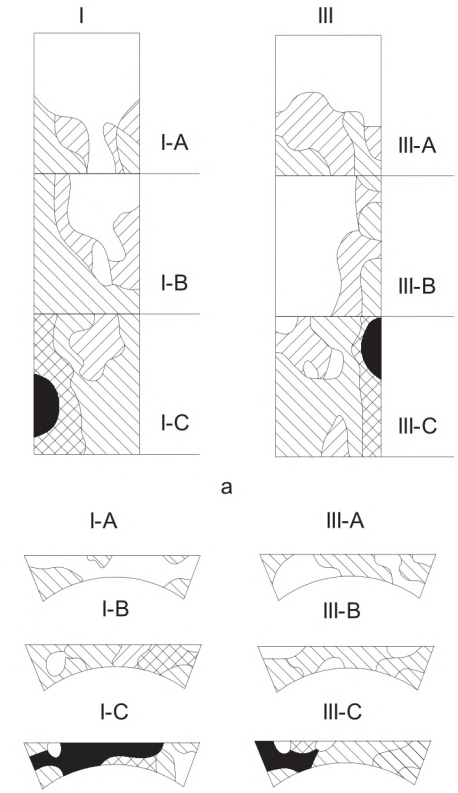

Fig. 3. Distribution of pressure among the elements of clamping devices

4. 2. Improving the reliability of fastening cylindrical parts

The design of the clamping device plays an important role in increasing the reliability of the fastening of cylindrical parts. In this regard, a new pipe clamping chuck was proposed, which can be used on pipe-working and coupling-screwing machines.

The pipe clamping chuck presented here provides a sufficiently high reliability of fastening of cylindrical parts. This is achieved due to the fact that the chuck is equipped with cams with shoes, which provide the possibility of rotation. The wedges are fixed in the grooves of the cams and interact with the support rollers of the liners (**Fig. 4**). The chuck drive mechanism includes a power cylinder and a lever self-braking transmission 2, cams 3 installed in the housing 4. Curved wedges 5 are fixed in the grooves of the cams and contact with support rollers 6, which are located in the liners 7 located in the pads 8. In the liners 7 installed floating jaws 9. Pads 8 are located in cams 3 and are under the action of return springs 10. Pads 8 are installed in cams 3 on rollers 11.

The principle of operation of the cartridge is as follows. When pressure enters the rod cavity of the power cylinder, the cams through curved wedges and support rollers press the liners with jaws to the pipe. The pads move and the pipe is pre-clamped. The clamping jaws fit snugly against the pipe surface as they align themselves (**Fig. 5**).

Further, when the pipe is screwed on under the action of a torque, it turns together with the jaws and liners. In this case, the support rollers are rolled on curved wedges fixed in the cams, while the liners begin to move towards the center, and perform an additional clamping of the pipe. The clamping force is proportional to the effective torque.

After processing the pipe, pressure is applied to the piston cavity of the cylinder. The cams move apart, and the springs return the pads with liners to their original position. In order to prevent the pads from falling out of the cams, rollers are installed on them.

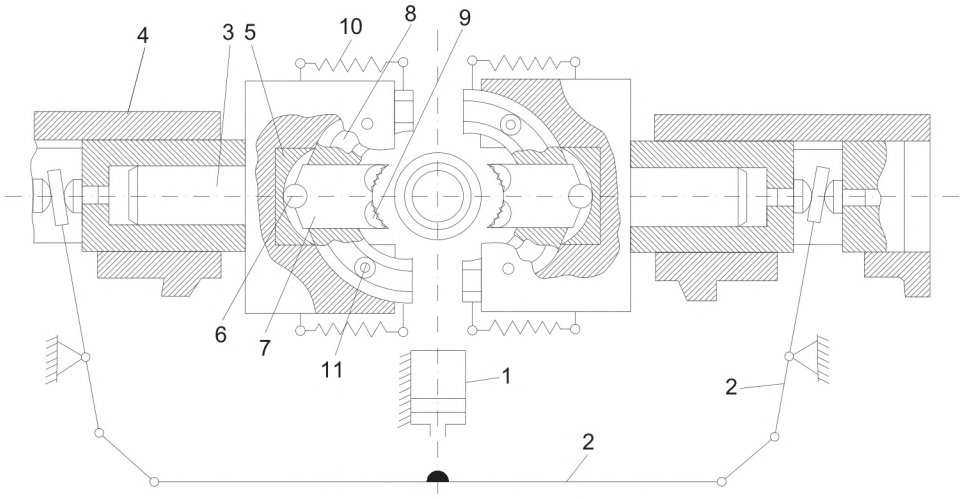

Fig. 4. Pipe clumping chuck

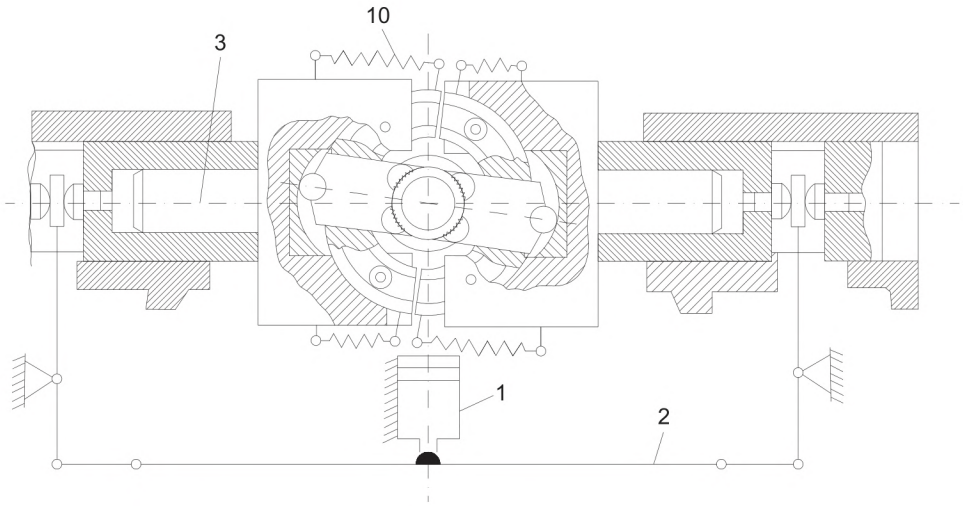

Fig. 5. Clamping chuck in clamping state

The pre-clamping of the pipe provides the amount of adhesion of the jaws that is necessary for a secure grip and prevention of rotation under the main load. The pre-clamping force can be adjusted by the pressure in the cylinder of the drive mechanism. The effectiveness of this device is ensured by the high reliability of fixing the processed cylindrical parts. The presented pipe clamping chuck is protected by copyright certificate No. 910370.

5. Discussion of the research results of pressure distribution over the elements of clamping devices

In the oil and gas industry, when clamping drill and casing pipes in the capture zone, stresses often exceed the yield strength. Multiple clamps in the same area of the pipe cause the pipe wall to shrink, leading to premature pipe failure.

As a rule, the clamping forces act in the same area of the pipe. In some cases, compressive stresses cause local plastic deformations in the gripping zone of the pipe in the clamping mechanism. The shape and dimensions of the elements of the clamping mechanisms also have a significant influence on the nature of the pipe deformations and stresses, as well as on the holding capacity of the clamping devices. This is due to the nature of the distribution of contact pressures on the surfaces of the parts of the clamping device.

In studies of the distribution of contact pressures, the method of prints was applied, based on the change in the translucency of paper as a result of its squeezing. The experiments were

carried out on a stand that simulates the operation of the clamping device in the process of round-trip operations (**Fig. 1**). In the wedge grip, 4 wedges, each equipped with three dies, simultaneously grip the pipe under the action of a clamping force. Subsequently, from the axial load (from the weight of the column), the final clamping of the pipe occurs. In this case, the parts of the clamping device are subjected to contact pressure at the joints. The results of squeezing paper sensors at different gripping points are shown in (**Fig. 3**). The results obtained are explained by the fact that the pressures on the supporting surfaces of the wedges are unevenly distributed. The highest pressures are noted at the ends of the lower jaw, which takes up the entire axial load.

The uneven distribution of pressures is a consequence of the influence of the design features of the clamping mechanism, in particular, the presence of a large number of joints, as well as some technological factors, such as the macro geometry of the contact surfaces, etc. At the moment, this problem has not been fully solved.

The limitations of this study are that drill pipes are its object, since they are most susceptible to deformations from axial and radial loads during tripping operations. However, despite the fact that the research carried out refers to drill pipes, the main conclusions can be applied to other cylindrical parts.

The design of the clamping device plays an important role in increasing the reliability of the clamping of cylindrical parts during processing. In this regard, a new pipe-clamping chuck was proposed, which can be used on pipe-working and coupling-screwing machines (**Fig. 4**). The effectiveness of this device is ensured by the high reliability of fixing the processed cylindrical parts.

Further development of this study can be continued taking into account other types of loads and different pipe materials.

6. Conclusions

As a research result, it was found that the pressure on the supporting surfaces of the wedges is distributed unevenly. In particular, contact pressures of up to 300 MPa are noted in the lower layers of the support plane, as well as in the lower parts of the surfaces of the backs of the lower jaw. The highest pressures are noted at the ends of the lower jaw, which takes up the entire axial load. The ends of the middle and upper jaws are practically unloaded.

In order to increase the reliability of the fastening of cylindrical parts during processing, a new pipe clamping chuck has been proposed, which can be used on pipe processing and coupling-screwing machines.

Acknowledgement

We express our gratitude to Professor I. Lopatukhin for his idea and participation in the creation of the pipe clumping chuck and other consultations.

References

[1] Markov, O., Gerasimenko, O., Khvashchynskyi, A., Zhytnikov, R., Puzyr, R. (2019). Modeling the techological process of pipe forging without a mandrel. Eastern-European Journal of Enterprise Technologies, 3 (1 (99)), 42–48. doi: https://doi.org/10.15587/1729-4061.2019.167077

[2] Afandiyev, E. M., Nuriyev, M. N. (2019). Studying the quality of drill pipes clamped in a wedge clamp. Eastern-European Journal of Enterprise Technologies, 4 (7 (100)), 16–21. doi: https://doi.org/10.15587/1729-4061.2019.174494

[3] Rukovodstvo po trubam neftyanogo sortamenta i ih soedineniyam, primenyaemym za rubezhom (1969). Moscow: Nedra, 296.

[4] Afandiyev, E. M., Nuriyev, M. N. (2020). Improving the retention capacity of clamping elements. Eastern-European Journal of Enterprise Technologies, 1 (1 (103)), 47–51. doi: https://doi.org/10.15587/1729-4061.2020.195193

[5] Rozanov, B. V., Lints, V. P., Shchegoleva, V. P. (1978). Svoystva bumagi, ispol'zuemoy v kachestve datchika pri izmerenii kontaktnyh davleniy. Vestnik mashinostroeniya, 12, 73–75.

[6] Wang, L., Guo, S., Gong, H., Shang, X. (2016). Research and development of a self-centering clamping device for deep-water multifunctional pipeline repair machinery. Natural Gas Industry B, 3 (1), 82–89. doi: https://doi.org/10.1016/j.ngib.2015.12.012

[7] Djukic, L. P., Sum, W. S., Leong, K. H., Hillier, W. D., Eccleshall, T. W., Leong, A. Y. L. (2015). Development of a fibre reinforced polymer composite clamp for metallic pipeline repairs. Materials & Design, 70, 68–80. doi: https://doi.org/10.1016/j.matdes.2014.12.059

[8] Markov, O., Gerasimenko, O., Aliieva, L., Shapoval, A. (2019) Development of the metal rheology model of high-temperature deformation for modeling by finite element method. EUREKA: Physics and Engineering, 2, 52–60. doi: https://doi.org/10.21303/2461-4262.2019.00877

[9] Efendiev, E. M., Lopatuhin, I. M. (1982). Trubozazhimnoy patron. Avtorskoe svidetel'stvo SSSR No. 910370. Byulleten' izobreteniy, 9.

[10] Yakhin, A. R., Ismakov, R. A., Garifullin, R. R., Yangirov, F. N. (2014). Surface hardening for drill pipe life improvement. Oil and Gas Business, 4, 381–399. doi: https://doi.org/10.17122/ogbus-2014-4-381-399

[11] Bulatov, A. I., Proselkov, Yu. M., Shamanov, S. A. (2013). Tehnika i tehnologiya bureniya neftyanyh i gazovyh skvazhin. Moscow, 1007. Available at: https://www.geokniga.org/books/12460

Received date 12.11.2020
Accepted date 20.01.2021
Published date 29.01.2021

Original Research Article: full paper

(2021), «EUREKA: Physics and Engineering»
Number 1

STUDY OF THE EFFICIENCY OF SQUEEZING MOISTURE-SATURATED PRODUCTS

Gayrat Bahadirov
Department of «Theory of Mechanisms and Machines»[1]
instmech@rambler.ru

Gerasim Tsoy
Department of «Theory of Mechanisms and Machines»[1]
tsoygeran@mail.ru

Ayder Nabiev
Research laboratory
Department of «Theory of Mechanisms and Machines»[1]
a.nabiev@mail.ru

[1]*Institute of Mechanics and Seismic Stability of Structures of the Academy of Sciences of the Republic of Uzbekistan*
33 Durmen yuli str., Tashkent, Uzbekistan, 100125

Abstract

The leather industry includes many technological machines; a squeezing roller machine is used in many operations, for example, in squeezing, degreasing, and after drum dyeing of a semi-finished leather product.

The paper presents the results of experimental studies obtained by determining the influence of multilayer wet leather semi-finished products with monshons under squeezing on the amount of the moisture extracted. Mathematical dependences of the amount of the moisture extracted, for each layer of a five-layer wet leather semi-finished product on the feed rate between the squeeze rollers and the roller pressure were obtained.

Experimental research is of scientific and practical importance for the development of a technological process for extracting moisture from wet leather semi-finished products used in the tannery, since the quality of the extraction affects the quality of subsequent technological operations, such as leather shaping and splitting.

An experimental study was performed using the method of mathematical statistics, namely, the method of mathematical planning of the experiment.

Mathematical models were obtained for the amount of extracted moisture from five wet leather semi-finished products depending on the rate of their simultaneous feed and the pressure of the squeezing rollers.

The results of the experiment showed that in squeezing a five-layer product, the productivity of the technological process of extracting moisture from wet leather semi-finished products increases by five times in comparison with existing squeezing roller machines.

The use of the results of the experimental study will contribute to a significant reduction in the energy consumption of the squeezing roller machine by simultaneous multi-layer processing of wet leather semi-finished products.

Keywords: semi-finished leather product, monshon, moisture content, multilayer squeezing, residual moisture, technological process, experimental stand, shafts, pressure, productivity.

DOI: 10.21303/2461-4262.2021.001606

1. Introduction

In modern industrial conditions, the manufacture of natural leather consists of a number of technological processes: preparatory processes (soaking, liming, pickling, softening, fermentation, degreasing), finishing processes – chemical (tanning), liquid, physicochemical (filling, dyeing, moisture extraction, drying, moisturizing), and mechanical processes (fleshing, shaping, setting, printing, tumbling, breaking, staking, rolling, buffing), surface dyed and other processes.

The study in [1] considers conditions for the primary processing of semi-finished leather products. The studies in [2–4] refer to the improvement of the technology of liquid processing of semi-finished leather products.

The analysis and study of the structure and properties of collagens in semi-finished leather after liquid processing with chemical additives are given in [5, 6].

[7–12] investigate the influence of technological, chemical, and other factors on the physico-mechanical, filtration, and qualitative properties of semi-finished leather.

The studies presented in [13–15] are devoted to the improvement of the roller equipment design, including the roller module interaction with the material being processed.

The studies in [16–19] are devoted to the development of the theory of calculation of technological processes for extracting moisture from a semi-finished leather product.

In order to increase the efficiency and productivity of technological process of extracting the excess moisture from wet semi-finished leather products, let's experimentally investigate the influence of such factors as the number of layers of semi-finished leather products and moisture-extracting materials (monshons) on the technological process of moisture extraction from wet semi-finished leather products under their vertical feed on the base plate.

In the leather industry, many technological machines are used, including a roller squeezing machine, which is used in many operations, for example, during pressing, degreasing and after drum dyeing of semi-finished leather products. The quality of the pressing operation determines the quality of subsequent technological operations, such as shaping and splitting of leather semi-finished products.

2. Materials and methods

The experiment was performed on a roll stand, where the squeeze rollers were installed horizontally and the base plate was made of a metal sheet 0.005 m thick, 0.1 m wide, 0.3 m long (**Fig. 1**). One layer of the package consisted of one semi-finished leather product and one layer of moisture-extracting material (monshons) made of LASCH cloth.

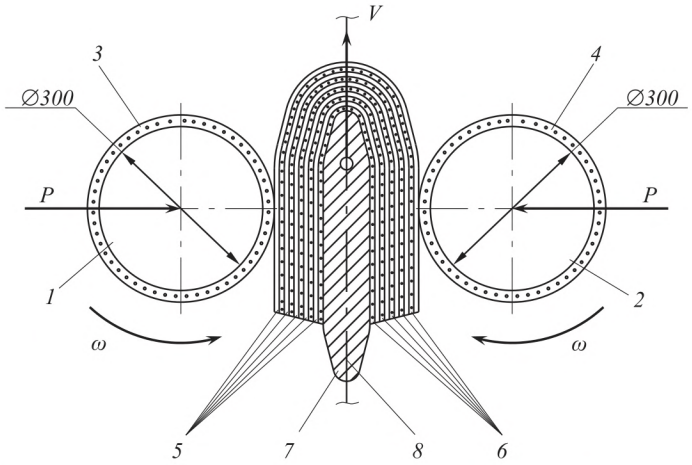

Fig. 1. Scheme of the squeezing five-layer wet leather semi-finished products:
1, 2 – squeeze rollers; 3, 4 – BM moisture-extracting materials; 5 – semi-finished leather products; 6 – LASCH moisture-extracting materials; 7 – base plate; 8 – traction chain

Leather material for the experiment was taken from a bovine of medium weight, after chrome tanning, double tanning. According to the International Standard ISO 2588-85, the number of leather samples was selected according to formula $n = 0.2\sqrt{x}$, where x is the number of leather samples for the experiment, taken from a batch of 2500 pcs, so, $n = 10$ pcs. From these 10 skin samples, the strips were cut out with a cutter across the backbone line, 0.05×0.25 m in size; the strips were numbered and assembled into groups of 5 pcs according to the scheme given in [7, 20].

The experiment was performed as follows: a 0.004 m thick strip of LASCH fiber cloth was put on a metal base plate, and then a semi-finished leather product was laid on it, and so on, a layer after layer. Then the stand was switched on, the spring compression was set by calibration to the required pressing force of the squeeze rollers, a rheostat controlled the rate, and a clock-type tachometer TCh 10P controlled the roller rotation frequency. Beforehand, the control skin samples were fed and the spring compression was measured, i. e., its deviation from the setting value. If the deviation exceeded 3 %, then the springs were adjusted by tightening the nuts. Then the main

leather samples were fed. The samples were weighed on a VLTE-500 laboratory balance, with resolution 0.01 g (ISO-9001) before and after the squeezing.

When processing the results of the experiment, the method of D-optimal planning of the second order was used with Kano planning matrix, since its application provides great accuracy in the regression coefficients estimates. It was taken into account that Kano planning matrix provides a variation of factors at three levels: at the lower level (–), at zero level (0) and at the upper level (+), which is appropriate for this study. On the basis of a priori information, the process of moisture extraction was studied taking into account three factors: x_1 – roller pressure P, kN/m; x_2 – feed rate V, m/s; the number of layers of leather with monshons was 10; the pressure range was chosen from 32 to 96 kN/m; the rate range of the squeeze rollers was from 0.17 to 0.34 m/s, and the number of feed replications of a five-layer package of semi-finished leather products was 5.

In the study, the diameter of the squeeze rollers was 0.3 m, covered with a 0.01 m thick coating made of BM cloth, one layer of LASCH cloth (0.004 m thick) was bent over the metal base plate; then came a layer of a semi-finished leather product (5 layers of semi-finished leather alternating 5 layers of moisture-extracting material), 10 layers in total.

Before conducting the experiment, the required number of measurements (the number of replications) was selected by the methods of mathematical statistics, which provided the required accuracy.

The working matrix was composed according to the Kano planning matrix for a two-factor experiment. Factors were encoded according to the formula:

$$x_i = \frac{c_i - c_{i0}}{t_0},$$

where x_i is the coding of the factors values; c_i, c_{i0} are the natural values of the factor at the current level and at zero level; t_0 is the natural value of the factor variation interval.

Target functions are approximated by a polynomial:

$$y = b_0 + \sum_{i=1}^{k} b_i x_i + \sum_{i,j=1}^{k} b_{ij} x_i x_j + \sum_{i=1}^{k} b_{ii} x_i^2,$$

where y is the amount of extracted moisture in coded form; b_0, b_i, b_{ij}, b_{ii} are the regression coefficients. The levels and ranges of experimental factor variation are given in **Table 1**.

Table 1

Levels and intervals of variation of the experiment factor

Indicator	Coded value of factors	Natural values of factors	
		x_1, kN/m	x_2, m/s
Upper level	+	96	0.340
Zero level	0	64	0.255
Lower level	–	32	0.170
Variation interval		32	0.085

After the implementation of the working matrix, the arithmetic mean values were obtained (**Tables 2, 3**).

The homogeneity of variances was assessed with the Cochran's test at a confidence level of $\alpha = 0.95$. Knowing the total number of variance estimates N and the number of degrees of freedom $f = k–1$, let's calculate the homogeneity of variance G from **Tables 2, 3**. Next, let's find $G_T = 0.358$, at $N = 9$, $f = k–1 = 5–1 = 4$. k is the number of parallel experiments.

$$S_{er}^2 = \frac{\sum_{1}^{n}(y - \bar{y})^2}{n-1}; \quad \sum_{1}^{N} S_i^2 = \frac{\sum_{1}^{N}\sum_{1}^{n}(y - \bar{y})^2}{N(n-1)}.$$

$$G_{cal1} = \frac{S^2_{\max}}{\sum_1^N S_i^2} = \frac{3.485}{16.3125} = 0.2136;\ G_{cal2} = \frac{S^2_{\max}}{\sum_1^N S_i^2} = \frac{5.725}{21.6875} = 0.21404;$$

$$G_{cal3} = \frac{S^2_{\max}}{\sum_1^N S_i^2} = \frac{5.9875}{19.5175} = 0.3068;\ G_{cal4} = \frac{S^2_{\max}}{\sum_1^N S_i^2} = \frac{8.04}{32.79} = 0.2452;\ G_{cal5} = \frac{S^2_{\max}}{\sum_1^N S_i^2} = \frac{5.305}{21.56} = 0.2461,$$

where $S^2_{\max}$ is the maximal variance; and $\sum S_i$ is the sum of all variances.

$G_{cal1} = 0.2136 < G_T = 0.358$; $G_{cal2} = 0.2140 < G_T = 0.38$; $G_{cal3} = 0.30686 < G_T = 0.358$; $G_{cal4} = = 0.2452 < G_T = 0.358$; $G_{cal5} = 0.2461 < G_T = 0.358$. Consequently, the study results are reproducible.

Determine the regression coefficients b_0, b_i, b_{ij}, b_{ii}.

For the first layer of a semi-finished leather product in coded form:

$$b_0 = 17.9903;\ b_{11} = -1.008;\ b_1 = 4.0255;\ b_{22} = 0.8965;\ b_2 = -2.8823;\ b_{12} = -0.15.$$

For the second layer of a semi-finished leather product in coded form:

$$b_0 = 17.6748;\ b_{11} = -1.2433;\ b_1 = 3.7255;\ b_{22} = 0.9567;\ b_2 = 2.8821;\ b_{12} = 0.05.$$

For the third layer of a semi-finished leather product in coded form:

$$b_0 = 17.4008;\ b_{11} = -1.2036;\ b_1 = 3.4951;\ b_{22} = 0.9252;\ b_2 = -2.8951;\ b_{12} = -0.025.$$

For the fourth layer of a semi-finished leather product in coded form:

$$b_0 = 16.9529;\ b_{11} = -1.3270;\ b_1 = 3.4166;\ b_{22} = 0.8121;\ b_2 = -2.8666;\ b_{12} = -0.075.$$

For the fifth layer of a semi-finished leather product in coded form:

$$b_0 = 16.8284;\ b_{11} = -1.2562;\ b_1 = 3.6146;\ b_{22} = 0.5938;\ b_2 = -3.0608;\ b_{12} = 0.15.$$

The following coded regression equations were obtained.

For the first layer of semi-finished leather:

$$y_1 = 17.99026 - 1.00804 \cdot x_1^2 + 0.89146 \cdot x_2^2 + 4.0255 \cdot x_1 - 2.8823 \cdot x_2 - 0.15 \cdot x_1 x_2.$$

For the second layer of semi-finished leather:

$$y_2 = 17.6748 - 1.2433 \cdot x_1^2 + 0.9567 \cdot x_2^2 + 3.7255 \cdot x_1 - 2.8821 \cdot x_2 + 0.05 \cdot x_1 x_2.$$

For the third layer of semi-finished leather:

$$y_3 = 17.4008 - 1.2036 \cdot x_1^2 + 0.9252 \cdot x_2^2 + 3.4951 \cdot x_1 - 2.8951 \cdot x_2 - 0.025 \cdot x_1 x_2.$$

For the fourth layer of semi-finished leather:

$$y_4 = 16.9529 - 1.3270 \cdot x_1^2 + 0.8121 \cdot x_2^2 + 3.4166 \cdot x_1 - 2.8666 \cdot x_2 - 0.075 \cdot x_1 x_2.$$

For the fifth layer of semi-finished leather:

$$y_5 = 16.8284 - 1.2562 \cdot x_1^2 + 0.5938 \cdot x_2^2 + 3.6146 \cdot x_1 - 3.0608 \cdot x_2 + 0.15 \cdot x_1 x_2.$$

Table 2

Experiment planning matrix

No.	P, x_1	V, x_2	No. Leth. semi-fin.	Measurements results, %					
				y_1	y_2	y_3	y_4	y_5	$\overline{y}$
1	0	0	1	18.8	19.3	17.1	17.0	16.8	17.8
			2	17.7	18.1	17.8	16.9	16.5	17.4
			3	17.8	18.0	18.2	16.2	15.8	17.2
			4	19.2	16.0	17.8	16.2	15.3	16.9
			5	17.8	15.1	17.5	16.9	16.2	16.7
2	+	+	1	19.3	20.4	21.0	18.3	16.0	19.0
			2	19.1	20.2	20.2	14.4	17.1	18.2
			3	18.8	17.9	17.2	14.4	17.1	18.2
			4	16.2	19.2	16.1	16.5	17.5	17.1
			5	18.3	16.5	18.0	15.4	15.8	16.8
3	–	+	1	11.2	10.5	11.6	12.2	9.5	11.0
			2	11.0	10.7	11.3	9.3	11.7	10.8
			3	10.8	11.3	10.5	11.3	9.6	10.7
			4	9.8	11.7	13.2	8.5	9.8	10.6
			5	10.5	10.4	7.4	9.1	9.6	9.4
4	–	–	1	17.1	17.4	16.2	16.9	16.4	16.8
			2	17.2	16.8	17.7	15.1	16.2	16.6
			3	16.8	17.1	14.8	17.0	15.8	16.3
			4	17.1	17.5	13.7	16.2	15.5	16.0
			5	17.2	16.8	13.5	15.1	16.4	15.8
5	+	–	1	25.7	25.5	26.2	21.8	23.8	24.6
			2	25.4	25.2	24.3	19.6	24.5	23.8
			3	24.5	26.2	24.5	20.3	20.5	23.2
			4	23.9	25.4	20.1	23.3	21.3	22.8
			5	23.5	24.2	19.7	22.4	23.2	22.6
6	+	0	1	22.5	21.8	22.4	20.2	20.1	21.4
			2	21.8	21.2	20.7	19.8	19.5	20.6
			3	21.4	20.1	20.9	18.3	18.8	19.9
			4	21.0	21.5	21.3	15.3	18.9	19.6
			5	21.4	21.1	20.5	16.0	18.5	19.5
7	0	+	1	17.4	16.8	14.5	15.5	15.8	16.0
			2	16.9	14.5	17.0	14.7	15.9	15.8
			3	16.7	16.5	12.6	15.1	15.6	15.3
			4	16.1	16.4	13.2	12.3	15.0	14.6
			5	15.8	16.2	10.5	15.3	14.2	14.4
8	–	0	1	15.1	14.8	11.9	11.2	11.0	12.8
			2	14.7	14.5	11.8	11.5	10.5	12.6
			3	12.8	13.5	14.2	9.3	12.2	12.4
			4	12.6	12.7	11.9	10.9	12.4	12.1
			5	12.4	12.5	11.3	11.2	11.6	11.8
9	0	–	1	23.1	22.3	22.1	21.6	20.9	22.0
			2	23.0	22.5	22.4	21.2	19.9	21.8
			3	22.8	22.3	23.1	20.1	19.7	21.6
			4	16.1	23.4	21.8	23.2	20.5	21.0
			5	21.7	21.5	21.1	19.8	19.6	20.6

Table 3

Experiment planning matrix

$\sum_{1}^{n}(y-\bar{y})^2$	S_{er}^2	y_{cal}	$\bar{y}-y_{cal}$	$(\bar{y}-y_{cal})^2$
4.38	1.095	18.0	0.2	0.04
1.80	0.45	17.7	0.3	0.09
4.96	1.24	17.4	0.2	0.04
9.96	2.49	16.95	0.05	0.025
3.50	0.875	16.8	0.1	0.01
13.94	3.485	18.88	0.12	0.0144
24.86	6.215	18.28	0.08	0.0064
24.86	6.215	18.28	0.08	0.0064
6.74	1.685	16.12	0.98	0.9604
6.74	1.685	16.86	0.06	0.0036
4.34	1.085	11.12	0.12	0.0144
3.11	0.7775	10.82	0.03	0.0009
1.98	0.495	10.41	0.29	0.0841
13.66	3.415	9.45	1.15	1.325
6.38	1.595	9.34	0.06	0.0036
0.98	0.245	16.58	0.22	0.0484
4.02	1.005	16.59	0.01	0.0001
3.88	0.776	16.50	0.2	0.04
9.04	2.26	15.02	0.98	0.9604
9.57	2.3925	15.76	0.04	0.0016
14.59	3.6475	24.94	0.34	0.1156
22.9	5.725	23.95	0.15	0.0225
23.95	5.9875	23.54	0.41	0.1681
13.36	3.34	21.99	0.81	0.6561
12.18	3.045	22.98	0.38	0.1444
5.5	1.375	21.0	0.38	0.1444
3.66	0.915	20.16	0.44	0.1936
7.06	1.765	19.52	0.38	0.1444
29.44	7.34	18.73	0.87	0.7569
21.22	5.305	19.18	0.32	0.1024
5.14	1.285	16.0	0	0
5.83	1.4575	15.75	0.05	0.0025
10.8	2.70	15.43	0.13	0.0169
12.02	3.005	14.41	0.19	0.0361
21.24	5.31	14.36	0.04	0.0016
13.70	3.425	12.96	0.16	0.0256
14.28	3.57	12.71	0.11	0.0121
14.3	3.575	12.70	0.30	0.09
1.70	0.425	11.91	0.19	0.0361
1.50	0.375	11.96	0.16	0.0256
2.68	0.67	21.76	0.24	0.0576
6.26	1.565	21.51	0.29	0.0841
8.04	2.01	20.56	1.06	1.1236
35.5	8.875	20.13	0.87	0.7569
3.91	0.9775	20.48	0.12	0.0144
Σ 65.25	Σ 16.31			Σ 0.4604
Σ 86.75	Σ 21.69			Σ 0.4202
Σ 78.07	Σ 19.52			Σ 3.0296
Σ 131.16	Σ 32.79			Σ 5.5129
Σ 86.24	Σ 21.56			Σ 0.3072

Substituting instead of $x_1 = (P-64)/32$, where P is the pressing force of the squeeze rollers and $x_2 = (V-0.255)/0.085$, where V is the feed rate of wet semi-finished leather, let's obtain the equation of moisture extracted from the wet leather semi-finished product in percent depending on the pressing force and the rate of wet leather semi-finished product fed between the rotating squeeze rollers.

The hypothesis of the adequacy of the equations obtained was tested with the Fisher criterion at a confidence level of α = 0.95 [7, 20].

$$F_{cal} = \frac{S_{ad}^2}{S^2\{y\}} < F_T,$$

where S_{ad}^2 is the residual variance, or the variance of the adequacy; $S^2\{y\}$ is the variance of reproducibility.

The arithmetic mean values of the experiment are shown in **Table 3**.

From **Tables 1–3** let's define S_{ad}^2 and $S^2\{y\}$.

For the first layer of semi-finished leather:

$$S_{ad1}^2 = \frac{\sum_1^N n\cdot(\overline{y}-y_{cal})^2}{N-\frac{(k+2)(k+1)}{2}} = \frac{5\cdot 0.4604}{3} = 0.7673;\quad S_1^2\{y\} = \frac{\sum_1^N\sum_1^n (y-\overline{y})^2}{N(n-1)} = \frac{65}{9(5-1)} = 1.805;$$

$$F_{cal1} = 0.425 < F_T = 2.87,$$

where N is the total number of experiments; k is the number of factors; n is the number of replications of the experiment; y_i is the result of a separate observation; $\overline{y}$ is the arithmetic mean of the result of the experiment; y_{cal} are the calculated values of the criterion according to the regression equation.

For the second layer of semi-finished leather:

$$S_{ad2}^2 = \frac{5\cdot 0.4202}{3} = 0.7003;\quad S_2^2\{y\} = \frac{86.75}{9(5-1)} = 2.41;\quad F_{cal2} = 0.2906 < F_T = 2.87.$$

For the third layer of semi-finished leather:

$$S_{ad3}^2 = \frac{5\cdot 3.0296}{3} = 5.0493;\quad S_3^2\{y\} = \frac{78.07}{9(5-1)} = 2.1686;\quad F_{cal3} = 2.3284 < F_T = 2.87.$$

For the fourth layer of semi-finished leather:

$$S_{ad4}^2 = \frac{5\cdot 5.5189}{3} = 9.1982;\quad S_4^2\{y\} = \frac{131.16}{9(5-1)} = 3.6433;\quad F_{cal4} = 2.5247 < F_T = 2.87.$$

For the fifth layer of semi-finished leather:

$$S_{ad5}^2 = \frac{5\cdot 0.3072}{3} = 0.512;\quad S_5^2\{y\} = \frac{86.24}{9(5-1)} = 2.3955;\quad F_{cal5} = 0.2137 < F_T = 2.87.$$

So, the values of F_{cal} and F_T were calculated for five layers of semi-finished leather products after moisture squeezing.

3. Results

So, the regression equations can be considered suitable with a 95 % confidence level that in the named form after decoding is:

For the first layer of semi-finished leather:

$$\Delta W_1 = 21.6798 - 0.9843\cdot 10^{-3}P^2 + 123.3854V^2 + 0.2659P - 93.3094V - 0.0552PV.$$

For the second layer of semi-finished leather:

$$\Delta W_2 = 22.8173 - 0.1214 \cdot 10^{-2} P^2 + 132.4152 V^2 + 0.2671 P - 02.6152 V + 0.184 PV.$$

For the third layer of semi-finished leather:

$$\Delta W_3 = 22.5086 - 0.1175 \cdot 10^{-2} P^2 + 128.0595 V^2 + 0.2620 P - 99.9582 V - 0.00919 PV.$$

For the fourth layer of semi-finished leather:

$$\Delta W_4 = 16.2208 - 0.12959 \cdot 10^{-2} P^2 + 112.4014 V^2 + 0.34295 P - 73.4046 V - 0.2757 PV.$$

For the fifth layer of semi-finished leather:

$$\Delta W_5 = 19.9962 - 0.12267 \cdot 10^{-2} P^2 + 82.1855 V^2 + 0.2559 P - 81.4531 V + 0.0552 PV.$$

Based on the results of the experiment (**Fig. 2, *a–c***) and mathematical processing, mathematical models of moisture extraction from wet leather semi-finished products were obtained for each layer and for the average of the five layers, depending on the roller pressure and the feed rate.

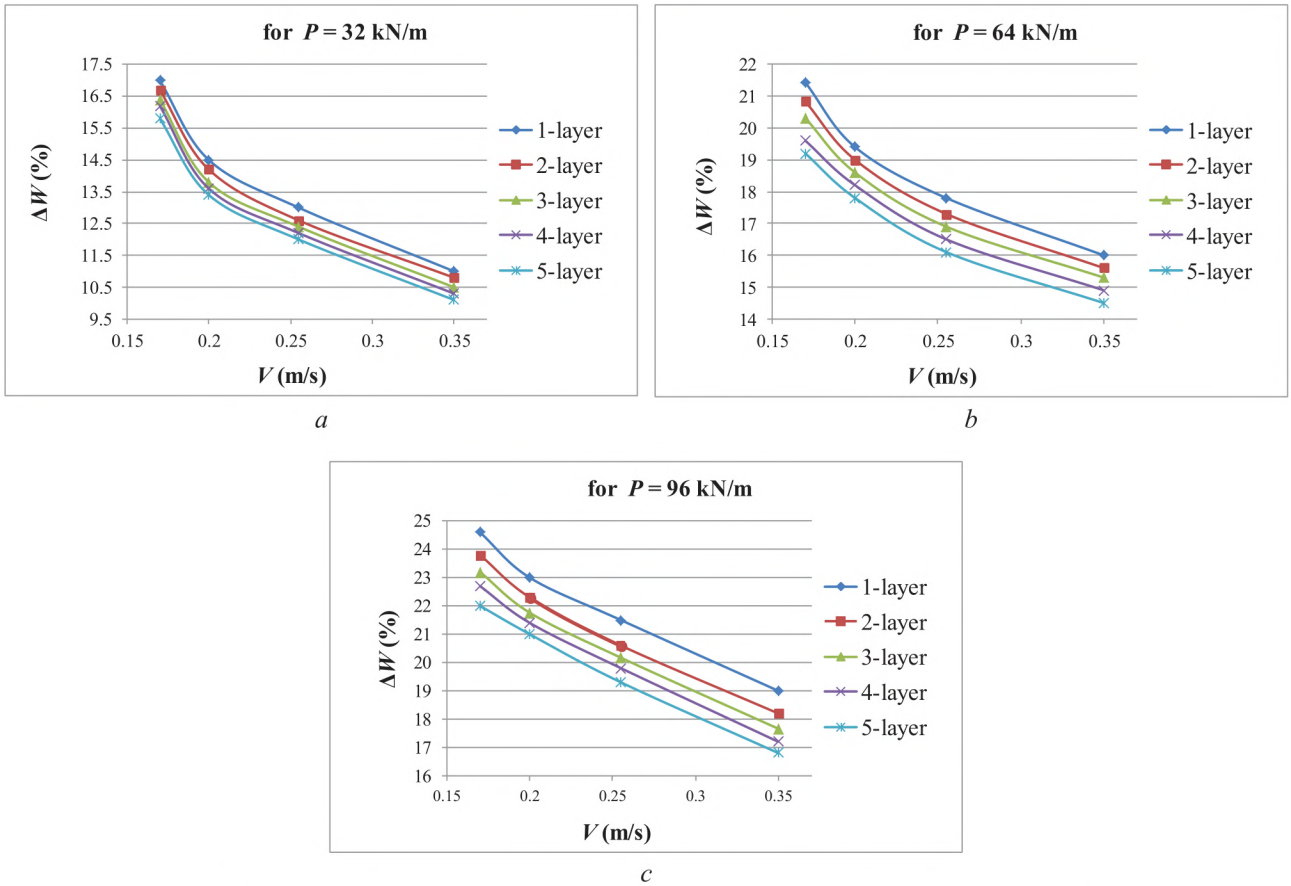

Fig. 2. Dependence of the amount of the moisture removed ΔW on the passage velocity V of each of the five layers of semi-finished leather under the pressing force of the squeeze rollers:
a – for $P = 32$ kN/m; *b* – for $P = 64$ kN/m; *c* – for $P = 96$ kN/m;
1 – the first layer; 2 – the second layer; 3 – the third layer; 4 – the fourth layer;
5 – the fifth layer of semi-finished leather products

So, mathematical models of the dependence of the amount of extracted moisture ΔW_1, ΔW_2, ΔW_3, ΔW_4 and ΔW_5 on the pressure of the squeezing rollers and the feed rate for each leather semi-finished product during their five-layer squeezing were obtained.

4. Discussion of experimental results

The effectiveness of the results of experimental studies is explained by the fact that the considered method of multilayer squeezing of fibrous materials is combined between a flat press and a roller squeezing.

For the first time, an experimental study of the extraction of moisture from fibrous materials in a multilayer bag is carried out. The research results in comparison with the existing technology for processing fibrous materials show an increase in processing productivity and a decrease in energy consumption for the technological process.

It should be noted that the proposed method can only be used if the dispersion is homogeneous, which is determined using the Cochran criterion.

The disadvantage of this method is that the experiment was carried out with insufficient (production) width of processing leather semi-finished products during their multilayer pressing.

Tables 2, **3** shows the results of the experiment for each of the five layers of leather semi-finished product and their processing according to the method of experiment planning. Data on the definition of the regression equation for the mathematical description of the experimental results are also given. According to **Tables 2, 3** the conditions for the reproducibility of the experimental results are determined, as well as the condition for the adequacy of the mathematical model in the form of a regression equation for each layer of the leather semi-finished product.

The experimental results show that the difference in the amount of removed moisture between the layers of the leather semi-finished product under the pressing force of the squeezing rollers $P = 32$ kN/m (**Fig. 2, *a***), $P = 64$ kN/m (**Fig. 2, *b***) and $P = 96$ kN/m (**Fig. 2, *c***) is less than 1 %, which meets the requirement of an allowable deviation (up to 5 %), established in the technology of extracting excess moisture from wet leather semi-finished products. The amount of moisture extracted during simultaneous squeezing of five layers of semi-finished leather from the outer layer (the first layer) of the semi-finished leather product is more than the amount extracted from the remaining subsequent layers of the semi-finished leather, respectively.

The regression equations obtained for the first layer ΔW_1, for the second layer ΔW_2, for the third layer ΔW_3, for the fourth layer ΔW_4, and the fifth layer ΔW_5 of the semi-finished leather product fully describe the dependence of the amount of moisture removed from the semi-finished leather product on the feeding speed and the pressing force between the squeezing rollers since the conditions of the experiment were as close as possible to the production ones. The technological parameters used in the experiment, for example, the feeding speed, the pressing force of the squeezing rollers, and others, will be useful in choosing the rational operating modes of the roller squeezing machine.

In the future, to ensure the best efficiency of the multilayer processing method used in the experiment, it is necessary to work out the conditions for an automatic feed of the processed layers of leather semi-finished product onto the transporting base plate and their automatic removal.

For this, in the future, it is planned to manufacture a full-scale model of the machine and the factors will be investigated taking into account the shortcomings that existed at the laboratory stand for squeezing moisture from semi-finished leather products.

5. Conclusions

For the investigated sample of semi-finished leather of bovine of medium weight after the tanning process for the shoe upper leather, the maximum moisture content in the belly section reached 73 %, and in the butt section it reached 65 %. The residual moisture content in the semi-finished leather product after pressing should be 55–60 %, depending on the leather section and function.

In the case of this experimental study, the residual moisture content should be about 60 %. Therefore, it is necessary to extract another 13 % of moisture when squeezing the semi-finished product in a roll stand.

The results of the experiments showed that it is possible to squeeze the moisture out of five layers of a semi-finished leather product simultaneously: under the pressure of the squeeze rollers of 32 kN/m at a feed rate of up to 0.25 m/s, the productivity of the technological process of the squeezing machine was five times higher; under the pressure of the squeeze rollers of 64 to 96 kN/m and at a feed rate of a five-layer leather semi-finished product of 0.34 m/s, the productivity of the technological process will be about ten times higher, when compared to the productivity of similar squeeze roller machines.

Analysis of experimental results shows that in a five-layer squeezing, the maximum productivity of the roller squeezing machine increases by 500 %. With multilayer squeezing of moisture from semi-finished leather products when they are fed bending over the base plate, the labor and energy costs for the technological process of squeezing in a roller squeezing machine are substantially reduced. Therefore, the technological process of moisture squeezing under consideration is more efficient than the method of single-layer squeezing currently used in production on roller pressing machines.

The method of implementing the technological process of moisture extraction can be used by the developers of new designs of technological machines to remove moisture from various materials, for example, in the textile and pulp and paper industries.

References

[1] Luo, F., Zhong, X., Gao, M., Peng, B., Long, Z. (2020). Progress and mechanism of breaking glycoconjugates by glycosidases in skin for promoting unhairing and fiber opening-up in leather manufacture. A review. Journal of Leather Science and Engineering, 2 (1). doi: https://doi.org/10.1186/s42825-020-00025-0

[2] Danylkovych, A., Bilinskiy, S., Potakh, Y. (2018). Plasticification of leather semifinished chrome tanning using biocatalitic modifier. EUREKA: Physics and Engineering, 1, 12–18. doi: https://doi.org/10.21303/2461-4262.2018.00527

[3] Liu, J., Luo, L., Hu, Y., Wang, F., Zheng, X., Tang, K. (2019). Kinetics and mechanism of thermal degradation of vegetable-tanned leather fiber. Journal of Leather Science and Engineering, 1 (1). doi: https://doi.org/10.1186/s42825-019-0010-z

[4] Danylkovych, A., Lishchuk, V. (2016). An improvement of the technology of manufacturing supple leather through enzymatic plasticizing of a structured semi-finished product. Eastern-European Journal of Enterprise Technologies, 4 (6 (82)), 18–22. doi: https://doi.org/10.15587/1729-4061.2016.73376

[5] Zhang, X., Xu, S., Shen, L., Li, G. (2020). Factors affecting thermal stability of collagen from the aspects of extraction, processing and modification. Journal of Leather Science and Engineering, 2 (1). doi: https://doi.org/10.1186/s42825-020-00033-0

[6] Zhang, Y., Buchanan, J. K., Holmes, G., Mansel, B. W., Prabakar, S. (2019). Collagen structure changes during chrome tanning in propylene carbonate. Journal of Leather Science and Engineering, 1 (1). doi: https://doi.org/10.1186/s42825-019-0011-y

[7] Amanov, A., Bahadirov, G., Amanov, T., Tsoy, G., Nabiev, A. (2019). Determination of Strain Properties of the Leather Semi-Finished Product and Moisture-Removing Materials of Compression Rolls. Materials, 12 (21), 3620. doi: https://doi.org/10.3390/ma12213620

[8] Mehta, M., Naffa, R., Maidment, C., Holmes, G., Waterland, M. (2020). Raman and atr-ftir spectroscopy towards classification of wet blue bovine leather using ratiometric and chemometric analysis. Journal of Leather Science and Engineering, 2 (1). doi: https://doi.org/10.1186/s42825-019-0017-5

[9] Fan, Q., Ma, J., Xu, Q. (2019). Insights into functional polymer-based organic-inorganic nanocomposites as leather finishes. Journal of Leather Science and Engineering, 1 (1). doi: https://doi.org/10.1186/s42825-019-0005-9

[10] Paiva, R. M., Marques, E. A., da Silva, L. F., Vaz, M. A. (2013). Importance of the surface treatment in the peeling strength of joints for the shoes industry. Applied Adhesion Science, 1 (1), 5. doi: https://doi.org/10.1186/2196-4351-1-5

[11] Kagunyu, A. W., Matiri, F., Ngari, E. (2013). Camel hides: Production, marketing and utilization in pastoral regions of northern Kenya. Pastoralism: Research, Policy and Practice, 3 (1). doi: https://doi.org/10.1186/2041-7136-3-25

[12] Preethi, S., Anumary, A., Ashokkumar, M., Thanikaivelan, P. (2013). Probing horseradish peroxidase catalyzed degradation of azo dye from tannery wastewater. SpringerPlus, 2 (1), 341. doi: https://doi.org/10.1186/2193-1801-2-341

[13] Bahadirov, G. A., Sultanov, T. Z., Abdukarimov, A. (2020). Comparative analysis of two gear-lever differential inter-roller transmission mechanisms. IOP Conference Series: Earth and Environmental Science, 614, 012102. doi: https://doi.org/10.1088/1755-1315/614/1/012102

[14] Mavlonov, T., Akhmedov, A., Saidakhmedov, R., Bakhadirov, K. (2020). Simulation modelling of cold rolled metal strip by asymmetric technology. IOP Conference Series: Materials Science and Engineering, 883, 012194. doi: https://doi.org/10.1088/1757-899x/883/1/012194

[15] Bahadirov, G. A., Sultanov, T. Z., Abdukarimov, A. (2020). Kinematic analysis of tooth-lever differential transmission mechanisms. IOP Conference Series: Earth and Environmental Science, 614, 012101. doi: https://doi.org/10.1088/1755-1315/614/1/012101

[16] Khusanov, K. (2020). Stabilization of mechanical system with holonomic servo constraints. IOP Conference Series: Materials Science and Engineering, 883, 012146. doi: https://doi.org/10.1088/1757-899x/883/1/012146

[17] Khusanov, K. (2020). Equations of motion of mechanical systems with nonlinear nonholonomic servoconstraints. IOP Conference Series: Materials Science and Engineering, 869, 072021. doi: https://doi.org/10.1088/1757-899x/869/7/072021

[18] Bahadirov, G., Sultanov, T., Umarov, B., Bakhadirov, K. (2020). Advanced machine for sorting potatoes tubers. IOP Conference Series: Materials Science and Engineering, 883, 012132. doi: https://doi.org/10.1088/1757-899x/883/1/012132

[19] Meistering, M., Stadtler, H. (2020). Stabilized-cycle strategy for a multi-item, capacitated, hierarchical production planning problem in rolling schedules. Business Research, 13 (1), 3–38. doi: https://doi.org/10.1007/s40685-019-0089-3

[20] Farooq, M. A., Nóvoa, H., Araújo, A., Tavares, S. M. O. (2016). An innovative approach for planning and execution of pre-experimental runs for Design of Experiments. European Research on Management and Business Economics, 22 (3), 155–161. doi: https://doi.org/10.1016/j.iedee.2014.12.003

Received date 19.10.2020
Accepted date 12.01.2021
Published date 29.01.2021

Original Research Article: full paper

(2021), «EUREKA: Physics and Engineering»
Number 1

ANALYSIS OF BEHAVIOR IN THE USE OF PLUG-IN HYBRID ELECTRIC VEHICLE AND HYBRID ELECTRIC VEHICLE IN THE TROPICS

Ghany Heryana
Research Center for Advanced Vehicles (RCAVe)[1]
ghany@stt-wastukancana.ac.id

DA Sumarsono
Research Center for Advanced Vehicles (RCAVe)[1]
danardon@eng.ui.ac.id

Mohammad Adhitya
Research Center for Advanced Vehicles (RCAVe)[1]
madhitya@rocketmail.com

Rolan Siregar
Research Center for Advanced Vehicles (RCAVe)[1]
rolansiregar@ft.unsada.ac.id

Nazaruddin
Research Center for Advanced Vehicles (RCAVe)[1]
nazaruddin@eng.unri.ac.id

Fuad Zainuri
Research Center for Advanced Vehicles (RCAVe)[1]
fuad.zainuri@mesin.pnj.ac.id

Sonki Prasetya
Research Center for Advanced Vehicles (RCAVe)[1]
sonki.prasetya@mesin.pnj.ac.id

[1]Faculty of Engineering Universitas Indonesia Depok
West Java, Indonesia, 16424

Abstract

This research aims to determine the pattern of Plug-In Hybrid Electric Vehicle (PHEV) usage and fuel consumption for the Jakarta metropolitan area, which includes the cities of Depok, Bogor, Tangerang, Bekasi, and Jakarta itself. Tests were carried out for approximately three months, with regular use. Other types of vehicles for comparison are the Internal Combustion Engine (ICE) and Hybrid Electric Vehicle (HEV) units. Fuel consumption data and vehicle usage patterns are acquired from data loggers. Economic studies are carried out in a simulation that involves the price of a vehicle, a battery, maintenance costs, and fuel prices. The results show that the best PHEV fuel consumption is for the range of 55–80 km, which is 35–40 km/liter. When compared with HEV, PHEV fuel consumption is 30 % more efficient. HEV's best fuel consumption is 22 km/liter. The ICE is far behind with 11 km/liter. However, looking at the economic side, it can be concluded that the price of PHEV is still challenging to reach for the middle class. PHEV is still classified as a luxury car for Indonesia. Assuming the amount of fuel is IDR 9,850/liter, and the vehicle service life is set at ten years, the energy cost for PHEV is around IDR 4,400–IDR 6,000/km. It is higher compare with the energy cost for a conventional car that is around IDR 3,400–IDR 3,900/km. PHEV buyers must receive incentive support from the government, not only at the time of purchase (zero tax) but also for maintenance costs and battery replacement. Indonesia has long experience in manufacturing ICE vehicles. Opening an electric vehicle industry is a strategic solution to reduce the price of these vehicles. The import tax for vehicles in Indonesia is quite high.

Keywords: Electric Vehicle, PHEV, Plug-In Hybrid Electric Vehicle, Power Consumption, Hybrid Electric Vehicle, HEV, Internal Combustion Engine.

DOI: 10.21303/2461-4262.2021.001617

1. Introduction

Research on the close relationship between economic growth and increased air pollution has been carried out for China and South Korea, and in general, the results are directly proportional [1]. The results of this research must be noted for other cities in the world. It can't be avoided except with a policy of reducing or prohibiting the use of ICE vehicles.

As the epicenter of an economy, Jakarta has become overcrowded by vehicle traffic activities. Congestion always occurs almost every hour of the workday, even on weekends. The number of ICE of more than 4 million certainly causes significant air pollution.

The PHEV success is if the population of its use continues to increase and is proven to reduce air pollution significantly [2]. In a specific range, if the SOC is 100 %, the BEV feature can be used in the city when going to the office until returning home [3]. A review of how big the ideal battery size for PHEV in Beijing had been carried out. In that study, the results showed that the PHEV battery suitable for use in the city of Beijing was 6–8 kWh [4], as well as in the United States and the European Union [5]. Similar research that aims to improve the performance of BEV on PHEV was to set the pattern on/off battery charging. As a result, the use of fuel was more efficient, around 17.3 % compared to the existing algorithm [6]. Other studies were strategies for optimizing energy management showed a significant increase in fuel efficiency and a longer battery life [7, 8]. Other efforts from the researchers to extend battery life are also carried out with the Intelligent Double-Layer Control Scheme [9].

Planning a trip route is also not spared into research related to improving PHEV performance. The travel expense estimation model was designed for this [10]. Maintaining the temperature of the battery is also proven to be able to optimize the battery's output power and extend its service life as well. The dynamic program method is used to solve the problem. And the research results showed significant benefits [11]. One crucial parameter that is considered by the buyers is the efficient use of fuel. Of the nine settings, one of the economic considerations of PHEV is fuel consumption to curb weight [12]. Research into the sensitivity of fuel used in conventional vehicles and hybrid vehicles linked to driving behavior was also conducted in the United States [13]. Research on the utility of using PHEV was also carried out in California. The results showed that UF of PHEV for short distances (less than 20 miles or 32 km) is very low [14].

The relevance of this research is to provide an overview and data on the development direction of electric vehicles in tropical countries, especially Indonesia. Until now, the manufacture of electric vehicles is still quite expensive. This is not only because the population of electric vehicles is still small, but also because of the addition of a battery which is still one of the most expensive parts of electric vehicles.

The transition from hybrid vehicles to fully electric vehicles will be crucial. Thus, data on the behavior of using electric vehicles is needed so that the determination of the capacity of the components will not be over or under. The hope is that the vehicle will still have good quality but at an affordable price for the middle class.

The more specific research objectives of this research are to determine the behavior and the average distance traveled by the vehicle during use in the weekday. This data will be developed to become a reference called the «drive cycle». Drive cycle is needed as the main data in the design simulation of vehicle power and torque capacity, in this case electric vehicles. This data is also needed to determine where the charging station should be built and what is its power capacity.

2. PHEV Technology

In designing a vehicle, considerations related to the maximum speed, acceleration, vehicle weight, load weight, aerodynamic drag, rolling resistance, and incline angle. Vehicle Longitudinal Dynamic Model can be solved by several equations; one of them is below eq. (1) [10, 15]:

$$P_{req}(t) = \left(m \cdot a + \frac{1}{2} \cdot \rho \cdot C_D \cdot A \cdot v(t)^2 + m \cdot g \cdot \sin\alpha + f_{rl} \cdot m \cdot g \right) \cdot v(t), \quad (1)$$

where P_{req} = power requirement; A = Frontal area; m = mass; v = velocity; a = acceleration; g = gravity; ρ = density of fluid (air); α = elevation angle; C_D = Drag coefficient; f_{rl} = rolling resistant.

For micro conditions that determine actual road conditions, more complex equations are necessary [16].

PHEV consists of 3 types, namely serial, parallel, and serial-parallel. In the parallel PHEV type, ICE and electric motors are mechanically connected to the gearbox. The torque can be calculated by eq. (2) [10]:

$$T_{wheel}(t) = T_{fuel\_path}(t) + T_{ele\_path}(t). \quad (2)$$

The PHEV serial type has only one vehicle driving power source, namely an electric motor as the main drive. The torque can be calculated by eq. (3):

$$T_{wheel}(t) = T_{ele\_path}(t), \quad (3)$$

where T_{wheel}=wheel torque; T_{fuel_path}=torque from ICE; T_{ele_path}=torque from electric motor.

The concept of serial/parallel PHEV (**Fig. 1**) is like a combination of serial types and parallel types. ICE and electric motors have a mechanical connection to the gearbox. ICE is also connected in such a way to the generator as a battery charger. ICE and electric motors can distribute mechanical power independently or in conjunction. The Prius PHEV is a vehicle that has successfully implemented a serial/parallel hybrid quite well.

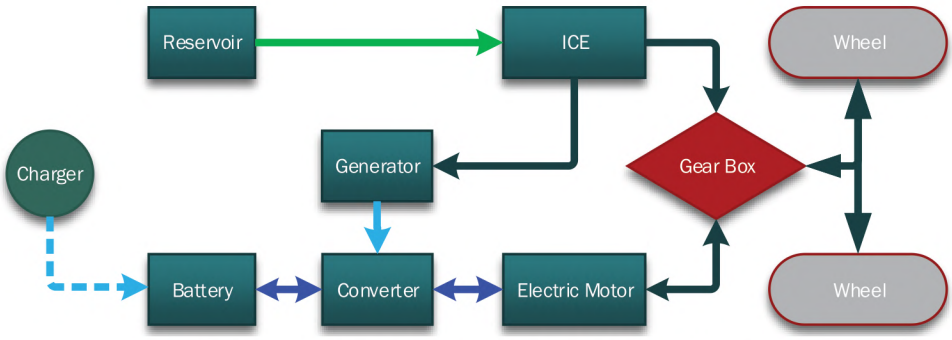

Fig. 1. Serial/Parallel Plug-In Hybrid Electric Vehicle

The total power requirements can be calculated by eq. (4):

$$P_{total}(t) = P_{PM}(t) + P_{EPS}(t) + P_{AC}(t) + P_{PW}(t) + P_{wipers}(t) + P_{accesories}(t), \quad (4)$$

where P_{total}=total power requirement; P_{PW}=power window power; P_{PM}=prime motor power; P_{wipers}=wipers power; P_{EPS}=electric power steering power; $P_{accessories}$=accessories power; P_{AC}=air conditioner power.

$$E_{battery} = V_{battery} \cdot Ih_{battery}, \quad (5)$$

where $E_{battery}$=power of battery; $V_{battery}$=voltage of battery; Ih_{batery}=battery current capacity.

Battery energy capacity is the multiplication of voltage (V) with the current hour (Ih) (eq. (5)).

3. Methods

This study involved six vehicles and six drivers with different driving behavior. The testing is carried out for three months. Similar research has been carried out in the North American area [17], but with a particular PHEV unit. On paper, in theory, PHEV will undoubtedly excel in terms of fuel efficiency, but how much superior is something else that must be tested quantitatively.

Each driver was asked to use the vehicle regularly daily, that is, from the place of residence to the office and back home. It is coupled with other goals that become his/her behavior. The testing

time is approximately three months. Especially for PHEV, there are additional regulations, namely charging at the office up to 100 % SOC. The charging mode is not explicitly set. A Standard or fast charging mode could be used. Other behaviors return to the driving style of each volunteer. The fuel used is determined using RON92.

The data is processed to determine the pattern of vehicle usage in Jakarta, fuel consumption, and overall efficiency.

4. Results and Discussion

4. 1. PHEV Fuel Economy and Driving Distance

Fig. 2 shows the efficiency of using PHEV fuel with regular use in the Jakarta area and its satellite cities. It appears that the highest efficiency of fuel use was in the range of 50–60 km. The efficiency continued to decline at a distance of more than 60 km. After that, the PHEV will operate as HEV. The best efficiency can reach more than 70 km/liter. The level of SOC is very influential in this result.

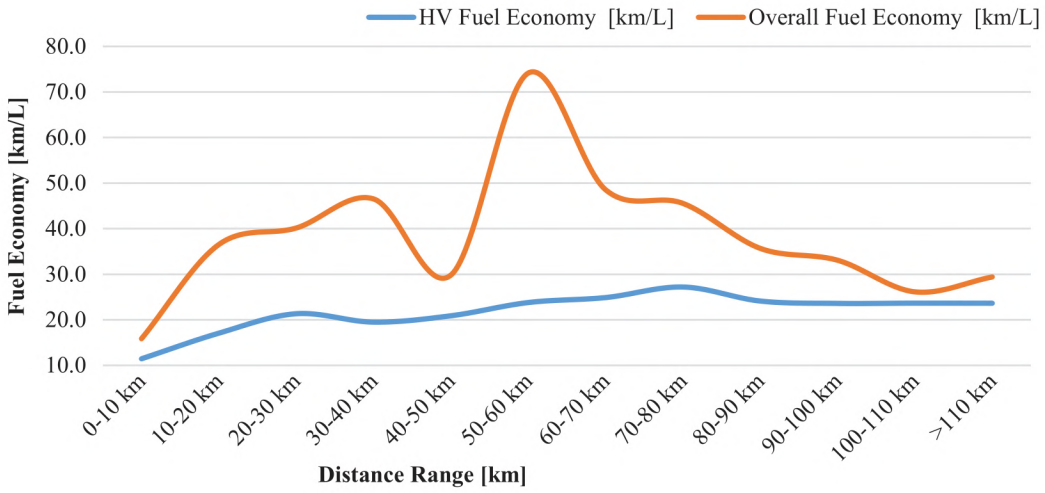

Fig. 2. Fuel Efficiency of PHEV base on the distance range

From **Fig. 3**, it can be seen that in the range of 30–40 km and 50–60 km, the use of electrical energy was higher than the fuel consumption. If the mileage were more than 60 km, the HV feature would tend to be dominant. Still in the graph [*b*], after a distance of more than 50 km, the battery capacity for the BEV mode had run out.

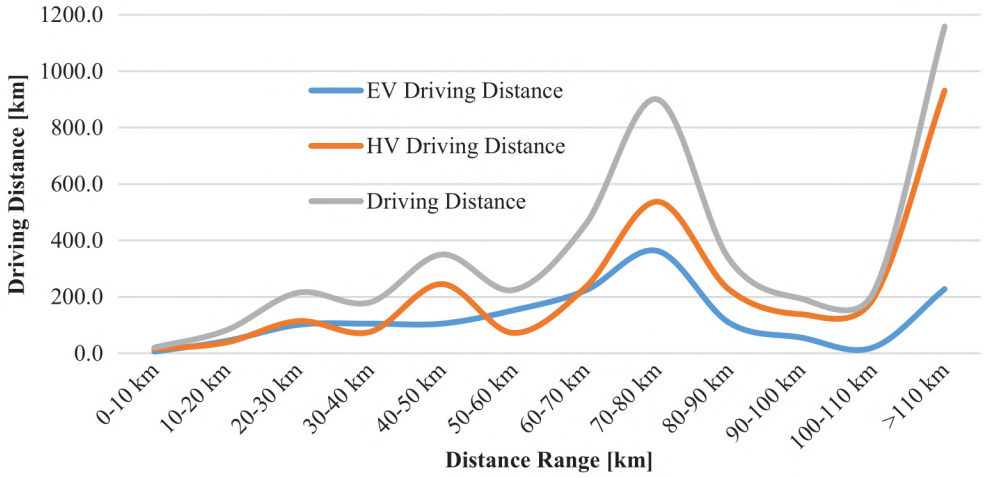

Fig. 3. The tendency of PHEV uses base on the distance range

In PHEV, the efficiency of fuel use can be increased or dropped dramatically. It is influenced by the frequency of the plug-in charging and the SOC level. It is a sampling form 1 of 2 PHEV units used as test vehicles.

4. 2. PHEV Energy and Power Consumption for Air Conditioner

Fig. 4 is the result of testing AC power consumption over a set period.

Fig. 5 shows the AC capacity needed at certain hours. Thus, for areas such as Jakarta, for sedan vehicles, cabin AC capacity is required around 1 kW.

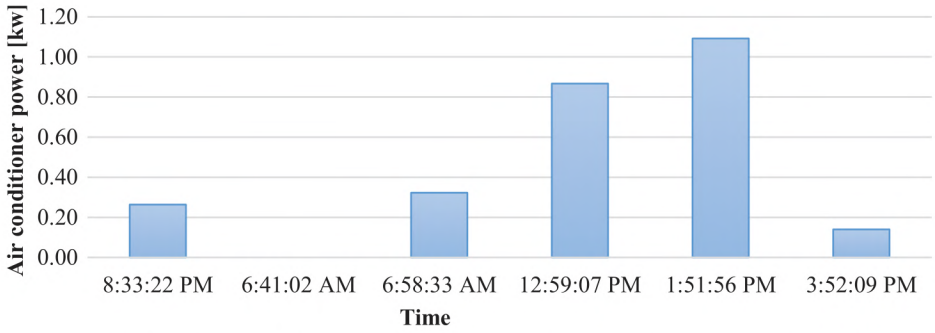

Fig. 4. Electric Vehicle vs. Air Conditioner Energy Consumption in PHEV

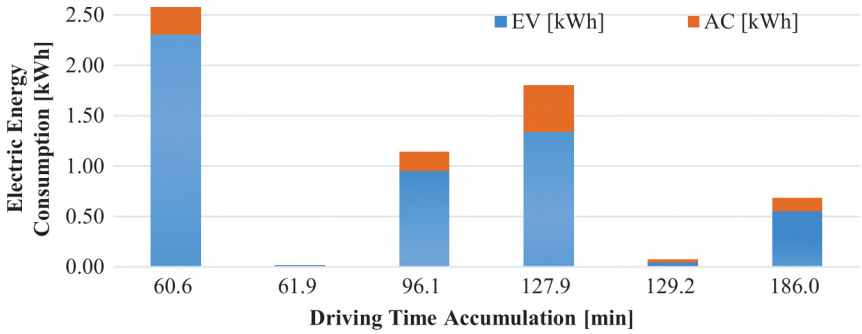

Fig. 5. Air Conditioner Power Consumption of PHEV base on what time it uses

4. 3. Resume Behavior Driving Data

HEV has better fuel efficiency compared to ICE. Its consumption is in the range of 20 km/liter (**Fig. 6**). There is no surge in fuel efficiency at HEV. It is because the battery capacity is limited, and there is no other source of charge for the battery apart from the energy available in the vehicle itself.

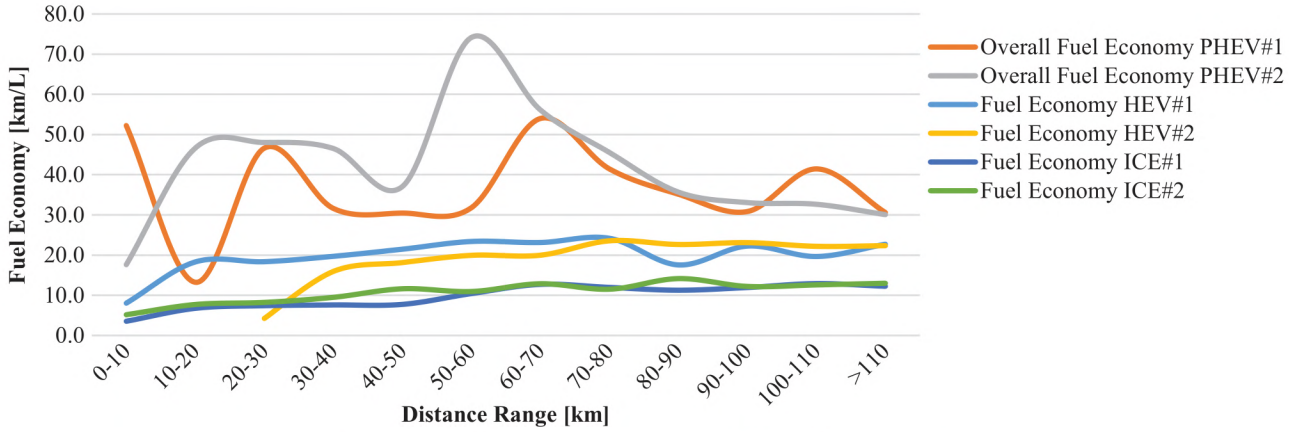

Fig. 6. Fuel Eff. comparison among PHEV, HEV, and ICE

The surge in fuel economy in the PHEV group shows that efficiency can still be increased continuously by improving driving behavior.

Fig. 7 provides an overview of driving behavior based on distance traveled. It appears that the driver range is dominant at 50–80 km. A distance of more than 100 km is if the driver travels out of town.

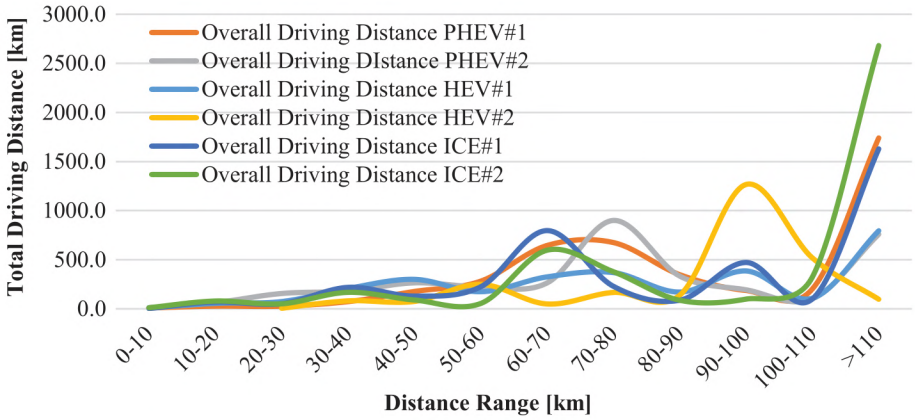

Fig. 7. Total Driving Distance comparison among PHEV, HEV, and ICE

Quantitative data can be found in the table below. From here it can be observed and analyzed in more detail for each vehicle. Both PHEVs consume far less fuel in all (**Table 1**).

Table 1
Resume of vehicle fuel consumption on regular using in Jakarta

Car Code	PHEV #1	PHEV #2	HEV #1	HEV #2	ICE #1	ICE #2
Number of days [day]	55	62	49	61	58	57
Driving time [minute]	10.904	9.373	8.153	11.965	11.226	11.807
Number of Charge [times]	51	32	N/A	N/A	N/A	N/A
Average Number of Charge [day/charge]	1.08	1.94	N/A	N/A	N/A	N/A
Average mileage [km/day]	79.89	55.66	60.74	71.67	69.22	81.10
Driving Distance [km]	4.393	3.450	2.976	4.371	4.014	4.622
Fuel Consumption [liter]	125.79	87.25	137.25	197.30	355.64	375.05
Average Fuel Economy [km/liter]	34.93	39.55	21.69	22.16	11.29	12.32
Average HV Fuel Economy [km/liter]	23.59	24.02	N/A	N/A	N/A	N/A
HV Driving Distance [km]	2.967	2.095	N/A	N/A	N/A	N/A
EV Driving Distance [km]	1.425	1.354	N/A	N/A	N/A	N/A

ICE drains almost three times that of PHEV. Regulations in Indonesia consider the amount of tax based on fuel consumption/km. Temporary conclusion, PHEV has an excellent opportunity to get tax incentives because of its fuel consumption.

4. 5. Feasibility of PHEV

Charging time required for Prius PHEV up to 100 % SOC is 3 hours, with 2.3 kW of power. So the energy should be 6.9 kWh (**Table 2**). In Indonesia, for that power, the home electricity

should be at 3500–5500 kVA class. It is the upper middle segment. The energy cost for that segment is IDR 1467.28/kWh.

Table 2
Power requirement and unit cost for energy

Charging Data	Value	Remark
Charging time (hour)	3	[18]
Charging power (kW)	2.3	[18]
Charging energy (kWh)	6.9	–
Energy Cost	–	–
Charging cost (IDR/kWh)	1467.28	[19]
Gasoline Price (IDR/liter) (RON 92)	9850	[20]

Base on **Table 2**, the ideal house to be fitted with a 2.3 kW capacity charger is one that has a minimum of 15 A or 3300 watts of electric power.

5. Discussion of Experimental Results

The results of this experiment show that there is still a lot of energy wasted from ICE which can be reused. And the combination of ICE with EV is one solution. This research is sufficient to provide a big picture that there will be fuel savings with the combination of these engines.

In addition, the data show that from the experimental results, the average distance traveled per day is around 50–60 km (**Table 1**). AC is always on.

Thus the battery capacity is less than or more than that will make vehicle performance not optimal. From the distance divided by time, it is known that the vehicle is in the speed range of 15–50 km/h. This will be the material for determining the motor power which does not need to be too large. The smaller the motor power, the smaller the battery consumption, and the farther the distance that can be achieved. With this drive cycle, acceleration and high speed are not the main things.

For the purposes of driving in the city, electric vehicles are designed to cover a distance of only about 50 km. Longer distances can be accommodated by offering a larger battery capacity. The main driving comfort facilities are air conditioners and entertainment devices. The main motor power of 10 KW is sufficient. Thus the battery capacity does not need to be too large. Component prices could be reduced if they could be manufactured in Indonesia. This is to reduce import taxes and to increase local and domestic content. For the quality of vehicle manufacturing, Indonesia has proven to have quite a good experience, both in terms of cost, quality and delivery. This has become Indonesia's main strength to produce and develop its own electric vehicles. Reasonable prices for HEV vehicles are affordable for the lower middle class, namely in the LCGC class (low cost green car), under 250 million rupiah.

However, this study still has shortcomings related to the number and types of vehicles sampled. This is because the pollution of electric vehicles in Indonesia is not as high as in developed countries. This study also has not been able to project how fuel efficiency will be if the vehicle has passed its useful life. Then it is necessary to research the waste battery that has been damaged. To find out the life of the battery, a discharge test is necessary.

6. Conclusions

Research and development of PHEV are still very strategic for the next decade or more. When the BEV era emerged, PHEV will not just disappear.

The fuel efficiency of PHEV is quite good, but it is still very possible to be improved if battery technology continues to develop until higher battery densities are found.

Marketing PHEV in a country is ideal when considering the driving behavior of its population. Also, traffic and climate conditions are essential to be taken into account.

To encourage the purchase of PHEV, in addition to determining the right PHEV specifications for Indonesia, also with government policies in reducing PHEV and BEV taxes, as well as providing other incentives.

The construction of PHEV factories in Indonesia can reduce the selling price of vehicles.

To target the lower middle class, the price of vehicles less than 250 million rupiah is expected to make the development of electric vehicles grow rapidly. The electric vehicle feature in Indonesia doesn't need to be too sophisticated. The only standard comfort needed is air conditioner and entertainment equipment. The motor power of about 50 kw can be reduced to just 10 kw.

Acknowledgments

The authors acknowledge the financial support from the KEMENTERIAN RISET DAN TEKNOLOGI/BADAN RISET DAN INOVASI NASIONAL (RISTEKDIKTI) for Penelitian Dasar Unggulan Perguruan Tinggi (PDUPT) Grant through Contract No. NKB-63/UN2.RST/HKP.05.00/2020 and PUTI UI (Publikasi Terindex Internasional Universitas Indonesia) Contract No. NKB-643/UN2.RST/HKP.05.00/2020.

References

[1] Jiang, M., Kim, E., Woo, Y. (2020). The Relationship between Economic Growth and Air Pollution – A Regional Comparison between China and South Korea. International Journal of Environmental Research and Public Health, 17 (8), 2761. doi: https://doi.org/10.3390/ijerph17082761

[2] Frey, H. C., Zheng, X., Hu, J. (2020). Variability in Measured Real-World Operational Energy Use and Emission Rates of a Plug-In Hybrid Electric Vehicle. Energies, 13 (5), 1140. doi: https://doi.org/10.3390/en13051140

[3] Heryana, G., Prasetya, S., Zainuri, F., Adhitya, M., Sumarsono, D. A., Nazaruddin, Siregar, R. (2020). Plug in hybrid electric vehicle power consumption analysis in tropical area. International conference on emerging applications in material science and technology: ICEAMST 2020. doi: https://doi.org/10.1063/5.0003756

[4] Hou, C., Wang, H., Ouyang, M. (2014). Battery Sizing for Plug-in Hybrid Electric Vehicles in Beijing: A TCO Model Based Analysis. Energies, 7 (8), 5374–5399. doi: https://doi.org/10.3390/en7085374

[5] Kamguia Simeu, S., Brokate, J., Stephens, T., Rousseau, A. (2018). Factors Influencing Energy Consumption and Cost-Competiveness of Plug-in Electric Vehicles. World Electric Vehicle Journal, 9 (2), 23. doi: https://doi.org/10.3390/wevj9020023

[6] Lee, S., Choi, J., Jeong, K., Kim, H. (2015). A Study of Fuel Economy Improvement in a Plug-in Hybrid Electric Vehicle using Engine on/off and Battery Charging Power Control Based on Driver Characteristics. Energies, 8 (9), 10106–10126. doi: https://doi.org/10.3390/en80910106

[7] Liu, Y., Li, J., Ye, M., Qin, D., Zhang, Y., Lei, Z. (2017). Optimal Energy Management Strategy for a Plug-in Hybrid Electric Vehicle Based on Road Grade Information. Energies, 10 (4), 412. doi: https://doi.org/10.3390/en10040412

[8] Nazaruddin, N., Zainuri, F., Siregar, R., Heryana, G., Adhitya, M., Sumarsono, D. (2019). Electric power steering: an overview of dynamics equation and how it's developed for large vehicle. IOP Conference Series: Materials Science and Engineering, 673, 012112. doi: https://doi.org/10.1088/1757-899x/673/1/012112

[9] Rahbari, O., Omar, N., Van Mierlo, J., A. Rosen, M., Coosemans, T., Berecibar, M. (2019). Electric Vehicle Battery Lifetime Extension through an Intelligent Double-Layer Control Scheme. Energies, 12 (8), 1525. doi: https://doi.org/10.3390/en12081525

[10] Zhang, Y., Chu, L., Fu, Z., Xu, N., Guo, C., Li, Y. et. al. (2017). An Economical Route Planning Method for Plug-In Hybrid Electric Vehicle in Real World. Energies, 10 (11), 1775. doi: https://doi.org/10.3390/en10111775

[11] Shojaei, S., McGordon, A., Robinson, S., Marco, J. (2017). Improving the Performance Attributes of Plug-in Hybrid Electric Vehicles in Hot Climates through Key-Off Battery Cooling. Energies, 10 (12), 2058. doi: https://doi.org/10.3390/en10122058

[12] Baodi Zhang, Fuyuan Yang, Lan Teng, Minggao Ouyang, Kunfang Guo, Weifeng Li, Jiuyu Du (2019). Comparative Analysis of Technical Route and Market Development for Light-Duty PHEV in China and the US. Energies, 12 (19), 3753. doi: https://doi.org/10.3390/en12193753

[13] Thomas, J., Huff, S., West, B., Chambon, P. (2017). Fuel Consumption Sensitivity of Conventional and Hybrid Electric Light-Duty Gasoline Vehicles to Driving Style. SAE International Journal of Fuels and Lubricants, 10 (3). doi: https://doi.org/10.4271/2017-01-9379

[14] Srinivasa Raghavan, S., Tal, G. (2019). Influence of User Preferences on the Revealed Utility Factor of Plug-In Hybrid Electric Vehicles. World Electric Vehicle Journal, 11 (1), 6. doi: https://doi.org/10.3390/wevj11010006

[15] Heryana, G., Prasetya, S., Adhitya, M., Sumarsono, D. A. (2018). Power consumption analysis on large-sized electric bus. IOP Conference Series: Earth and Environmental Science, 105, 012041. doi: https://doi.org/10.1088/1755-1315/105/1/012041

[16] Edie, L. C. (1961). Car-Following and Steady-State Theory for Noncongested Traffic. Operations Research, 9 (1), 66–76. doi: https://doi.org/10.1287/opre.9.1.66

[17] Boston, D., Werthman, A. (2016). Plug-in Vehicle Behaviors: An analysis of charging and driving behavior of Ford plug-in electric vehicles in the real world. World Electric Vehicle Journal, 8 (4), 926–935. doi: https://doi.org/10.3390/wevj8040926

[18] Toyota Prius Plug-in Hybrid (Typ 1). Available at: https://www.mobilityhouse.com/int_en/electric-cars/toyota/toyota-prius-plug-in-typ1.html#toyota-prius-hybrid-type1-charging-information

[19] Daftar Tarif Listrik Terbaru 2021 Kementerian ESDM [Harga kWh]. Available at: https://lifepal.co.id/media/daftar-tarif-listrik-terbaru/

[20] Harga BBM: Pertalite, Premium, Pertamax, dan Pertamax Turbo. Available at: https://www.otosia.com/berita/harga-pertalite-premium-pertamax-dan-pertamax-turbo-mei-2018-kln.html

Received date 25.11.2020
Accepted date 21.01.2021
Published date 29.01.2021

Original Research Article: full paper

(2021), «EUREKA: Physics and Engineering»
Number 1

SATURATION OF GLASS PARTICLES WITH METAL DURING SINTERING OF A COMPOSITE MATERIAL OF THE IRON-CAST IRON-GLASS SYSTEM

Tahir Gaffar Jabbarov
Department of Mechanical and Materials Science Engineering[1]
tahir196041@gmail.com

Jamaladdin Nuraddin Aslanov
Department of Oil and Gas Equipment[1]
camaladdin.aslanov@asoiu.edu.az

Rafiga Sakhavat Shahmarova
Department of Mechanical and Materials Science Engineering[1]
shahmarova_1970@mail.ru

[1]*Azerbaijan State Oil and Industry University*
16/21 Azadlıq str., Baku, Azerbaijan, Az 1010

Abstract

Sintering of multicomponent systems is characterized by a number of features, consisting in the fact that sintering of dissimilar materials is a complex eutectic process. Along with self-diffusion, which causes the transfer of mass to the contact area of the particles, there is mutual diffusion, which ensures the homogenization of the composition by equalizing the concentrations of unlike atoms within the sample. Under conditions of limited solubility or complete insolubility of the components, sintering of the system is complicated by the isolation of homogeneous particles from mutual contact, hindering self-diffusion and thereby worsening the sintering conditions.

The saturation of particles of vacuum glass brand S88-5 (GOST 11.027.010-75, Russia) and glass «Pyrex» (TS, Russia), which are part of iron and «iron-cast iron glass» materials, depending on the sintering temperature, has been studied.

To improve the interfacial interaction, and, consequently, to increase the mechanical and tribotechnical properties of powdered iron-glass materials, the effect of the glass melting temperature on the saturation of glass with metal was investigated. The dependences of the content of base metal and silicon ions in glass on the sintering temperature are plotted. The effect of the glass melting temperature on increasing the saturation of glass with metal is predicted.

The saturation of the glass with the base metal depends on the viscosity of the glass at sintering temperatures and is accompanied by an increase in microhardness and refractive indices up to 1.2 times compared to the initial state of the glass.

The microhardness of particles of vacuum glass of grade S88-5 after sintering of metal-glass samples increases noticeably than in samples with Pyrex glass.

When sintering «iron-cast iron-glass» materials, the metal base is saturated with silicon, which leads to an increase in the hardness of iron up to 1.8 times.

Keywords: interdiffusion, sintering, pressing, composite material, sitall, glass saturation, microhardness, viscosity.

DOI: 10.21303/2461-4262.2021.001619

1. Introduction

During sintering of metal-glass materials, glass is sitalized [1] and it is necessary to develop such modes of glass that would ensure crystallization in the entire volume of glass inclusions, which contributes to an increase in the strength of the material [2]. In addition, when glass is in contact with iron for a long time in the temperature range 1000–1200 °C, the glass becomes greenish, which indicates its saturation with iron [3].

To improve the mechanical properties and wear resistance of iron of glass materials obtained by cold pressing with subsequent sintering in a protective environment, it is necessary to add components that have better glass wettability to the composition of the charge [4]. The use of cast iron powder as part of the charge leads to such an effect [5]. Since cast iron contains a relatively large amount of silicon and manganese, which, during heating, form corresponding hardly reducible oxides, which improve the wettability of the metal frame with glass during sintering [6].

Saturation of glass is accompanied by an increase in the refractive index [7], and under certain conditions, a crystalline phase may appear in it, which includes ions of iron and other metals [8].

In sintered metal-glass materials, glass particles are surrounded by metal on all sides, which creates favorable conditions for saturation with metal oxides [9]. With an increase in the sintering temperature, the glass becomes more fluid, the contact area between the metal and the glass increases, and, consequently, the possibility of saturating it with metal oxide increases [10].

2. Materials and methods of research

The saturation of particles of vacuum glass grade S88-5 (GOST 11.027.010-75, Russia) and glass «Pyrex» (TS, Russia), which are part of iron and «iron-iron glass» materials, depending on the sintering temperature, has been studied.

The metal basis of the samples used for the study consisted of: powders of iron, gray cast iron obtained by grinding, as well as stearic acid zinc for the perfumery and cosmetic industry. Iron powder grade PZhRV 2.200.28 (GOST 9849-86, Sulin) was used in a fineness of – 160+50 μm. Cast iron powder of grade SCh – 20 obtained by mechanical grinding had a fineness of – 100+50 μm. The sizes of glass particles were in the range of – 100+50 μm, and the amount of glass and cast iron was 6 and 30 % (by weight), respectively. To improve the compressibility of charge materials, stearic acid zinc for the perfumery and cosmetic industry was used – grade «Ch» (TU 6-09-4473-77, Russia), in an amount of 1.0 % (by weight) [7].

Samples with dimensions 55×10×10 mm were pressed on a hydraulic press model HPM-100S (Russia) at a constant pressing pressure of 1000 MPa. Glass-metal specimens with a porosity of 8–16 % were sintered in the temperature range 1000–1200 °C for 1 hour in an endothermic gas environment in a continuous furnace.

The microhardness of glass particles was investigated using a PMT-3 microhardness meter. The weight of 50 g was selected in such a way that glass cracking did not occur when measuring microhardness. On each sample, sintered at a certain temperature, 30 measurements of microhardness were carried out and the percentage composition of the obtained values was determined.

3. Results and discussion

In the process of sintering of powdered iron-glass materials, the bond between the metal base and the glass phase is improved.

To study the saturation degree of the glass, X-ray microanalysis, the petrographic method, and the method of measuring the microhardness were used.

By the method of micro-X-ray spectral analysis when comparing the intensities of the excited rays in the samples and standards, the average content of saturated metal and silicon in glass particles that were part of iron-glass, iron-cast iron-glass materials was determined (**Fig. 1**).

With increasing sintering temperature, the color of glass particles in the samples changed. In the iron-glass with vacuum glass of the S88-5 grade – from colorless to green, and in the iron-glass with Pyrex glass – to black. In the «iron-glass» ones with vacuum glass of the S88-5 brand – up to light green, and in the «iron-glass» ones with «Pyrex» glass – up to violet. The change in the color of the glass particles indicated its saturation with metal ions (**Fig. 1**).

Fig. 2, 3 show the change in the content of base metal ions and silicon in glass from the sintering temperature. With its increase, the saturation with a metal increases, and a direct relationship is seen between the saturation of glass with a metal and the affinity of this metal for oxygen. The most saturated particles are particles with vacuum glass of grade S88-5 (**Fig. 2**), the least – with glass «Pyrex», which were part of the «iron-cast iron-glass» samples.

The saturation of glass with metal is significantly affected by the melting temperature of the glass. Thus, in metal-glass samples with Pyrex glass, the saturation of glass particles with metal and a decrease in the silicon content is less intense than in vacuum glass of S88-5 grade. This is due to the fact that Pyrex glass at the same temperatures has a higher viscosity [11] than glass of grade S88-5, due to which the contact between the metal and glass deteriorates, the mobility of the glass decreases. In addition, with an increase in the sintering temperature, the content iron in the matrix decreases and silicon increases.

An increase in the silicon content in the matrix indicates that with an increase in the sintering temperature (especially at 1150–1200 °C), the matrix is saturated with glass components. In turn, the glass is saturated with iron, that is, mutual diffusion occurs between the matrix and the glass phase.

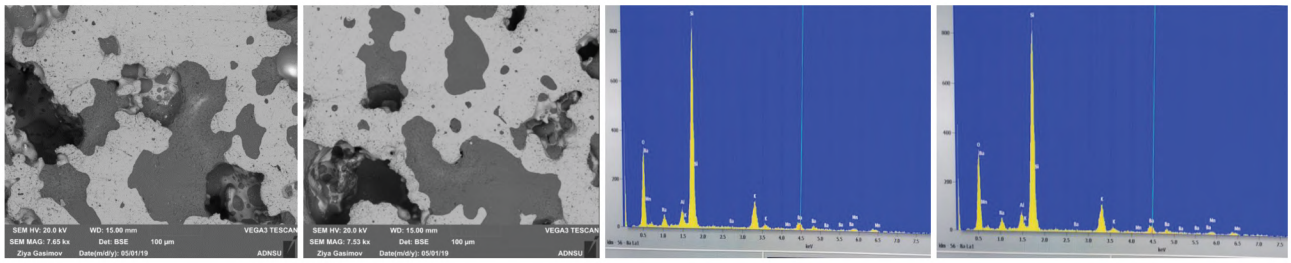

a *b* *c* *d*

Fig. 1. The average content of saturated metal and silicon in glass particles that were part of iron-, «iron-cast iron-glass» materials: *a*, *b* – iron-glass; *c*, *d* – «iron-cast iron-glass»

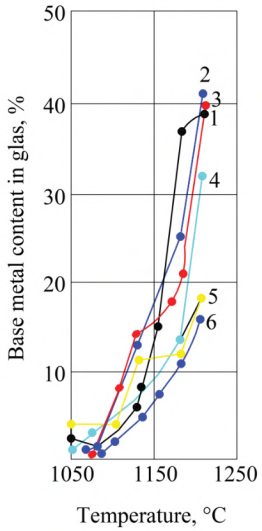

Fig. 2. Changes in the iron content in glass, depending on the sintering temperature of metal-glass samples: 1, 2, 3 – iron cast with vacuum glass of grade S88-5; 4, 5, 6 – iron-cast iron with Pyrex glass

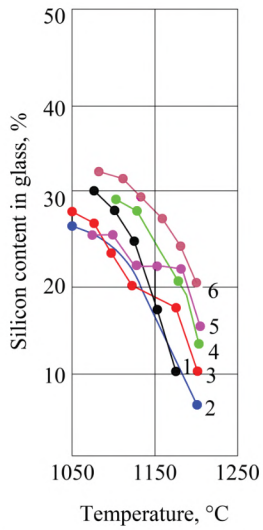

Fig. 3. Changing the silicon content in glass, from the sintering temperature of metal-glass samples: 1, 2, 3 – iron-cast iron with Pyrex glass; 4, 5, 6 – iron-cast iron with vacuum glass, grade S88-5

For the construction of graphic images (**Fig. 2, 3**), particles of approximately the same size were selected. When the size of the glass particle changes, its saturation with the base metal also changes. For example, in iron-glass samples with Pyrex glass sintered at a temperature of 1150 °C, an increase in the size of a glass particle by 1.5 times led to a drop in the iron content from 9 to 5 %.

Usually towards the edge of the glass particle, the saturation metal content increases. In addition, even at temperatures of 1000–1050 °C, crystals of precipitating metals are noticeable in the glass. Consequently, the glass is no longer homogeneous in chemical composition.

Fig. 4 shows the determination of the refractive indices of glass particles that were part of the sintered samples. At a temperature of 1050 °C in iron-glass specimens with glass of grade S88-5, the refractive index ranges from 1.514 to 1.523; at 1150 °C from 1.521 to 1.537; at 1200 °C from 1.529 to 1.580. Apparently, glass with a low refractive index corresponds to those areas of the particle where minerals are released. In general, an increase in the sintering temperature of metal-glass samples with S88–5 glass leads to an increase in refractive indices (**Fig. 4**).

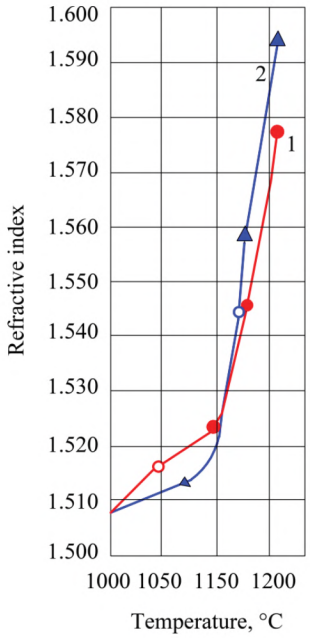

Fig. 4. Change in the refractive index of vacuum glass of grade C88-5 from the sintering temperature of metal-glass materials: material: 1 – iron-glass, 2 – «iron-cast iron-glass»

In samples with Pyrex glass (**Fig. 5**), an increase in the refractive index is observed in iron and iron-cast iron-glass samples up to a certain limit (1150 °C), then the refractive index of the glass decreases. The drop in the refractive index in the samples sintered at temperatures above 1150 °C is obviously associated with the intense crystallization of the glass. In iron-glass samples sintered at a temperature of 1250 °C, it was not possible to measure the refractive index, since non-crystallized glass could not be separated from the sample.

Most of the minerals released in glass during sintering of metal-glass minerals have a higher hardness than glass. For example, the microhardness of quartz is 10230–12360 MPa; magnetite – 5350–6950 MPa; fayalite Fe_2SiO_4 – 6890–7480 MPa, etc. [12]. Consequently, the release of minerals should affect the microhardness of the particles that make up the sintered metal-glass materials. **Table 1** shows the limits of the microhardness of the glass phase of the samples sintered at temperatures from 1000 to 1200 °C.

From the **Table 1** it is possible to see that with an increase in the sintering temperature, the spread of microhardness values increases and in all samples a tendency to an increase in microhardness is observed. The microhardness of the glass phase of samples with S88-5 glass increases especially. In iron-glass specimens sintered at 1200 °C, 17 % of all measurements fall on areas

with a microhardness of 10780 MPa and 29 % on areas of microhardness (7430 MPa) are almost twice as high as that of the original glass.

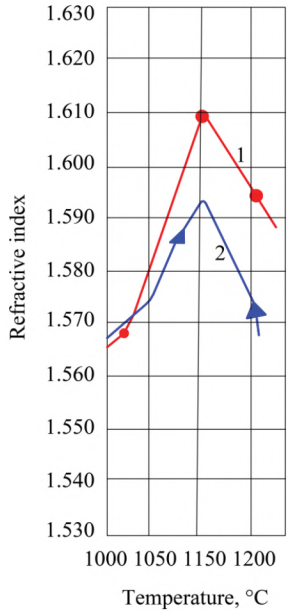

Fig. 5. Change in the refractive index of Pyrex glass from the sintering temperature of metal-glass materials: material: 1 – iron-glass, 2 – «iron-cast iron-glass»

Table 1

Limits of microhardness of the glass phase of the samples

No.	Sintering temperature, °C	Microhardness of the glass phase in materials, MPa							
		with glass of C88–5 brand				with glass of «Pyrex» brand			
		iron-glass		iron-cast iron-glass		iron-glass		iron-cast iron-glass	
		from	to	from	to	from	to	from	to
1	1000	4280	6360	3890	5776	3420	7030	3480	5200
2	1050	4980	7430	4540	6360	4800	6380	3400	5000
3	1150	3800	8400	4900	8800	4240	7100	3450	4950
4	1200	4874	10780	4876	8910	3850	7200	3450	5330

In specimens with Pyrex glass, the spread of microhardness values is small, especially for «iron-cast iron-glass» specimens, and it does not increase as noticeably as in specimens with S88-5 glass. This is explained by the fact that metal-glass samples with Pyrex glass are less crystallized, as established by metallographic analysis. The reason for this is that Pyrex glass at the same temperatures has a higher viscosity [11] than with C88 glass-5. Due to this, the contact between the metal and glass worsens, and the mobility of the glass decreases. As a result, the matrix is not completely wetted with the Pyrex glass.

Intensive crystallization of glass at temperatures of 1150–1200 °C in samples with glass of the S88–5 brand is accompanied by a sharp increase in the average microhardness (**Fig. 6**). In samples with Pyrex glass, its crystallization and saturation with metal is less intense, which affects the microhardness. As can be seen from Table 1, in the temperature range 1000–1050 °C, a decrease in microhardness is observed, especially its lower limit. In samples with S88-5 grade glass, such a drop is not observed. This is due to the fact that, at these temperatures, the Pyrex glass has a significantly higher viscosity than the C88–5 glass and the gas released when the samples are heated, and great obstacles are created for reaching the surface. Due to the fact that particles of Pyrex glass at these temperatures contain many gas bubbles, this leads to a decrease in microhardness.

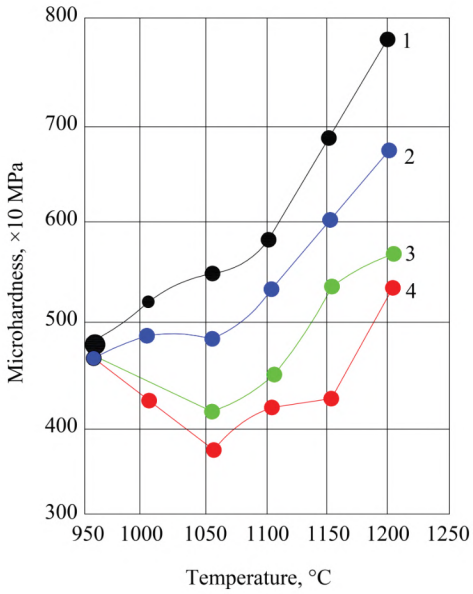

Fig. 6. Change of microhardness of glass particles of metal-glass materials from sintering temperature. With vacuum glass of grade C88-5: 1 – iron-cast iron; 2 – iron with Pyrex glass; 3 – iron-cast iron; 4 – iron

By measuring the microhardness of «iron-cast iron-glass» materials, let's found that in the samples sintered at temperatures above 1000 °C, the glass becomes very fragile and porous, therefore, when the microhardness changes, the glass regions are destroyed. However, at 1250 °C, there are quite strong glass areas, the microhardness of which is 10157 MPa (**Fig. 7, *d***).

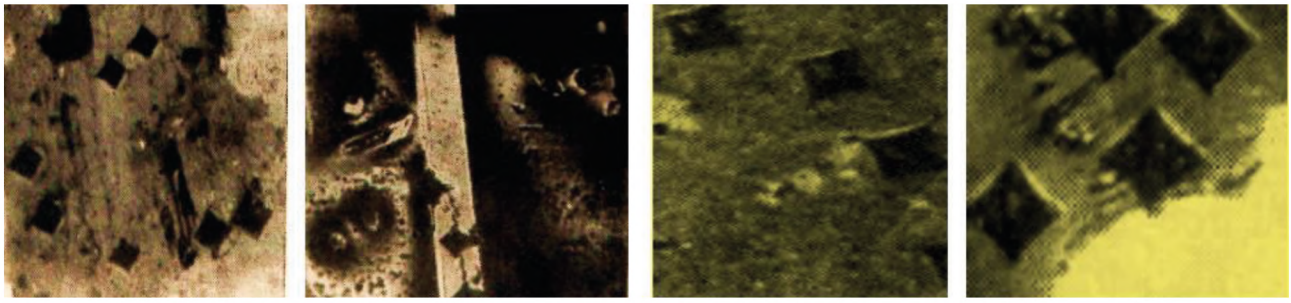

a *b* *c* *d*

Fig. 7. Distribution of microhardness in glass particles. *a, b* – iron with S88-5 grade glass and with Pyrex glass, sintering temperature 1150 °C, respectively; *c, d* – iron cast with glass of grade S88-5, sintering temperature 1000 and 1200 °C, respectively

At a temperature of 1000 °C, the microhardness of glass particles is in the range from 4280 to 5200 MPa, then it drops sharply. At 1150 °C – 1200 °C, along with brittle areas, there is a small number of areas with high microhardness. At a temperature of 1000 °C, apparently, saturation of the metal base with silicon occurs, since the hardness of iron at the boundary with glass increases to 4280–4980 MPa, although further from the boundary the microhardness drops to 1200 MPa (**Fig. 7, *c***). At a temperature of 12000 C, the microhardness of the iron base metal was 5200–5330 MPa. In some cases, when the sizes of crystalline inclusions allowed for detailed measurements, the microhardness of some minerals was determined. As a rule, the microhardness of the crystalline phase was higher than that of glass (**Fig. 7, *a*, *b***). For example, the microhardness of crystals of the «iron-cast iron-glass» base in the «iron-cast iron-glass» samples was equal to 9780–10487 MPa.

The results obtained and the recommendations given can be applied in the ranges of conditions that apply to parts of household appliances operating under conditions of intense wear at

a contact load of 2–8 MPa, friction rate $V = 2.1$ m/s. The highest mechanical and antifriction properties are exhibited by samples containing 30–50 wt % cast iron with particle sizes from 100 to 160 μm and 2–6 wt % glass powder (50–200 μm), the rest being iron.

The results obtained substantiate the use of the investigated powdered iron-cast iron-glass composite material with a porosity of 8–16 % as an antifrictional purpose for parts of household appliances.

4. Conclusions

The proposed approach to the problem of saturation of glass with a metal, taking into account mutual diffusion, makes it possible to establish: saturation of glass with a base metal depends on the viscosity of glass at sintering temperatures and is accompanied by an increase in microhardness and refractive indices; the saturation of glass with the base metal depends on the degree of affinity of this metal for oxygen.

It is shown that the microhardness of particles of vacuum glass of grade S88-5 after sintering metal-glass samples increases by 27 % than in samples with Pyrex glass.

When sintering «iron-cast iron-glass» materials, the metal base is saturated with silicon, which leads to an increase in the hardness of iron by 1.8 times.

The results obtained substantiate the use of the investigated powdered iron-cast iron-glass composite material as an antifriction material.

References

[1] Raichenko, O. I. (2016). Model of Compaction Process of a Porous Powder Elastic-Viscous Material at Electric Sintering. Metallofizika i noveishie tekhnologii, 38 (5), 635–645. doi: https://doi.org/10.15407/mfint.38.05.0635

[2] Dinesh, M., Ravindran, R. (2018). Fabrication of Aluminium AA7075 Reinforced by Zinc Metal Matrix Composites and Their Wear Behaviour Analysis. Metallofizika i noveishie tekhnologii, 39 (11), 1497–1510. doi: https://doi.org/10.15407/mfint.39.11.1497

[3] Vasil'ev, V. V., Protasov, V. D. (1990). Kompozitsionnye materialy. Moscow: Mashinostroenie, 512.

[4] Aslanov, J. N., Abasova, S. M., Huseynli, Z. S. (2020). The management of characteristics of the new two-layer rubber matrix seals. EUREKA: Physics and Engineering, 5, 60-68. doi: https://doi.org/10.21303/2461-4262.2020.001401

[5] Lyubimova, O. N., Solonenko, E. P. (2016). Modeling of the mismatched glass-to-metal interface behavior with regard to joint properties. Fizicheskaya mezomehanika, 19 (2), 114–119. doi: http://doi.org/10.24411/1683-805X-2016-00058

[6] Lyubimova, O. N., Morkovin, A. V., Dryuk, S. A., Nikiforov, P. A. (2014). Structure and constitution of glass and steel compound in glass-metal composite. AIP Conference Proceedings, 1623, 379. doi: https://doi.org/10.1063/1.4901492

[7] Dzhabbarov, T. G. (1992). Razrabotka kompozitsionnyh poroshkovyh materialov «Zhelezo-chugun-steklo» dlya detaley bytovoy tehniki. Novocherkassk.

[8] Vlasova, S. G. (2013). Osnovy himicheskoy tehnologii stekla. Ekaterinburg: Izd-vo Ural. un-ta, 108.

[9] Merer, H. (2011). Diffuziya v tverdyh telah. Moscow: Intellekt, 536.

[10] Aslanov, J. N. (2020). New model rubber matrix for connectors application of sealers. Equipment. Technologies. Material, 1 (3).

[11] Babanli, M. B. (2018). Theory and Practice of Material Development Under Imperfect Information. Advances in Intelligent Systems and Computing, 4–14. doi: https://doi.org/10.1007/978-3-030-04164-9_4

[12] Babanli, M., Karimov, R., Bayramov, A., Abbasov, I. I. (2019). An impact of the ladle lining on the refining of reinforced steel when blowing with powders. Eastern-European Journal of Enterprise Technologies, 5 (1 (101)), 65–71. doi: https://doi.org/10.15587/1729-4061.2019.178015

Received date 21.07.2020
Accepted date 25.01.2021
Published date 29.01.2021

Original Research Article: full paper

(2021), «EUREKA: Physics and Engineering»
Number 1

COMPARATOR IDENTIFICATION IN THE CONDITIONS OF BIFUZZY INITIAL DATA

Lev Raskin
Department of Distributed information systems and cloud technologies[1]

Oksana Sira
Department of Distributed information systems and cloud technologies[1]
topology@ukr.net

Tetiana Katkova
Department of Cyber security
University of Customs and Finance
2/4 V. Vernadsky str., Dnipro, Ukraine, 49000
777-kit@ukr.net

[1]*National Technical University «Kharkiv Polytechnic Institute»*
2 Kyrpychova str., Kharkiv, Ukraine, 61002

Abstract

When solving a large number of problems in the study of complex systems, it becomes necessary to establish a relationship between a variable that sets the level of efficiency of the system's functioning and a set of other variables that determine the state of the system or the conditions of its operation. To solve this problem, the methods of regression analysis are traditionally used, the application of which in many real situations turns out to be impossible due to the lack of the possibility of direct measurement of the explained variable. However, if the totality of the results of the experiments performed can be ranked, for example, in descending order, thus forming a system of inequalities, the problem can be presented in such a way as to determine the coefficients of the regression equation in accordance with the following requirement. It is necessary that the results of calculating the explained variable using the resulting regression equation satisfy the formed system of inequalities. This task is called the comparator identification task.

The paper proposes a method for solving the problem of comparator identification in conditions of fuzzy initial data. A mathematical model is introduced to describe the membership functions of fuzzy parameters of the problem based on functions (L–R)-type. The problem is reduced to a system of linear algebraic equations with fuzzy variables.

The analytical relationships required for the formation of a quality criterion for solving the problem of comparator identification in conditions of fuzzy initial data are obtained. As a result, a criterion for the effectiveness of the solution is proposed, based on the calculation of membership functions of the results of experiments, and the transformation of the problem to a standard problem of linear programming is shown. The desired result is achieved by solving a quadratic mathematical programming problem with a linear constraint. The proposed method is generalized to the case when the fuzzy initial data are given bifuzzy.

Keywords: regression analysis, comparator identification problem, fuzzy and bifuzzy values of the initial data.

DOI: 10.21303/2461-4262.2021.001609

1. Introduction

In the process of studying complex systems of various natures, it becomes necessary to build a mathematical model in the form of a regression equation. Such equations set the level of efficiency of the system operation depending on the variables that determine the state of the system or the conditions of its operation. Traditionally, the method of least squares is used to calculate the coefficients of the regression model, and the task may be to determine the coefficients of the regression equation in such a way that the results of calculating the explained variable using the resulting regression equation satisfy the formed system of inequalities. This task is called the comparator identification task.

The problem of comparator identification is a special, non-template version of regression analysis [1, 2], which arises in the following case. Let's suppose that as a result of a series of experiments in j-th of them, a set of values of factors (explanatory variables) $F_{j1}, F_{j2},\ldots, F_{jm}$ is obtained influencing the outcome of the experiment, and the value of the explained variable in this experiment – $y_j, j=1, 2,\ldots, n$. The resulting array of initial data is jointly processed in order to find a set of unknown coefficients $x_0, x_1,\ldots, x_m$ that define the regression equation:

$$y_j = x_0 + x_1F_{j1} + x_2F_{j2} + ... + x_mF_{jm}, \quad j = 1,2,...,n, \tag{1}$$

determining the dependence of the explained variable on the explanatory ones. The required set $X=(x_0, x_1,\ldots, x_m)$ is found by the least squares method using the formula:

$$X = (H^T H)^{-1} H^T Y,$$

where

$$H = \begin{pmatrix} 1 & F_{11} & F_{12} & ... & F_{1m} \\ 1 & F_{21} & F_{22} & ... & F_{2m} \\ ... & ... & ... & ... & ... \\ 1 & F_{n1} & F_{n2} & ... & F_{nm} \end{pmatrix}, \quad X = \begin{pmatrix} x_0 \\ x_1 \\ ... \\ x_m \end{pmatrix}, \quad Y = \begin{pmatrix} y_1 \\ y_2 \\ ... \\ y_n \end{pmatrix}. \tag{2}$$

Here F_{ji} – value of the i-th factor in the j-th experiment.

Let now, for some reason, the value of the explained variable in each experiment can't be determined, but they can be ranked, for example, in ascending order. Then (after renumbering) let's obtain a chain of inequalities:

$$y_1 < y_2 < ... < y_n. \tag{3}$$

Now the task is to find the vector X, which, taking into account (1), ensures the fulfillment of inequalities (3). The problem formulated in this way is called the comparator identification problem [3]. The following method for solving this problem is known [4–8]. Using (3), taking into account (1), let's form the following system of inequalities:

$$\begin{aligned} &y_1 - y_2 = x_1(F_{11} - F_{21}) + x_2(F_{12} - F_{22}) + ... + x_m(F_{1m} - F_{2m}) < 0, \\ &y_2 - y_3 = x_1(F_{21} - F_{31}) + x_2(F_{22} - F_{32}) + ... + x_m(F_{2m} - F_{3m}) < 0, \\ &..... \\ &y_{n-1} - y_n = x_1(F_{n-1,1} - F_{n1}) + x_2(F_{n-1,2} - F_{n2}) + ... + x_m(F_{n-1,m} - F_{nm}) < 0. \end{aligned} \tag{4}$$

System of inequalities (4) by adding positive $x_{m+1}, x_{m+2},\ldots, x_{m+n-1}$ is transformed to the system of equalities:

$$\sum_{i=1}^{m} x_i r_{ji} + x_{m+j} = 0, \quad j = 1,2,...,n-1,$$

$$x_i \geq 0, \quad x_{m+j} > 0, \tag{5}$$

$$r_{ji} = F_{ji} - F_{j+1,i}, \quad i = 1,2,...,m, \quad j = 1,2,...,n-1.$$

The problem is to find a set of variables $x_0, x_1, \ldots, x_m, x_{m+1}, x_{m+2},\ldots, x_{m+n-1}$, satisfying equations (5). In order to eliminate the trivial zero solution to the problem ($x_i=0$, $i=1, 2,\ldots, m+n-1$), let's add one more constraint:

$$\sum_{i=1}^{m} x_i + \sum_{j=1}^{n-1} x_{m+j} = 1. \tag{6}$$

The resulting system of linear algebraic equations (5), (6) is redefined and, possibly, inconsistent. Therefore, a natural approach to solving it is to minimize the quadratic form:

$$L(X) = \sum_{j=1}^{n-1} \left(\sum_{i=1}^{m} x_i r_{ji} + x_{m+j} \right)^2. \tag{7}$$

Taking into account the constraint (6).

Let's solve the formulated problem of mathematical programming by the method of indefinite Lagrange multipliers. The Lagrange function has the form.

$$\Phi(X)=\sum_{j=1}^{n-1}\left(\sum_{i=1}^{m}x_i r_{ji}+x_{m+j}\right)^2-\lambda\left(\sum_{i=1}^{m}x_i+\sum_{j=1}^{n-1}x_{m+j}-1\right). \tag{8}$$

So,

$$\frac{d\Phi(X)}{dx_k}=2\sum_{j=1}^{n-1}\left(\sum_{i=1}^{m}x_i r_{ji}+x_{m+j}\right)r_{jk}-\lambda=2\left[\sum_{i=1}^{m}x_i\sum_{j=1}^{n-1}r_{ji}r_{jk}+\sum_{j=1}^{n-1}x_{m+j}\cdot r_{jk}\right]-\lambda=$$

$$=2\sum_{i=1}^{m}x_i c_{ki}+2\sum_{j=1}^{n-1}x_{m+j}\cdot r_{jk}-\lambda=0,$$

$$c_{ki}=\sum_{j=1}^{n-1}r_{ji}\cdot r_{jk},\quad k=1,2,...,m.$$

Hence,

$$\sum_{i=1}^{m}x_i c_{ki}+\sum_{j=1}^{n-1}x_{m+j}\cdot r_{jk}=\frac{\lambda}{2},\quad k=1,2,...,m. \tag{9}$$

Further,

$$\frac{d\Phi}{dx_{m+j}}=2\left(\sum_{i=1}^{m}x_i r_{ji}+x_{m+j}\right)-\lambda=0,$$

hence,

$$\sum_{i=1}^{m}x_i r_{ji}+x_{m+j}=\frac{\lambda}{2},\quad j=1,2,...,n-1. \tag{10}$$

Relations (9) and (10) form a system of linear algebraic equations containing $m+n-1$ equations and the same number of unknowns. Let's introduce the matrix M of coefficients in front of the unknowns, the vector column of unknowns $X^T=(x_1,\ \ldots,\ x_m,\ x_{m+1},\ldots,\ x_{m+n-1})$, as well as the column of free terms $\Lambda^T=1/2(\lambda,\lambda,...,\lambda)$, $\dim\Lambda=(n-1)\times 1$. Then the control system (9), (10) in matrix form has the form:

$$MX=\Lambda.$$

Hence,

$$X=M^{-1}\Lambda. \tag{11}$$

Using (9) and (10), let's consider the structure of the matrix M.

$$M=\left(\begin{array}{cccc|cccc}
c_{11} & c_{12} & ... & c_{1m} & r_{11} & r_{21} & ... & r_{n-1,1}\\
c_{21} & c_{22} & ... & c_{2m} & r_{12} & r_{22} & ... & r_{n-1,2}\\
... & ... & ... & ... & ... & ... & ... & ...\\
c_{m1} & c_{m2} & ... & c_{mn} & r_{1m} & r_{2m} & ... & r_{n-1,m}\\
- & - & - & - & - & - & - & -\\
r_{11} & r_{12} & ... & r_{1m} & 1 & 0 & ... & 0\\
r_{21} & r_{22} & ... & r_{2m} & 0 & 1 & ... & 0\\
... & ... & ... & ... & ... & ... & ... & ...\\
r_{n-1,1} & r_{n-1,2} & ... & r_{n-1,m} & 0 & 0 & ... & 1
\end{array}\right)=\left(\begin{array}{c|c}
C & R\\
- & -\\
R^T & I
\end{array}\right),$$

$$\dim C=m\times m,\ \ \dim R=m\times(n-1),\ \ \dim I=(n-1)\times(n-1),$$

$$\dim M=(m+n-1)\times(m+n-1)=Q\times Q.$$

The block character of the matrix M allows to use the Frobenius formula [9]:

$$M^{-1}=\begin{pmatrix} M_1 & M_2 \\ M_3 & M_4 \end{pmatrix}^{-1}=\left(\begin{array}{c|c} M_1^{-1}+M_1^{-1}M_2H^{-1}M_3M_1^{-1} & -M_1^{-1}M_2H^{-1} \\ \hline -H^{-1}M_3M_1^{-1} & H^{-1} \end{array}\right),$$

$$H=M_4-M_3M_1^{-1}M_2.$$

Let's rewrite this formula taking into account that:

$$M_1=C,\ \ M_2=R,\ \ M_3=R^T,\ \ M_4=I.$$

Thus let's obtain:

$$M^{-1}=\begin{pmatrix} C & R \\ R^T & I \end{pmatrix}^{-1}=\left(\begin{array}{c|c} C^{-1}+C^{-1}RH^{-1}R^TC^{-1} & -C^{-1}RH^{-1} \\ \hline -H^{-1}R^TC^{-1} & H^{-1} \end{array}\right)=$$

$$=\begin{pmatrix} m_{11} & m_{12} & \ldots & m_{1q} & \ldots & m_{1Q} \\ m_{21} & m_{22} & \ldots & m_{2q} & \ldots & m_{2Q} \\ \ldots & \ldots & \ldots & \ldots & \ldots & \ldots \\ m_{q1} & m_{q2} & \ldots & m_{qq} & \ldots & m_{qQ} \\ \ldots & \ldots & \ldots & \ldots & \ldots & \ldots \\ m_{Q1} & m_{Q2} & \ldots & m_{Qq} & \ldots & m_{QQ} \end{pmatrix},$$

$$H=I-R^TA^{-1}R.$$

Since the dimensions of the matrices C and are less than the dimension of the matrix M, the block inversion of the matrix M simplifies the procedure for obtaining a set of dependences of the values of the variables x_q on λ, $q=1, 2,\ldots, Q$, $Q=m+n-1$.

Then from (11):

$$X=\begin{pmatrix} x_0 \\ x_1 \\ \ldots \\ x_Q \end{pmatrix}=\frac{1}{2}\begin{pmatrix} m_{11} & m_{12} & \ldots & m_{1Q} \\ m_{21} & m_{22} & \ldots & m_{2Q} \\ \ldots & \ldots & \ldots & \ldots \\ m_{Q1} & m_{Q2} & \ldots & m_{QQ} \end{pmatrix}\cdot\begin{pmatrix} \lambda \\ \lambda \\ \ldots \\ \lambda \end{pmatrix}=\frac{\lambda}{2}\begin{pmatrix} m_{11} & m_{12} & \ldots & m_{1Q} \\ m_{21} & m_{22} & \ldots & m_{2Q} \\ \ldots & \ldots & \ldots & \ldots \\ m_{Q1} & m_{Q2} & \ldots & m_{QQ} \end{pmatrix}\cdot\begin{pmatrix} 1 \\ 1 \\ \ldots \\ 1 \end{pmatrix}.$$

Hence,

$$x_s=\frac{\lambda}{2}\sum_{q=1}^{Q}m_{sq},\ \ s=1,2,\ldots,Q.$$

Now, using (6), let's find the value λ:

$$\sum_{s=1}^{Q}x_s=\frac{\lambda}{2}\sum_{s=1}^{Q}\sum_{q=1}^{Q}m_{sq}=1.$$

Hence,

$$\frac{\lambda}{2}=\frac{1}{\sum\limits_{s=1}^{Q}\sum\limits_{q=1}^{Q}m_{sq}}.$$

Then

$$x_s = \frac{\sum_{q=1}^{Q} m_{sq}}{\sum_{s=1}^{Q}\sum_{q=1}^{Q} m_{sq}}, \quad s = 1,2,...,Q.$$

The solution to the problem is obtained. However, it should be noted that the problem of comparator identification becomes much more complicated if its initial data are not accurate. Let, for example, the values of factors in a series of experiments are described unclearly [10]. In this case, let's assume that on the basis of all available information, membership functions of the corresponding fuzzy numbers can be constructed. It is clear that the method described above for solving the standard problem of comparator identification under these conditions can't be used. The indistinctness of the initial data gives rise to the indistinctness of the result. Based on this, it should be recognized that the research is relevant, the results of which allow to solve this problem.

The paper proposes a method for solving the problem of comparator identification in conditions of fuzzy initial data. A mathematical model is introduced to describe the membership functions of fuzzy parameters of the problem based on functions (L–R)-type. The problem is reduced to a system of linear algebraic equations with fuzzy variables.

The desired result is achieved by solving a quadratic mathematical programming problem with a linear constraint. The proposed method is generalized to the case when the fuzzy initial data are given bifuzzy.

2. The aim and objectives of research

The aim of research is to develop a method for solving the problem of comparator identification with indistinctly specified initial data.

To achieve the aim, the following objectives must be solved:

1. Formulate the correct formulation of the comparator identification problem under conditions when the uncertainty of the initial data is described in terms of fuzzy mathematics.

2. Justify the quality criterion for solving the comparator identification problem with fuzzy initial data.

3. Develop a procedure for solving the problem of comparator identification when choosing fuzzy numbers (L–R)-type as input data.

3. Results of developing a method for solving the problem

3. 1. Problem statement

Let a series of experiments be carried out, in each of which the values of influencing factors are fuzzy numbers with known membership functions $\mu(F_{ji})$, $j=1, 2,\ldots, n$, $i=1, 2,\ldots, m$. Let, in addition, the unknown values of the explained variable can be ranged, as a result of which a system of inequalities (3) is obtained. It is required to find a vector X that provides the calculation of a set of values of the explained variable, which satisfies (3) and optimizes the selected criterion.

Let's consider the following scheme for solving the problem of comparator identification. First, let's choose the type of analytical description of the membership functions of fuzzy initial data. Then let's construct a mathematical model of the problem, on the basis of which let's formulate a naturally interpreted and easily computable criterion for the quality of the solution to the identification problem. At the end of the solution, let's develop a method for optimizing the selected criterion.

3. 2. Justification of the quality criterion for solving the problem of comparator identification with fuzzy initial data

In the practice of solving various problems of fuzzy mathematics, an extensive set of types of membership functions of fuzzy numbers is used, for example, triangular, trapezoidal, Gaussian and many others. At the same time, recently more and more often the method of constructing

membership functions is used, based on the approximation of known types of membership functions by so-called functions (*L*–*R*)-type. The attractiveness of using membership functions (*L*–*R*)-type is explained by two important properties. First, these functions are easily and conveniently defined by a fixed set of values of numeric parameters. Secondly, in relation to numbers with a membership function (*L*–*R*)-type, a strict system of rules for performing algebraic operations has been developed [11]. To implement these rules, it is necessary and sufficient to know the values of the sets of numerical values of the parameters of the membership functions of fuzzy numbers – the operands. At the same time, in most practical problems, it is acceptable to use three-parameter membership functions (*L*–*R*) – of the type, having the form:

$$\mu(x)=\begin{cases}0, & x<m-\alpha,\\ L\left(\dfrac{m-x}{\alpha}\right), & m-\alpha\le x<m,\\ R\left(\dfrac{x-m}{\beta}\right), & m\le x\le m+\beta,\\ 0, & x>m+\beta.\end{cases} \tag{12}$$

Here m – modal value of the fuzzy number x, α – left fuzzy factor of the number x, β – right fuzzy factor of the number x.

Functions $L((m-x)/\alpha)$ and $R((x-m)/\beta)$ are arbitrary monotone functions for which:

$$L: \mathbf{R}\to[0;\,1],\ R: \mathbf{R}\to[0;\,1],\ L(0)=R(0)=1.$$

In what follows, using the generally accepted notation, to describe three-parameter fuzzy numbers (*L*–*R*)-type, instead of the cumbersome relation (12), let's use a much shorter symbolism:

$$y=<m,\ \alpha,\ \beta>.$$

3. 3. The procedure for solving the problem of comparator identification when choosing fuzzy numbers (*L*–*R*)-type as input data

In accordance with the proposed general scheme for solving the problem of comparator identification, let's introduce a regression model (1) and a system of inequalities (4). However, unlike the previous one, all components in (4) are fuzzy numbers. Therefore, all the differences $y_j-y_{j+1}, j=1, 2,\ldots, n-1$, are also fuzzy. Let's introduce a set of variables $\xi_j=y_j-y_{j+1}, j=1, 2,\ldots, n-1$, and in accordance with the rules for performing arithmetic operations on fuzzy numbers of the (*L*–*R*)-type [11], let's calculate the membership functions of fuzzy numbers $\xi_j, j=1, 2,\ldots, n-1$. Let's write down the corresponding summary of the rules for performing binary operations. Let's introduce a pair of fuzzy numbers:

$$F_1=<m_1,\alpha_1,\beta_1>\ \text{and}\ F_2=<m_2,\alpha_2,\beta_2>. \tag{13}$$

Then, when adding, let's obtain:

$$Z=F_1+F_2=<m_Z,\alpha_Z,\beta_Z>,$$

$$m_Z=m_1+m_2,\ \ \alpha_Z=\alpha_1+\alpha_2,\ \ \beta_Z=\beta_1+\beta_2;$$

subtracting let's obtain:

$$Z=F_1-F_2=<m_Z,\alpha_Z,\beta_Z>,$$

$$m_Z=m_1-m_2,\ \ \alpha_Z=\alpha_1+\beta_2,\ \ \beta_Z=\beta_1+\alpha_2;$$

multiplying let's obtain:

$$Z = F_1 \cdot F_2 =< m_Z, \alpha_Z, \beta_Z >, \tag{14}$$

$$m_Z = m_1 \cdot m_2, \quad \alpha_Z = m_1 \cdot \alpha_2 + m_2 \cdot \alpha_1 - \alpha_1 \cdot \alpha_2, \quad \beta_Z = m_1 \cdot \beta_2 + m_2 \cdot \beta_1 + \beta_1 \cdot \beta_2;$$

dividing let's obtain:

$$Z = F_1 \cdot F_2 =< m_Z, \alpha_Z, \beta_Z >,$$

$$m_Z = \frac{m_1}{m_2}, \quad \alpha_Z = \frac{m_2 \cdot \alpha_1 + m_1 \cdot \beta_2}{m_2 (m_2 + \beta_2)}, \quad \beta_Z = \frac{m_1 \cdot \alpha_2 + m_2 \cdot \beta_1}{m_2 (m_2 - \alpha_2)}.$$

Then

$$\xi_j = y_j - y_{j+1} = x_1 (F_{j1} - F_{j+1,1}) + x_2 (F_{j2} - F_{j+1,2}) + ... + x_m (F_{j-1,m} - F_{jm}).$$

Because

$$F_{ji} =< m_{ji}, \alpha_{ji}, \beta_{ji} >, \quad F_{j+1,i} =< m_{j+1,i}, \alpha_{j+1,i}, \beta_{j+1,i} >,$$

then

$$F_{ji} - F_{j+1,i} = r_{ji} =< m_{r_{ji}}, \alpha_{r_{ji}}, \beta_{r_{ji}} >,$$

$$m_{r_{ji}} = m_{ji} - m_{j+1,i}, \quad \alpha_{r_{ji}} = \alpha_{ji} + \beta_{j+1,i}, \quad \beta_{r_{ji}} = \beta_{ji} + \alpha_{j+1,i},$$

$$j = 1,2,...,n-1, \quad i = 1,2,...,m.$$

From relation (14), which determines the result before multiplying two fuzzy numbers, let's obtain formulas for the result of multiplying a fuzzy number by a crisp number.

Let's write a crisp number x_i using the notation used for describing fuzzy numbers (L–R)-type: x_i=<x_i, 0, 0>. Then the fuzzy result of multiplying the crisp number x_i by the fuzzy number r_{ji} will be:

$$x_i r_{ji} = \Delta_{ji} =< m_{\Delta_{ji}}, \alpha_{\Delta_{ji}}, \beta_{\Delta_{ji}} > .$$

Then

$$\xi_j = \sum_{i=1}^{m} x_i r_{ji} =< m_{\xi_j}, \alpha_{\xi_j}, \beta_{\xi_j} >, \tag{15}$$

$$m_{\xi_j} = \sum_{i=1}^{m} x_i m_{r_{ji}}, \quad \alpha_{\xi_j} = \sum_{i=1}^{m} x_i (\alpha_{ji} + \beta_{j+1,i}), \quad \beta_{\xi_j} = \sum_{i=1}^{m} x_i (\beta_{ji} + \alpha_{j+1,i}).$$

So,

$$\xi = \sum_{j=1}^{n-1} \xi_j = \sum_{j=1}^{n-1} \sum_{i=1}^{m} x_i r_{ji} =< m_\xi, \alpha_\xi, \beta_\xi >, \tag{16}$$

$$m_{\xi_j} = \sum_{j=1}^{n-1} m_{\xi_j} = \sum_{j=1}^{n-1} \sum_{i=1}^{m} x_i m_{r_{ji}}, \quad \alpha_\xi = \sum_{j=1}^{n-1} \alpha_{\xi_j} = \sum_{j=1}^{n-1} \sum_{i=1}^{m} x_i (\alpha_{ji} + \beta_{j+1,i}),$$

$$\beta_\xi = \sum_{j=1}^{n-1} \beta_{\xi_j} = \sum_{j=1}^{n-1} \sum_{i=1}^{m} x_i (\beta_{ji} + \alpha_{j+1,i}). \tag{17}$$

All analytical relationships required for the formation of a quality criterion for solving the problem of comparator identification in conditions of fuzzy initial data are obtained. The required set ($x_1, x_2,\ldots, x_m$), satisfying the normalization condition (6), should be chosen so that all fuzzy numbers $\xi_j, j=1, 2,\ldots, n–1$, are non-positive.

It is clear that the requirement of non-positiveness of the fuzzy numbers $\xi_j, j=1, 2,\ldots, n–1$, can't be met if the fuzzy numbers F_{ji} specifying the values of ξ_j are defined on an infinite carrier. However, if these fuzzy numbers are given on a compact medium, then the problem can be solved. Let, for example, fuzzy numbers F_{ji} have a triangular membership function:

$$\mu\left(F_{ji}\right)=\begin{cases}0, & F_{ji}<m_{ji}-\alpha_{ji},\\ \dfrac{F_{ji}-(m_{ji}-\alpha_{ji})}{\alpha_{ji}}, & m_{ji}-\alpha_{ji}\le F_{ji}<m_{ji},\\ \dfrac{(m_{ji}+\beta_{ji})-F_{ji}}{\beta_{ji}}, & m_{ji}\le F_{ji}<m_{ji}+\beta_{ji},\\ 0, & F_{ji}>m_{ji}+\beta_{ji}.\end{cases}$$

In this case, the maximum value of the fuzzy number F_{ji} is equal to $m_{ji}+\beta_{ji}$, and the maximum value of the number $F_{ji}–F_{j+1}$ is equal to $m_{ji}–m_{j+1,i}+\beta_{ji}+\alpha_{j+1,i}$.

Then the maximum possible value ξ_j on the set ($x_1, x_2, \ldots, x_m$) is determined by the relation:

$$\xi_{j\max}=\max_{x}\left[\sum_{i=1}^{m}x_i\left(m_{ji}-m_{j+1,i}+\beta_{ji}+\alpha_{j+1,i}\right)\right]. \tag{18}$$

In this case, the problem can be formulated as follows: find a set ($x_1, x_2, \ldots, x_m$) that satisfies the system of equations:

$$\sum_{i=1}^{m}x_i\left(m_{ji}-m_{j+1,i}+\beta_{ji}+\alpha_{j+1,i}\right)+x_{m+j}=0, \tag{19}$$

$$\sum_{i=1}^{m}x_i=1, \tag{20}$$

$$x_i\ge 0,\quad x_{m+j}\ge 0,\quad j=1,2,...,n-1,\quad i=1,2,...,m. \tag{21}$$

Simultaneous fulfillment of conditions (19), (21) ensures the non-positiveness of ξ_j, $j=1, 2,\ldots, n–1$. In the system of equations (19)–(21), the number of unknowns exceeds the number of equations. Therefore, as before, it is advisable to go over to the problem of minimizing a quadratic form.

In some cases, in accordance with the meaning of the identification problem, it is required that the inequalities $\xi_j<0, j=1, 2,\ldots, n–1$ are satisfied as convincingly as possible. Then the condition for maximizing the linear form can be added to (19)–(21):

$$L(x)=\sum_{i=1}^{n-1}x_{m+j}. \tag{22}$$

In this case, problem (19)–(22) is transformed to a standard linear programming problem. Its solution is the desired solution to the comparator identification problem under conditions of fuzzy input data.

Practice shows that uncertainty models formed using standard fuzzy mathematics tools make it possible to obtain an acceptable solution to a larger number of emerging problems. However, in many real-life situations, the nature of uncertainty is more complex than usual. In particular, this situation arises when trying to describe the uncertainty of demand with a fuzzy number with a triangular membership function. It turns out that the values of the lower and upper boundaries of the

uncertainty interval, as well as the modal value of this fuzzy number, based on the results of statistical processing of the initial data, can't be determined accurately. It seems natural to consider these values fuzzy. For a correct description of uncertainty in this case, it is advisable to use fuzzy numbers, the parameters of the membership functions of which are also fuzzy. The numbers obtained in this case were introduced by L. Zadeh in [10] and were called fuzzy numbers of type 2 (or fuzzy numbers of the second order, or bifuzzy numbers). Correct rules for performing arithmetic operations on second-order fuzzy numbers naturally generalize the rules proposed in [11]. Let's present those of them that will be used in the future for calculating the bi-fuzzy analogue of the objective function (19) in the problem of comparator identification. Let's introduce a pair of bifuzzy numbers F_1 and F_2 equal to:

$$F_1 =< m_1,\alpha_1,\beta_1 >,\quad F_2 =< m_2,\alpha_2,\beta_2 >,$$

$$m_1 =< m_{m_1},\alpha_{m_1},\beta_{m_1} >,\quad \alpha_1 =< m_{\alpha_1},\alpha_{\alpha_1},\beta_{\alpha_1} >,\quad \beta_1 =< m_{\beta_1},\alpha_{\beta_1},\beta_{\beta_1} >,$$

$$m_2 =< m_{m_2},\alpha_{m_2},\beta_{m_2} >,\quad \alpha_2 =< m_{\alpha_2},\alpha_{\alpha_2},\beta_{\alpha_2} >,\quad \beta_2 =< m_{\beta_2},\alpha_{\beta_2},\beta_{\beta_2} >.$$

Then, in accordance with (14),

$$z = F_1 - F_2 =< m_z,\alpha_z,\beta_z >,$$

$$m_z = m_1 - m_2 =< m_{m_1},\alpha_{m_1},\beta_{m_1} > - < m_{m_2},\alpha_{m_2},\beta_{m_2} >=< m_{m_z},\alpha_{m_z},\beta_{m_z} >,$$

$$m_{m_z} = m_{m_1} - m_{m_2},\quad \alpha_{m_z} = \alpha_{m_1} + \beta_{m_2},\quad \beta_{m_z} = \beta_{m_1} + \alpha_{m_2},$$

$$\alpha_z = \alpha_1 + \beta_2 =< m_{\alpha_1},\alpha_{\alpha_1},\beta_{\alpha_1} > + < m_{\beta_2},\alpha_{\beta_2},\beta_{\beta_2} >=< m_{\alpha_z},\alpha_{\alpha_z},\beta_{\alpha_z} >,$$

$$m_{\alpha_z} = m_{\alpha_1} - m_{\beta_2},\quad \alpha_{\alpha_z} = \alpha_{\alpha_1} + \alpha_{\beta_2},\quad \beta_{\alpha_z} = \beta_{\alpha_1} + \beta_{\beta_2};$$

$$\beta_z = \beta_1 + \alpha_2 =< m_{\beta_1},\alpha_{\beta_1},\beta_{\beta_1} > + < m_{\alpha_2},\alpha_{\alpha_2},\beta_{\alpha_2} >=< m_{\beta_z},\alpha_{\beta_z},\beta_{\beta_z} >,$$

$$m_{\beta_z} = m_{\beta_1} - m_{\alpha_2},\quad \alpha_{\beta_z} = \alpha_{\beta_1} + \alpha_{\alpha_2},\quad \beta_{\beta_z} = \beta_{\beta_1} + \beta_{\alpha_2}.$$

The obtained relations set the parameters of the membership function of the bifuzzy number $\xi_1 = F_1 - F_2$. The relations for the binomial numbers $\xi_j = F_j - F_{j+1}$, $j = 1, 2, \ldots, n-1$. Let's write the result of multiplying the number ξ_1 by the constant x_1. Using (14), it is easy to show that when multiplying a bifuzzy number by a constant, a bifuzzy number will be obtained, all the parameters of the membership functions of which will be equal to the corresponding parameters of the bifuzzy factor multiplied by this constant. Then:

$$\Delta_1 = \xi_1 x_1 =< m_\Delta,\alpha_\Delta,\beta_\Delta >,$$

$$m_\Delta =< m_{m_1}x_1,\alpha_{m_1}x_1,\beta_{m_1}x_1 >;\quad \alpha_\Delta =< m_{\alpha_1}x_1,\alpha_{\alpha_1}x_1,\beta_{\alpha_1}x_1 >;\quad \beta_\Delta =< m_{\beta_1}x_1,\alpha_{\beta_1}x_1,\beta_{\beta_1}x_1 >.$$

Finally, let's obtain a relation for calculating the parameters of the sum of bifuzzy numbers $\Delta_i = \xi_i x_i$. Wherein

$$\Delta = \sum_{i=1}^{m} \Delta_1 = \sum_{i=1}^{m} \xi_1 x_1 =< m_\Delta,\alpha_\Delta,\beta_\Delta >.$$

Because,

$$\Delta_i = \xi_i x_i =< m_{\Delta_i},\alpha_{\Delta_i},\beta_{\Delta_i} >,$$

$$m_{\Delta_i} =< m_{m_{\Delta_i}}x_i,\alpha_{m_{\Delta_i}}x_i,\beta_{m_{\Delta_i}}x_i >,\quad \alpha_{\Delta_i} =< m_{\alpha_{\Delta_i}}x_i,\alpha_{\alpha_{\Delta_i}}x_i,\beta_{\alpha_{\Delta_i}}x_i >,\quad \beta_{\Delta_i} =< m_{\beta_{\Delta_i}}x_i,\alpha_{\beta_{\Delta_i}}x_i,\beta_{\beta_{\Delta_i}}x_i >,$$

so,

$$m_\Delta = < \sum_{i=1}^{m} m_{m_{\Delta_i}} x_i, \sum_{i=1}^{m} \alpha_{m_{\Delta_i}} x_i, \sum_{i=1}^{m} \beta_{m_{\Delta_i}} x_i >,$$

$$\alpha_\Delta = < \sum_{i=1}^{m} m_{\alpha_{\Delta_i}} x_i, \sum_{i=1}^{m} \alpha_{\alpha_{\Delta_i}} x_i, \sum_{i=1}^{m} \beta_{\alpha_{\Delta_i}} x_i >,$$

$$\beta_\Delta = < \sum_{i=1}^{m} m_{\beta_{\Delta_i}} x_i, \sum_{i=1}^{m} \alpha_{\beta_{\Delta_i}} x_i, \sum_{i=1}^{m} \beta_{\beta_{\Delta_i}} x_i > .$$

Now, similarly to the previous one, let's write down the maximum value ξ_j.

$$m_\Delta = < \sum_{i=1}^{m} m_{m_{\Delta_i}} x_i, \sum_{i=1}^{m} \alpha_{m_{\Delta_i}} x_i, \sum_{i=1}^{m} \beta_{m_{\Delta_i}} x_i >,$$

$$\xi_{j\max} = \max_x \left[\sum_{i=1}^{m} m_{m_{\Delta_i}} x_i + \sum_{i=1}^{m} \beta_{m_{\Delta_i}} x_i + \sum_{i=1}^{m} m_{\beta_{\Delta_i}} x_i + \sum_{i=1}^{m} \beta_{\beta_{\Delta_i}} x_i \right] =$$
$$= \max_x \left(m_{m_{\Delta_i}} + \beta_{m_{\Delta_i}} + m_{\beta_{\Delta_i}} + \beta_{\beta_{\Delta_i}} \right) x_i.$$

Then the problem is formed as follows: find a set x_i, $i=1, 2,\ldots, m$, satisfying the system of equations:

$$\sum_{i=1}^{m} x_i (m_{m_{\Delta_i}} + \beta_{m_{\Delta_i}} + m_{\beta_{\Delta_i}} + \beta_{\beta_{\Delta_i}}) + x_{m+j} = 0, \tag{23}$$

$$\sum_{i=1}^{m} x_i = 1, \quad x_i \geq 0, \quad x_{m+j} \geq 0, \quad j = 1,2,...,n-1, \quad i = 1,2,...,m. \tag{24}$$

It is clear that the joint satisfaction of conditions (23), (24) ensures the non-positiveness of $\xi_j, j=1, 2,\ldots, n–1$, as required. Just as before, if for a specific identification problem it is necessary that the non-positiveness of ξ_j be maximally convincing, then the requirement of maximizing the linear form (22) is added to (23), (24), which reduces to a linear programming problem. It is clear that the solution obtained in this case is better than the previous one, since it is more stable with respect to possible errors in estimating the numerical values of the parameters of the membership functions of fuzzy initial data.

4. Discussion of the results of solving the problem of comparator identification in conditions of fuzzy initial data

Comparative identification is a method for solving the problem of regression analysis, the purpose of which is to establish the dependence of the explained variable on the explanatory variables (factors) that affect the explained variable. The comparator identification problem and the method for its solution have been developed and applied in cases when during the collection of initial data it is not possible to measure the values of the variable being explained, but the results of experiments can be ranked. The paper considers a variant of the comparator identification problem, which is important for practice, when the measurement of the values of the factors in each experiment is not clearly specified. Such problems arise in various practical applications: to increase the efficiency of vocational guidance activities of educational institutions [12], to predict the emergence and development of social processes, including negative trends in society [13], in the management of industrial waste [14] and technological processes in industry [15], construction [16]. The expediency of applying the proposed solutions in these areas is justified by the complexity, and sometimes the impossibility of measuring and evaluating the variables that describe the processes. If, in addition to the resulting uncertainties caused by these objective facts, take into account the uncertainties caused by the need to attract expert opinion and obtain appropriate

expert assessments, there is reason to assert the effectiveness of comparator identification in conditions of fuzzy description. The latter is especially important in areas with an increased level of requirements for the safety of the operation and operation of facilities [17–19]. Taking into account the fact that the solution of problems arising in these applications by traditional methods of regression analysis is impossible, the method proposed in this work, which reduces the problem to solving the arising system of linear algebraic equations, the parameters of which are given indistinctly, is an effective mathematical apparatus. For the case when all fuzzy parameters are specified on a compact carrier, the method provides a solution to a fuzzy system of linear algebraic equations. The proposed computational procedure has been developed and can be applied in a situation where the uncertainty in the value of factors is described in terms of second-order fuzzy numbers. The paper also considered a possible enhancement of the method, which consists in the following. From the set of feasible options for solving the problem, the most stable is selected with respect to possible errors in setting the parameters of the membership functions of fuzzy initial data.

A possible direction for further research is the development of a method for solving the comparator identification problem for the case when the initial data are specified inaccurately [20]. To solve the problem, it is possible to use the technologies proposed in [21, 22].

5. Conclusions

1. The correct formulation of the comparator identification problem is formulated for the case when the initial data are given in terms of fuzzy mathematics. In this case, to describe the membership function of the corresponding fuzzy numbers, functions (L–R)-type are selected.

2. All analytical relationships required for the formation of a quality criterion for solving the problem of comparator identification in conditions of fuzzy initial data have been obtained. As a result, a criterion for the effectiveness of the solution is proposed, based on the calculation of membership functions of the results of experiments, and the transformation of the problem to a standard problem of linear programming is shown. The solution to the latter is what is sought for comparator identification under conditions of fuzzy initial data.

3. A procedure for solving the problem of comparator identification is proposed, when the initial data are fuzzy numbers (L–R)-type. The solution obtained by its implementation is more stable with respect to possible errors in estimating the numerical values of the parameters of the membership functions of fuzzy initial data.

References

[1] Vuchkov, I., Bachdzhieva, L., Solakov, B. (1987). Prikladnoy lineyniy regressionnyy analiz. Moscow: Finansy i statistika, 239.

[2] Rao, J. N. K., Subrahmaniam, K. (1971). Combining Independent Estimators and Estimation in Linear Regression with Unequal Variances. Biometrics, 27 (4), 971. doi: https://doi.org/10.2307/2528832

[3] Petrov, K. E., Kryuchkovskiy, V. V. (2009). Komparatornaya strukturno-parametricheskaya identifikatsiya modeley skalyarnogo mnogofaktornogo otsenivaniya. Kherson: Oldi-plyus, 294.

[4] Dotsenko, N. V., Kosenko, N. V. (2012). Comparator authentication of parameters of model of multifactor evaluation. Systemy upravlinnia, navihatsiyi ta zviazku, 2 (1 (21)), 140–143

[5] Bondarenko, M. F., Shabanov-Kushnarenko, Yu. P., Sharonova, N. V. (2010). The ideas algebra interpretations. Bionics of Intelligence, 2 (73), 74–86.

[6] Petrov, E., Petrov, K. (2014). Komparatornaya identifikatsiya modeley mnogofaktornogo otsenivaniya. Saarbrucken: Palmarium Academic Publishing, 224.

[7] Suprun, T. S., Shabanov-Kushnarenko, S. Y. (2014). Isomorphism of predicate model comparator identification. Radio Electronic, Computer Science, Control, 14–24.

[8] Raskin, L. G., Seraja, O. W. (2015). Information problems of canonical regression analysis. Systemy obrobky informatsiyi, 10, 230–234.

[9] Gantmaher, F. R. (2004). Teoriya matrits. Moscow: Fizmatlit, 560.

[10] Zadeh, L. A. (1965). Fuzzy sets. Information and Control, 8 (3), 338–353. doi: https://doi.org/10.1016/s0019-9958(65)90241-x

[11] Raskin, L., Sira, O. (2020). Performing arithmetic operations over the (L–R)-type fuzzy numbers. Eastern-European Journal of Enterprise Technologies, 3 (4 (105)), 6–11. doi: https://doi.org/10.15587/1729-4061.2020.203590

[12] Yeremenko, B., Ryabchun, Y., Ploska, G. (2018). The introduction of intellectual system for evaluating professional abilities of applicants into the activities of educational institutions. Technology audit and production reserves, 6 (2 (44)), 22–26. doi: https://doi.org/10.15587/2312-8372.2018.149680

[13] Mulesa, O. (2015). Adaptation of fuzzy c-means method for determination the structure of social groups. Technology Audit and Production Reserves, 2 (2 (22)), 73–76. doi: https://doi.org/10.15587/2312-8372.2015.41014

[14] Baranova, A., Samoilenko, N., Pitak, I. (2020). Forecasting of formation of pharmaceutical glass waste taking into account the COVID-19 database. ScienceRise, 4, 46–52. doi: https://doi.org/10.21303/2313-8416.2020.001392

[15] Domin, D. (2013). Artificial orthogonalization in searching of optimal control of technological processes under uncertainty conditions. Eastern-European Journal of Enterprise Technologies, 5 (9 (65)), 45–53. doi: https://doi.org/10.15587/1729-4061.2013.18452

[16] Popyk, N. (2014). Ontological approach and fuzzy modeling to describe objects of living environment. Technology Audit and Production Reserves, 6 (4 (20)), 7–9. doi: https://doi.org/10.15587/2312-8372.2014.32875

[17] Kartavykh, S., Komandyrov, O., Kulikov, P., Ploskyi, V., Poltorachenko, N., Terenchuk, S. (2020). Adaptation of fuzzy inference system to solve assessment problems of technical condition of construction objects. Technology Audit and Production Reserves, 3 (2 (53)), 52–55. doi: https://doi.org/10.15587/2706-5448.2020.205364

[18] Grigorovskiy, P., Terentyev, O., Mikautadze, R. (2017). Development of the technique of expert assessment in the diagnosis of the technical condition of buildings. Technology Audit and Production Reserves, 2 (2 (40)), 10–15. doi: https://doi.org/10.15587/2312-8372.2018.128548

[19] Pasko, R., Terenchuk, S. (2020). The use of neuro-fuzzy models in expert support systems for forensic building-technical expertise. ScienceRise, 2, 10–18. doi: https://doi.org/10.21303/2313-8416.2020.001278

[20] Pawlak, Z. (1982). Rough sets. International Journal of Computer & Information Sciences, 11 (5), 341–356. doi: https://doi.org/10.1007/bf01001956

[21] Raskin, L., Sira, O. (2016). Fuzzy models of rough mathematics. Eastern-European Journal of Enterprise Technologies, 6 (4 (84)), 53–60. doi: https://doi.org/10.15587/1729-4061.2016.86739

[22] Raskin, L., Sira, O. (2016). Method of solving fuzzy problems of mathematical programming. Eastern-European Journal of Enterprise Technologies, 5 (4 (83)), 23–28. doi: https://doi.org/10.15587/1729-4061.2016.81292

Received date 20.05.2020
Accepted date 15.01.2021
Published date 29.01.2021